Nonlinear photonics in mid-infrared quantum cascade lasers

Louise Jumpertz

ParisTech
INSTITUT DES SCIENCES ET TECHNOLOGIES
PARIS INSTITUTE OF TECHNOLOGY

TELECOM ParisTech

2016-ENST-0064

EDITE - ED 130

Doctorat ParisTech

T H È S E

pour obtenir le grade de docteur délivré par

TELECOM ParisTech

Spécialité « Electronique et Communications »

présentée et soutenue publiquement par

Louise JUMPERTZ

le 03 novembre 2016

Photonique non-linéaire dans les lasers à cascade quantique moyen infrarouges

Directeur de thèse : **Frédéric GRILLOT**
Co-encadrement de la thèse : **Mathieu CARRAS**

Jury

Prof. Krassimir PANAJOTOV, Vrije Universiteit Brussel, Belgique	Rapporteur
Prof. Carlo SIRTORI, Université Paris Diderot, France	Rapporteur
Dr. Philippe ADAM, Direction Générale de l'Armement, France	Examinateur
Prof. Wolfgang ELSÄSSER, Technische Universität Darmstadt, Allemagne	Examinateur
Dr. Tim NEWELL, US Air Force Research Laboratories, USA	Examinateur
Prof. Marc SCIAMANNA, CentraleSupélec Metz, France	Examinateur

TELECOM ParisTech
école de l'Institut Mines-Télécom - membre de ParisTech
46 rue Barrault 75013 Paris - (+33) 1 45 81 77 77 - www.telecom-paristech.fr

T H È S E

Nonlinear photonics in mid-infrared quantum cascade lasers

Louise Jumpertz

Abstract

Mid-infrared quantum cascade lasers are unipolar semiconductor lasers, which have become widely used sources for applications such as gas spectroscopy, free-space communications or optical countermeasures. Applying external perturbations such as optical feedback or optical injection leads to a strong modification of the quantum cascade laser properties. Optical feedback impacts the static properties of mid-infrared Fabry-Perot and distributed feedback quantum cascade lasers, inducing power increase, threshold reduction, modification of the optical spectrum, which can become either single- or multimode, and enhanced beam quality of broad-area transverse multimode lasers. It also leads to a different dynamical behavior, and a quantum cascade laser subject to optical feedback can oscillate periodically or even become chaotic: this work provides the very first analysis of optical instabilities in the mid-infrared range. A numerical study of optical injection furthermore proves that quantum cascade lasers can injection-lock over a few gigahertz, where they should experience enhanced stability and especially improved modulation bandwidth. Furthermore, some promising dynamics appear outside the locking range with periodic oscillations at a tunable frequency or high-intensity events. A quantum cascade laser under external control could therefore be a source with enhanced properties for the usual mid-infrared applications, but could also address new applications such as tunable photonic oscillators, extreme events generators, chaotic LIDAR, chaos-based secured communications or unpredictable countermeasures.

Résumé

Les lasers à cascade quantique émettant dans le moyen-infrarouge sont des lasers semi-conducteurs unipolaires qui sont devenus des sources couramment utilisées pour des applications telles que la spectroscopie de gaz, les communications en espace libre ou les contre-mesures optiques. Appliquer une perturbation externe, typiquement une contre-réaction optique ou de l'injection optique, entraîne une forte modification des propriétés d'émission du laser à cascade quantique. La contre-réaction optique influe sur les propriétés statiques du laser Fabry-Perot ou à contre-réaction répartie, conduisant à une augmentation de la puissance, à une diminution du seuil, à une modification du spectre optique qui peut devenir monomode ou multimode, et à une amélioration de la qualité de faisceau dans les lasers à ruban large fortement multimode transverses. Cela induit également un comportement dynamique différent, et un laser à cascade quantique soumis à de la contre-réaction peut osciller périodiquement ou même devenir chaotique : ce travail présente la toute première observation d'instabilités optiques dans le moyen-infrarouge. De plus, une étude numérique de l'injection optique montre que les lasers à cascade quantique peuvent se verrouiller optiquement sur une plage de plusieurs gigahertz, sur laquelle leur stabilité devrait être accrue et leur bande passante de modulation significativement augmentée. Une dynamique prometteuse apparaît également en dehors de la zone de verrouillage, avec l'apparition d'oscillations périodiques à une fréquence accordable ainsi que des événements isolés de forte intensité. Un laser à cascade quantique soumis à un contrôle externe peut donc être une source très performante pour les applications moyen-infrarouges usuelles, mais pourrait aussi en adresser de nouvelles, telles que des oscillateurs photoniques accordables, des générateurs d'événements rares, des LIDAR chaotiques, des communications sécurisées par chaos ou des contre-mesures imprévisibles.

Acknowledgments

I would like to express my deepest gratitude to both my supervisors, Prof. Frédéric Grillot and Dr. Mathieu Carras, whose guidance made these three years a fruitful and memorable experience. Mathieu, thank you for our fruitful discussions and for your always pertinent advice. Frédéric, thank you so much for your time, support, advice and guidance, which allowed me to take the best out of my PhD.

Special thanks to Grégory for his valuable advice and for the time he spend to help me with the lab work, and to Fahem and Ali for their technical support. Kevin as well, with your help I became an expert in simulations and Matlab, thank you so much !

I am grateful to the research teams at III-V Lab, mirSense and Télécom ParisTech for making me feel welcome in all three places. Thank you to Prof. Marc Sciamanna from CentraleSupélec Metz, Prof. Wolfgang Elsässer from TU Darmstadt, Dr. Tim Newell from US Air Force Research Labs and the team at Université Rennes 1 for the fruitful collaborations. I acknowledge the Direction Générale de l'Armement for founding this PhD, and am especially grateful to Dr. Philippe Adam, who helped us link the research with the possible applications.

Many thanks to my friends at Télécom for their advices, encouragements and for the wonderful journeys we did through joyful lunches, cultural exchanges, endless debates or culinary discoveries. I will miss you guys ! A special thanks also to Clément and Simon for all the good work we did together and for everything else (gaming nights doesn't sound so politically correct in English).

Many thanks also to my friends from Supop or elsewhere, always ready to meet with me when I needed to do something else. Sophie, I miss our coffee breaks since I moved away from TRT. Aurore, Delphine and Marie-Aude, our swimming session was sometimes the

best moment of the week. BenJ, thanks for enduring us speaking non-stop about our PhDs during our trips across Europe (and in Brittany). Pauline, your 10 E-Mails a day helped me survive (and sometimes it was even about scientific issues). And Elsa, thanks for always having a stupid joke to cheer me up.

Finally, none of this would have been possible without the support of my family, thanks for always being there, for acting as if you understood what I'm talking about, and lately for your encouragements in my search for a job, very enthusiastic when the opportunity is far away in a nice touristic country ! Marie and Etienne, next year it's your turn to suffer, so best of luck to you both :-)

In *Witches abroad*, Terry Pratchett wrote:

" Because the universe was full of ignorance all around and the scientist panned through it like a prospector crouched over a mountain stream, looking for the gold of knowledge among the gravel of unreason, the sand of uncertainty. [...] But the trouble was that ignorance became more interesting, [...] and people stopped patiently building their little houses of rational sticks in the chaos of the universe and started getting interested in the chaos itself - partly because it was a lot easier to be an expert on chaos, but mostly because it made really good patterns that you could put on a t-shirt."

So let's study chaos...

Contents

List of Figures

List of Tables

Acronyms

AM Amplitude Modulation

BA Broad-area

CPR Chirp to Power Ratio **CW** Continuous-Wave

DFB Distributed Feedback

DT Double Trench

ESA Electrical Spectrum Analyzer

FM Frequency Modulation

FP Fabry-Perot

FTIR Fourier Transform Infrared

FWHM Full-Width at Half-Maximum

HR High-Reflectivity

HVPE Hydride Vapor Phase Epitaxy

ICL Interband Cascade Laser

IR Infrared

LEF Linewidth Enhancement Factor

LFF Low Frequency Fluctuations

LOC Large Optical Cavity

MBE Molecular Beam Epitaxy

MCT Mercury-Cadmium-Telluride

MOCVD Metal-Organic Chemical Vapor Deposition

OPO Optical Parametric Oscillator

PPLN Periodically Poled Lithium Niobate

QCL Quantum Cascade Laser

RAM Residual Amplitude Modulation

RIN Relative Intensity Noise

RF Radio-Frequency

SEM Scanning Electron Microscopy

SNR Signal to Noise Ratio

VCSEL Vertical-Cavity Surface-Emitting Laser

Foreword

Quantum cascade lasers are unipolar semiconductor lasers offering access to wavelengths from the mid-infrared to the terahertz domain and promising impact on various applications such as free-space communications, high-resolution spectroscopy, LIDAR remote sensing or optical countermeasures. Unlike bipolar semiconductor lasers, stimulated emission in quantum cascade lasers is obtained via electronic transitions between discrete energy states inside the conduction band. Recent technological progress has led to quantum cascade lasers operating in pulsed or continuous-wave mode, at room temperature in single- or multi-mode operation, with high powers up to a few watts for mid-infrared devices.

Mid-infrared applications require sources with extremely high performances, in terms of output power, modulation bandwidth, single-mode emission or narrow linewidth. In interband laser diodes, these properties can usually be significantly improved using external control, either optical injection or optical feedback. The former consists in injecting the light emitted by a first master laser into a second slave laser, whereas in the latter configuration, the light from a single laser is reinjected in its own active region. In the case of optical feedback, depending on the external cavity length and the feedback ratio, i.e. the ratio between reinjected and emitted light, the emission characteristics can either be greatly improved or significantly deteriorated. The dynamical behavior of the laser will also be impacted, leading to stable, periodic or chaotic emission. Furthermore, optical feedback can reduce the complex spatial nonlinearities occurring in broad-area lasers, such as beam steering or filamentation.

The carrier lifetime of quantum cascade lasers is three orders of magnitude faster than in interband lasers, and the α-factor is expected to be much smaller, the dynamical response of these structures to optical feedback would therefore be different from that of laser diodes. However, this phenomenon has almost never been studied in quantum cascade lasers, and

it is worth verifying whether optical feedback can improve the emission properties of such devices. Furthermore, since parasitic optical feedback may arise from the experimental setups, it is also of prime importance to see whether a quantum cascade laser can destabilize and eventually become chaotic when subjected to this effect. Finally, optical injection might be able to improve the laser properties much more than optical feedback.

Therefore, the objective of this thesis is to study the nonlinear dynamics of quantum cascade lasers subject to optical feedback or optical injection. This work is a collaboration between Télécom ParisTech, mirSense and the Direction Générale de l'Armement (DGA), to make the most of the expertise of each structure.

Chapter 1

Introduction

This introduction chapter will present the general context of this study, i.e. the applications at mid-infrared wavelengths and the existing sources. The organization of the dissertation will furthermore be described.

1.1 The need for mid-infrared sources

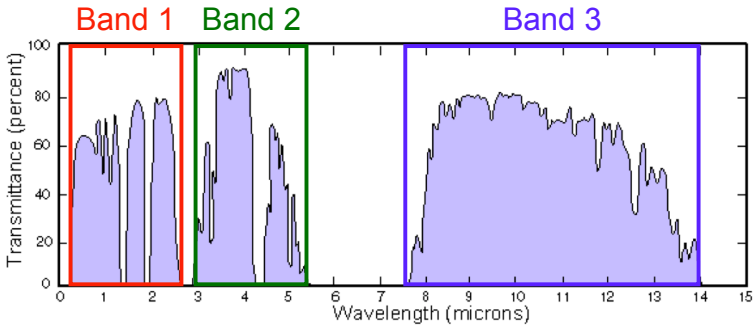

Figure 1.1: Atmospheric optical windows.

The atmosphere is transparent in three ranges of wavelengths, as depicted in Figure 1.1: from 400 nm to about 2.5 μm, i.e. in the visible and near-infrared range, and in the mid-infrared (IR), from 3 to 5 μm and from 8 to 14 μm. Many light sources exist in the first atmospheric window, but some applications are optimized at mid-infrared wavelengths, hence the need to develop sources in this wavelength range.

1.1.1 Applications at mid-infrared wavelengths

The very first application in the mid-IR range is molecular spectroscopy. Due to their vibrations in the medium, most molecules will absorb light at one specific wavelength, that is a characteristic of the molecule. The presence of a given molecule can therefore be measured by illuminating the medium and detecting either directly the optical transmission spectrum, showing absorption peaks at the molecule vibrational frequencies, or through photo-acoustic detection, consisting in measuring with loudspeakers the vibration frequency of the molecule, which will be modified due to heating in case of absorption of optical light [1]. Furthermore, the amplitude of the absorption peak or of the acoustic signal is directly related to the quantity of the specific molecule in the studied medium, and molecular spectroscopy can be used to monitor toxic or polluting gases for industrial control, to detect explosives or drugs for safety applications or to monitor glucose in blood in the medical domain. The fundamental vibrational mode of most of these molecules of interest is located in the mid-IR range, as shown in Figure 7.2. It is therefore strategic to illuminate the medium in this range of wavelengths, instead of using the harmonics in the near-IR, where the spectroscopy would be 2 to 3 orders of magnitude less efficient.

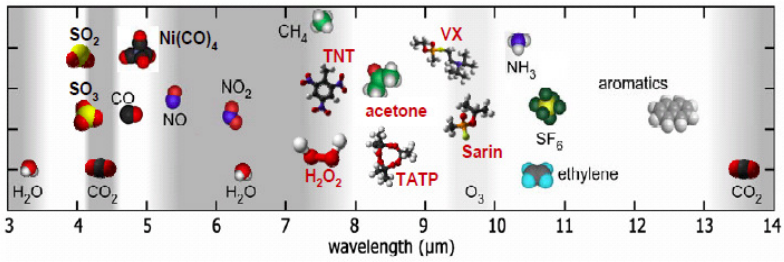

Figure 1.2: Absorption wavelength of a few molecules of interest.

Another important application at mid-IR wavelength is free-space optical communications [2]. Communications networks need to transport always more information at higher bit-rate. In order to increase the bit-rate, increasing the carrier frequency is a good solution: radio frequency (RF) communications shifted from the 3 - 30 GHz range (microwaves) to the 30 - 300 GHz range (millimeter waves), and it seems logical to shift to optical wave-

lengths to achieve even higher carrier frequencies. Free-space optical communications are being developed for military purposes, since the RF network is saturated and directional laser beams would be harder to intercept than RF waves. However, one can also imagine free-space optical communications for general public applications as a complement to the optical fibers, which are expensive to install and repair, and are on the verge of becoming saturated. Furthermore, free-space optical communications would be a solution to ensure high bit-rate down to the end user, instead of using WIFI shared by many users for the last few meters. The principle of operation of free-space optical communications is similar to fibered communications: the laser carrier is modulated and propagates through the atmosphere. Afterwards, the signal is collected on a photodetector and processed to retrieve the information. However, atmospheric turbulence on the propagation path will significantly deteriorate the optical signal causing e.g. beam spreading, beam wandering, scintillation or loss of spatial coherence. In this case, the scintillation will be the predominant phenomenon, corresponding to intensity fluctuations of the propagated beam. This effect evolves as a function of $\lambda^{-7/6}$, it will therefore be less significant at higher wavelength [2], hence the advantage of mid-IR waves for free-space optical communications.

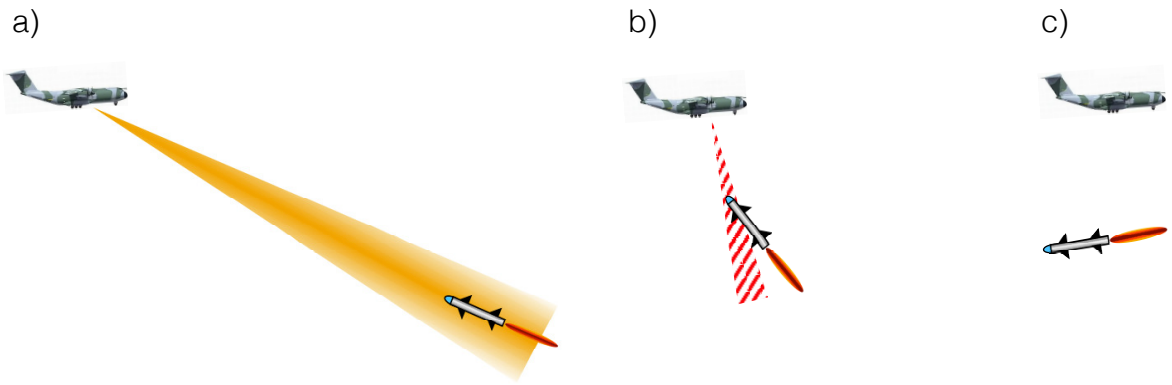

Figure 1.3: Scenario of optical countermeasure. a) A missile is detected while tracking the plane heat signature. b) A strong mid-infrared signal is sent from the plane to jam the missile. c) The missile trajectory is deviated.

Finally, the third main application for mid-IR sources are optical countermeasures. Mis-

siles with infrared-based guiding systems, that identify and follow their target based on its heat signature, have caused many casualties to both military and civil aircrafts. Depending on the technology, these missiles will operate in the 0.5 - 2.5 μm range to follow very hot sources such as airplane nozzles, in the 3 - 5 μm range to follow targets emitting between 300 and 1000 K, or in the 8 - 14 μm range to follow cold sources such as naval vessels. Two solutions exist to counter these threats from the airplane: they can be decoyed by sending objects with a heat signature close to the airplane, or they can be jammed, i.e. they can be blinded by a powerful modulated mid-IR beam, as shown in Figure 7.3. For this application, it is therefore necessary to use a compact, low-consumption, powerful mid-IR source that can be loaded on the airplane.

1.1.2 Available mid-infrared sources

Different sorts of mid-IR sources have been developed to be exploited in the aforementioned applications, as presented in Figure 1.4.

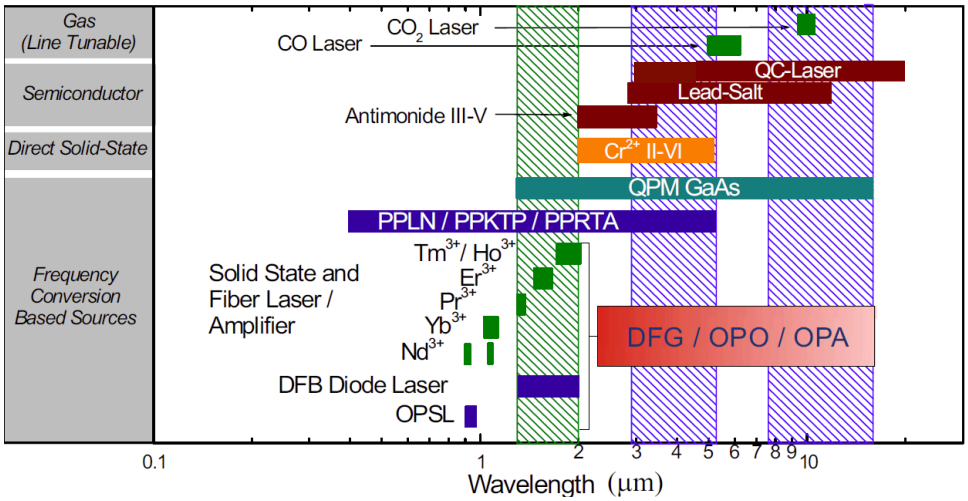

Figure 1.4: Main infrared sources and their emission range.

Mid-IR gas lasers are often used in the manufacturing industry for their high output powers. For instance, CO_2 lasers [3] can emit over 100 W in continuous-wave operation in the range between 9.6 and 10.6 μm, with electrical to optical conversion efficiency over 20%. Similarly, CO lasers produce high energies in the range 5 to 8 μm when operated on

the fundamental roto-vibrational mode and in the range 2.5 to 4 μm on the first harmonic. However, these devices are cumbersome, especially due to their cooling systems.

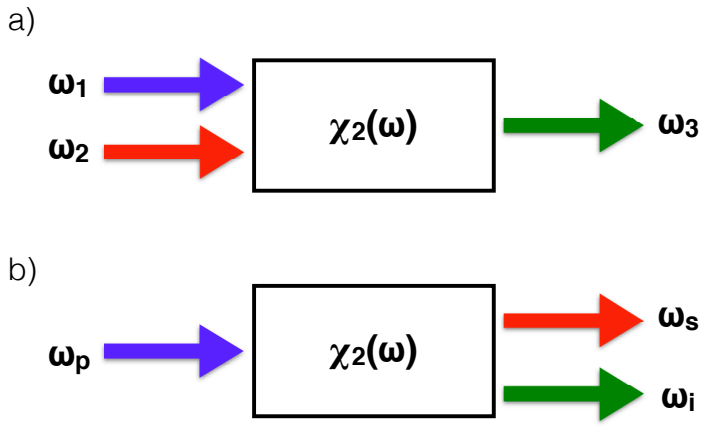

Figure 1.5: a) Difference frequency generation, with $\omega_3 = \omega_1 - \omega_2$. b) Optical parametric oscillator, with $\omega_s = \omega_p - \omega_i$.

By exploiting the second order nonlinearities of some crystals, mid-IR optical waves can be also obtained from waves at visible or near-IR wavelengths. Two nonlinear effects can be used: difference frequency generation in crystals such as $LiNbO_3$ converts two waves at angular frequencies ω_1 and ω_2 in a single wave at frequency $\omega_3 = \omega_1 - \omega_2$ (see Figure 1.5 a and [4]). On the other hand, one can also obtain a signal wave at ω_s and an idler wave at ω_i from a single pump wave at ω_p, with $\omega_s = \omega_p - \omega_i$ (see Figure 1.5 b). This is the principle of optical parametric oscillators (OPOs), based on crystals such as periodically poled lithium niobate (PPLN) [5]. In these crystals, the orientation of the lithium niobate is alternatively switched, in order to ensure quasi-phase matching: all photons will propagate with the same phase and constructive interferences will therefore appear in the crystal, leading to strong optical powers at the output. Furthermore, the period of the PPLN crystal will determine the emission wavelength, and strong tunability can be achieved with OPOs by using multi-period PPLN crystals. These mid-IR sources based on nonlinear crystals are performant and can operate easily at room temperature, but the need for optical pumping leads to cumbersome devices, and the alignment of the crystal is very sensitive, difficulties may therefore appear when using OPOs outside of the lab.

Another type of mid-IR laser source are lead-salt lasers. These semiconductor lasers based on PbSe, PbTe or PnS have a direct bandgap, but the transition does not occur at the Γ point (i.e. at the center of the Brillouin zone), but at one of the four L points, corresponding to off-centered band minima. Furthermore, the effective mass of the electrons and holes are similar, and there are therefore only few Auger recombinations, leading to a possible population inversion and laser effect. The achievable wavelength ranges from 3 to 30 μm depending on the addition of Cd, Sn, Eu or Yb [6, 7]. These lasers emit typically a few hundreds of μW, but continuous-wave operation can only be reached at cryogenic temperatures, which is not practical. Furthermore the performances of such devices are strongly unstable with a small temperature fluctuation.

Antimony-based semiconductor lasers can also emit up to 4 μm, for instance AlGaIn/AsSb below 3 μm [8] or GaInSb/InAs between 3 and 4 μm [9]. There are however no solutions based on antimony to reach longer wavelengths, and these sources do not deliver very high powers.

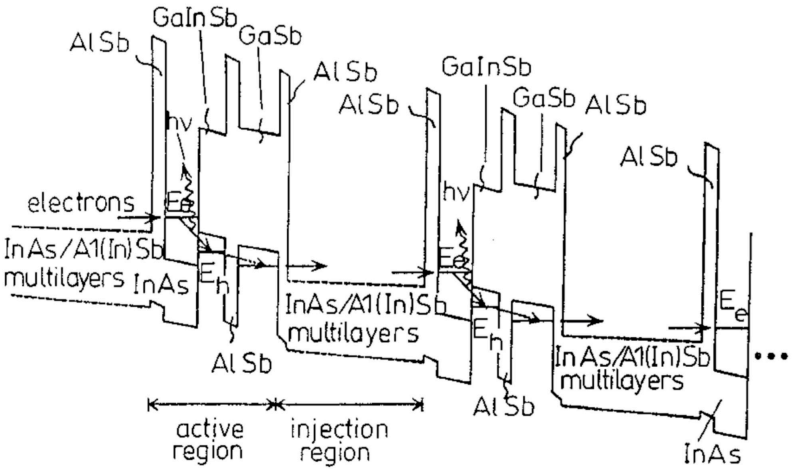

Figure 1.6: Schematic of the first ICL (courtesy of [10]).

To improve the performances of the mid-IR laser diodes, in particular those based on antimony, a cascading design has been proposed by Yang [11]. Interband cascade lasers (ICLs) are constituted of a succession of interband active areas in order to increase the wall-plug efficiency of the device. The first realization of an ICL was performed by Lin *et al.* [10], as shown in Figure 1.6. Since then, the performances of ICLs improved significantly

and they have become suitable sources for spectroscopic applications [12]. However, these structures are very complex to design, the achievable wavelengths remain limited and the maximum output power is relatively low.

Finally, quantum cascade lasers (QCLs) are also based on a cascading structure, but the optical transition occurs between two subbands of the conduction band, leading to a large range of accessible wavelengths from 3 to 250 μm [13]. These performant devices, that can emit up to a few watts at room-temperature with thermo-electrical cooling, in continuous-wave or pulsed mode, have become privileged mid-IR sources for the three previously-mentioned applications.

1.2 Organization of the dissertation

The principle of operation of the QCLs will be explained in the next chapter. Some theoretical elements will be given in order to fully understand these devices, and the importance of the linewidth enhancement factor will be detailed. Furthermore, a specific QCL structure providing both Fabry-Perot and distributed feedback lasers around 5.6 μm will be characterized both numerically to obtain the complete set of internal parameters and experimentally to measure for instance the L-I-V characteristic curves, gain curves or optical spectra of several devices.

Optical feedback will be described in the third chapter. This phenomenon consists in reinjecting part of the emitted light back into the laser, it can be voluntary after reflection on a mirror or parasitic when the reflection occurs on a fiber tip or on an optical component of the experimental setup. Optical feedback has been widely studied in interband laser diodes, where it can either improve or deteriorate the laser properties depending on the two main parameters that are the external cavity length, or feedback delay, and the feedback ratio, defined as the ratio between reinjected and emitted powers. An overview of the influence of optical feedback on the static and dynamical properties of a laser diode will be given in chapter three, including reduction of the laser threshold, increase of the output power, modification of the optical spectra and of the laser linewidth and chaotic operation.

In order to improve the QCL performances in terms of linewidth or emitted power, optical

feedback can turn out useful. On the other hand, it is important to know if parasitic optical feedback can make a single-mode QCL multimode or chaotic. There have however been very few studies on the impact of optical feedback on a mid-infrared QCL. Chapter four proposes a detailed study of the static and dynamical properties of a QCL subject to optical feedback, both experimentally and numerically, in comparison to the typical response of a laser diode to this external perturbation. The amount of optical feedback originating from a mid-infrared chalcogenide fiber is also estimated, in order to verify that fibered QCLs will present satisfactory performances. In this chapter, the linewidth enhancement factor of a mid-infrared QCL structure is furthermore derived from two measurement techniques based on optical feedback.

In interband lasers, optical feedback can also significantly impact the emission properties of broad-area lasers, in terms of filamentation or mode control. However, broad-area diode lasers have few applications and are not widely developed whereas in QCL structures, broad-area devices will lead to high output powers, which is crucial for e.g. optical countermeasures. The use of these broad-area QCLs remains limited because these lasers are transverse multimode or subject to beam steering. In the fifth chapter, optical feedback is applied on 40 μm-, 14 μm- or 32 μm-wide QCLs emitting around 4.6 μm, in order to suppress the beam steering or to make a transverse multimode laser single-mode by modifying the near-field mode pattern.

To go further, optical injection, consisting in injecting the light from a first laser, called master laser, into a second laser, or slave laser, can be even more efficient than optical feedback to improve the slave laser performances. When the master and the slave frequencies are identical, optical injection is similar to optical feedback, but with much higher injection strength, hence a higher impact. The detuning, i.e. the frequency difference between master and slave is also important and induces a more complex nonlinear response. The influence of optical injection on a Fabry-Perot QCL emitting around 5.6 μm is studied theoretically in chapter six.

Finally, the last chapter will draw the conclusions of this work and propose some perspectives for a future work.

Chapter 2

Quantum cascade lasers: performant mid-infrared sources

A superlattice is an artificial semiconductor material consisting of a large number of periods, with each time at least two layers of different materials presenting different gap energies but similar lattice constants. Kazarinov and Suris [14] predicted in 1971 the possibility for a semiconductor superlattice to amplify light using intersubband transitions. However, the first quantum cascade lasers (QCLs) were reported by Faist *et al* [15] only in 1994, after significant improvement of the epitaxial growth and development of molecular beam epitaxy (MBE) and metal-organic chemical vapor deposition (MOCVD). After this first QCL in AlInAs/GaInAs emitting up to 8.5 mW peak power around 4.6 μm, in pulsed mode and at 88 K, this technology rapidly developed. Mid-infrared QCLs now exist in several III-V semiconductors, they can operate both in pulsed and continuous-wave (CW) mode, at room-temperature in single- or multi-mode regime, with high powers up to a few watts [16, 17, 18].

QCLs emitting in the terahertz (THz) have also been realized [20], i.e. in the wavelength range from 30 μm to 1 mm, although they do not operate at room-temperature yet, because of the appearance of thermal relaxation mechanisms between upper and lower laser levels through optical phonons preventing from population inversion when increasing the temperature. Some solutions exist to operate THz QCLs at room temperature, such as the application of a strong magnetic field above 16 T, in order to suppress the inter-Landau-level non-radiative scattering [21]. Another technique based on difference frequency generation in a mid-IR QCL to obtain room-temperature monolithic THz devices has been proposed [22] and has led to the best output power performances at these wavelengths.

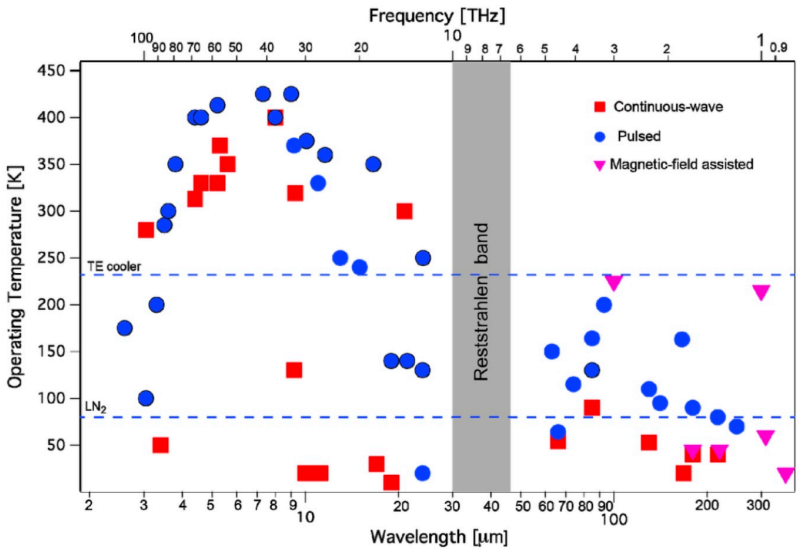

Figure 2.1: QCL performances reported in the literature, as a function of wavelength and operating temperature (courtesy of [19]).

Figure 2.1 presents the QCL performances reported in the literature, over the mid-infrared and THz ranges from 3 to 250 μm and their operating temperature. The graph shows the existence of a wavelength range from 28 to 50 μm where no QCLs were realized: it corresponds to the Restrahlen band, where the III-V materials are absorbant due to optical phonon absorption. In the following, we will focus on mid-infrared QCLs, since room-temperature operation is more convenient for experimental work.

This chapter will present the principle of operation and theory of QCLs. The α-factor, key parameter of semiconductor lasers but not well-known in QCLs, will then be defined, before studying in details a specific QCL structure, from which both Fabry-Perot (FP) and distributed feedback (DFB) devices emitting around 5.6 μm were fabricated.

2.1 Principle of operation

In interband laser diodes, the laser transition occurs between the conduction band and the valence band of the semiconductor material, and the laser frequency ν is determined by the energy gap E_g between these two bands, with the relation $E_g \leq h\nu \leq F_c - F_v$, with F_c and F_v the quasi-Fermi levels associated with the conduction and valence bands, respectively. The laser diode wavelengths are therefore limited below 2 μm, because the energy gaps of the III-

V materials are in this range. On the other hand, QCL operation is based on intersubband transitions within the conduction band of the III-V semiconductor, as shown in Figure 7.1. Therefore, the emission wavelength is no longer limited by the gap of the material but by the energy spacing between the subbands, which is determined by quantum engineering of the active area. The only limitation in wavelength is the thickness of the quantum well where the laser transition takes place, which rules the spacing between the subbands: if the quantum well is too narrow, the upper subband will be too close to the continuum, the electron will no longer be confined and no photon will be emitted. There are therefore no QCLs emitting below 3 μm at room temperature, and the ones emitting between 3 and 4 μm are mostly based on newly developed structures containing antimony [23]. On the contrary, if the quantum well is too wide, the subbands will be very close from one another and thermal relaxation will compete with the radiative transitions, hence limiting the operation of THz QCLs to cryogenic temperatures.

A cascading effect is added to the structure in order to improve the efficiency, as shown in Figure 7.1. Each electron will cascade through several active regions and will each time produce a photon. A QCL is typically constituted of 20 to 40 periods and the electrons transfer from one active region to the other through tunneling effect.

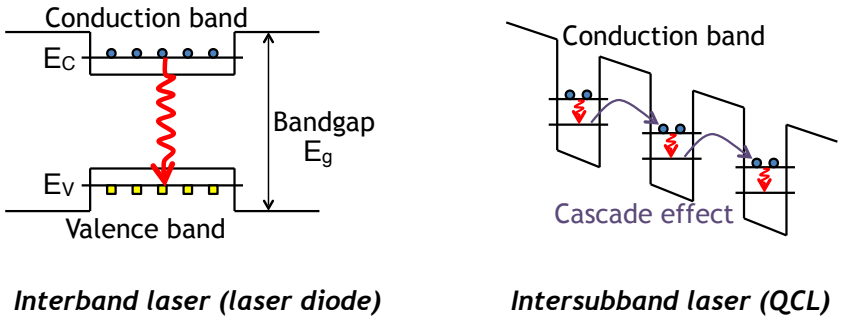

Figure 2.2: Intersubband transitions and cascade effect.

As shown in Figure 2.3, the actual design of a QCL structure is much more complex than previously described. The laser transition indeed occurs in a multi-quantum well active region that is a 3-level laser [24]: the photon is emitted during the transition from an upper

level $|3\rangle$ to a lower level $|2\rangle$. Then the electron relaxes through an optical phonon in level $|1\rangle$, from which it will tunnel into a injector region, i.e. a succession of narrow quantum wells called minibands that will lead the electron to the upper level $|3\rangle$ of the next active region.

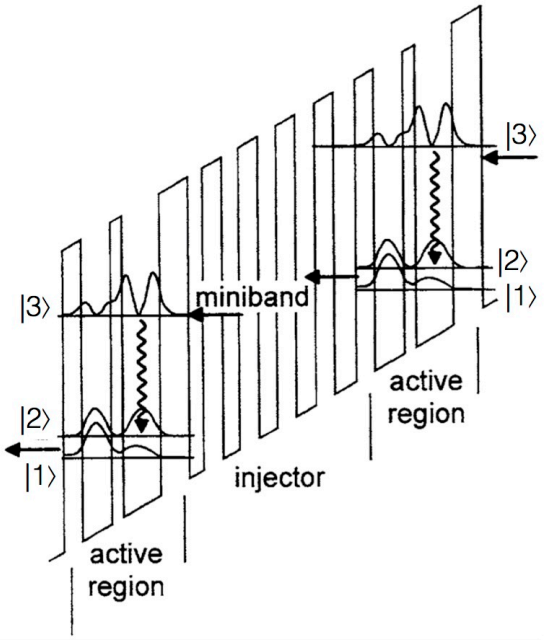

Figure 2.3: Schematic of a QCL structure, including the wave funtions in the active area (courtesy of [24]).

2.2 Theory

2.2.1 Heterostructure

The active region of a QCL is a heterostructure, which allows to confine the electrons along the growth direction. This one-direction confinement leads to discrete energy levels. In the slowly varying envelope approximation, the eigenstates of the heterostructure can be expressed as [25]:

$$\psi(\mathbf{r}) = \sum_m \varphi_m(\mathbf{r}) u_{m,\mathbf{k}=0}(\mathbf{r}) \tag{2.1}$$

where m is one of the band taken into account for the calculation, $u_{m,\mathbf{k}=0}(\mathbf{r})$ is the Bloch function and $\varphi_m(\mathbf{r})$ is a slowly varying envelope. The Bloch functions are assumed to be

similar in all the layers of the heterostructure. Therefore, due to the translation invariance in the plane of the layers:

$$\varphi_m(\mathbf{r}) = \frac{1}{\sqrt{A}} e^{i\mathbf{k}_\parallel \mathbf{r}_\parallel} \chi_m(z) \tag{2.2}$$

with A the area of the laser, $\mathbf{k}_\parallel \mathbf{r}_\parallel = k_x x + k_y y$ and χ_m an envelope function for the band m.

The conduction band component $\chi_c(z)$ of this equation has to satisfy the Schrödinger-like equation [26]:

$$\left[-\frac{\hbar^2}{2} \frac{d}{dz} \left(\frac{1}{m^*(E,z)} \frac{d}{dz} \right) + E_c(z) \right] \chi_c(z) = E \chi_c(z) \tag{2.3}$$

where $m^*(E) = m^*(E_c) \left[1 + \frac{E - E_c}{E_G} \right]$ is the effective mass, that is a function of the energy to express the band non-parabolicity.

When assuming $\mathbf{k}_\parallel = 0$ and a constant effective mass m_{eff}, ie. parabolic bands, the energies E_k of the band k are given by:

$$E_k = \left(\frac{\hbar^2 \pi^2}{2 m_{eff} l^2} \right) k^2 \tag{2.4}$$

with l the quantum well width. The energy of the produced photon $E_{phot} = h\nu$, ν being the frequency, corresponds to the energy difference between two consecutive subbands of the conduction band. For instance, for $k = 2$:

$$E_{phot} = E_2 - E_1 = \frac{3\hbar^2 \pi^2}{2 m_{eff} l^2} \tag{2.5}$$

2.2.2 Spontaneous emission and material gain calculation

The electromagnetic wave at frequency ν will interact with the two subbands i and f of the conduction band. The stimulated emission rate $W^{st}_{i \to f}$ can be expressed as a function of the spontaneous emission rate $W^{sp}_{i \to f}$ as [27]:

$$\frac{1}{\tau^{st}_{if}} = W^{st}_{i \to f} = W^{sp}_{i \to f} \frac{3c^2}{8\pi h \nu^3 n^2} E(\nu) \tag{2.6}$$

where c is the light velocity, $E(\nu)$ the energy density of the wave at frequency ν and n the refractive index.

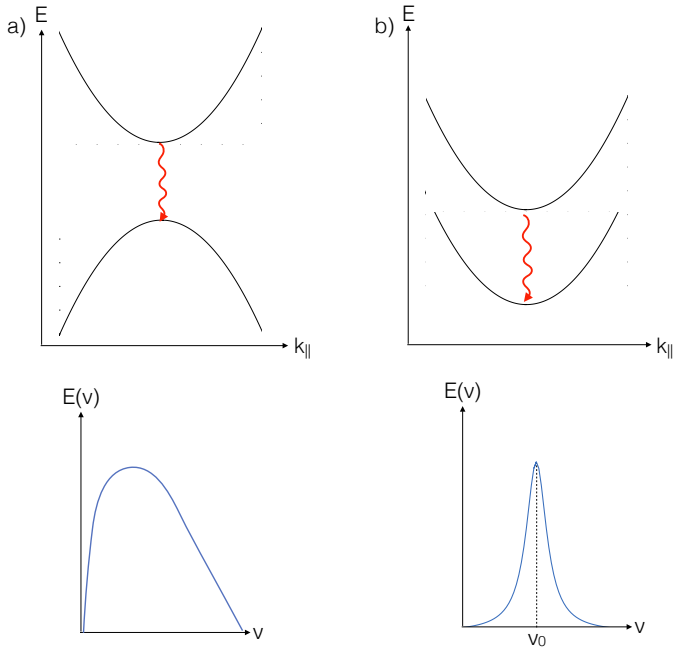

Figure 2.4: Comparison between interband laser (a) and QCL (b). The upper curves represent the place where the lasing transition takes place, and the lower ones show the energy density $E(\nu)$.

The energy density can be written as $E(\nu) = L(\nu)I(\nu)$ with $I(\nu)$ the light intensity propagating in the structure and $L(\nu)$ the lineshape function of the energy, corresponding to the width of the energy level due to the electron lifetime. In a QCL, the broadening of the energy level is homogeneous, and $L(\nu)$ has the shape of a lorentzian, as shown in Figure 2.4 b:

$$L(\nu) = \frac{2}{\pi} \frac{\gamma_{if}}{(\nu - \nu_0)^2 + \gamma_{if}^2} \tag{2.7}$$

The optical power can be expressed both as a function of the electron density multiplied by the photon energy and as the product between the material gain and the intensity, following Beer-Lambert's law. Therefore:

$$P_{opt} = (N_i W_{i\to f}^{st} - N_f W_{f\to i}^{st})h\nu = \Delta N W_{i\to f}^{st} h\nu = g(\nu)I(\nu) \tag{2.8}$$

with N_i and N_f the carrier density of levels i and f, $\Delta N = N_i - N_f$.

This lead to the following expression for the material gain:

$$g(\nu) = W_{i\to f}^{sp} \frac{3c^2}{8\pi\nu^2 n^2} \Delta N L(\nu) \tag{2.9}$$

Furthermore, the rate of spontaneous emission can be expressed by applying Fermi's golden rule to the electric dipole hamiltonian $H_{DE} = -q\mathbf{E}\cdot\mathbf{r}$ [26]:

$$\frac{1}{\tau_{sp}} = W_{i\to f}^{sp} = \frac{q^2 n}{3\pi c^3 \epsilon_0 \hbar^4} (h\nu)^3 |z_{if}|^2 \tag{2.10}$$

where q is the elementary electron charge, ϵ_0 the vacuum permittivity and $|z_{if}|$ the dipole matrix element, which is inversely proportional to ν [26, 13]. Therefore, the material gain is directly proportional to $L(\nu)$ and can be written as:

$$g(\nu) = \frac{2\pi^2 q^2}{\epsilon_0 n h c} \nu |z_{if}|^2 \Delta N L(\nu) \tag{2.11}$$

The gain of a QCL has therefore the shape of a lorentzian, centered around a value ν_0 that depends on the active region materials and on the dimensions of the quantum wells.

2.2.3 QCL rate equations

In a QCL, each active region is a 3-level laser. Assuming that all active regions are identical, the rate equations for carriers and photons in active region j can be expressed as [28]:

$$\frac{dN_3^j}{dt} = \eta \frac{I_{in}^j}{q} - \frac{N_3^j}{\tau_{32}} - \frac{N_3^j}{\tau_{31}} - G_0 \Delta N^j S^j \tag{2.12}$$

$$\frac{dN_2^j}{dt} = \frac{N_3^j}{\tau_{32}} - \frac{N_2^j}{\tau_{21}} + G_0 \Delta N^j S^j \tag{2.13}$$

$$\frac{dN_1^j}{dt} = \frac{N_3^j}{\tau_{31}} + \frac{N_2^j}{\tau_{21}} - \frac{I_{out}^j}{q} \tag{2.14}$$

$$\frac{dS^j}{dt} = \left(G_0 \Delta N^j - \frac{1}{\tau_p} \right) S^j + \beta \frac{N_3^j}{\tau_{sp}} \tag{2.15}$$

where N_k^j is the carrier density of level k, $\Delta N^j = N_3^j - N_2^j$. I^j is the bias current entering the active region j. η is the conversion efficiency, τ_{kl} corresponds to the carrier lifetime from level

k to level l, τ_{sp} is the spontaneous emission lifetime, τ_p is the photon lifetime inside the laser cavity and β the spontaneous emission factor, which represents the fraction of spontaneous emission coupled into the lasing mode. G_0 corresponds to the net modal gain over one period normalized by the group velocity v_g, expressed in s^{-1}, and can be defined as [28]:

$$G_0 = \frac{\Gamma_{opt} v_g g}{\Delta N^j A} \tag{2.16}$$

with Γ_{opt} the confinement factor, v_g the group velocity, g the gain in cm^{-1} and A the area of the laser cavity. Let us stress that the rate equations 2.12 to 2.15 correspond to the single-mode scenario. In case of multimode operation, the photon rate equation for each mode can be obtained by adding to the single-mode photon density a term S_m, corresponding to the photon population for the m^{th} longitudinal mode oscillating at the frequency ω_m [29].

In eq. 2.12 to 2.15, the electron will escape from level N_1^j to enter level N_3^{j+1}. Therefore:

$$\frac{I_{out}^j}{q} = \frac{N_1^j}{\tau_{out}} \tag{2.17}$$

$$\frac{I_{in}^j}{q} = \frac{N_1^{j-1}}{\tau_{out}} \tag{2.18}$$

where τ_{out} is the characteristic time for the electron to tunnel into the injector.

This complete QCL model leads to complicated resolution, since $4 \times N_{pd}$ have to be taken into account, with N_{pd} the number of periods. Therefore, the QCL is often considered as a global virtual 3-level system ruled by:

$$\frac{dN_3}{dt} = \eta \frac{I}{q} - \frac{N_3}{\tau_{32}} - \frac{N_3}{\tau_{31}} - G_0 \Delta N S \tag{2.19}$$

$$\frac{dN_2}{dt} = \frac{N_3}{\tau_{32}} - \frac{N_2}{\tau_{21}} + G_0 \Delta N S \tag{2.20}$$

$$\frac{dN_1}{dt} = \frac{N_3}{\tau_{31}} + \frac{N_2}{\tau_{21}} - \frac{N_1}{\tau_{out}} \tag{2.21}$$

$$\frac{dS}{dt} = \left(N_{pd} G_0 \Delta N - \frac{1}{\tau_p} \right) S + \beta \frac{N_3}{\tau_{sp}} \tag{2.22}$$

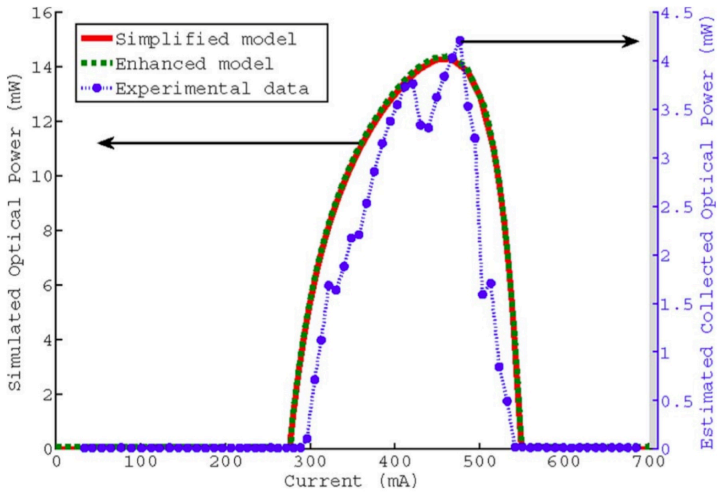

Figure 2.5: Comparison between complete set of equations in green, and simplified model in red (courtesy of [28]).

This simplified model is most of the time sufficient and gives accurate results, as shown in Figure 2.5. However, for some calculations such as small-signal analysis, it is better to consider the full model, since key parameters such as the time for the electrons to pass through the successive active regions and injectors are not taken into account in the simplified model.

2.2.4 QCL modulation response

A small-signal analysis of the QCL is realized, by considering small variations around the steady-state values $N_i^j = N_{i,st}^j + \delta N^j$, where $i = 1, 2, 3$ and j the period number, and $S = S_{st} + \delta S$. Under external perturbation $I = I_0 + \delta i$, using the full set of rate equations, the modulation response of a QCL can be written as [30]:

$$H(j\omega) = \frac{\omega_r^2}{\omega_r^2 - \omega^2 + j\omega\Gamma} \tag{2.23}$$

with:

$$\omega_r^2 = \frac{\frac{1}{\tau_p \tau_{st}} \left(1 + \frac{\tau_{21}}{\tau_{31}}\right)}{1 + \frac{\tau_{21}}{\tau_{31}} + \frac{\tau_{21}}{\tau_{32}} + \frac{\tau_{in}}{\tau_3} + \frac{\tau_{21}}{\tau_{st}} \left(2 + \frac{\tau_{in}}{\tau_3}\right)} \tag{2.24}$$

$$\Gamma = \frac{\frac{1}{\tau_{st}} \left(1 + \frac{\tau_{21}}{\tau_{31}}\right) + \frac{1}{\tau_{31}} + \frac{1}{\tau_{32}} + \frac{\tau_{21}}{\tau_p \tau_{st}} \left(2 + \frac{\tau_{in}}{\tau_3}\right)}{1 + \frac{\tau_{21}}{\tau_{31}} + \frac{\tau_{21}}{\tau_{32}} + \frac{\tau_{in}}{\tau_3} + \frac{\tau_{21}}{\tau_{st}} \left(2 + \frac{\tau_{in}}{\tau_3}\right)} \tag{2.25}$$

where $1/\tau_3 = 1/\tau_{31} + 1/\tau_{32}$, τ_{in} is the characteristic time for the electron to tunnel from the injector into the upper level and τ_{st} is the differential lifetime associated with stimulated and spontaneous photon emission [30].

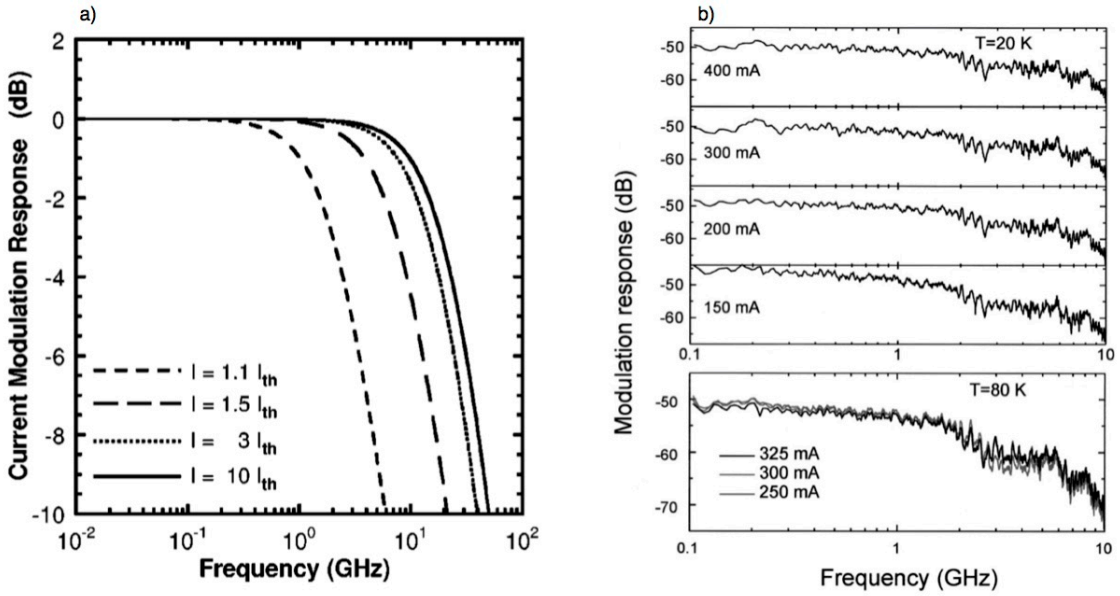

Figure 2.6: a) Numerical modulation response (courtesy of [30]). b) Experimental modulation response (courtesy of [31]).

The eigenvalues that drive the damping of perturbations applied to the laser steady-states can be written as:

$$f_{\pm} = -\Gamma \pm \sqrt{\Gamma^2 - f_r^2} \tag{2.26}$$

where $f_r = \omega_r/2\pi$ is a characteristic frequency, typically called relaxation oscillation frequency in interband lasers, and Γ is the damping rate, which is much higher than the characteristic frequency in a QCL. The eigenvalues are therefore real since the term un-

der the square root remains always positive. Hence, no relaxation oscillations appear on the modulation response of a QCL, both numerically and experimentally [31], as shown in Figure 2.6.

2.3 Linewidth enhancement factor

2.3.1 Definition

Also called linewidth broadening factor or α-factor, the linewidth enhancement factor (LEF) is an important parameter for semiconductor lasers. It quantifies the coupling between the real and imaginary parts of the nonlinear susceptibility, i.e. between the differential gain and the refractive index, or equivalently the coupling between the amplitude and the phase of the electric field in the laser cavity.

$$\alpha = -\frac{d\left[\Re(\chi(N))\right]/dN}{d\left[\Im(\chi(N))\right]/dN} = \frac{-4\pi}{\lambda}\frac{dn/dN}{dg/dN} \;\Leftrightarrow\; \frac{d\phi/dt}{dI/dt} = \frac{\alpha}{2I} \tag{2.27}$$

The α-factor quantifies the minimum linewidth that can be achieved for a semiconductor laser: compared to the intrinsic linewidth limit defined by Schawlow and Townes [32], the limit linewidth for a semiconductor laser is broadened by a factor $(1+\alpha^2)$, hence the name given to this parameter. It was first introduced simultaneously in May 1967 by Lax [33] and Haug and Haken [34]. Using either a classical approach based on density matrix calculations or a semi-classical approach based on quantum mechanics, they both introduced a term $(1+\alpha^2)$ in the theoretical expression of the noise-induced phase fluctuations, that also appears in the linewidth expression. However, the former did not further exploit the obtained linewidth expression, whereas the latter assumed that the LEF was very small compared to 1 and neglected it. In 1982, Henry [35] reintroduced the α-factor and compared his theoretical linewidth expression with several experimental linewidth measurements, resulting in LEF values around 2 to 5 for interband semiconductor lasers.

The α-factor also impacts many important aspects of the semiconductor lasers, such as brightness, modulation properties or filamentation in broad-area semiconductor lasers [36]. Furthermore the LEF significantly influences the nonlinear dynamics of a semiconductor

laser subject to optical injection or optical feedback, and nonlinear dynamics can only be observed in lasers for which $\alpha > 0$ [37].

2.3.2 Measurements methods

As seen in the previous paragraph, the α-factor can be retrieved directly from linewidth measurements. However, this method can be complex to implement, and other measurements techniques have been proposed.

The most common method to measure the linewidth broadening factor was developed by Hakki and Paoli [38] and Henning [39]. It is based on the analysis of the sub-threshold spontaneous emission spectrum, as illustrated in Figure 2.7. The gain and wavelength evolution of this amplified spontaneous emission spectrum with the bias current directly gives the α-factor since:

$$\frac{d\lambda}{\lambda} = \frac{dn}{n} \tag{2.28}$$

For this method, one must however be careful to consider solely the wavelength shift due to the carrier density evolution and not that due to the heating of the structure when increasing the bias current even below threshold.

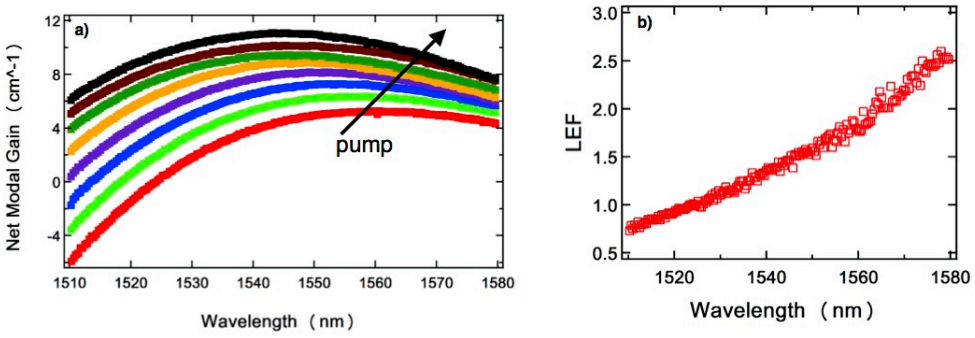

Figure 2.7: Illustration of the Hakki-Paoli method for a quantum dot laser. a) Gain shift as a function of the sub-threshold bias current. b) Deduced α-factor. (Courtesy of [40]).

However, studies have shown that, above threshold, some additional effects such as gain compression significantly impact the α-factor. For instance, LEF values between 0.1 and 0.7 have been reported in InAs quantum-dot lasers far below threshold, before the appearance

of gain saturation [41]. Therefore, several other methods have been developed to measure the above-threshold, room-temperature linewidth broadening factor [42]. For instance, it can be retrieved from the FM-AM ratio of the laser under modulation, as illustrated by Figure 2.8 a. At high modulation frequency $f_m \gg f_c$, where f_c is the corner frequency, by defining β and m the modulation indices in frequency and amplitude, respectively, the $2\beta/m$ coefficient reaches a plateau where:

$$\frac{2\beta}{m} = \alpha\sqrt{1 + \left(\frac{f_c}{f_m}\right)^2} \to \alpha \tag{2.29}$$

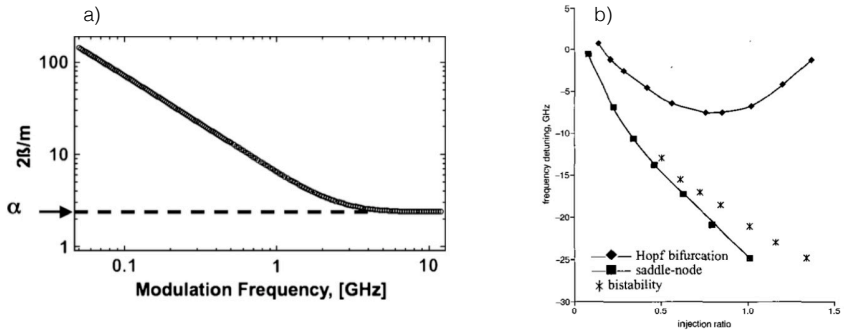

Figure 2.8: a) Measurement of the α-factor using FM-AM ratio (courtesy of [42]). b) Minimum of the Hopf bifurcation of a laser under optical injection, giving a LEF of 3.2 (courtesy of [43]).

As shown in Figure 2.8 b, the LEF can also be retrieved from the minimum point of the Hopf bifurcation ω_{min} of the semiconductor laser under optical injection, i.e. the limit curve between stable and unstable locking, since [43]:

$$\omega_{min} \approx -\sqrt{\frac{(\alpha^2 - 1)^3}{32\alpha^2}} \tag{2.30}$$

This method gives an effective α-factor, which value depends on the operating conditions of the device. However, in the limit case where the laser is operated just above threshold, this effective LEF should be equal to the material LEF obtained with other techniques.

Recently, a new technique has been proposed by Wang *et al.* [44], also based on optical injection. By injecting far from the maximum gain mode of a Fabry-Perot laser, and studying

the evolution of the residual side-mode under stable injection locking when modifying the master laser frequency, the α-factor can be retrieved from the expression:

$$\alpha = -\frac{2\pi}{L\delta\lambda}\frac{d\lambda/d\lambda_m}{dG_{net}/d\lambda_m} \tag{2.31}$$

where λ_m is the master laser wavelength. Although the measurements are performed above threshold, this method is insensitive to thermal effects, bias current or choice of injection-locked mode and gives the material sub-threshold α-factor.

Typically, the LEF values reported for quantum well lasers range from 1 to 3, whereas for more complex structures, such as quantum dot lasers, the α-factor is higher, between 3 and 10 [45]. A record value as high as $\alpha = 57$ in InAs quantum dot lasers emitting both on ground state and excited state has even been reported [46].

2.3.3 α-factor of QCLs

An estimation of the α-factor can be obtained based on the gain asymmetry. As shown previously, the gain of a QCL has the shape of a lorentzian and is almost symmetrical (see Figure 2.9), the linewidth broadening factor of a QCL was therefore expected to be almost zero.

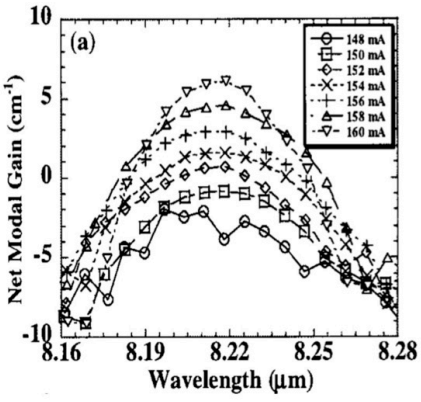

Figure 2.9: Experimental gain curve of a QCL, showing good symmetry (courtesy of [47]).

Based on the lorentzian lineshape of the QCLs, another theoretical expression can be

deduced from the linewidth equation [13]:

$$\alpha_{QCL}(\nu) = -\left(\frac{\nu - \nu_{32}}{\gamma_{32}}\right) \tag{2.32}$$

with ν_{32} the center frequency of the gain spectrum and γ_{32} its half-width at half-maximum. This expression leads to a theoretical zero linewidth broadening factor at the center frequency, and to very small values around the peak for DFB QCLs.

Typically for mid-infrared QCLs, the measured sub-threshold α-factor using this Hakki-Paoli technique varies between -0.6 and 0.3 [47, 48, 49]. This value is low, but definitely non-zero. It is also important to point out, that most of these measurements were performed at cryogenic temperature. When increasing the temperature up to 300 K, thermal agitation of phonons will lead to broader linewidth, and hence to higher linewidth broadening factor values.

Furthermore, the spatial hole burning is very large in QCLs compared to laser diodes [50] and the above-threshold α-factor is expected to be significantly different from that measured below threshold. There are very few reports of above-threshold linewidth broadening factor measurements at room temperature for a mid-infrared QCL. Using the fit of the L-I curves while controlling the internal laser temperature, Hangauer *et al.* [51] reported values between 0.167 and 0.483 close to threshold. Moreover, von Staden *et al.* [52] deduced the α-factor from the self-mixing interferometers and obtained values between 0.26 and 2.4, strongly increasing with the bias current. One measurement of the FM-AM ratio using optical heterodyning led to α-factor values of 0.02 ± 0.2 at 243 K [53]. This measurement has the advantage at high frequency to be independent of the thermal effects, but it might lead to some issues when considering structures with complex carrier dynamics, such as quantum dot lasers or QCLs. It would be interesting to apply techniques such as optical injection far from the maximum gain mode to measure the LEF of a QCL, to obtain temperature independent values.

2.4 Detailed study of a QCL design

In this thesis, we will focus mainly on a specific QCL structure that produced performant lasers, both Fabry-Perot and DFB, emitting around 5.6 μm.

2.4.1 Fabrication of QCL devices

The active area follows a custom design inspired by [54] and consists of 30 periods of AlInAs/GaInAs grown by molecular beam epitaxy on a low-doped (10^{17} cm^{-3}) InP cladding. The upper InP cladding is then grown by metal organic chemical vapor epitaxy. In the case of the DFB QCL, the upper cladding was designed following [55] to enable single-mode emission. A top metal grating was added, with a coupling efficiency of $\kappa \approx 4$ cm^{-1}, leading to a κL is close to unity. Contrary to buried gratings or conventional top gratings with a highly doped dielectric layer between the cladding and the grating, which are based on gain-guiding, this technology is based on index-guiding. The modulation of the refractive index originates from the coupling between the guided modes in the active region and the surface mode, also called plasmon-polariton, which is confined at the interface between metal and upper cladding, two materials with permittivities of opposite signs [27].

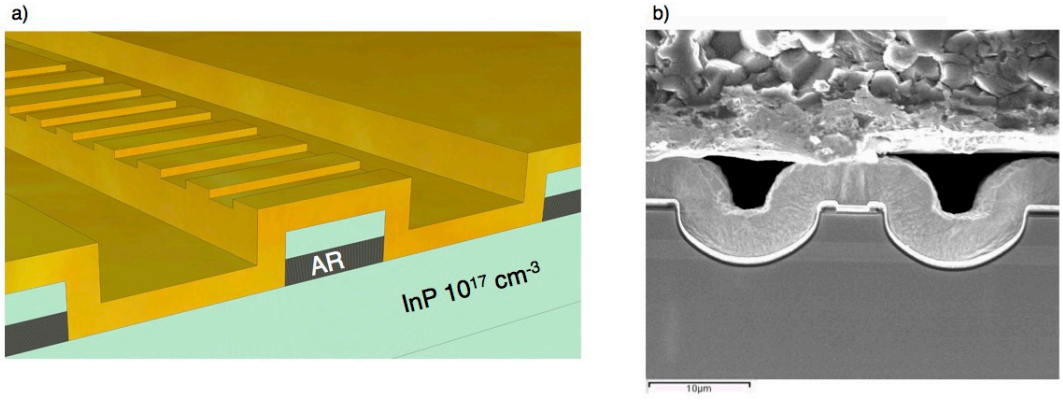

Figure 2.10: a) Schematic and b) SEM picture of the DBF QCL under study. The active region, labeled 'AR' in a), appears in b) in lighter gray.

The wafer is then processed using double-trench technology, in order to reduce the lateral

current spreading in the device, and therefore to reduce the self-heating of the laser [56, 13].

To improve the performances, a high-reflectivity (HR) coating (R>95%) on the back facet reduces mirror losses, while the front facet is leaved as cleaved ($R = 0.3$). Finally, for efficient heat extraction, the QCL is most of the time episide-down mounted with gold-tin soldering on AlN submount. Figure 7.4 shows a schematic and a scanning electron microscopy (SEM) picture of the DFB device under study.

2.4.2 QCL internal parameters

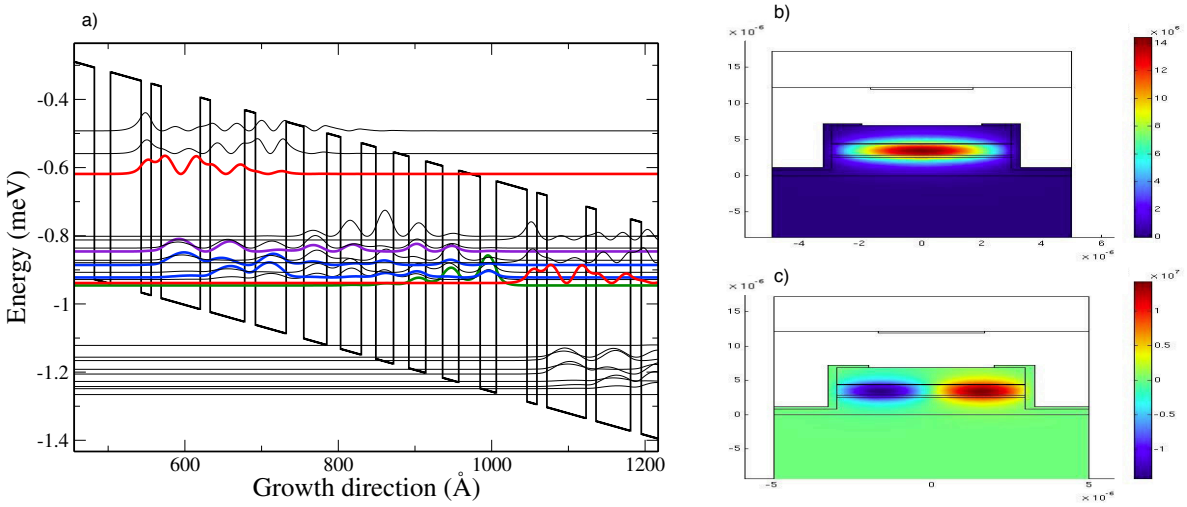

Figure 2.11: a) Wave functions of the QCL structure under study, simulated with METIS. In red, levels $|3\rangle$ of two consecutive periods, in violet level $|2\rangle$, in blue level $|1\rangle$ split into two phonon states, in green injector state. b) Fondamental mode TM0 simulation using COMSOL. c) TM1 simulation.

Most internal parameters of the laser are properties of the active area design and can be retrieved using a homemade heterostructure simulation software named METIS. It is based on semi-classical Boltzmann-like equations with thermalized subbands and takes into account coherent tunneling through the barrier, optical and acoustic longitudinal phonons, absorption of photons, roughness scattering and spontaneous and stimulated emission. The potential, energy states, wave functions and electronic scattering times can be calculated, with very good agreement between simulation and experiment [57]. The active area design

and wave-functions of the studied QCL are represented in Figure 7.6 a.

Furthermore, the repartition of the modes inside the QCL can be simulated using COMSOL, as shown in Figure 7.6 b and c, presenting the simulations of the fondamental mode TM0 and first order mode TM1, respectively. The group refractive index and the confinement factor can be retrieved.

All the simulated parameters of the specific structure under study are summarized in Table 7.1. The missing values are the conversion efficiency η, ratio between the optical and electrical powers, which depends on each device and will be retrieved from the L-I characteristic curves, as well as the α-factor, which measurement will be developed later on.

Parameter	**Value**	**Parameter**	**Value**
Carrier lifetime 3-2 τ_{32}	2.27 ps	Group index n_g	3.2
Carrier lifetime 3-1 τ_{31}	2.30 ps	Confinement factor Γ_{opt}	68%
Carrier lifetime 2-1 τ_{21}	0.37 ps	Net modal gain G_0	1.2×10^4 s^{-1}
Carrier escape time τ_{out}	0.54 ps	Photon lifetime τ_p	4.74 ps

Table 2.1: Laser parameters

2.4.3 Laser static properties

For the following experiments, it is necessary to know precisely the characteristics and performances of the QCLs under study in free-running operation, i.e. without any external perturbations. These lasers are based on the active region previously described.

The DFB QCLs are 2 mm long and 9 μm wide, there are epi-side down mounted with a high-reflectivity coating on the back facet. The lasers can be operated both in continuous-wave and pulsed mode. The L-I-V characteristic curves of such a QCL in continuous-wave operation at 10°, 20°, 30° and 40°C are represented in Figure 2.12 a. For instance, at 20°C, the laser threshold is at 421 mA (current density of J_{th} = 2.34 kA/cm^2), and 9.22 V and the maximum emitted power is 140.4 mW, but these characteristics may slightly vary from one laser to the other and depending on the current source and detection optics used in

the experimental setup. The dip that appears sometimes in the L-I curves, for instance at 581 mA at 10°C, is a measurement artifact due to the strong water absorption on the path between laser and detector at this wavelength.

As shown in Figure 2.12 b, the DFB QCLs are perfectly single-mode all along the L-I curve, and the wavelength red-shifts from 1769.5 cm^{-1} (5.651 μm) to 1764.4 cm^{-1} (5.668 μm) when increasing the bias current. Finally, the far-field of the DFB QCL is drawn in Figure 2.12 c, presenting a relatively round beam. The full width at half maximum of the far-field is 47° horizontally and 59° vertically.

Figure 2.12 d presents the electroluminescence spectra of the DFB QCL, measured in pulsed mode, with a pulse length of 300 ns and a repetition rate of 100 kHz, using a lock-in amplifier and sensitive mercury-cadmium-telluride (MCT) photodetector at cryogenic temperature. The red curve corresponds to a measurement far below threshold, where the electroluminescence spectrum follows the gain shape. It is centered around 1782 cm^{-1} (5.61 μm) and it full width at half maximum (FWHM) is 138 cm^{-1} (FWHM = 44 μm expressed in wavelength). Furthermore, it is worth noticing that the spectrum is not perfectly symmetrical, which suggests a non-symmetrical gain, and hence a non-zero α-factor. The blue curve was measured just below threshold. In this case, the electroluminescence spectrum is much narrower, with a FWHM of 15 cm^{-1} (FWHM = 5 μm in terms of wavelength), showing clear gain saturation.

Several Fabry-Perot QCLs are used depending on the performances needed for the experiments. One of them is epi-side up mounted and cleaved on both facets, with a 3 mm-long and 6 μm-wide active region. The others are epi-side down mounted with a high-reflectivity coating on the back facet, their dimensions are 3 mm × 6 μm, 4 mm × 6 μm and 4 mm × 12 μm, respectively. The thermal management of the epi-up QCL is less efficient, and therefore the laser can only be operated in pulsed mode. Figure 2.12 e shows the L-I-V curves of this laser at several temperatures. At 20°C, with pulses of 300 ns and a repetition rate of 100 kHz, the threshold is around 499 mA (J_{th} = 2.77 kA/cm^2) and 9.87 V, and the maximum emitted power is around 13 mW. From the threshold measurements at different

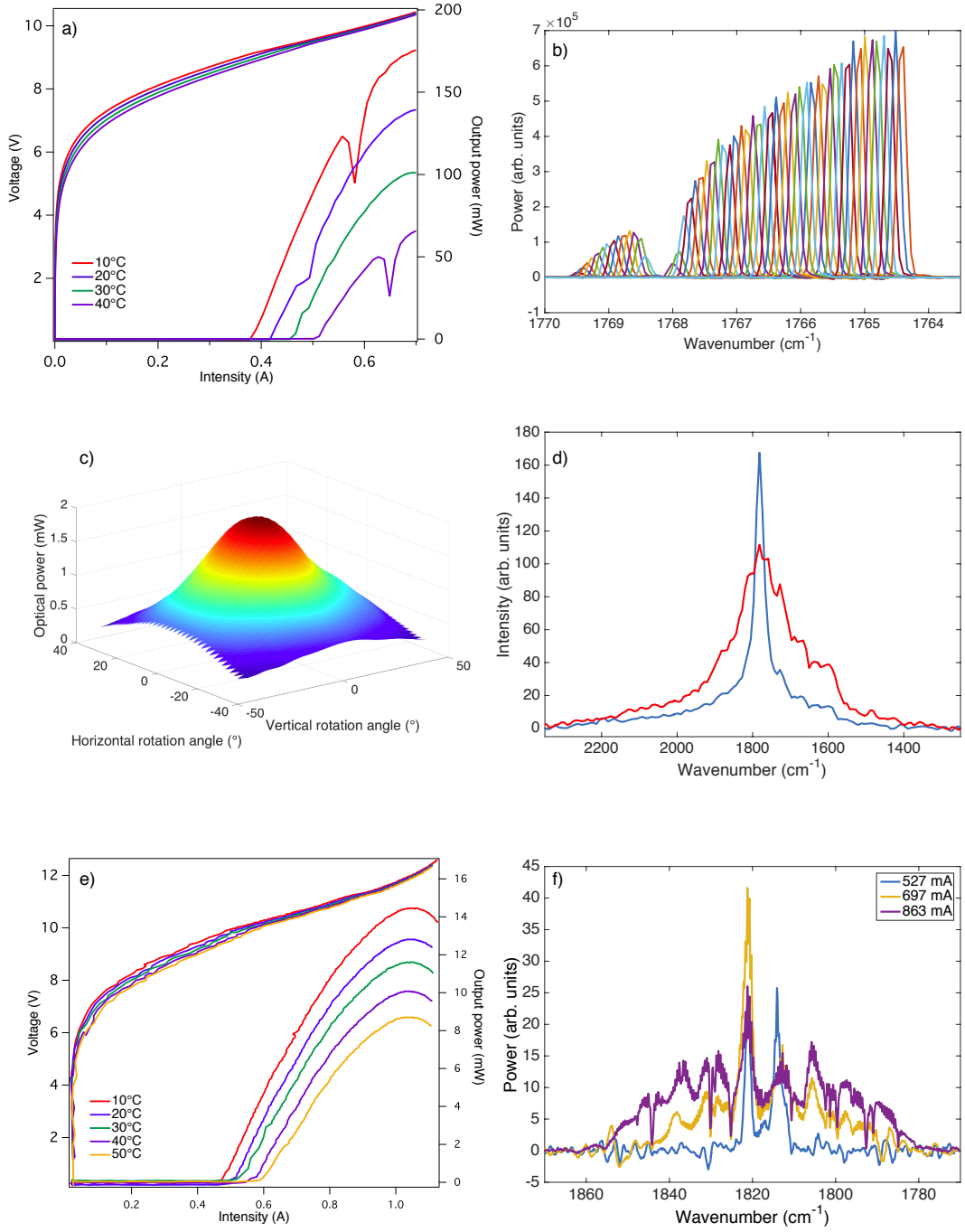

Figure 2.12: a) L-I-V characteristic curves of a 2 mm× 9 μm epi-down DFB QCL operated in continuous-wave at different temperatures. b) Corresponding optical spectra at 20°C for several bias current, showing the wavelength red-shift with active area heating. c) Far-field of the DFB QCL. d) Electroluminescence spectra of the DFB QCL far from threshold (in red) and just below threshold (in blue). e) L-I-V characteristic curves of a 3 mm × 6 μm epi-up FP QCL operated in pulsed mode (100 kHz, 300 ns) at different temperatures. f) Optical spectra of the same laser at 300 ns, 50 kHz and 15°C for several bias current, showing the broadening of the FP spectrum.

temperatures between 10°C and 50°C, the T_0 of the laser can be extracted, with:

$$I(T) = I_0 e^{T/T_0} \tag{2.33}$$

For this structure, the extracted value is T_0 = 184 K between 10°C and 50°C, which is of the order of magnitude of the usual values in QCL structures [13]. The epi-down lasers have better thermal management and can therefore achieve higher optical powers. The 3 mm × 6 μm QCL threshold is located at 591 mA (J_{th} = 3.28 kA/cm^2) and 9.50 V and the laser emits up to 72 mW in continuous-wave mode at 20°C. The 4 mm × 6 μm QCL starts to lase at 843 mA (J_{th} = 3.51 kA/cm^2) and 9.85 V and the laser emits up to 50 mW. Finally, the 4 mm × 12 μm QCL has its threshold at 1.20 A (J_{th} = 2.5 kA/cm^2) and 8.87 V and can emit up to 255 mW.

The optical spectra of the epi-up FP QCL at 15°C, with pulses of 300 ns and a repetition rate of 50 kHz, are represented in Figure 2.12 f for several bias currents, clearly showing the broadening of the gain and hence of the FP spectrum when increasing the pump current. In this case, the center frequency is around 1820 cm^{-1} (5.45 μm), but it can vary depending on the laser geometry.

2.4.4 QCL gain measurements

The gain of the QCL structure can be measured using the method proposed by Benveniste *et al.* [58]. It consists in injecting the light emitted by a DFB QCL into a Fabry-Perot QCL operated below threshold, as depicted in Figure 2.13. In our case, the DFB QCL is 2 mm long and 9 μm wide and runs in continuous-wave, whereas the Fabry-Perot laser is 3 mm long and 6 μm wide, cleaved on both facets and operated in pulsed mode.

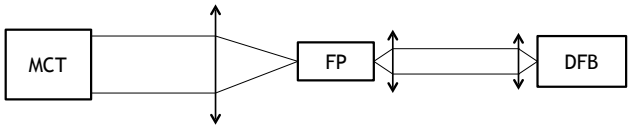

Figure 2.13: Experimental setup for the below threshold gain measurements.

The temporal chirp during the pulse will lead to the appearance of fringes in the optical

power time traces, which can be fitted with Airy function when expressed as a function of the chirp or refractive index variations, as shown in Figure 2.14 a. The gain of the Fabry-Perot QCL can then be retrieved from:

$$G - \alpha_M - \alpha_{ISB} - \alpha_W = \frac{1}{L} ln \left(\frac{k-1}{k+1} \right) \tag{2.34}$$

with L the laser length and $k = \sqrt{I_{max}/I_{min}}$, where I_{max} and I_{min} are two consecutive maximum and minimum of the DFB optical power transmitted through the Fabry-Perot laser. The mirror losses are $\alpha_M = 4$ cm^{-1}. The waveguide losses α_W can be estimated by studying the transverse electrical (TE) transmission of the DFB through the Fabry-Perot. However, it was not possible in our setup to rotate the Fabry-Perot QCL, and the value was taken at $\alpha_W \approx 10$ cm^{-1}, as measured in a previous work for a similar DFB QCL. However, this value varies significantly from one device to the other, especially with the laser length, and must therefore be considered carefully. Finally, the intersubband losses α_{ISB} could be extracted from a measurement far below threshold, where the gain is negligible. However, no signal was detected at such a low bias current, and these losses could not be extracted for this QCL. The evolution of $G - \alpha_{ISB} - \alpha_W$ with the Fabry-Perot current density is presented in Figure 2.14 b, when the DFB QCL is operated at 589 mA and 9.8 V.

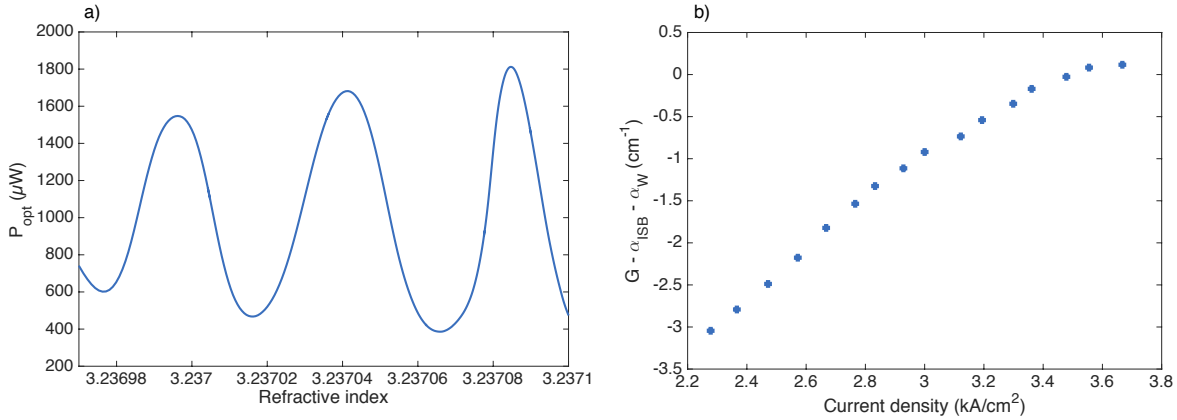

Figure 2.14: a) DFB transmitted intensity as a function of the FP refractive index, for a current density in the Fabry-Perot laser of 3.35 kA/cm^2. b) Fabry-Perot QCL modal gain evolution as a function of the bias current below threshold, at constant DFB laser operating conditions 589 mA and 9.8 V.

The last point of Figure 2.14 b was measured just below threshold. However, at threshold we expect $G - \alpha_M - \alpha_{ISB} - \alpha_W = 0$, which is not the case in our measurement. This could be explained by the existence of a shift between the maximum gain peak and the DFB wavelength, leading to gain measurement that does not correspond to the maximum gain equal to the total losses at threshold [58]. Indeed, from the electroluminescence spectrum (Figure 2.12 d), we deduce that the laser hits the gain at about 92% of its maximum and we expect a maximum gain of $G_{max} = 0.92 \times (\alpha_m + \alpha_W + \alpha_{ISB})$, although it can not be verified here.

2.4.5 Intensity noise measurements

For a given intensity emitted by the laser $I_{laser}(t) = \overline{I_{laser}} + i(t)$, the linear relative intensity noise (RIN) is defined as :

$$RIN = \frac{\overline{i^2}}{\overline{I_{laser}}^2} = \frac{\sigma^2_{i\,laser}}{\overline{I_{laser}}^2} \tag{2.35}$$

where $\overline{I_{laser}}$ is the average flux intensity and $i(t)$ the temporal fluctuations of the emitted signal, and $\sigma^2_{i\,laser}$ the variance of the laser noise, as described in Figure 2.15.

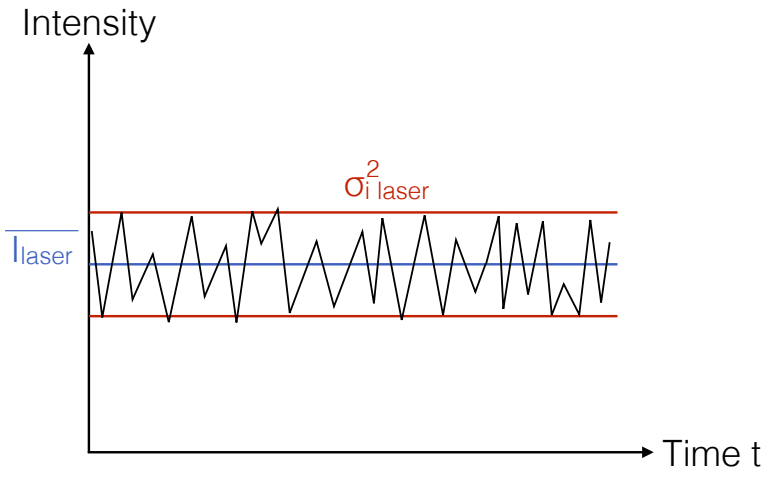

Figure 2.15: Definition of the RIN.

This laser noise originates mainly from the beating between stimulated and spontaneous

emissions [59]. The existence of spontaneous emission indeed leads to photons with random polarization, direction and phase, that will compete with the coherent light from stimulated emission and generate noise.

A good knowledge of the RIN is important for spectroscopic applications. The signal to noise ratio (SNR), quantifying the sensitivity of the detector, indeed depends on the detected signal I_{signal}, directly proportional to the flux intensity emitted by the laser I_{laser} and on the noise standard deviation, $\sigma_{i\,total}$, which takes into account all noises including laser noise, background noise and detection noise (detector thermal and photon noise and preamplifier noise):

$$SNR = \frac{I_{signal}}{\sigma_{i\,total}} \tag{2.36}$$

Therefore, the SNR depends on the RIN. In the case of optical spectroscopy, the detected signal intensity is directly proportional to the light intensity emitted by the laser and to the absorbance α_{abs}, with $I_{signal} = \alpha_{abs} I_{laser}$. Therefore, the SNR can be expressed as:

$$SNR = \sqrt{\frac{t}{RIN}}\,\alpha_{abs} \tag{2.37}$$

with t the integration time.

In this paragraph, the RIN of a DFB QCL is measured both in continuous-wave and pulsed operation, in order to conclude whether the studied QCL structure can be used for spectroscopic applications.

The RIN can be retrieved from the signal detected on a photodiode, here a MCT detector operating at cryogenic temperature. After a preamplifier with a gain coefficient $V = 100$, the electrical signal is analyzed simultaneously on a real-time scope and on an electrical spectrum analyzer (ESA). The average DC signal U_{DC} is measured on the scope and the AC signal corresponding to the mean value of the electrical spectrum at a given frequency ν, $Sp(\nu)$, is measured for a given resolution bandwidth B of the ESA, here 200 Hz. The center frequency ν can be taken in the frequency range of the detector, by carefully avoiding the range where the signal is dominated by the $1/f$ noise of the detector, in our case between

10 kHz and 1 MHz. The RIN at a given frequency can be expressed as :

$$RIN(\nu) = \frac{Sp(\nu)R_{ESA}}{U_{DC}^2 BV} \tag{2.38}$$

where R_{ESA} is the input resistance of the ESA. The usual unity of a RIN is dB/Hz. The uncertainty of the RIN obtained with this method is 2 dB/Hz, calculated over 10 measurements.

The RIN of the DFB QCL operated in continuous-wave was measured at TU Darmstadt with two different sources : a commercial one, ILX, and a homemade low-noise battery. The RIN at 400 kHz is plotted in Figure 2.16 as a function of the normalized pump parameter $a = I/I_{th} - 1$, showing an exponential decrease of the RIN when increasing the pump current, with values ranging from -110 and -155 dB/Hz.

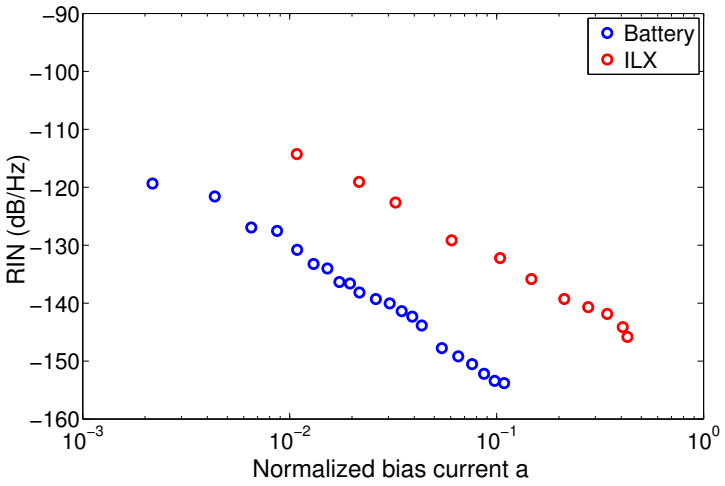

Figure 2.16: Continuous-wave RIN values for two different sources at 400 kHz.

The RIN of the laser using the ARMEXEL source at a repetition rate of 100 kHz is measured under several operating conditions. In pulsed mode, the RIN does not decrease exponentially with the bias current as in continuous-wave operation, but oscillates around -110 dB/Hz after a short decrease for low bias currents. Figure 2.17 a presents the RIN at different center frequencies within the detector range, showing little dependence of the RIN with the measurement frequency. However, the study of the RIN evolution with the pulse width at a fixed center frequency of 20 kHz shows that a longer pulse duration results in a

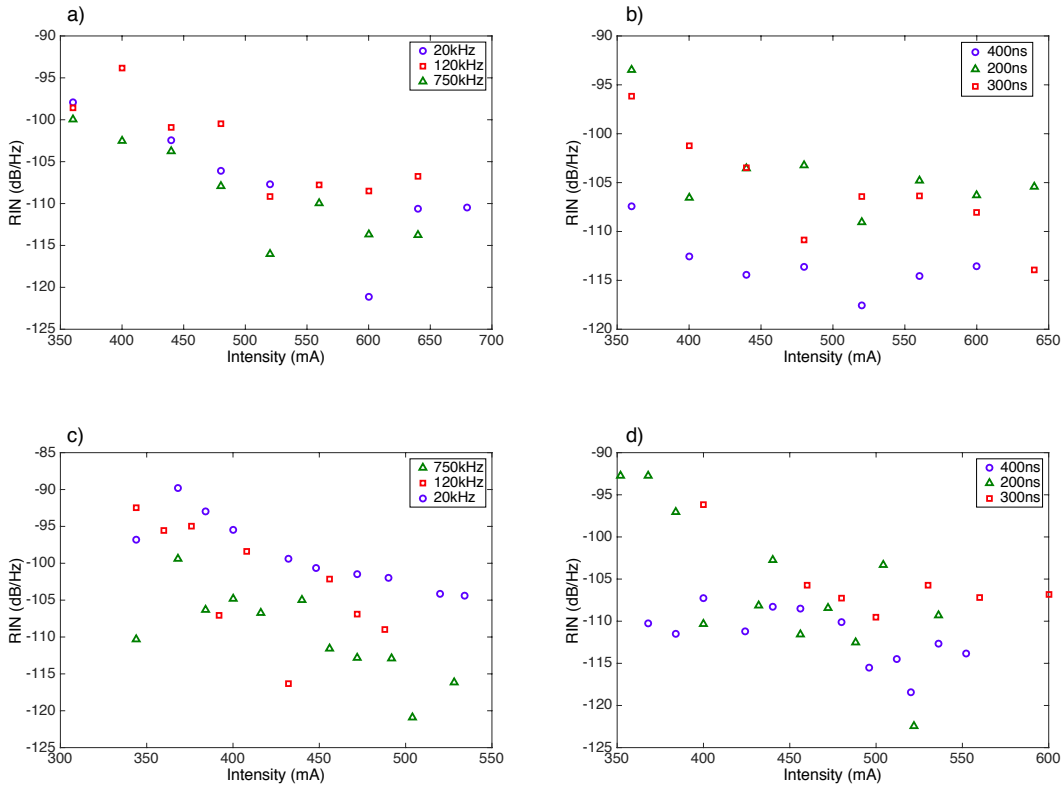

Figure 2.17: a) ARMEXEL RIN evolution with current for 300 ns pulses at 100 kHz at several measurement frequencies. b) ARMEXEL RIN evolution with current at a repetition rate of 100 kHz measured at 20 kHz for several pulse widths. c) PICOLAS RIN evolution with current for 300 ns pulses at 100 kHz at several measurement frequencies. d) PICOLAS RIN evolution with current at a repetition rate of 100 kHz measured at 20 kHz for several pulse widths.

lower RIN (figure 2.17 b).

The RIN measurements are repeated with the PICOLAS source at a repetition rate of 100 kHz. The RIN evolution with the bias current has the same tendency as with the ARMEXEL source, and oscillates around the same value of -110 dB/Hz after a short decrease for low bias currents. The study of the RIN at different center frequencies (Figure 2.17 c) shows that this source is optimized at higher frequency, with a RIN decreasing as the measurement frequency increases. However, the RIN remains almost constant with the pulse duration at a center frequency of 20 kHz (Figure 2.17 d).

The laser noise, characterized by the RIN, is therefore stronger in pulsed operation than in continuous wave. The intensity fluctuations in pulsed mode originate from the temporal

variations of the pulse duration and period, as well as from amplitude fluctuations between two consecutive pulses.

The measured RIN values are higher than the typical ones for single-mode interband laser diodes (around -160 dB/Hz, see [59]), but are consistent with other measurements realized on QCLs [60]. Typical RIN values acceptable for spectroscopic applications are below -150 dB/Hz. The QCL under study can therefore be used for spectroscopy easily in continuous-wave, but also in pulsed mode by averaging over a longer acquisition time t, since the key parameter remains the SNR, which is proportional to $\sqrt{t}$. This can be a drawback for some applications, but several techniques can be implemented to improve the SNR, such as matched filter, synchronous detection or use of a reference path.

2.5 Conclusions

In this chapter, the QCL technology has been studied. Thanks to their intersubband transitions, the QCLs can operate from 3 μm up to 250 μm, depending on the active region design. They are compact sources with high output power, and have therefore become favored lasers sources for mid-infrared applications.

The specific QCL design that will be used in the following chapters has been characterized in details. Both Fabry-Perot and DFB QCLs emitting around 5.6 μm are available, with output power as high as 255 mW in continuous wave operation at 20°C.

Chapter 3

Optical feedback in interband lasers

Optical feedback consists in reinjecting part of the emitted light of a laser into the laser cavity. This phenomenon can originate from parasitic reflections in the experimental setups, either on an optical component or on a fiber extremity. Therefore, optical feedback has been deeply studied in interband semiconductor lasers since the early seventies [61, 62].

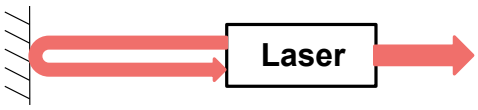

Figure 3.1: Principle of optical feedback.

This chapter aims to give an overview of the response of an interband laser to conventional optical feedback in static and dynamic regimes, both experimentally and numerically. Other phenomena such as filtered optical feedback, consisting in adding a spectral filter on the feedback path, or phase-conjugate optical feedback will not be described in this study. The latter consists in reinjecting light after reflection on a phase conjugator, resulting in reverse propagation direction but also reversed phase of each plane wave component of the optical beam. An extensive study of all sorts of optical feedback can be found e.g. in Ref. [63].

Furthermore, we will describe the dynamical behavior of class A gas lasers subject to optical feedback. Shortly after the laser invention, Maiman *et al.* [64] indeed observed that they can destabilize under some conditions. Furthermore, according to the Poincaré-

Bendison theorem, a dynamical system requires at least three degrees of freedom in order to destabilize and exhibit deterministic chaos [65]. There are three rate equations governing the behavior of a laser [66]:

$$\frac{dN}{dt} = f(N, E, P) \tag{3.1}$$

$$\frac{dE}{dt} = g(N, E, P) \tag{3.2}$$

$$\frac{dP}{dt} = h(N, E, P) \tag{3.3}$$

where N is the carrier density, E the electric field and P the polarization. Arecchi *et al.* [67] proposed a laser classification based on the photon, carrier and polarization lifetimes, τ_p, τ_c and τ_{pol}, respectively. In class C lasers, τ_p, τ_c and τ_{pol} are of the same order of magnitude. This is the case for instance for NH_3 lasers: the system is described by three rate equations, and the laser can become chaotic on its own [68]. Semiconductor laser diodes are class B lasers, meaning that $\tau_c \geq \tau_p \gg \tau_{pol}$. Since the polarization responds quickly to changes of carrier density or electrical field, the third equation governing the polarization can be replaced by its steady-state solution. With only two degrees of freedom, the laser can not destabilize by itself, an additional degree of freedom is required, induced e.g. by Q-switching [69] or by external control such as optical injection or optical feedback. It has recently been demonstrated that vertical cavity surface emitting lasers (VCSELs) can become chaotic without any external perturbation, and the additional degree of freedom comes from the dual polarization of such structures [70]. Finally, in class A lasers, $\tau_p \gg \tau_c \sim \tau_{pol}$. In that case, for instance for gas lasers, both the carrier density and the polarization can be adiabatically eliminated and replaced by their steady-state values. In order to become chaotic, such laser would need two additional degrees of freedom [71].

3.1 Analysis of the optical spectrum of a laser diode under optical feedback

The first observation of the impact of optical feedback on a laser diode was the feedback-induced evolution of the optical spectrum. Depending on the feedback conditions, the

spectrum can either become single-mode with a narrow linewidth (see ref. [72], where the linewidth decreases from 6 MHz down to 30 kHz), or become strongly multimode [73].

In 1986, Tkach and Chraplyvy [74] realized a systematic experimental study and drew the cartography of a DFB quantum well laser under optical feedback, representing the spectral behavior of the laser as a function of the two feedback parameters that are the feedback ratio, defined as the ratio between reinjected and emitted powers, and the external cavity length. They identified five distinct feedback regimes that appear successively when increasing the feedback ratio at a fixed external cavity length (see Figure 3.2).

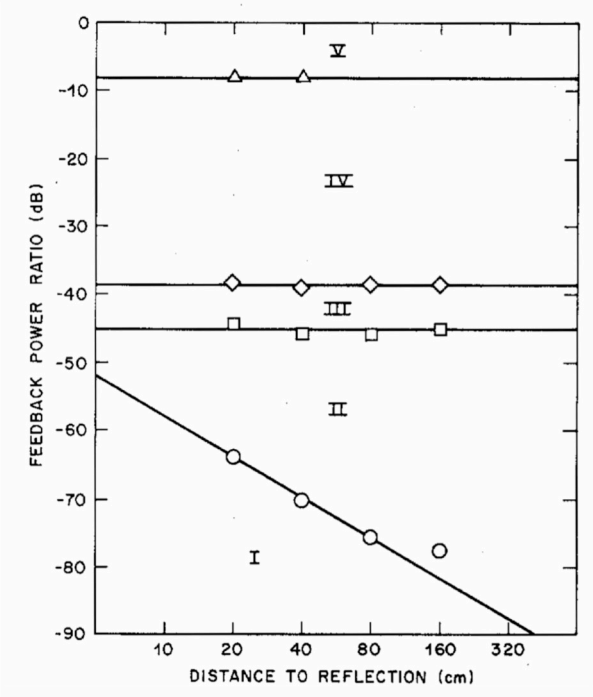

Figure 3.2: Cartography of optical feedback in a DFB quantum well laser (courtesy of [74]).

At very low feedback ratios, the first regime is stable and single-mode, and the laser linewidth as well as output power depend on the feedback phase. Then, the laser enters the second regime, characterized by a bistability: the laser remains single-mode, but jumps from the DFB mode to the mode with the smallest linewidth and vice versa. On the optical spectra both peaks appear simultaneously due to the integration time, but the ratio between the amplitudes of the two peaks depends on the feedback phase. Furthermore, the feedback ratio at which the transition between the first and second regimes occurs, depends

on the external cavity length: the laser becomes more sensitive to optical feedback for longer external cavities.

When further increasing the feedback ratio, the laser enters a third regime where the laser is single-mode on the mode with the smallest linewidth. After this narrow regime the laser enters the coherence collapse regime, characterized by a drastic decrease of the coherence length, a strong linewidth broadening, an increase of the spectrum pedestal and an enhancement of the side-modes. Finally, for very high feedback ratios, the laser is stable and single-mode again, with very high output power. It is important to point out that an anti-reflection coating had to be added on the laser facet to achieve high enough feedback ratios. This regime corresponds to the extended cavity regime, where the laser operates as a small gain medium in a long cavity.

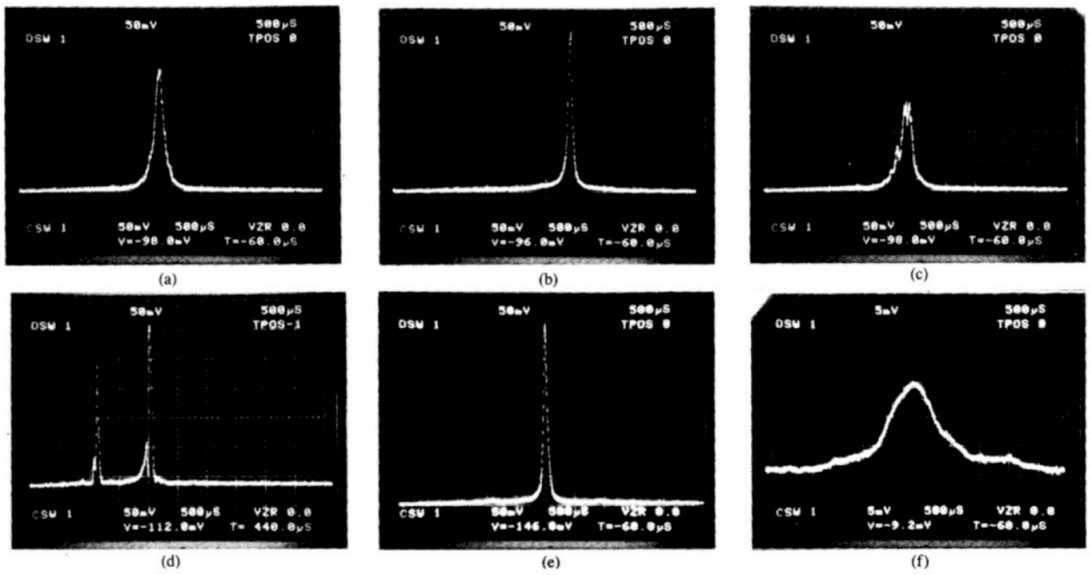

Figure 3.3: Example of optical spectra for a VCSEL at different feedback ratios, representative of the regimes (courtesy of [75]). a) Free-running laser. b) and c) Regime I, at $f_{ext} = -72$ dB for several phase conditions. d) Regime II, at $f_{ext} = -52$ dB. e) Regime III, at $f_{ext} = -38$ dB. f) Regime IV, at $f_{ext} = -23$ dB.

This cartography remains valid for all single-mode semiconductor lasers so far, for which the influence of optical feedback has been studied (see for instance Figure 3.3 in the case of an vertical cavity surface emitting laser, or VCSEL). The feedback ratios at which the

transitions between regimes occur remain of the same order of magnitude, although the third regime can sometimes become very narrow and difficult to locate, especially in the case of quantum dot lasers [63]. Over the years, this cartography has been complemented, especially to describe sub-regimes of the coherence collapse [76] or to address the small-cavity regime [77], defined when $f_r\tau_{ext} < 1$, with f_r the relaxation oscillation frequency and τ_{ext} the external cavity roundtrip time.

3.2 Analytical approach of optical feedback

3.2.1 Rate equations of a laser diode under optical feedback

The formalism of a semiconductor laser under optical feedback was originally proposed by Lang and Kobayashi [78]. In this case, only one roundtrip in the external cavity is considered, which suggests a relatively small amount of feedback. If E is the slowly varying envelop of the complex electric field and N the carrier density of the upper laser state, the rate equations of the laser subject to optical feedback are expressed as:

$$\frac{dN}{dt} = \frac{I}{q} - \frac{N}{\tau_c} - G(N)|E|^2 \tag{3.4}$$

$$\frac{dE}{dt} = \frac{1+i\alpha}{2}\left(G(N) - \frac{1}{\tau_p}\right)E + kE(t-\tau_{ext})e^{-i\omega_0\tau_{ext}} \tag{3.5}$$

where I is the bias current, q the electron charge, τ_c the carrier lifetime, τ_p the photon lifetime, $G(N)$ the gain per unit time, α the linewidth enhancement factor and ω_0 the free-running laser angular frequency. The feedback appears in the last term of equation 3.5, with τ_{ext} the external cavity roundtrip time and k the feedback coefficient:

$$k = \frac{1}{\tau_{in}} 2C_l\sqrt{f_{ext}} \tag{3.6}$$

where τ_{in} is the internal cavity roundtrip time and C_l is an external coupling coefficient that can be expressed for a FP laser as:

$$C_l = \frac{1-R_2}{2\sqrt{R_2}} \tag{3.7}$$

with R_2 the reflection coefficient of the laser front facet subjected to the reinjection. In the case of a DFB laser, the expression of C_l becomes much more complex and depends on the complex reflectivity at both laser facets [79]:

$$C_l = \frac{2(1-|\rho_l|^2)e^{-i\varphi_l}(q^2+\kappa^2)L^2}{i\kappa L(1+\rho_l^2)-2\rho_l qL} \frac{1}{2qL - \sum_{k=l,r} \frac{(1-\rho_k^2)\kappa L}{2iqL\rho_k + \kappa L(1+\rho_k^2)}} \tag{3.8}$$

In this equation, $\rho_k = |\rho_k|e^{i\varphi_k}$ with $k = l,\ r$, is the complex reflectivity at the left or right facet, respectively (the right facet being the one towards the external cavity). L is the laser length, κ the coupling coefficient of the DFB grating and q can be expressed as $q = \alpha_{tot} + i\delta_0$ with α_{tot} the total internal losses and δ_0 the Bragg detuning, defined as the deviation between the lasing and the Bragg wavenumbers.

By writing $E = \sqrt{S}e^{i\phi}$, two rate equations can be deduced from eq. 3.5 for the amplitude and phase of the electric field:

$$\frac{dS}{dt} = \left(G(N) - \frac{1}{\tau_p}\right) S + 2k\sqrt{S(t-\tau_{ext})}\sqrt{S(t)}\ \cos(\omega_0\tau_{ext} + \phi(t) - \phi(t-\tau_{ext})) \tag{3.9}$$

$$\frac{d\phi}{dt} = \frac{\alpha}{2}\left(G(N) - \frac{1}{\tau_p}\right) - k\sqrt{\frac{S(t-\tau_{ext})}{S(t)}}\ \sin(\omega_0\tau_{ext} + \phi(t) - \phi(t-\tau_{ext})) \tag{3.10}$$

3.2.2 Feedback-induced frequency shift

Under steady state, the photon density S_s is constant $S_s = S_s(t) = S_s(t-\tau_{ext})$. Therefore, the term in the cosine $\omega_0\tau_{ext} + \phi_s(t) - \phi_s(t-\tau_{ext})$ must be time insensitive and the steady-state phase ϕ_s can be written without loss of generality as $\phi_s = (\omega_s - \omega_0)t$.

Eq. 3.10 under steady-state gives [80]:

$$\omega_s - \omega_0 = -k\left[\alpha\ \cos(\omega_s\tau_{ext}) + \sin(\omega_s\tau_{ext})\right] \tag{3.11}$$

This leads to several solutions for ω_s, that are the angular frequencies of the external cavity modes, or fixed points. Among these frequencies, the laser will tend to operate on the

mode with minimum linewidth, corresponding to the best phase stability [81].

3.2.3 Threshold reduction due to optical feedback

The steady-state equation resulting from eq. 3.9 gives:

$$G(N) - \frac{1}{\tau_p} + 2\,k\,\cos(\omega_s \tau_{ext}) = 0 \tag{3.12}$$

where ω_s is the solution of eq. 3.11 that has the minimum linewidth.

Therefore, optical feedback has an influence on the threshold gain and hence on the threshold current of the laser, compared to the free-running. Osmundsen and Gade [82] derived the expression of the threshold current by considering multiple roundtrips in the external cavity. In the limit case of small feedback ratios ($f_{ext} \ll 1$), they obtained:

$$I_{th} = I_0\,(1 - 2\,k\,\cos(\omega_s \tau_{ext})) \tag{3.13}$$

This equation fits really well the experimental results, as shown in Figure 3.4.

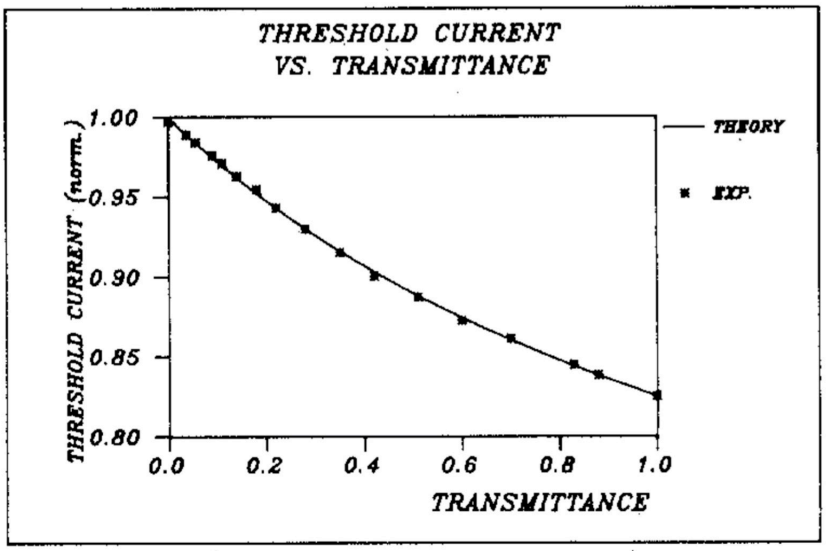

Figure 3.4: Threshold reduction with optical feedback, experimentally and numerically. The transmittance in x-axis is proportional to the feedback ratio. Courtesy of [82].

3.2.4 Linewidth evolution with optical feedback

The linewidth of a semiconductor laser is due to the existence of spontaneous emission and to phase-amplitude coupling, leading to phase fluctuations that result in a frequency noise [83]. In order to characterize the laser linewidth, Langevin noise terms, F_S, F_ϕ and F_N respectively, as well as the spontaneous emission rate R_{sp} must be added to the rate equations 3.4, 3.9 and 3.10 [59]. By defining the phase fluctuation as $\Delta\phi = \omega_0\tau_{ext} + \phi(t) - \phi(t-\tau_{ext})$, the rate equations can be expressed as:

$$\frac{dS}{dt} = \left(G(N) - \frac{1}{\tau_p}\right) S + R_{sp} + 2k\sqrt{S(t-\tau_{ext})S(t)}\,\cos(\Delta\phi) + F_S(t) \tag{3.14}$$

$$\frac{d\phi}{dt} = \frac{\alpha}{2}\left(G(N) - \frac{1}{\tau_p}\right) - k\sqrt{\frac{S(t-\tau_{ext})}{S(t)}}\,\sin(\Delta\phi) + F_\phi(t) \tag{3.15}$$

$$\frac{dN}{dt} = \frac{I}{q} - \frac{N}{\tau_c} - G(N)S + F_N(t) \tag{3.16}$$

These rate equations can be solved by considering a small fluctuation around the steady-state results and assuming slow variations of the phase and intensity of the electric field. Considering the power spectrum then leads to [83]:

$$\Delta\nu = \frac{\Delta\nu_0}{\left[1 + k\tau_{ext}\sqrt{1+\alpha^2}\cos(\omega_s\tau_{ext} + atan(\alpha))\right]^2} \tag{3.17}$$

with $\Delta\nu_0$ the linewidth of the free-running laser [35]:

$$\Delta\nu_0 = \frac{(1+\alpha^2)v_g^2 h\nu_0 G n_{sp}\alpha_m}{8\pi P_{opt}} \tag{3.18}$$

where v_g is the group velocity, h the Planck constant, ν the emission frequency, G the gain, $n_{sp} = R_{sp}/v_g G$ the so-called spontaneous emission factor and P_{opt} the optical power.

Schunk and Petermann [85] linked the phase condition 3.11 and the linewidth equation 3.17 to the different feedback regimes observed experimentally on the optical spectra. By defining a feedback parameter $C = k\tau_{ext}\sqrt{1+\alpha^2}$, they re-defined the first regime as the regime where eq. 3.11 has only one solution, i.e. the case $C < 1$. As shown in Figure 3.5 a

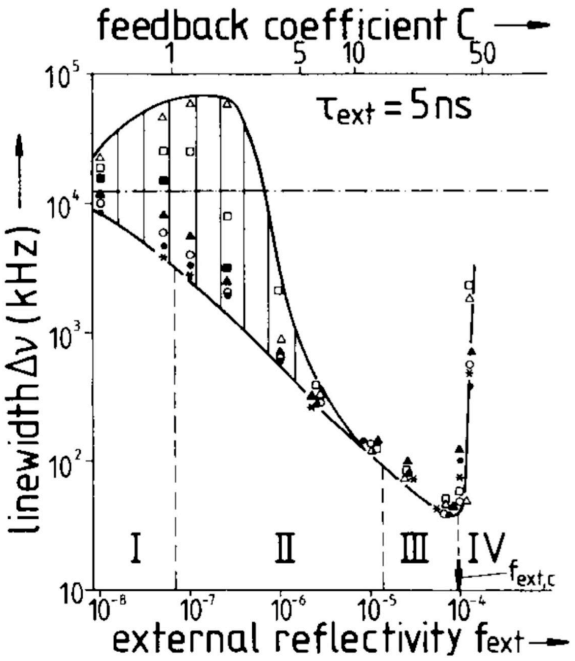

Figure 3.5: Evolution of the laser linewidth as a function of the feedback ratio, for several initial phase conditions (courtesy of [84]).

for an output power of 5 mW and a 5 ns delay, the linewidth can however vary depending on the initial phase $\omega_0\tau_{ext}$. The second regime appears for $C > 1$, where the phase condition 3.11 has several solutions. The solutions of equation 3.11, that gives the laser wavelength as a function of the feedback parameters, lie on an ellipse in the ΔG - $\Delta\omega$ space, with $\Delta\omega = \omega_s - \omega_0 = -k\left[\alpha\cos(\omega_s\tau_{ext}) + \sin(\omega_s\tau_{ext})\right]$ and $\Delta G = G_N\Delta N = -2k\cos(\omega_s\tau_{ext})$ the gain change induced by optical feedback [86]:

$$(2\Delta\omega - \alpha\Delta G)^2 + (\Delta G)^2 = 4k^2 \tag{3.19}$$

The stable solutions are the modes of the external cavity (fixed points) and are located on the lower half of the ellipse (blue circles in Figure 3.6), whereas the unstable solutions, called antimodes, appear on the upper half of the ellipse (red circles in Figure 3.6). Levine *et al.* [87] proved that, although the most stable mode is the mode with maximum gain (also the mode with minimum threshold, corresponding to the external cavity mode closest to lowest point of the ellipse given by $\omega_s\tau_{ext} = 0$), the laser subject to optical feedback will tend to stabilize on the mode with minimum linewidth, which is the closer one to the free-running

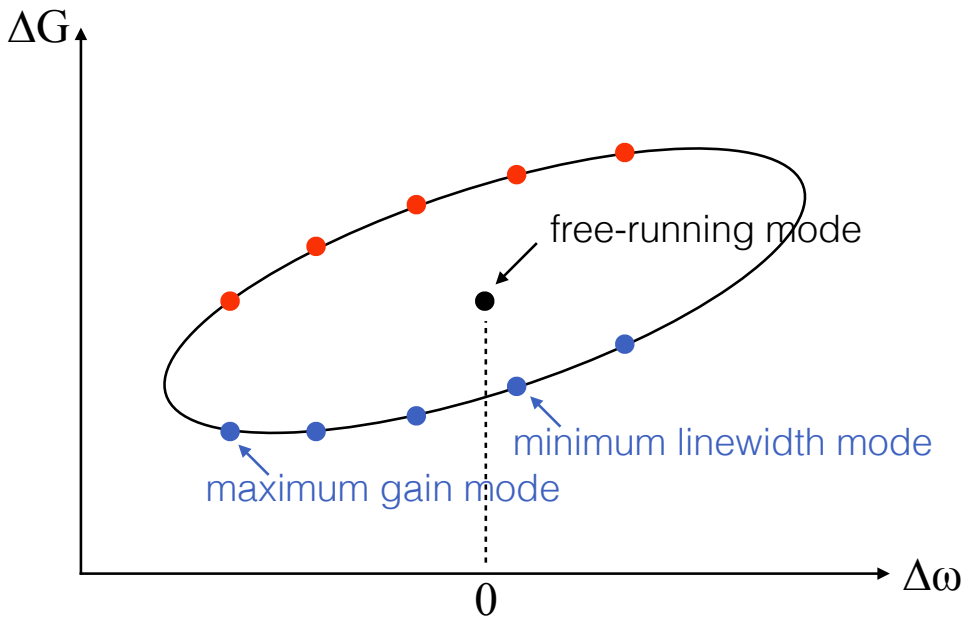

Figure 3.6: Ellipse of the feedback modes and anti-modes. In blue circles, stable external cavity modes, and in red circles, unstable antimodes.

state, as illustrated in Figure 3.6. This corresponds to the third feedback regime. However, these two modes will enter in competition and the coherence collapse regime occurs.

This term coherence collapse was introduced by Lenstra *et al.* [88], by realizing that the feedback terms in the amplitude and the phase of the Lang and Kobayashi equations 3.14 and 3.15 were interfering in the case of relatively strong optical feedback and therefore that these equations could no longer be linearized. By considering this inter-dependence of amplitude and phase, a drastic linewidth broadening as well as a strong decrease of the coherence length compared to the free-running case were obtained numerically, that are in good agreement with the experimental results.

3.2.5 Undulations on the L-I curves

As shown is Figure 3.7, some undulations appear in the light-current characteristic curve of a laser under optical feedback, as well as hysteresis. This phenomenon, explained in [78]

and [89], is due to a competition between the internal cavity modes (or to the laser frequency in the case of a DFB) and the external cavity modes.

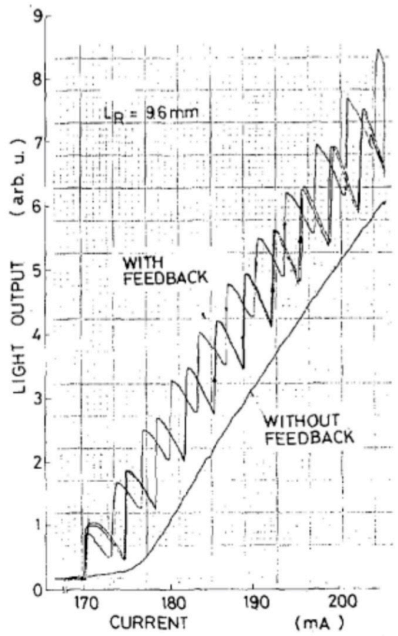

Figure 3.7: Experimental L-I curves of a laser diode with and without optical feedback. The feedback case presents undulations and hysteresis (courtesy of [78]).

At a given bias current, these two different sets of modes can interfere either constructively, leading to a maximum output power, or destructively, resulting in a decrease of the power, as explained in Figure 3.8. When increasing the bias current, the heating of the active area induces an increase of the refractive index and of the effective internal cavity length, and therefore a reduction of the laser free spectral range (or a wavelength shift for DFB lasers). When the external cavity length is an integer multiple of the effective internal cavity length, the interferences are constructive, whereas they are destructive when the external cavity length is an half-integer multiple of the effective internal cavity length, hence the undulations in the L-I curves.

Furthermore, since this phenomenon is due to a heating of the active area, a strong hysteresis appears between an increase and a decrease of the bias current.

These interferences are however only visible for relatively short external cavities, where the free spectral ranges of the external and internal cavities are of the same order of mag-

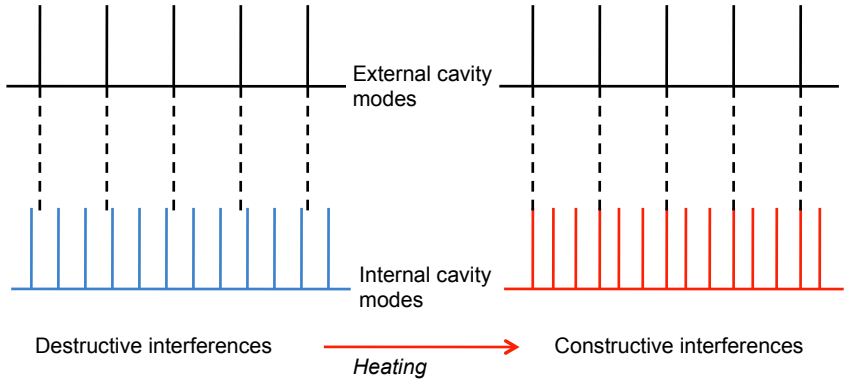

Figure 3.8: Schematic to understand the appearance of undulations in the L-I curves of a laser under optical feedback.

nitude. For very long external cavity of several meters (typically in fibered systems), too many modes exist in the external cavity and no undulations are observed on the L-I curves.

3.3 Dynamical properties of a laser diode under optical feedback

3.3.1 Dimensionless rate equations with optical feedback

The dynamics of a laser diode subject to optical feedback is usually studied using dimensionless parameters [90], that can be extracted from the complex rate equations 3.4 and 3.5.

In these equations, the above threshold gain per unit time can be expressed as :

$$G(N) = \frac{1}{\tau_p} + G_N(N - N_{th}) \tag{3.20}$$

where N_{th} is the carrier density at threshold and G_N is the differential gain.

Then, by normalizing the rate equations with respect to the photon lifetime τ_p, with $s = t/\tau_p$ the normalized time, and defining the new set of variables (Y,Z), with Y the normalized

complex electric field and Z the normalized carrier density, by:

$$Y = \sqrt{\frac{\tau_c G_N}{2}} E \tag{3.21}$$

$$Z = \left(\frac{\tau_p G_N}{2}\right)(N - N_{th}) \tag{3.22}$$

The normalized rate equations can therefore be written as:

$$\frac{dY}{ds} = (1 + i\alpha)ZY + \eta e^{-i\Omega\theta} Y(s - \theta) \tag{3.23}$$

$$T\frac{dZ}{ds} = P - Z - (1 + 2Z)|Y|^2 \tag{3.24}$$

with $\eta = k\tau_p$ the normalized feedback ratio, $\Omega = \omega_0 \tau_p$ the normalized free-running frequency, $\theta = \tau_{ext}/\tau_p$ the normalized external cavity roundtrip time, $T = \tau_c/\tau_p$ the carrier to photon lifetime ratio and P the pump parameter, defined as:

$$P = \frac{\tau_p G_N N_{th}}{2}\left(\frac{I}{I_{th}} - 1\right) \tag{3.25}$$

In this last equation, the threshold current I_{th} and the carrier density at threshold N_{th} are linked by $I_{th} = N_{th} q/\tau_c$ with q the electron charge.

3.3.2 Bifurcation diagram representing the laser dynamics

The rate equations 3.23 and 3.24 are solved by using the Runge-Kutta method (RK4). For a given set of initial conditions, including a given feedback ratio, the numerical time trace of the laser under optical feedback is built by iterations. The final point of the time trace will then be used as the initial condition for the next feedback ratio value. In this work, all simulations were realized in collaboration with CentraleSupelec Metz.

A bifurcation diagram [65] is then built that represents the intensity extrema, extracted from the time series when excluding the transient part of the trace, as a function of the feedback ratio. Figure 3.9 a presents an example of such diagram, for a typical interband laser in typical operating conditions, with a carrier to photon lifetime ratio T = 1700 and an α-factor of 3, biased at P = 0.5, and for an external cavity length of 30 cm. The diagram

shows a succession of stable and unstable behaviors when increasing the feedback ratio.

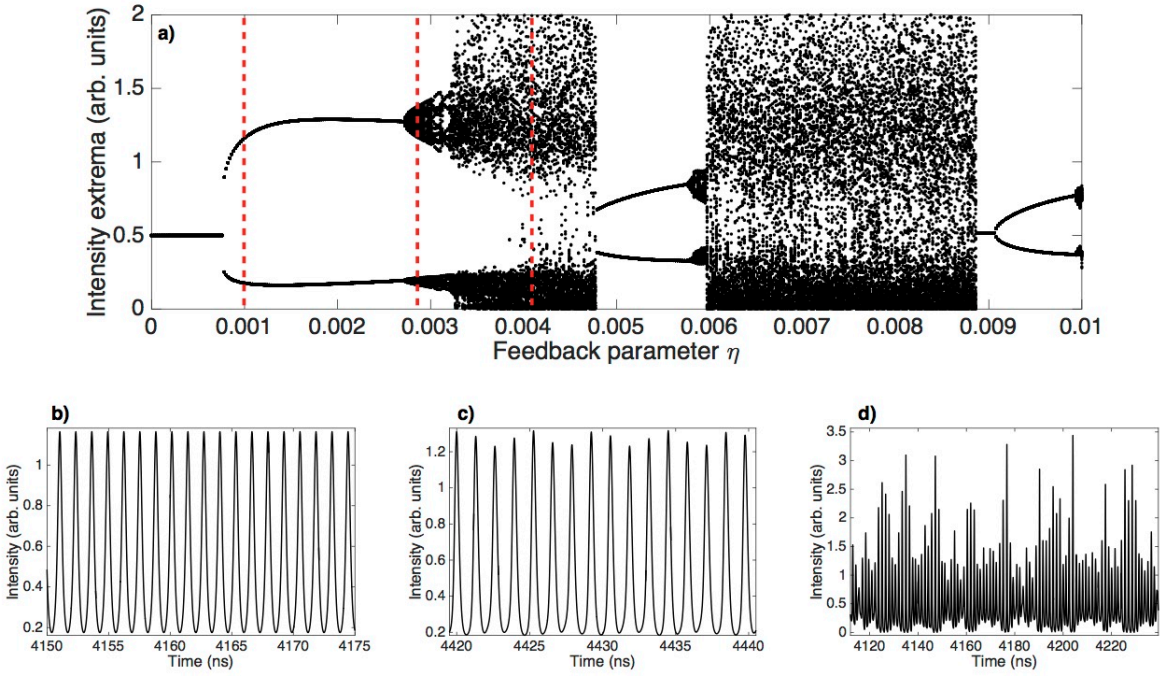

Figure 3.9: a) Numerical bifurcation diagram for T = 1700, P = 0.5, $\theta = 500$ ($L_{ext} \approx 30$ cm) and $\alpha = 3$. b) Corresponding time trace for $\eta = 0.001$. c) Time trace for $\eta = 0.0027$. d) Time trace for $\eta = 0.0042$.

For very low levels of feedback, the laser emission is stable, there is only one line on the bifurcation diagram and the only perturbation that appears on the time trace is due to noise. At a critical feedback level, here $\eta \approx 0.0008$, the minimum and maximum of intensity split significantly. This particular point is called Hopf bifurcation (or Hopf point), and it corresponds in the appearance in the time trace of a periodic oscillation at the relaxation oscillation frequency (see Figure 3.9 b). This regime is also called period 1 (P1). For higher feedback ratios, the diagram splits again as another oscillation frequency appears, that is superimposed on the first one (Figure 3.9 c). More and more frequencies are involved, until the oscillations become totally aperiodic (Figure 3.9 d). These random pulsations do not correspond to noise, since they strongly depend on the initial conditions and are purely deterministic, i.e. they can be fully anticipated by using a complete numerical model: the laser has a chaotic behavior.

When further increasing the feedback ratio, the laser restabilizes on an external cav-

ity mode, and the cycle starts again. Sometimes, although this was not observed in this particular example, for very strong feedback, the periodic oscillations occur at the external cavity frequency, but the first oscillations just after the first Hopf point always occur at the relaxation oscillation frequency.

These results are consistent with experiments conducted on several interband lasers [91] and with other numerical analyses in the literature [92, 93]. The nonlinear dynamics described here are called quasi-periodic route to chaos [94].

3.3.3 Influence of the bias current, the external cavity length and the α-factor on the bifurcation diagram

The evolution of the laser dynamical behavior under optical feedback as a function of the bias current is depicted in Figure 3.10 a, b and c, corresponding to T = 1700, $\alpha = 3$, $\theta = 500$ and P = 0.02, P = 0.5 and P = 1 respectively. It can be seen that the first chaotic area strongly expends with the pump parameter. Furthermore, the feedback ratio at which the first Hopf bifurcation occurs increases with the bias current. When the laser is operated just above threshold, the dynamics is different from the one explained before. After the Hopf bifurcation, the laser does enter the period 1 regime and oscillates at the relaxation oscillation frequency (Figure 3.11 a), but the destabilization towards chaos occurs through period-doubling, i.e. the second frequency that appears is exactly twice the relaxation oscillation frequency. This dynamical regime is called period 2 or P2 (see Figure 3.11 b). Afterwards, the period keeps on doubling until reaching the chaotic region [95].

Figure 3.10 d, e and f represent the evolution of the bifurcation diagram when increasing the external cavity length, i.e. $\theta = 50$, $\theta = 500$ and $\theta = 1000$ respectively, at fixed T = 1700, $\alpha = 3$ and pump parameter P = 0.5. The position of the first Hopf point does not change significantly with the external cavity length, which is in agreement with the cartography of optical feedback (Figure 3.2). However, the extent of the chaotic zone increases significantly with the external cavity length. For the shortest cavity in this example, the time trace remains much longer in period 1, and the chaos occurs only at very high feedback ratios (please note the larger x-scale of Figure 3.10 d compared to the others). The limit case, as observed in the literature, is the disappearance of chaos for ultra-short cavities [96, 97, 98].

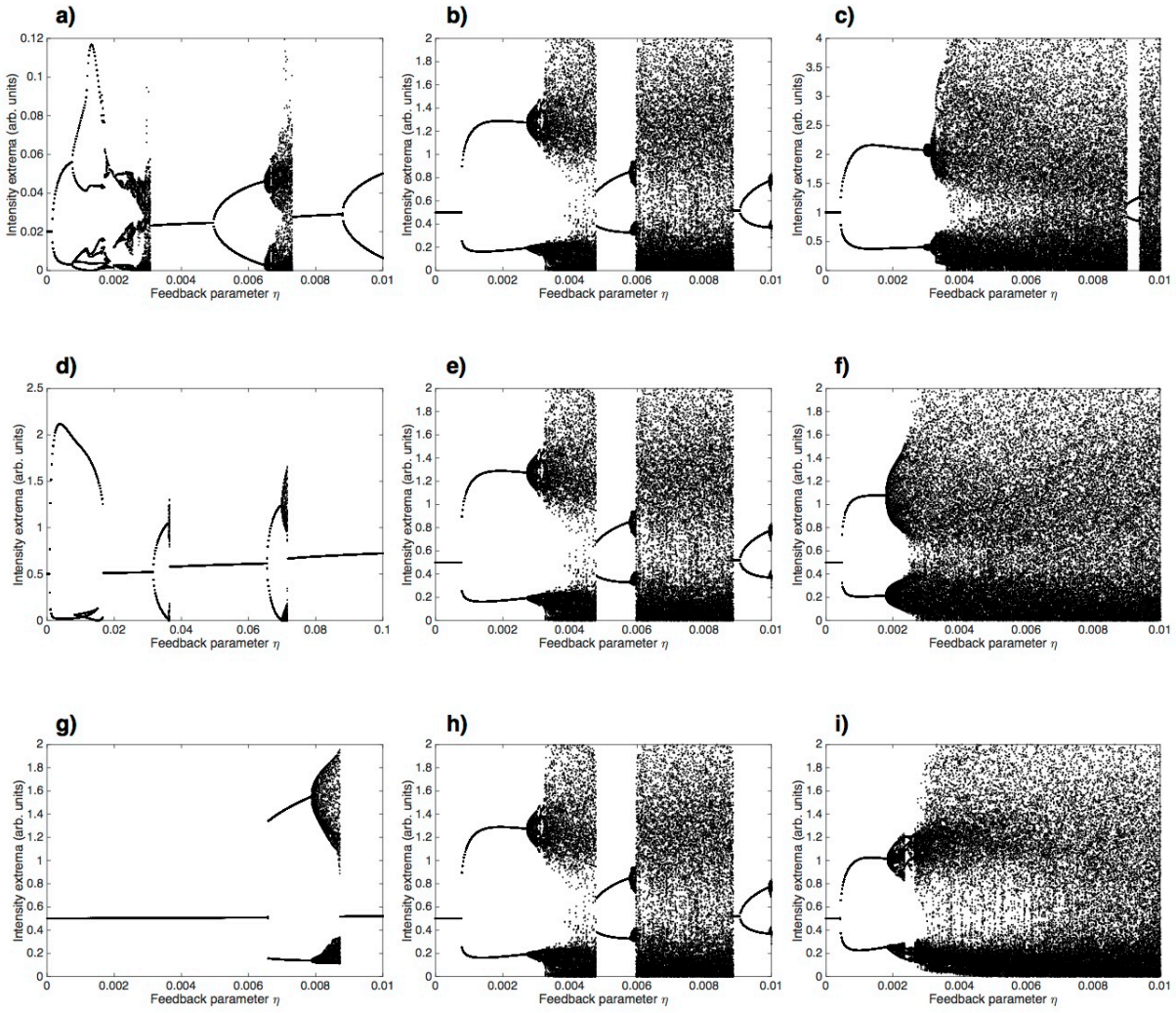

Figure 3.10: Evolution of the bifurcation diagram, calculated by increasing the feedback ratio for T = 1700, as a function of the main parameters. First row: evolution with the pump current, for $\alpha = 3$ and $\theta = 500$. a) P = 0.02. b) P = 0.5. c) P = 1. Second row: evolution with the external cavity length, for $\alpha = 3$ and P = 0.5. d) $\theta = 50$ ($L_{ext} \approx 3$ cm). e) $\theta = 500$ ($L_{ext} \approx 30$ cm). f) $\theta = 1000$ ($L_{ext} \approx 60$ cm). Third row: evolution with the α-factor, for P = 0.5 and $\theta = 500$. a) $\alpha = 1$. b) $\alpha = 3$. c) $\alpha = 5$.

This occurs in the short-cavity regime, i.e. when the external cavity roundtrip time verifies $f_r \tau_{ext} < 1$, where f_r is the relaxation oscillation frequency.

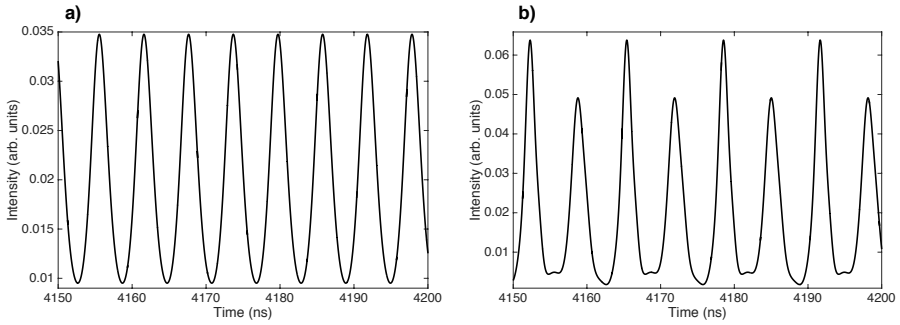

Figure 3.11: Time traces corresponding to Figure 3.10 a. a) Period 1, for $\eta = 2 \times 10^{-4}$. b) Period 2, for $\eta = 8 \times 10^{-4}$.

Finally, Figure 3.10 g, h and i show the influence of the α-factor on the bifurcation diagram, with $\alpha = 1$, $\alpha = 3$ and $\alpha = 5$ respectively, which correspond to typical values for laser diodes, at given T = 1700, P = 0.5 and $\theta = 500$. Increasing the α-factor results in decreasing the feedback ratio at which the first Hopf bifurcation occurs, as well as extending the chaotic area. Furthermore, for very small α values, the shape of the Hopf bifurcation differs significantly from the higher α case [99]. The bifurcation occurs on an external cavity antimode, this is called subcritical Hopf bifurcation. Supercritical Hopf bifurcations are the most common scenario in interband lasers under optical feedback, and correspond to bifurcations leading to stable periodic solutions, whereas subcritical bifurcations lead to unstable periodic solutions, and occur mainly in the short-cavity regime [99]. For extremely low α-factors, no chaos appears, and the dynamics correspond to a cascade of supercritical and subcritical Hopf bifurcations.

It is important to stress that, contrary to the two previous parameters, the α-factor is not a degree of freedom during the experiment. However, the analysis of the influence of this parameter on the bifurcation diagram allows explaining the difference in behavior that has been observed from one structure to another when subject to optical feedback.

3.3.4 Phase diagrams

Another representation of the laser dynamics consists in plotting the phase diagrams, corresponding to the carrier number versus optical power curves. When the emitted power remains constant, i.e. when the laser is under steady-state, it operates on an external cavity mode at an angular frequency ω_s, as shown in Section 1.2.2. On the phase diagram, it is represented by a single point (see the first curve of Figure 3.12). Figure 3.12 a represents period 1 operation and the phase diagram is a circle around the steady-state point. Period 2 corresponds to the appearance of a second circle of different radius (Figure 3.12 b), whereas chaos involves many frequencies, represented on the phase diagram by multiple concentric trajectories of various radii (Figure 3.12 c).

All these phase diagrams are centered on the steady-state point. Therefore, the external cavity modes are also called fixed points, or attractors.

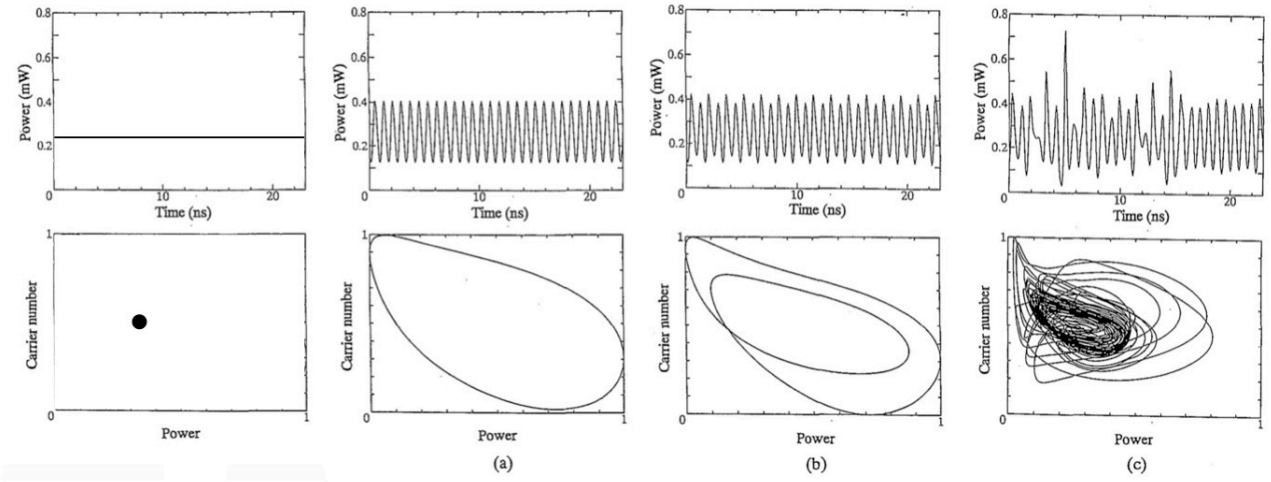

Figure 3.12: Numerical time traces and associated phase diagrams (a,b and c are courtesy of [100]).

3.3.5 Coherence collapse and chaos

The chaos predicted numerically from the Lang and Kobayashi equations was also observed experimentally, and was proven to coincide with the coherence collapse regime.

The first hint of the appearance of chaos within the coherence collapse regime originated from the analysis of the experimental electrical spectra of a laser, which was shown to match the power spectral density derived from the numerical time traces [101]. A few years later, the time resolution of the photodiodes became sufficient to observe directly the experimental time series and experimental phase diagrams [94] (see Figure 3.13). The two predicted routes to chaos, quasi-periodic or through period-doubling, were observed experimentally, the occurrence of one scenario or the other depending on the laser intrinsic characteristics and on the initial conditions.

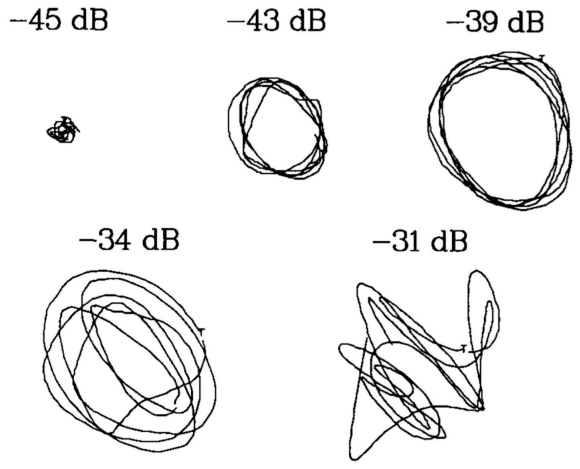

Figure 3.13: Experimental phase diagrams showing the route to chaos (courtesy of [94]).

A careful sweep of the feedback ratio in the experiment sometimes enables to observe the whole route to chaos on the optical spectra, as shown in Figure 3.14 from measurements performed at Telecom ParisTech on a DFB quantum well laser. While the optical spectrum is broadening, some peaks may appear on the spectrum corresponding to the relaxation oscillation frequency, as verified on the electrical spectrum. Then these peaks disappear, leaving a very broad spectrum both in the wavelength and frequency domains.

The critical feedback level $f_{ext,c}$ corresponding to the onset of coherence collapse, that was defined from the maximum frequency shift with respect to the free-running. It therefore corresponds to the occurrence of an unstable behavior in the laser, and can be considered as the maximum parasitic feedback ratio that can be tolerated for stable operation. Several

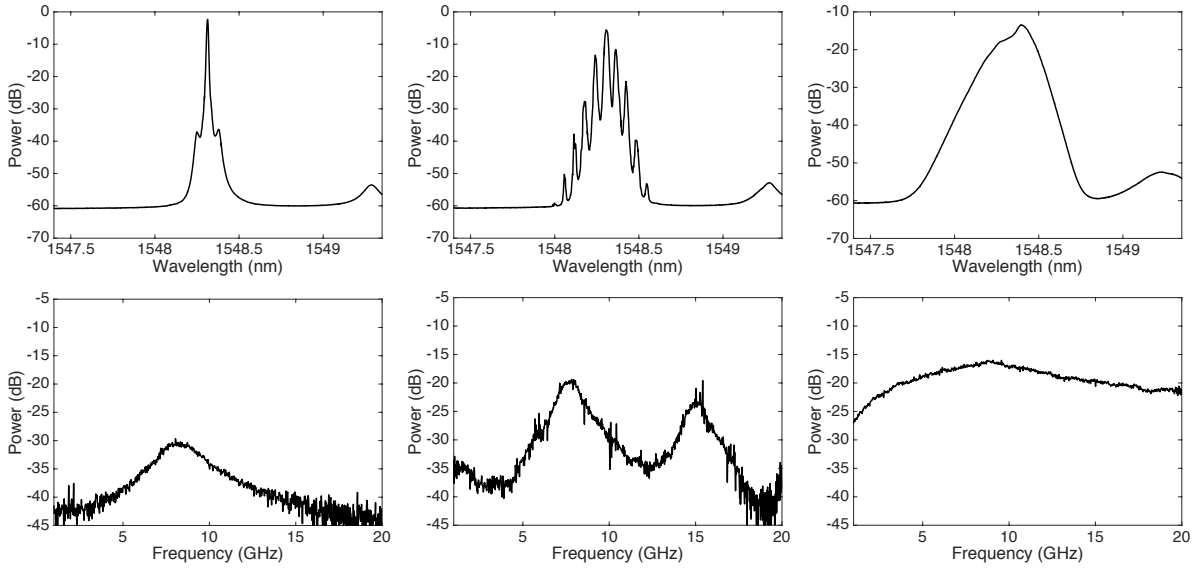

Figure 3.14: Optical and electrical spectra of a DFB quantum well laser under optical feedback, presenting the progressive appearance of coherence collapse.

approximated expressions exist in the literature, such as [102]:

$$f_{ext,c} = \left(\Gamma \frac{\tau_{in}}{4C_l}\right)^2 \frac{1+\alpha^2}{\alpha^4} \tag{3.26}$$

where Γ is the damping rate associated to the relaxation oscillation frequency.

3.3.6 Low frequency fluctuations

Another form of chaos may appear, different from the aperiodic pulsations described above. It is usually observed just above threshold and takes the form of random power drop-outs followed by a progressive recovery, or build-up, as illustrated in Figure 3.15. This phenomenon is called low frequency fluctuations (LFF).

Many attempts have been made to explain the origin of such power drop-outs. Henry and Kazarinov [86], followed by Mørk *et al.* [104], attributed the LFF to a bistability between the mode with maximum gain and the mode with lower linewidth, and to the switching between the two modes due to noise and spontaneous emission. With this potentiel model, they were able to reproduce qualitatively one deterministic power drop-out and the associated recovery.

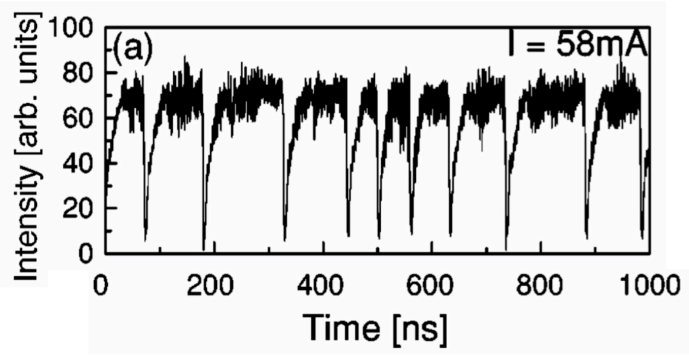

Figure 3.15: Experimental observation of LFF (courtesy of [103]).

However, this model can not explain the existence of more than one drop-out.

The satisfying explanation was given by Sano [105] by studying the feedback ellipse representing the modes and anti-modes. A schematic representation is given in Figure 3.16.

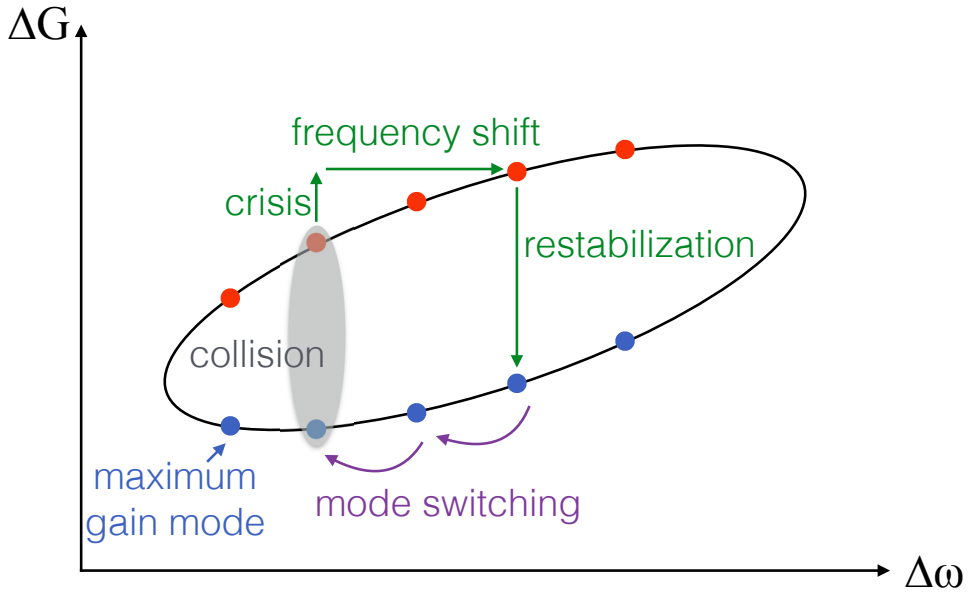

Figure 3.16: Schematic of the scenario leading to LFF. In blue circles, stable external cavity modes, and in red circles, unstable antimodes.

During LFF, the build-up process comes from mode switching towards the mode with maximum gain, located at the lower extremity of the ellipse (purple arrows in Figure 3.16). However, a so-called crisis [105] occurs during the process, corresponding to a collision be-

tween a quasi-attractor, i.e. an external cavity mode that temporarily looses its stability due to the occurrence of chaos, and the associated antimode. Due to the crisis, the ΔG value will increase, and in order to restabilize, the laser frequency will shift until it meets the ellipse again on an antimode, and the stabilization then occurs on the corresponding low-power external cavity mode (green process in Figure 3.16).

This explanation allows to understand the origin of LFF, and also to conclude that the presence of LFF in the dynamics of a laser under optical feedback is a manifestation of deterministic chaos.

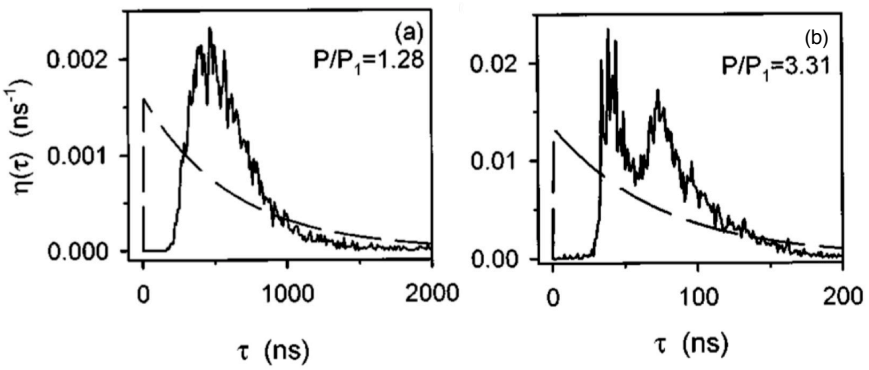

Figure 3.17: Statistics of the period between two consecutive drop-outs. a) τ_{ext} = 10 ns and P = 1.28. b) τ_{ext} = 1 ns and P = 3.31. ($P_1 = 1$) (courtesy of [106]).

Many different phenomena can lead to slow fluctuations in a laser diode under optical feedback, such as a misaligned optical cavity [107]. To recognize LFF among these fluctuations, the study of the statistics of the period between two consecutive drop-outs is necessary [106, 108, 109]. As shown in Figure 3.17, the statistics of the LFF is characterized by a minimum period of typically $10 \times \tau_{ext}$ below which no events occur. Furthermore, it has the shape of a decaying exponential at low bias current, and a second maximum appears for higher bias current. Such statistical distribution is typical of the LFF and therefore of the presence of chaotic behavior in a laser under optical feedback.

In most cases, the LFF appear very close to threshold, but it has also been observed at higher bias currents, where LFF and coherence collapse may coexist, until the fully-developped coherence collapse regime takes over at high bias current or high feedback ratios. LFF can even coexist with stable emission close to threshold at very high feedback ratios

(see Figure 3.18 and Ref [103]).

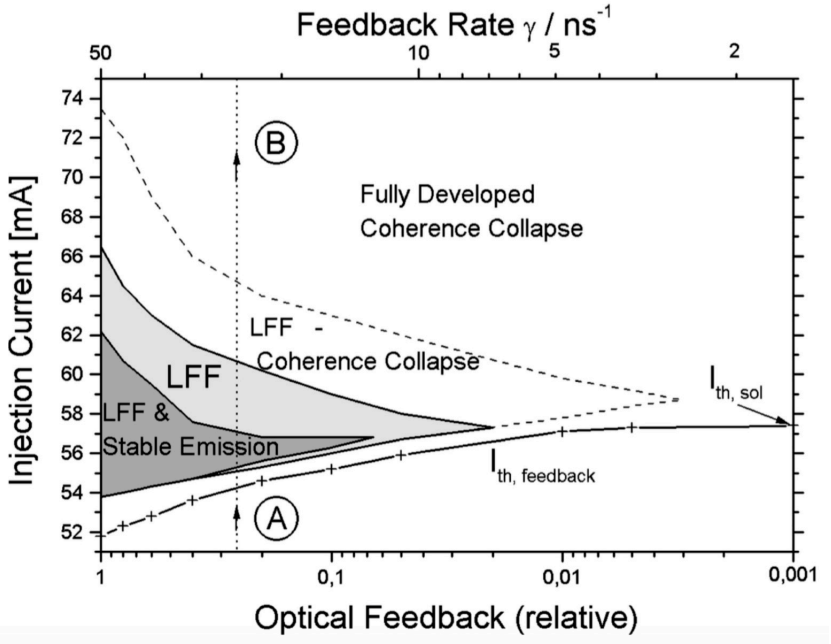

Figure 3.18: Mapping of the appearance of LFF as a function of the feedback ratio and the bias current (courtesy of [103]).

3.3.7 Extension to the dynamics of a class-A laser under optical feedback

Until now, the whole study was centered on laser diodes, that are class B semiconductor lasers, i.e. $\tau_p \leq \tau_c$. All class B lasers follow a dynamical scenario based on the relaxation oscillations, as described in the previous section (see for instance [110] for the case of VCSEL). Another scenario exists, where the periodic oscillations arising from the first Hopf bifurcation are directly at the external cavity frequency. As a reminder, this frequency may occur in class B dynamical scenarios, but only for very high feedback ratios, after several chaotic areas (Figure 3.9).

This bifurcation at the external cavity frequency has been reported by Kuwashima *et al.* [111, 112] in He-Ne lasers subject to optical feedback, that are class A lasers since $\tau_p \gg \tau_c$. Furthermore, chaotic operation of such lasers was observed experimentally, characterized by the appearance of LFF. It was obtained using a periodic fluctuation of the tilt of the feedback mirror to induce the third degree of freedom necessary for chaos to appear. However, these

LFF have the opposite trend compared to the one described in the previous paragraph, since here the power decay is progressive and the recovery is really fast. This might be due to the very fast carrier dynamics. The dynamics of the class A laser is depicted in Figure 3.19.

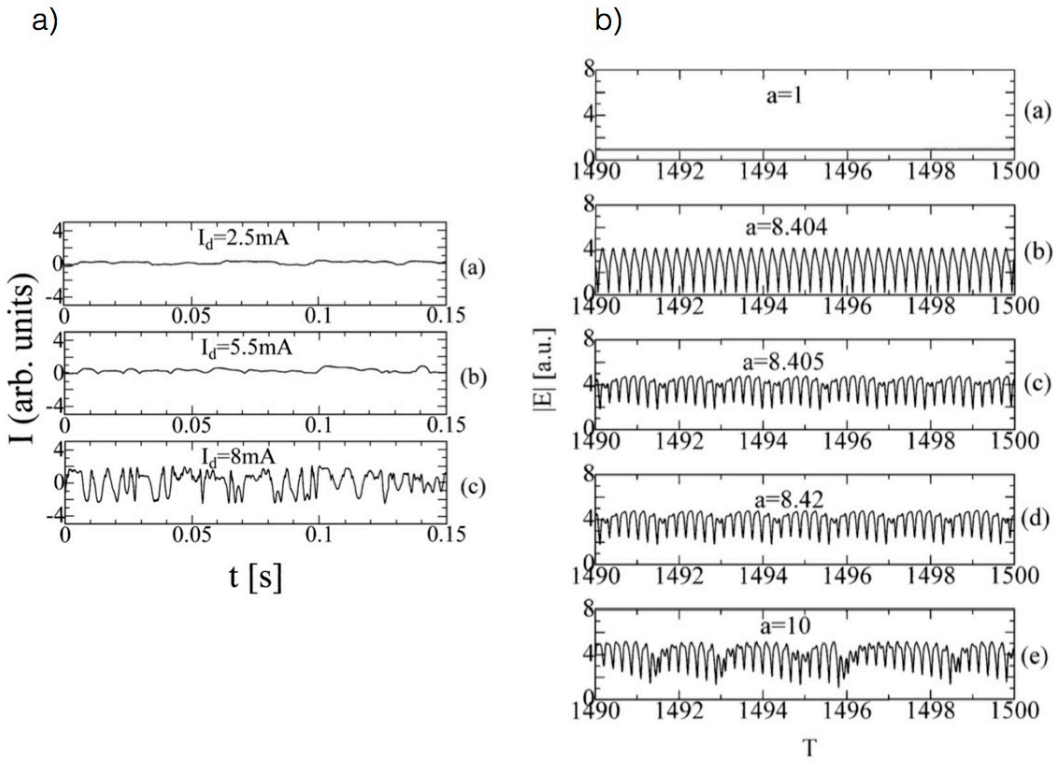

Figure 3.19: a) Experimental time traces of a class A laser for several feedback parameters a (equivalent to k) showing the appearance of LFF (courtesy of [111]). b) Numerical time traces of a class A for several feedback parameters showing oscillations at the external cavity frequency followed by LFF (courtesy of [112]).

This class A-like scenario can be retrieved for a class B laser by studying limit cases of the Lang and Kobayashi equations 3.4 and 3.5. The first condition for which oscillations at the external cavity were obtained numerically is the zero-bias case, leading to a relaxation oscillation frequency equal to zero, but this presents little interest in practice. The second case that was studied by Pieroux and Mandel [113] is the long external cavity limit, focusing on $\theta \times \tau_p \rightarrow \infty$. In this configuration, they also obtained numerically a class A scenario, with periodic oscillations at the external cavity length, followed by a quasi-periodic route to chaos, itself characterized by LFF with fast recovery time. Finally, the last limit case leading to a class A-like scenario is the strong damping scenario. Especially for quantum dot lasers, that

present stronger damping compared to quantum well lasers, around 10 GHz [45], theoretical studies showed that their dynamics tend to resemble the one of class A lasers when subject to optical feedback [114, 115]. However, there has been no experimental evidence of a class A dynamical scenario in quantum dot lasers under optical feedback so far.

3.3.8 Chaotic laser diodes and applications

While the appearance of chaos in the emission of a laser diode subject to optical feedback rapidly becomes a hinder for the usual applications, leading for instance to a strong increase of noise in fiber communications [116], a chaotic laser diode can be used for a wide range of new applications [117, 118].

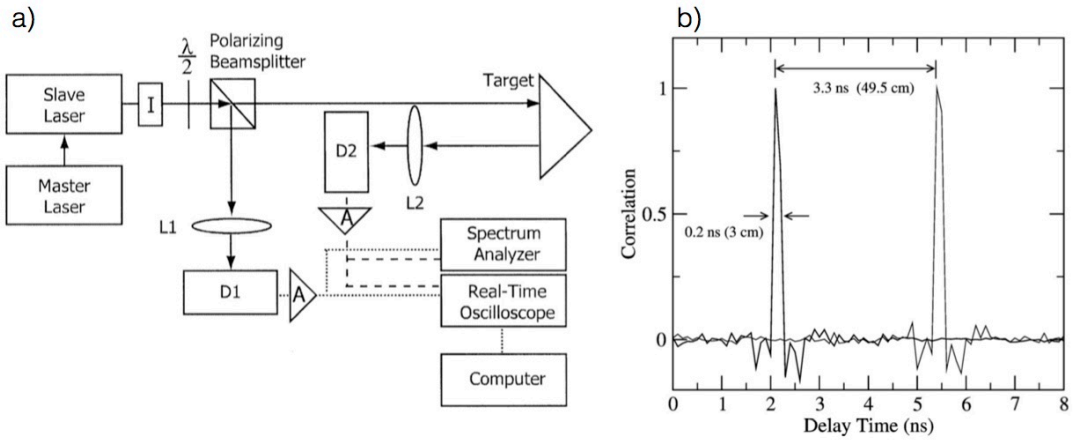

Figure 3.20: a) Experimental setup of a chaotic LIDAR. In this case, the chaos is obtained from optical injection. b) Experimental result, showing a precise measurement of the 50 cm separated targets, with a range resolution of 3 cm (courtesy of [119]).

Lin and Liu [119] proposed a chaotic-based LIDAR (or CLIDAR). There are two categories of LIDARs, one based on lasers with ultra-short pulses and the second one based on modulated CW lasers. For the latter, the information on the target are recovered from the correlation between the signal back-reflected on the target and the delayed emitted signal. The advantage of this technique is its low price, since a simple laser diode can be used rather than an expensive laser delivering ultra-short pulses. However, high-performance signal generation algorithms are required to ensure that the modulation does not repeat itself,

which would lead to the measurement of a false delay time. Chaotic lasers diodes offer a signal with high bandwidth, easy to generate and to amplify, leading to very high resolutions better than the ones obtained with the two conventional techniques, down to 1 cm range resolution for targets separated by 50 cm at 2 m distance, limited by the bandwidth of the oscilloscope. Furthermore, the chaotic behavior of the laser guaranties that the signal will not repeat itself, leading to systems with higher performances. Figure 3.20 represents the typical experimental setup of such CLIDAR, here with chaos obtained from optical injection.

Similarly, the chaotic signal emitted by a semiconductor laser under external perturbation can be collected on a photodetector and converted into a chaotic microwave signal, that can be exploited for chaotic RADAR (CRADAR) detection [120]. Generating chaotic light is indeed much easier than directly modulating a microwave source. A high range resolution of 9 cm was obtained experimentally, once again limited by the bandwidth of the antennas and the oscilloscope and not by the chaos bandwidth. Furthermore, the use of chaotic signal instead of modulated wave leads to RADARs resistant to noise and jamming.

Chaotic lasers can also be used for chaos communications [118]. By injecting the light emitted by a chaotic laser in a second similar laser, under strong injection and locking conditions, the second laser will become chaotic and reproduce the chaos of the first laser, as shown in Figure 3.21 a and b: this is called chaos synchronization. Using this technique with chaos-based message encryption methods, such as chaos masking or chaos modulation [121], a secured message can be transmitted from a transmitter to a receiver. Figure 3.21 c describes this process: the emitters sends a chaotic encrypted message to a receiver as well as a key, consisting of information on the static properties of the laser. The receiver will analyze the message twice: the encrypted message will be detected, and the chaotic carrier will be retrieved using chaos synchronization on a laser similar to the one used for the emission. By substracting the two signals, the message can be securely obtained, as shown in Figure 3.21 d.

Moreover, some applications such as authentification protocols, online gaming or Monte-Carlo simulations require the generation of random bit sequences. Various methods exist to provide such sequences, but they are based on pseudo-random bit generation, meaning

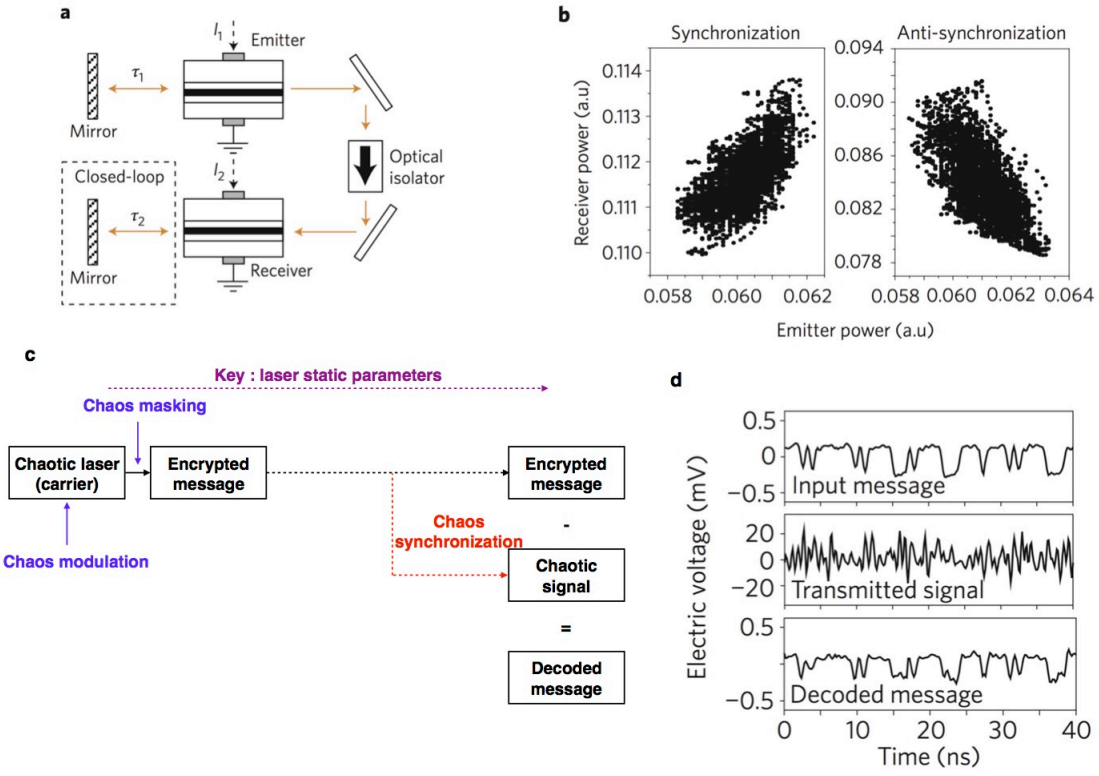

Figure 3.21: Chaos-based communications. a) Setup for chaos synchronization. b) Experimental results showing synchronization and anti-synchronization. c) Principle of chaos-encrypted communications. d) Example of chaos-based communications. (a, b and d are courtesy of [118])

that they are vulnerable if the starting point can be guessed. Chaotic semiconductor lasers offer pseudo-random bit generation with extremely high bit-rate, using strongly diverging trajectories, with a starting point almost impossible to recover once the optical signal has been converted to digital signal [122, 117, 123].

Finally, another application of chaotic semiconductor lasers is chaos masking in reservoir computing [124, 125]. Reservoir computing is a neural network where the input signal is mapped into a high dimensional space, which facilitates classification and time series prediction. The connections between this high dimension input layer and the network (or reservoir), as well as inside the network are then determined randomly, but kept fixed. Compared to other neural networks, the learning algorithm is simpler and requires small calculation power. In reservoir computing, consistency is really important, i.e. the same

output signal must be observed when repeating the same input signal, which is determined by a temporal mask applied on the input signal. If the input signal is the signal emitted by a laser diode, the temporal mask can be based on chaos, and the light emitted by the chaotic laser is then injected in the reservoir, which is based on the dynamical response of a second laser diode subject to optical feedback. Recent numerical predictions by Nakayama *et al.* [126] show that chaos masking leads to a normalized mean-square error between the input and output signals 8 times smaller than for a binary mask, which is the one usually used in laser-based reservoir computing, meaning that the consistency using chaos masking is very high.

3.4 Conclusions

In this chapter, the impact of optical feedback, induced by a reflection on a fiber extremity or on a mirror, on the static and dynamical properties of a laser diode has been reviewed. Depending on the two parameters that are the external cavity length and the feedback ratio, optical feedback will either increase the laser stability, leading to single-mode emission with extremely narrow linewidth, or destabilize the laser, with very broad optical emission spectrum.

From a dynamical viewpoint, when increasing the feedback ratio the laser diode will first oscillate at the relaxation oscillation frequency, and then will have a transition towards chaos either through period-doubling or through quasi-periodic fluctuations. The chaos itself takes the form of aperiodic oscillations or of low-frequency fluctuations, consisting in power drop-outs followed by a progressive recovery. Another route to chaos exists, where the laser starts to oscillate at the external cavity frequency directly after the first Hopf bifurcation, but it has only been observed in class A gas lasers so far, even though it can numerically be achieved in limit cases of the Lang and Kobayashi equations.

Finally, although parasitic optical feedback is a hinder in most cases and especially in fibered configurations, hence requiring the integration of optical isolators in packaged lasers, a controlled amount of optical feedback can improve the laser emission properties, and even chaotic laser diodes can be used for a number of applications ranging from the chaotic LIDAR

to chaos-based communications.

Chapter 4

Impact of optical feedback on quantum cascade lasers

As mentioned in the previous chapter, optical feedback can either significantly improve laser properties such as linewidth or output power, or completely destabilize the laser, rendering its emission chaotic. Furthermore, optical feedback can appear through any parasitic reflection in the experimental setup. It is therefore important to fully characterize the laser response to this phenomenon in order to control its stability.

In quantum cascade lasers, there have been very few comprehensive studies on optical feedback. In this chapter, we propose to study both experimentally and numerically the impact of optical feedback on the static and dynamical properties of a QCL. In particular, the birth of optical instabilities leading to temporal chaos is reported for the first time.

4.1 Previous studies

Optical feedback is regularly used in external-cavity QCLs: by reflecting the emitted light from a Fabry-Perot QCL on a grating and re-injecting only one wavelength, the laser becomes single-mode and a widely tunable source is obtained, where the wavelength is shifted by changing the incident angle on the grating, as shown in Figure 4.1. [127].

Some experimental studies have also shown that optical feedback strongly reduces the relative intensity noise of a QCL, up to a 9.5 dB reduction when optimizing the feedback conditions, as illustrated in Figure 4.2 [128, 129].

Moreover, a theoretical study pointed out the expected high stability for a QCL subject to optical feedback [130, 131], with the appearance of mode switching when increasing the

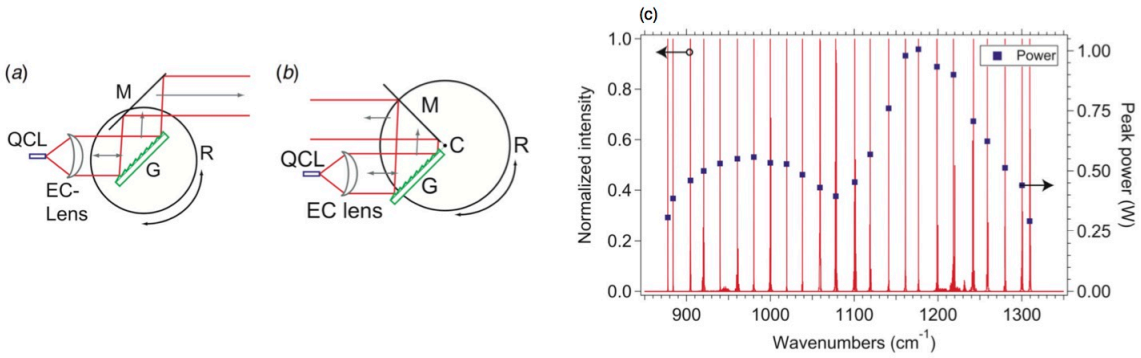

Figure 4.1: a,b) External-cavity QCL in different configurations. c) Achievable wavelengths by tilting the grating. (Courtesy of [127]).

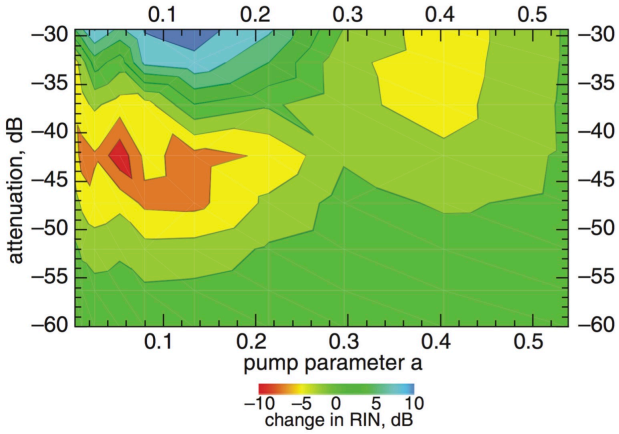

Figure 4.2: Evolution of the relative intensity noise as a function of the feedback parameters (courtesy of [128]).

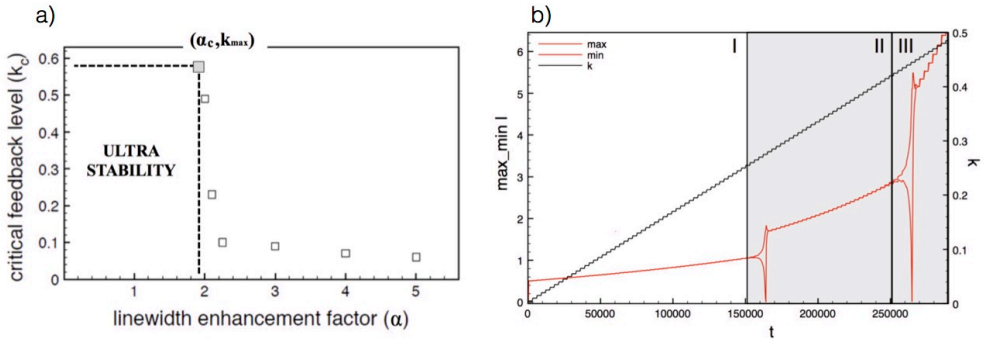

Figure 4.3: a) Critical feedback level for a THz QCL, which becomes very high when the α-factor becomes small (courtesy of [130]). b) Numerical evolution when increasing the feedback coefficient k, showing mode switching (courtesy of [131]).

feedback ratio but no chaos (see Figure 4.3). However, this study is based on the assumption that the linewidth enhancement factor of a QCL is almost zero, hypothesis that will be discussed in a following section.

Finally, chaotic operation has been observed before in QCL-based structures. Gmachl *et al.* [132] demonstrated spatial chaos in a micro-cylinder laser based on an external resonator with a QCL active region. Furthermore, Bonilla and Grahn [133] showed that a superlattice under external control presents nonlinear dynamics and chaos, and predicted that QCLs should be sensitive to external control and may present temporal chaos. However, no temporal chaos has been observed in QCLs so far.

4.2 Experimental setup

In order to characterize the QCL behavior under optical feedback, the laser is inserted in the experimental setup described in Figure 7.5. The emitted light is collimated at the output of the laser using a lens with a very short focal length ($f = 1.87$ mm), a high numerical aperture ($NA = 0.87$) and an 80% transmission at 5.6 μm. The beam is then split into a feedback path and a detection path using a 60/40 beam splitter.

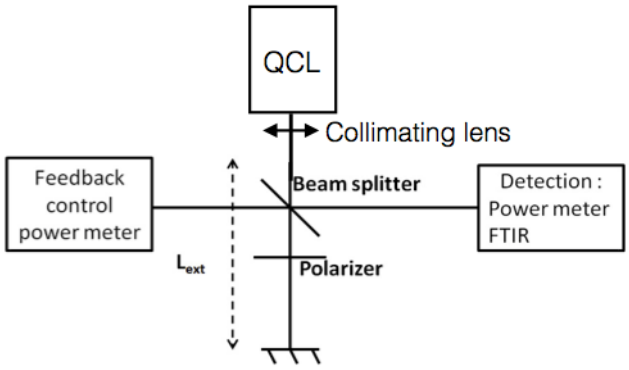

Figure 4.4: Schematic of the experimental setup for optical feedback in QCLs.

On the feedback path, part of the light is re-injected in the laser after reflection on a mirror. Two important feedback parameters that will determine the feedback impact appear

here. The first one is the external cavity length L_{ext}, that corresponds to the distance between the laser front facet and the mirror, or equivalently the external cavity roundtrip time $\tau_{ext} = 2L_{ext}/c$, c being the light velocity. With this setup, the external cavity length can be tuned between 12 cm and 1 m. The second parameter is the feedback ratio f_{ext}, defined as the ratio between reinjected and emitted power. This ratio is tuned using a polarizer inserted in the feedback external cavity and monitored in real-time with a power meter. The polarizer induces parasitic reflections into the laser, and is therefore tilted so that these reflections do not enter the laser cavity.

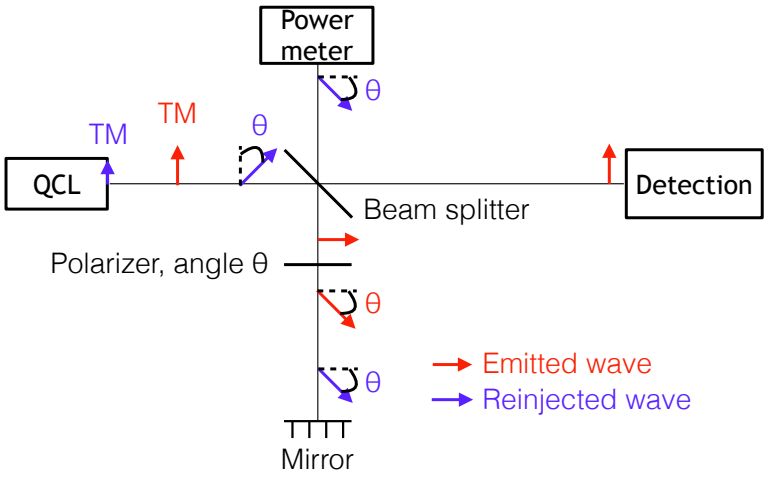

Figure 4.5: Polarization evolution during the propagation.

Since the QCL is polarized in TM, only the projection of the returning light on the TM polarization axis can be coupled back into the cavity. Therefore, when the polarizer angle $\theta = 90°$ (TE polarization), the feedback is completely turned off. On the other hand, when $\theta = 0°$, the totality of the light that arrives back at the laser facet is coupled into the cavity. The attenuation comes mainly from the beam splitter and lens transmission of 80%: the transmission of the polarizer being over 99%, these losses are neglected. For an arbitrary polarization angle θ, the light intensity is attenuated by a factor $0.8 \times \cos^4(\theta)$. As shown in Figure 4.5, a first factor $\cos^2(\theta)$ indeed appears when the light first crosses the polarizer on the path from the laser to the mirror (in red), due to a shift of θ of the polarization

angle. The light is then reflected, with a change of sign of the polarization, which becomes $-\theta$. Therefore, the beam crosses again the polarizer without additional losses. However, a second factor $\cos^2(\theta)$ on the intensity is added when the reinjected light couples back into the TM laser cavity, since only the intensity projected on the TM axis must be considered (in blue).

In this setup, the reinjected power used to calculate the feedback ratio is measured with a power-meter facing the mirror but on the other side of the beam-splitter, as shown in Figure 4.6. Therefore, the first $\cos^2(\theta)$ originating from the two crossings of the polarizer is already included in the measurement, and only a factor $0.8 \times \cos^2(\theta)$ is added on the power in order to evaluate the reinjected power. The maximum feedback ratio was measured to be 27% with the DFB QCL and 36% with the Fabry-Perot QCL.

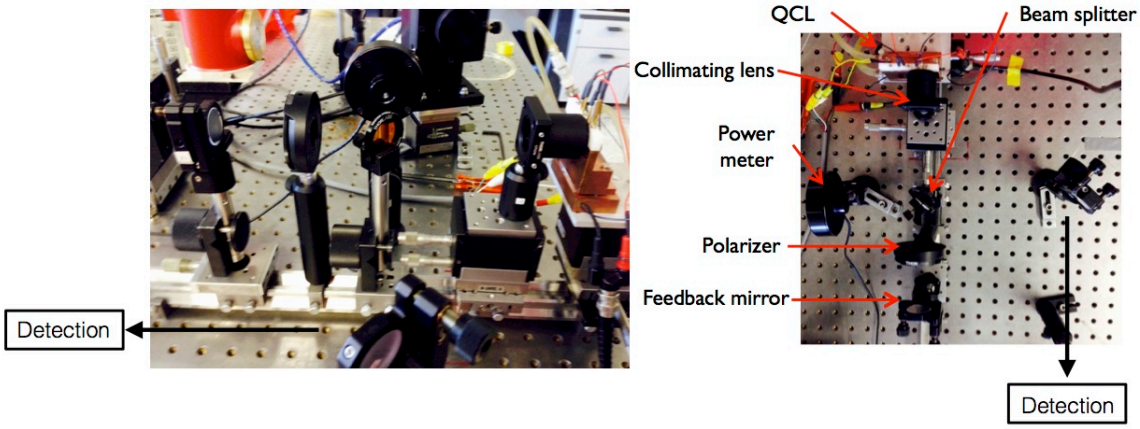

Figure 4.6: Experimental setup for optical feedback in QCLs.

The properties of the laser beam are analyzed on the detection path, either using a power-meter, a fast MCT photodiode to retrieve the time traces or electrical spectra or a Fourier transform infrared (FTIR) spectrometer to obtain the optical spectra with a resolution of 0.125 cm^{-1}.

4.3 Numerical model

Similarly to the Lang and Kobayashi equations, if the complex electrical field is defined as $E = \sqrt{S}e^{i\phi}$, the QCL under optical feedback is characterized by the following rate equations:

$$\frac{dN_3}{dt} = \eta\frac{I}{q} - \frac{N_3}{\tau_{32}} - \frac{N_3}{\tau_{31}} - G_0\Delta NS \tag{4.1}$$

$$\frac{dN_2}{dt} = \frac{N_3}{\tau_{32}} - \frac{N_2}{\tau_{21}} + G_0\Delta NS \tag{4.2}$$

$$\frac{dN_1}{dt} = \frac{N_3}{\tau_{31}} + \frac{N_2}{\tau_{21}} - \frac{N_1}{\tau_{out}} \tag{4.3}$$

$$\frac{dS}{dt} = \left(N_{pd}G_0\Delta N - \frac{1}{\tau_p}\right)S + \beta N_{pd}\frac{N_3}{\tau_{sp}} + 2k\sqrt{S(t)S(t-\tau_{ext})}\cos(\Delta\phi) \tag{4.4}$$

$$\frac{d\phi}{dt} = \frac{\alpha}{2}\left(N_{pd}G_0\Delta N - \frac{1}{\tau_p}\right) - k\sqrt{\frac{S(t-\tau_{ext})}{S(t)}}\sin(\Delta\phi) \tag{4.5}$$

In equations 7.1 to 7.5, N_j is the carrier density of level j, with $\Delta N = N_3 - N_2$, η is the conversion efficiency, I is the bias current. τ_{ij} corresponds to the carrier lifetime from level i to level j, τ_{out} is the characteristic time for the electron to tunnel into the injector, τ_{sp} is the spontaneous emission lifetime, τ_p is the photon lifetime inside the laser cavity. G_0 corresponds to the net modal gain for one period, N_{pd} to the number of periods, α to the linewidth enhancement factor and β to the spontaneous emission factor. $\Delta\phi$ is defined as $\Delta\phi = \omega_0\tau_{ext} + \phi(t) - \phi(t-\tau_{ext})$, with τ_{ext} the external cavity roundtrip time. Finally, k is the feedback coefficient, defined as:

$$k = \frac{1}{\tau_{in}}2C_l\sqrt{f_{ext}} \tag{4.6}$$

where τ_{in} is the internal cavity roundtrip time and C_l is the external coupling coefficient as defined in interband lasers (see Eq. 7.7 and 3.8).

In the previous equations, we can neglect the spontaneous emission term, since its characteristic time is three orders of magnitude slower than other lifetimes.

The steady-state solutions of these rate equations give the external cavity modes ω_s

verifying:

$$N_3 = \frac{\tau_{31}\tau_{21}}{\tau_{31}+\tau_{21}}\left[\eta\frac{I}{q} + \frac{1}{N_{pd}G_0\tau_{21}}\left(\frac{1}{\tau_p} - 2k\cos(\omega_s\tau_{ext})\right)\right] \tag{4.7}$$

$$N_2 = \frac{\tau_{31}\tau_{21}}{\tau_{31}+\tau_{21}}\left[\eta\frac{I}{q} - \frac{1}{N_{pd}G_0\tau_{31}}\left(\frac{1}{\tau_p} - 2k\cos(\omega_s\tau_{ext})\right)\right] \tag{4.8}$$

$$N_1 = \tau_{out}\eta\,\frac{I}{q} \tag{4.9}$$

$$S = \frac{N_{pd}}{\frac{1}{\tau_p} - 2k\cos(\omega_s\tau_{ext})}\frac{1}{\tau_{32}(\tau_{31}+\tau_{21})}\left[\tau_{31}(\tau_{32}-\tau_{21})\eta\,\frac{I}{q} - \frac{\tau_{32}+\tau_{31}}{N_{pd}G_0}\left(\frac{1}{\tau_p} - 2k\cos(\omega_s\tau_{ext})\right)\right] \tag{4.10}$$

$$\phi(t) = (\omega_s - \omega_0)t \tag{4.11}$$

From equation 7.5, we can furthermore deduce:

$$\omega_s - \omega_0 = -k\left[\alpha\cos(\omega_s\tau_{ext}) + \sin(\omega_s\tau_{ext})\right] \tag{4.12}$$

The wavelength of the QCL under optical feedback will therefore evolve with the feedback conditions. However, eq. 4.12 is only valid under steady-state, and in the feedback conditions where eq. 7.1 to 7.5 can apply, i.e. for low feedback ratios.

4.4 Linewidth enhancement factor measurement

In this section, we present two methods based on optical feedback to obtain experimentally the above-threshold room temperature α-factor of a mid-infrared QCL. The first method is based on the wavelength evolution of a Fabry-Perot spectrum with optical feedback, and the second one on self-mixing interferometry.

4.4.1 Wavelength shift with optical feedback

When a QCL is subject to optical feedback, its wavelength will slightly shift following 4.12. This shift can well be observed for Fabry-Perot QCLs subject to low feedback ratios, whereas the wavelength of DFB lasers remains controlled by the grating. By tracking the wavelength

evolution with optical feedback, one can obtain the α-factor from:

$$\alpha = \frac{\omega_0 - \omega_s}{k\cos(\omega_s \tau_{ext})} - \tan(\omega_s \tau_{ext}) \tag{4.13}$$

This method is applied to a Fabry-Perot QCL emitting a 5.6 μm operated at 10°C close to threshold, at 614 mA . The laser is 3 mm long and 6 μm wide and the external cavity length under study here is 15 cm. For better precision, a gaussian fit was applied to the optical spectra in order to determine the wavelength as precisely as possible. The obtained linewidth enhancement factor was $\alpha = 1.3 \pm 0.5$.

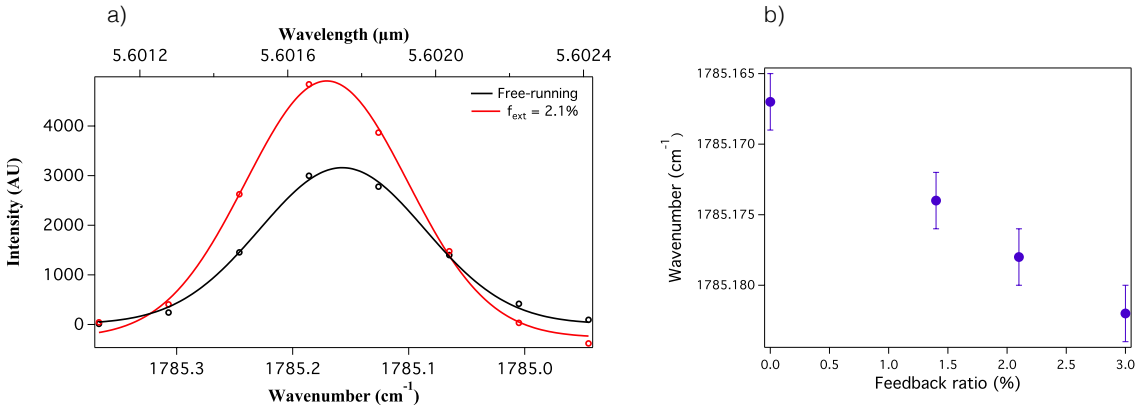

Figure 4.7: Wavelength evolution of the QCL under optical feedback. a) Optical spectra and gaussian fits without feedback and with low feedback $f_{ext} = 2.1\%$. b) Experimental wavelength shift as a function of the feedback ratio.

This value is consistent with other above-threshold room temperature α-factor for mid-infrared QCLs reported in the literature. However, the uncertainty remains relatively high on this measurement. The value of 40% uncertainty was obtained by iterating the measurement. It originates from the limited FTIR resolution of 0.125 cm^{-1} that is not totally compensated by the curve fitting, from the uncertainty on the external cavity length around 0.1 cm and from the uncertainty on the feedback ratio, related to the uncertainty on the measured power, estimated around 10^{-4} W.

This result does not depend on the feedback ratio, as long as it remains low enough,

or external cavity length, hence being consistent with the literature on interband lasers. Furthermore, results of the same order of magnitude were obtained for a 4 mm-long FP QCL with the same active area, for which the LEF was measured to be $\alpha = 0.9$ close to threshold.

4.4.2 Self-mixing interferometry

When the light reinjected in a laser under optical feedback is modulated, typically through a sine motion applied to the feedback mirror, interferences appear in the emission time traces [134, 135]. This so-called self-mixing interferogram gives some information on experimental parameters such as velocity, distance or vibrations. As shown by Yu *et al.* [136], the linewidth enhancement factor of a DFB laser can be retrieved from the self-mixing interferogram. This method cannot be applied to Fabry-Perot lasers, due to the appearance of multiple wavelength interferences rendering the interferogram too complex to be exploited.

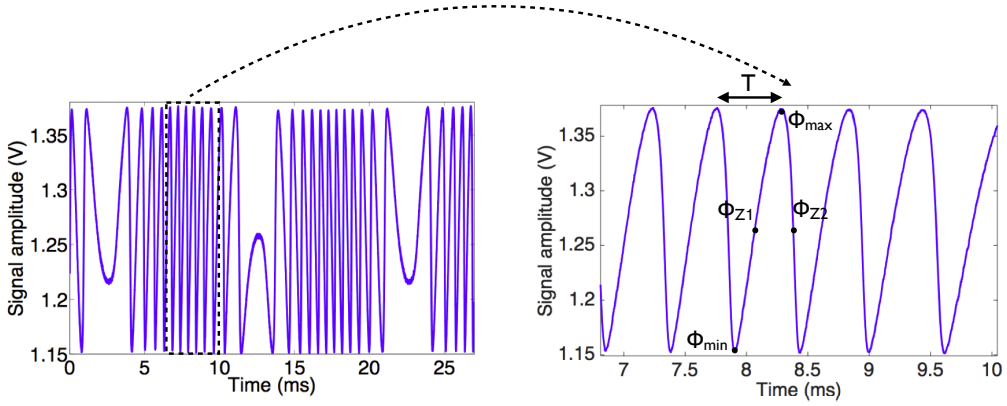

Figure 4.8: Self-mixing interferometer of the QCL under study.

The α-factor calculation is based on the extraction of remarkable points on the interferometer that exist only for high feedback ratios. The self-mixing interferometry technique was therefore adapted to QCLs and low feedback ratios by von Staden *et al.* [52]. As shown in Figure 7.8, the linewidth enhancement factor can be calculated from the position of two consecutive zeros Φ_{Z1} and Φ_{Z2}, a minimum Φ_{min} and a maximum Φ_{max} , as well as from the

period T of the interferogram:

$$\alpha = \frac{\Phi_{max} - \Phi_{min} - 0.5T}{\Phi_{Z2} - \Phi_{Z1} - 0.5T} \tag{4.14}$$

The linewidth enhancement factor measurements based on self-mixing were performed at TU Darmstadt. The experimental setup relies on the same principle as the one described at the beginning of the chapter. However, the feedback ratio is controlled with optical densities, and the feedback mirror is placed on a piezo-electrical actuator with a sinusoidal motion in order to obtain the interferogram, that is then measured with a MCT photodiode.

The α-factor of a DFB QCL is calculated with this method. To compare to the results obtained with the first method, although self-mixing interferometry can not be applied to Fabry-Perot QCLs, the laser under study has the same effective area as the Fabry-Perot laser previously tested with the wavelength shift technique and its dimensions are 2 mm over 9 μm. Measurements were performed at 10°C for several bias currents, with a feedback coefficient around $k = 3 \times 10^8$ s^{-1} and an external cavity length around 30 cm.

The results are presented in Figure 7.9 a as a function of the normalized bias current with respect to threshold a, with:

$$a = \left(\frac{I}{I_{th}} - 1\right) \tag{4.15}$$

As already stressed in interband lasers, this experiment reveals a significant increase of the linewidth broadening factor with the bias current, from 0.8 to 2.9. It is furthermore interesting to point out that the measurements with the two methods are perfectly consistent since the first result using the wavelength shift corresponds to $\alpha = 1.3$ at a ≈ 0.03 for the 3 mm-long laser and $\alpha = 0.9$ at $a \approx 0.01$ for the 4 mm-long QCL.

These two linewidth enhancement factor measurements led to values that are slightly higher than typical values reported in the literature. However, the α-factor measured here can be considered as an effective α, which is different from the pure material α extracted from the Hakki-Paoli method or from the dynamic α measured with high-frequency modulation techniques (FM/AM). However, this effective α was extracted directly from the Lang and Kobayashi equations and can therefore legitimately be re-injected in these equations for optical feedback studies. In the following, the α-factor will be considered as a fitting parameter

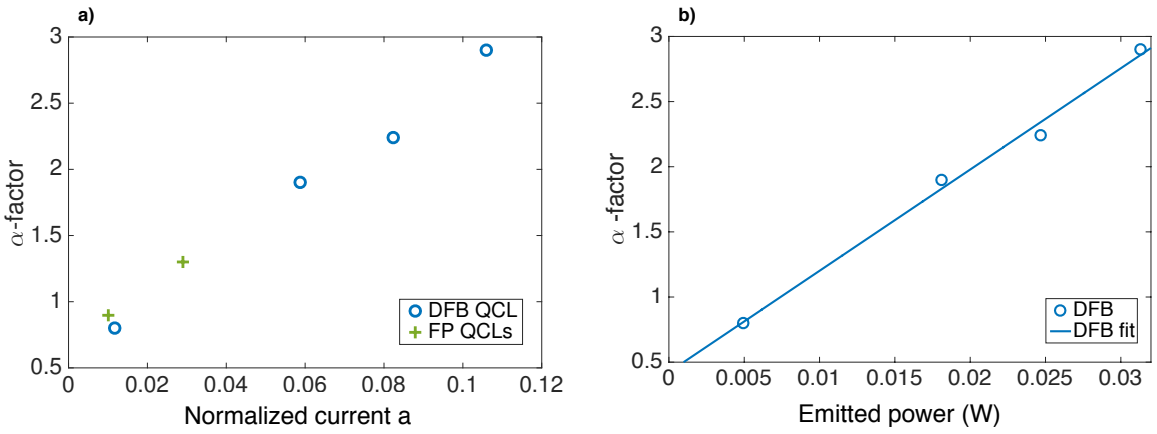

Figure 4.9: a) α-factor evolution as a function of the normalized current and comparison between the two methods at 10°C. b) α-factor evolution as a function of the emitted power for the DFB QCL.

in the simulation, taking values between 1 and 3 depending on the pump conditions.

4.4.3 Gain compression coefficient

Gain compression in interband semiconductor lasers corresponds to the decrease of the gain coefficient with optical intensity [137]. This phenomenon must not be mistaken for gain saturation, which corresponds to an equilibrium between the stimulated emission and the refill of the upper lasing level by the pump (see Figure 4.10 a). As shown in Figure 4.10 b, gain compression corresponds to a depletion of the gain in the upper level.

It originates from gain nonlinearities caused by processes such as carrier heating, spatial or spectral hole burning [138]. Spectral hole burning appears from the fast stimulated emission lifetime, which will lead to a carrier depletion in the upper level if it is faster than the intraband relaxation time of the carrier, and hence to a reduction of the gain around the lasing wavelength. On the other hand, spatial hole burning comes from the existence of two contra-propagating waves in the cavity and leads to an inhomogeneous gain distribution along the cavity. Finally, the carrier heating effect is due to the stimulated emission and to the free-carrier absorption, which result in gain reduction, since the gain is dependent on

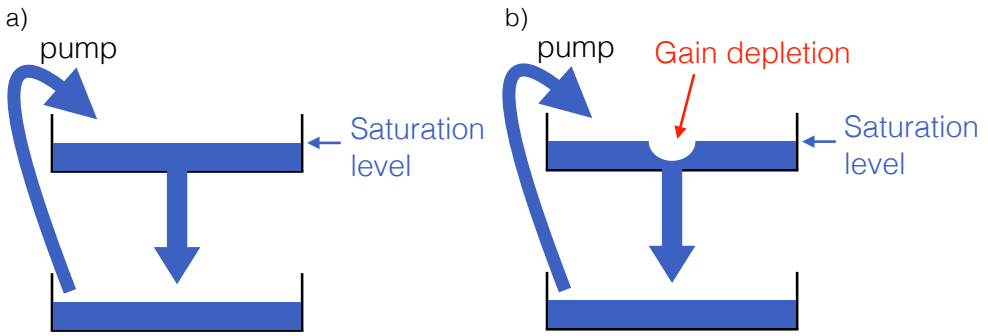

Figure 4.10: Gain saturation (a) versus gain compression (b).

the carrier temperature.

Gain compression limits the modulation dynamics of directly modulated transmitters through adiabatic chirp and is also responsible for the bending of the light-current characteristic curves [139]. It is quantified by the gain compression coefficient ϵ_S associated with the photon density S through the following adiabatically-corrected gain expression [137]:

$$G = \frac{G_0}{1 + \epsilon_S S} \tag{4.16}$$

with G_0 the linear gain. A more rigorous solution can be retrieved from a approximation on the density of state functions, leading to $G \propto (1 - \epsilon_S S)^{-1/2}$.

The gain compression coefficient can also be expressed as a function of the emitted power, and the conversion from ϵ_S to ϵ_P is straightforward, as $\epsilon_S S = \epsilon_P P_{opt}$. Moreover, the photon density S can be expressed as a function of the output power P_{opt} as:

$$P_{opt} = h\nu V v_g \alpha_m S \tag{4.17}$$

with h the Planck constant, ν the laser frequency, V the volume of the active area, v_g the group velocity and α_m the mirror losses of the laser cavity.

In a homogeneously-broadened gain medium, the carrier density difference between upper and lower lasing levels is clamped at threshold, and the change of the effective α-factor

is mostly due to the decrease of the differential gain from gain compression. Indeed, by definition:

$$\alpha = -\frac{dn/dN}{dG/dN} \tag{4.18}$$

Furthermore, $G_0 = 1/\tau_p + G_N(N - N_{th})$ and eq. 7.13 can be approximated as $G = [1/\tau_p + G_N(N - N_{th})]\,(1 - \epsilon_P P)$, leading to:

$$\frac{dG}{dN} = G_N(1 - \epsilon_P P_{opt}) \tag{4.19}$$

and:

$$\alpha = -\frac{dn/dN}{G_N(1 - \epsilon_P P_{opt})} \tag{4.20}$$

Therefore, the effective α-factor which evolves with the optical power can be expressed as:

$$\alpha = \alpha_0(1 + \epsilon_P P_{opt}) \tag{4.21}$$

where α_0 is the linewidth enhancement factor at threshold. Since the carrier distribution is clamped, α_0 itself does not change as the output power increases.

In interband lasers, the gain compression coefficient ϵ_S is typically around 10^{-17} cm^3 for quantum well lasers and 10^{-16} to 10^{-15} cm^3 for quantum dot lasers [138, 140]. The stronger gain compression in quantum dot lasers leads to a much more pronounced increase of the damping rate and α-factor with the pump current compared to quantum well lasers, as observed experimentally. In QCLs, the gain compression is not yet well characterized, and there are very few values of gain compression coefficient. One can mention the work of Hangauer *et al* [51], reporting an experimental saturation power, defined as the inverse of ϵ_P, of $P_{sat} = 85$ mW for a QCL emitting at 9.6 μm. Furthermore, the origin of gain compression in QCLs is not fully understood yet. It would come from the carrier heating, as in interband lasers, but also from the upper level depletion due to the time necessary for the electrons to tunnel through the injector and from the fixed number of electrons available in the active region, which will lead to a saturation at high bias currents. Finally the spatial hole burning is very strong in QCLs, due to an extremely fast gain grating lifetime linked to the upper

state lifetime of few picoseconds [50].

In QCLs, the strong increase of the α-factor with the bias current also corresponds to an increase with the laser output power, as shown in Figure 7.9 b. The linewidth enhancement factor values measured on the DFB QCL (blue circles) are fitted linearly using eq. 7.12 (blue line), leading to a threshold value of $\alpha = 0.42$, consistent with sub-threshold measurements in QCLs at room temperature. Furthermore, the fit gives a value of $P_{sat} = 5.4$ mW, corresponding to $\epsilon_S = 4.5 \times 10^{-15}$ cm^3. Such a high value would explain the very high damping rate in QCLs, as well as the strong dependency of the α-factor on the bias current, and therefore the difference between the α-factor measured below and above threshold in QCLs.

4.5 Influence of the optical feedback on the QCL L-I characteristic curves

4.5.1 Case of the DFB QCL

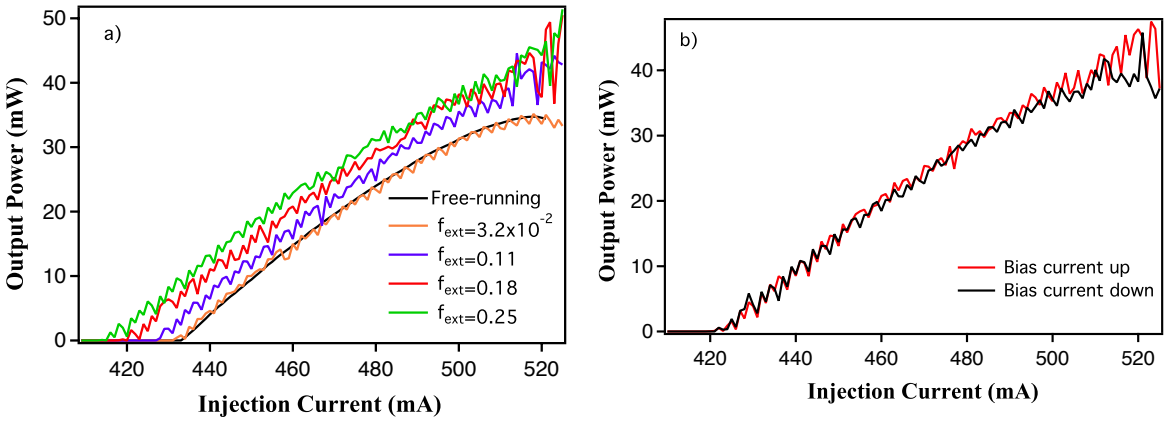

Figure 4.11: Impact of optical feedback on the DFB QCL L-I curves. a) L-I characteristic curves for several feedback ratios, with an external cavity length of 15 cm. b) Appearance of hysteresis at high feedback ratios $f_{ext} = 0.18$.

The measurement of the light versus current (L-I) characteristic curves of the DFB QCL at 10°C for an external cavity length of 15 cm and several feedback ratios, presented in Figure 4.11, clearly shows the influence of optical feedback on the laser emission. First

there is a significant power increase, associated with a diminution of the laser threshold from 433 mA down to 416 mA.

Furthermore, some undulations appear on the L-I characteristic curves for high feedback ratios, as well as hysteresis. These undulations have the same origin as in interband lasers, corresponding to alternatively constructive and destructive interferences between the internal and external cavity modes, as discussed previously.

4.5.2 Case of the Fabry-Perot QCL

Optical feedback has a similar effect on the 4 mm × 6 μm Fabry-Perot QCL L-I characteristic curves, here plotted for an external cavity length of 13 cm. The output power increases, the threshold decreases and undulations appear for high feedback ratios, as shown in Figure 7.10 a. However, it is worth noting that the maximum power is not obtained for the higher feedback strength but for a rather low feedback ratio.

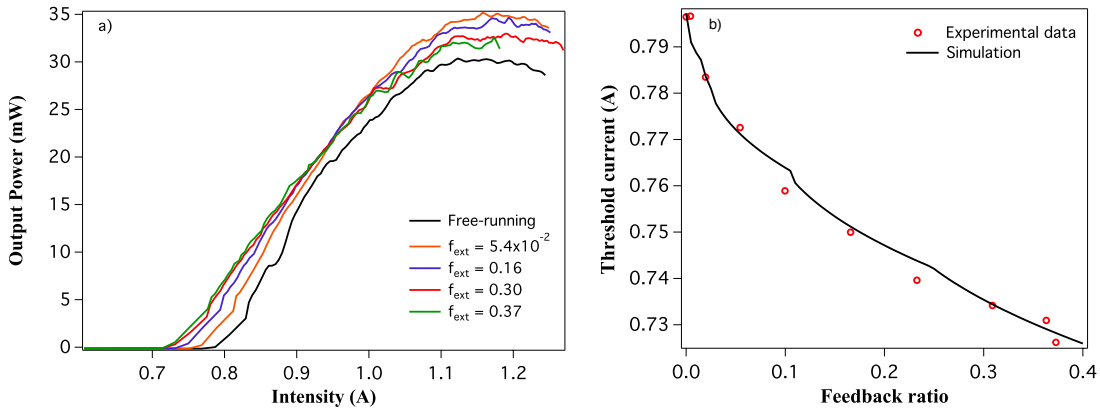

Figure 4.12: Impact of optical feedback on the 4 mm × 6 μm FP QCL L-I curves. a) L-I characteristic curves for several feedback ratios, with an external cavity length of 13 cm. b) Experimental and numerical threshold reduction as a function of the feedback ratio.

In the case of Fabry-Perot lasers, since the wavelength is not determined by a Bragg grating, it is possible to calculate the wavelength of the laser as a function of the feedback ratio from eq. 4.12. Out of all possible solutions, the lasing wavelength is the one for which the linewidth reaches a minimum. Once the laser wavelength is known, the threshold current can be extracted by solving $S = 0$ in eq. 4.10, resulting in:

$$I_{th} = \frac{q}{\eta} \frac{\tau_{32} + \tau_{31}}{\tau_{31}(\tau_{32} - \tau_{21})} \frac{1}{N_{pd} G_0} \left[\frac{1}{\tau_p} - 2k \cos(\omega_s \tau_{ext}) \right] \tag{4.22}$$

By considering $\alpha = 1.3$ and adjusting η to match the free-running threshold, the simulation fits really well the experimental threshold reduction (see Figure 7.10 b).

4.5.3 Optical feedback from a mid-infrared fiber

Recently, mid-infrared fibers have been developed, that could be used in QCL experiments for instance for distant gas analysis, where the laser and detection cell would be operated far from the medium under study and where the light would be guided to and from the medium using an optical fiber. Since conventional silica fibers do not guide mid-infrared wavelengths, new glasses have been studied. Université Rennes I and SelenOptics are developing new chalcogenide glasses to produce microstructured optical fibers optimized in the mid-infrared [141, 142]. These fibers are currently vertically cleaved, hence the optical feedback on the QCL from these fibers should not be negligible and could influence the laser emission.

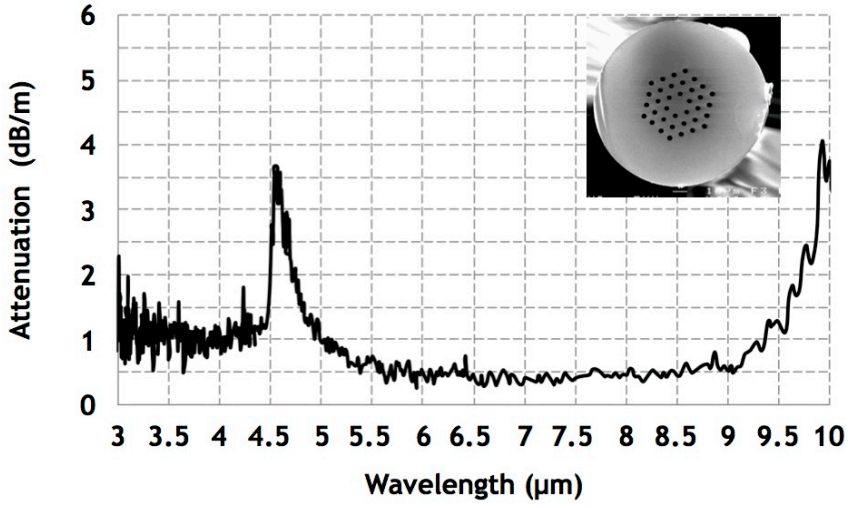

Figure 4.13: Attenuation of the fiber core as a function of the wavelength. Inset: cross-section of the chalcogenide microstructured optical fiber.

The 1 m-long optical fiber used for the experiments is fabricated from the chalcogenide

glass $As_{38}Se_{62}$. Before drawing, the preform has been elaborated by a molding method as described in [141]. This method consists in heating up the chalcogenide glass rod and in letting it flow into a silica mold, whose design corresponds to the negative shape of the final preform. Then the perform is placed in a silica enclosure under helium flowing and heated thanks to an annular electrical furnace. During fiber drawing, the hole diameters are controlled by applying an inert gas (He) pressure in the holes of the preform. The inset in Figure 4.13 presents a section of the fiber. It is a microstructured fiber constituted of 36 holes with an outer diameter of 120 μm and a central solid core of 12 μm. Besides, its attenuation is below 1 dB/m from 3 to 9.6 μm, except an absorption peak around 4.6 μm corresponding to the Se-H band, as shown in Figure 4.13.

Based on eq. 7.14, the amount of optical feedback originating from reflections on the fiber can be obtained by measuring the threshold reduction of a QCL coupled to the fiber. In this case, the QCL under study is a 3 mm-long Fabry Perot laser, with a free-running threshold at 20°C of 668 mA and 9.64 V. The threshold of the laser under feedback is obtained by recording the L-I curve after optimization of the coupling through maximization of the output power after the fiber. The external cavity length was estimated around 200 μm between the QCL facet and the fiber tip.

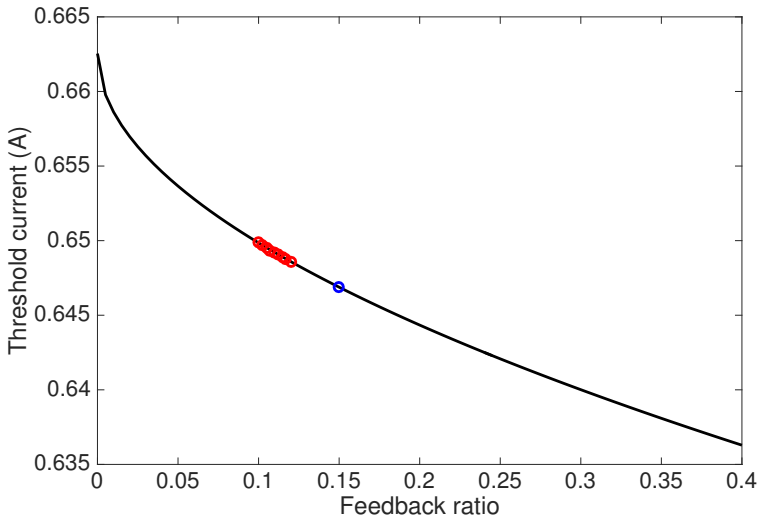

Figure 4.14: Threshold reduction due to optical feedback on the fiber for the two sets of measurements, in red and blue respectively, and associated feedback ratios obtained by following the simulation curve in black.

A first set of measurements (red dots on Figure 7.11) led to a threshold of 649 ± 1 mA, the uncertainty being obtained by iterating the fiber alignment. This corresponds to a feedback ratio of $f_{ext} = 11 \pm 1\%$. A second set of measurements was performed after a cleaner cleavage of the fiber, i.e. a different cleavage leading to an optimized coupling of the QCL in the fiber, and hence to a higher output power. The threshold was measured at 646 mA (blue dot on Figure 7.11), resulting in a feedback ratio of $f_{ext} = 15 \pm 1\%$.

This amount of optical feedback is significant. Feedback ratios between 11 and 15% could impact the stability and the emission properties of a QCL coupled to a fiber. Theoretically, one could reach feedback ratios as high as 22% depending on the beam divergence and distance between the QCL facet and the fiber, since the reflective index of the fiber is around 2.77, i.e. twice that of near-infrared fibers. However, this measurement does not enable to determine whether the totality of the feedback comes from the fiber tip, or if internal backscattering along the fiber also contributes. The simulated threshold obtained from eq. 7.14 indeed shows little variation when changing the external cavity length. Therefore, further studies are required to better understand the origin of the optical feedback from a chalcogenide fiber and see its impact on the QCL behavior. Some studies on the fiber itself are moreover currently on-going in order to limit the amount of optical feedback, either by adding an anti-reflective coating of the fiber tip, or by applying a tilt during the cleavage.

4.6 Feedback regimes in a mid-infrared QCL

4.6.1 Optical spectra of a QCL under optical feedback

The analysis of the optical spectra of the DFB QCL reveals five feedback regimes appearing successively when increasing the feedback ratio at a given external cavity length of 15 cm and a fixed bias current of 435 mA. The first feedback regime is stable and single-mode, emitting at the free-running wavelength, but with an increased and phase-dependent output power. For slightly higher feedback ratios, a beating between two modes occurs, one of them being the free-running wavelength and the other one an external cavity mode. Moreover,

in this second regime, the intensity of each mode also depends on the feedback phase. The third regime appears for intermediate feedback ratios, the laser is stable and single-mode again, but it emits on the adjacent mode identified in the second regime. The fourth regime is unstable, the spectral pedestal and the intensity of the side-modes, that are otherwise well-suppressed, increases significantly. Finally, the fifth regime for very high feedback ratios is a stable single-mode regime on an external cavity mode with high output power. It corresponds to the extended cavity regime, where the laser is equivalent to a small active area in a long cavity, one of the cavity mirrors being the feedback mirror. This is also the regime used in the fabrication of external-cavity QCLs.

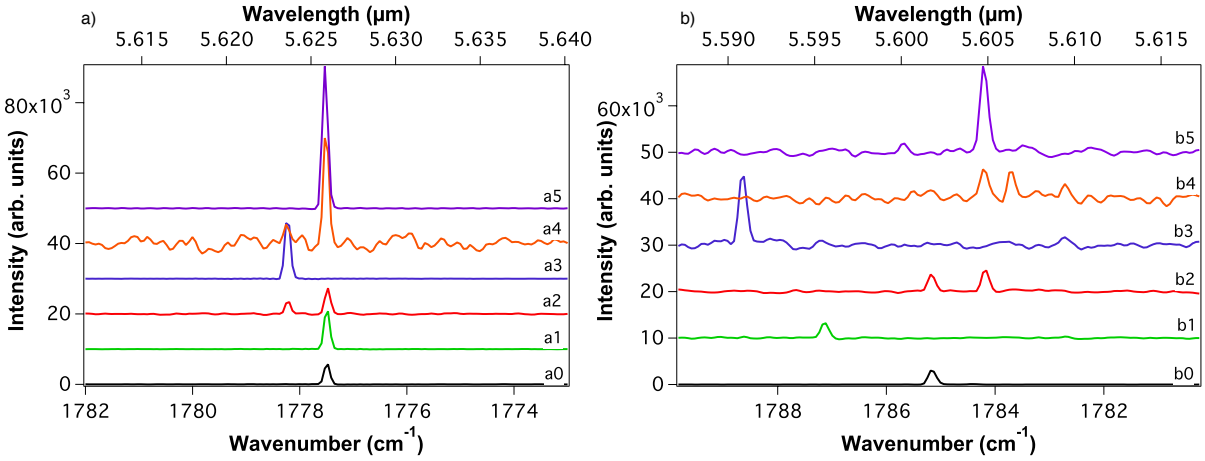

Figure 4.15: Feedback regimes of QCLs under optical feedback. a) DFB QCL, with an external cavity length of 15 cm. a0: Free-running case. a1: Regime I, $f_{ext} = 9.1 \times 10^{-4}$. a2: Regime II, $f_{ext} = 5.1 \times 10^{-3}$. a3: Regime III, $f_{ext} = 3.2 \times 10^{-2}$. a4: Regime IV, $f_{ext} = 0.13$. a5: Regime V, $f_{ext} = 0.25$. b) FP QCL, with an external cavity length of 13 cm. b0: Free-running case. b1: Regime I, $f_{ext} = 1.4 \times 10^{-3}$. b2: Regime II, $f_{ext} = 1.7 \times 10^{-2}$. b3: Regime III, $f_{ext} = 0.14$. b4: Regime IV, $f_{ext} = 0.18$. b5: Regime V, $f_{ext} = 0.25$.

These five regimes are very similar to the ones observed in interband lasers, as described in the previous chapter. Using the FTIR, the laser linewidth can unfortunately not be measured, it is impossible to conclude whether the third regime has very low linewidth or whether the linewidth is phase-dependent in regimes I and II. The absence of clear spectral broadening in the fourth regime does not enable any conclusion on whether this regime corresponds to the coherence collapse as defined in interband lasers, some further measurements

will be necessary.

In the case of the 3 mm × 6 μm Fabry-Perot QCL under optical feedback, five similar regimes were also observed based on the optical spectra when increasing the feedback strength. However, as observed in interband lasers, the wavelength varies much more since it is not fixed by the DFB grating. Furthermore, the side-mode suppression ratio in the single-mode regimes is not as good as in the case of the DFB laser.

4.6.2 Feedback cartography of the DFB QCL

By recording the optical spectra of the DFB QCL for different feedback conditions, one can identify for a given external cavity length the feedback ratios at which the transitions between the five previously-described feedback regimes occur. Thanks to the high stability and reproducibility of the measurements, iterating this method for several external cavity lengths allows to draw the feedback cartography of the DFB QCL. The estimated uncertainty on the transitions position is about 20%.

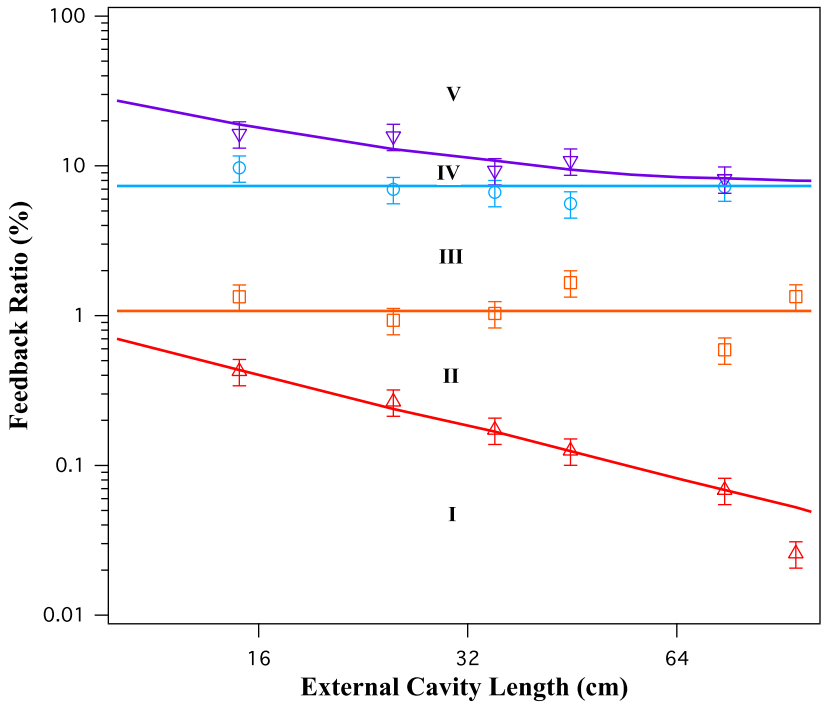

Figure 4.16: Feedback cartography of the different regimes of the DFB QCL as a function of the external cavity length and the feedback ratio, measured at 10°C for a bias current of 435 mA.

This cartography can be compared with the one realized by Tkach and Chraplyvy [74] for a quantum-well DFB laser emitting at 1.55 μm (see Figure 3.2). Despite the fact that the transitions occur for much higher feedback ratios in the case of the QCL, the cartographies look very similar, except for the fourth regime. This regime is indeed much narrower in the QCL case, thus comforting the prediction that these structures are much more resistant to optical feedback than conventional laser diodes. Furthermore, instead of a transition between regimes IV and V at constant feedback ratio for all external cavity lengths, the width of the fourth regime appears to decrease when increasing the external cavity length. For the last measurement point at $L_{ext} = 95$ cm, no unstable regime was found.

The enhanced stability of QCLs subject to optical feedback is also underlined by the fact that the three stable regimes (I, III and V) are much broader than in the case of interband lasers. The third regime is for instance relatively broad, whereas it does not always appear in conventional laser diodes, depending on the structure. Moreover, the fifth regime can easily be reached in QCLs, whereas for the cartography of a quantum-well laser, it was necessary to add an anti-reflective coating on the front facet to obtain high-enough reflectivities and reach stable emission again.

All these arguments confirm that the QCLs are more resistant to optical feedback than their interband counterparts. However, the fourth unstable regime is worth studying, and further experiments are necessary to conclude whether it does correspond to coherence collapse or not.

4.7 Nonlinear dynamics and chaos in a QCL under optical feedback

4.7.1 Time series and electrical spectra

In order to study in more details the fourth regime identified through the optical spectra analysis, the time series and electrical spectra of the DFB QCL were recorded for several feedback ratios and several external cavity lengths. To this end, the emitted signal was collected on an ultra-fast MCT photodiode. The need of high speed and high bandwidth, here around 500 MHz, led to the use of an MCT photodiode with an integrated high-pass

preamplifier, thus requiring the QCL to be operated in pulsed mode.

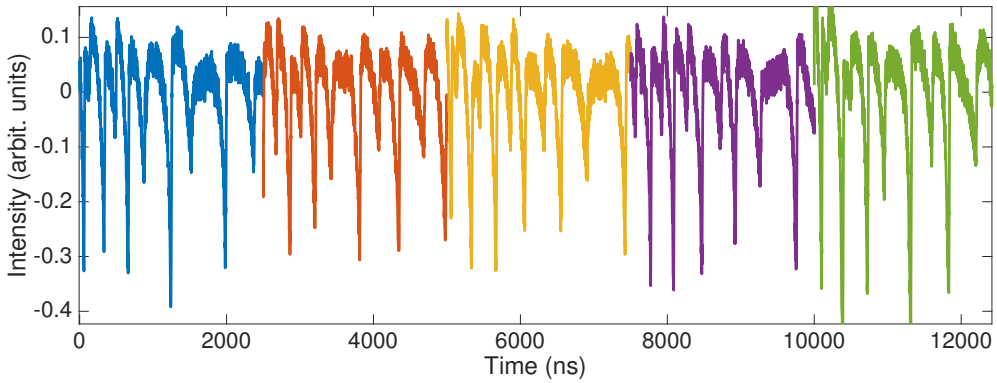

Figure 4.17: Example of time traces used for the analysis, with L_{ext} = 35 cm, P = 0.02 and f_{ext} = 2.7%, considering the last 2.5 μs of several pulses.

To achieve temperature stability and a quasi continuous-wave regime, several pulse lengths were considered. For pulses shorter than 2 μs, the transient regime that appears at the beginning of the pulse due to the internal heating of the structure was still dominant and the pulse generator distorted long pulses, therefore a pulse duration of 5 μs was chosen as the best compromise. A hundred time traces were recorded for each operation point, and only the end of these pulses were taken into account, as depicted in Figure 4.17. The signal collected on the photodiode was then analyzed simultaneously on a 10 gigasample-per-second real-time oscilloscope and an electrical spectrum analyzer.

In this experiment, the aim was to observe instabilities and if possible chaos. Therefore, the laser was operated close to threshold, where these effects are supposedly enhanced, i.e. the pump parameter P was very small. As a reminder, P is defined according to:

$$P = \frac{\tau_p G_N N_{th}}{2} \left(\frac{I}{I_{th}} - 1 \right) \tag{4.23}$$

with, in the case of a QCL, $G_N = N_{pd} G_0$.

The time trace and electrical spectrum of the DFB QCL under optical feedback with f_{ext} = 3.13%, L_{ext} = 45 cm and P = 0.02 are represented in Figure 7.14. Two oscillation frequencies can be identified on these plots: slow oscillations appear that are modulated by faster oscillations. From the analysis of the electrical spectrum, the fast oscillations occur

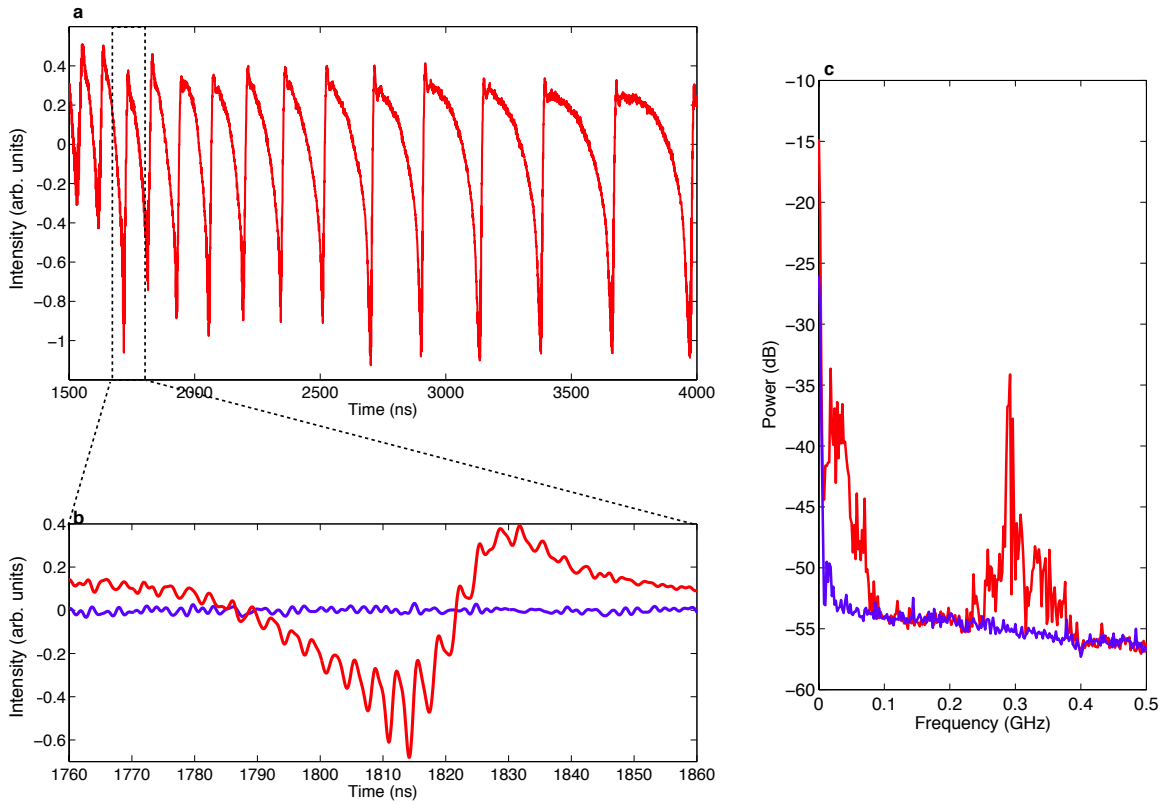

Figure 4.18: Typical experimental results, for $P = 0.02$, $L_{ext} = 45$ cm and $f_{ext} = 3.13\%$. a) Time trace with slow fluctuations. b) Zoom on one slow period, a faster fluctuation appears at the external cavity frequency (in red), comparison with the free-running case (in blue). c) Electrical spectra that confirms the appearance of the external cavity frequency and of a slower frequency (in red), comparison with the free-running case (in blue).

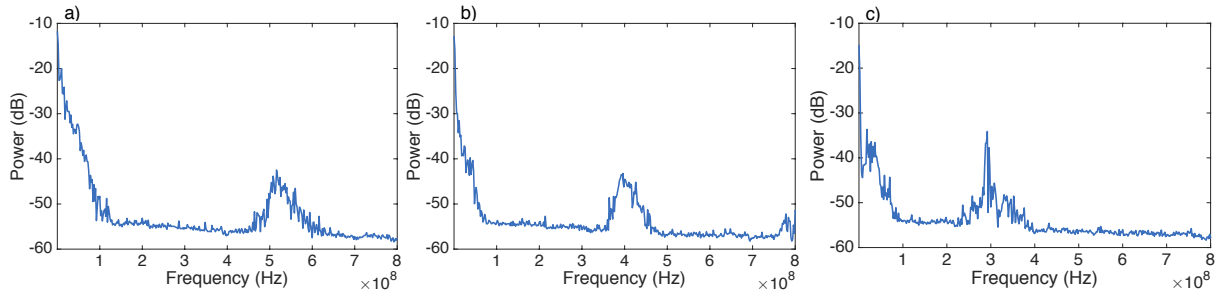

Figure 4.19: Experimental electrical spectral at $f_{ext} = 3.1\%$ and $P = 0.02$ for several external cavity lengths, showing both the external cavity frequency and a low frequency corresponding to LFF. a) $L_{ext} = 25$ cm. b) $L_{ext} = 35$ cm. c) $L_{ext} = 45$ cm.

at the external cavity roundtrip frequency, here 0.33 GHz for 45 cm. This observation was confirmed by varying the external cavity length: the fast oscillations remain at the external cavity frequency (see Figure 4.19). The origin of the slower fluctuations is not as easy to understand, it does not correspond to any cavity of the experimental setup. It could however be low frequency fluctuations, and therefore could correspond to the appearance of chaotic dynamics in the QCL under optical feedback.

4.7.2 Low frequency fluctuations

Oscillations at low frequency as observed in the QCL under optical feedback can have various origins. In order to confirm that these are actual low frequency fluctuations (LFF), the statistics of the period between two consecutive drop-outs are studied at $L_{ext} = 35$ cm for two bias currents and two associated feedback ratios: close to threshold with $P = 0.02$ and $f_{ext} = 3.5\%$, and for $P = 0.10$ and $f_{ext} = 11\%$, as shown in Figure 4.20. The result is then compared with the statistics typically obtained for LFF in an interband laser diode.

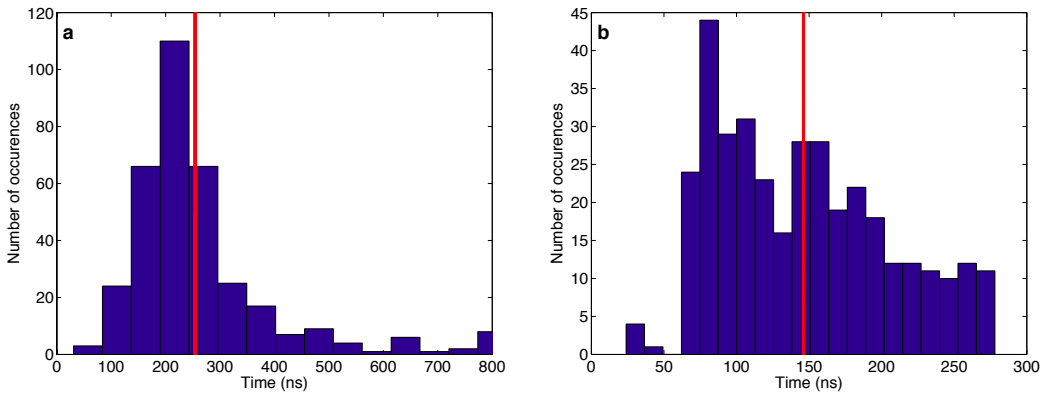

Figure 4.20: Statistical distributions of the slow fluctuations, for $L_{ext} = 35$ cm. a) $P = 0.02$ and $f_{ext} = 3.5\%$. b) $P = 0.10$ and $f_{ext} = 0.11$. In both cases, the red line indicates the average value.

The histograms evidence the appearance of a forbidden period, ranging from 0 to a few tens of the external cavity roundtrip time, where no oscillations separated by such periods were observed. Furthermore, the histogram for $P = 0.02$ takes the shape of a decreasing exponential, and a second peak appears on the decreasing exponential for $P = 0.10$. Moreover, both the minimum and the average time between two drop-outs become smaller when

increasing the bias current. All these observations enable to conclude that the oscillations at low frequency occurring in the QCL under precise feedback conditions do correspond to LFF, thus confirming the appearance of chaos in a QCL.

4.7.3 Experimental bifurcation diagram

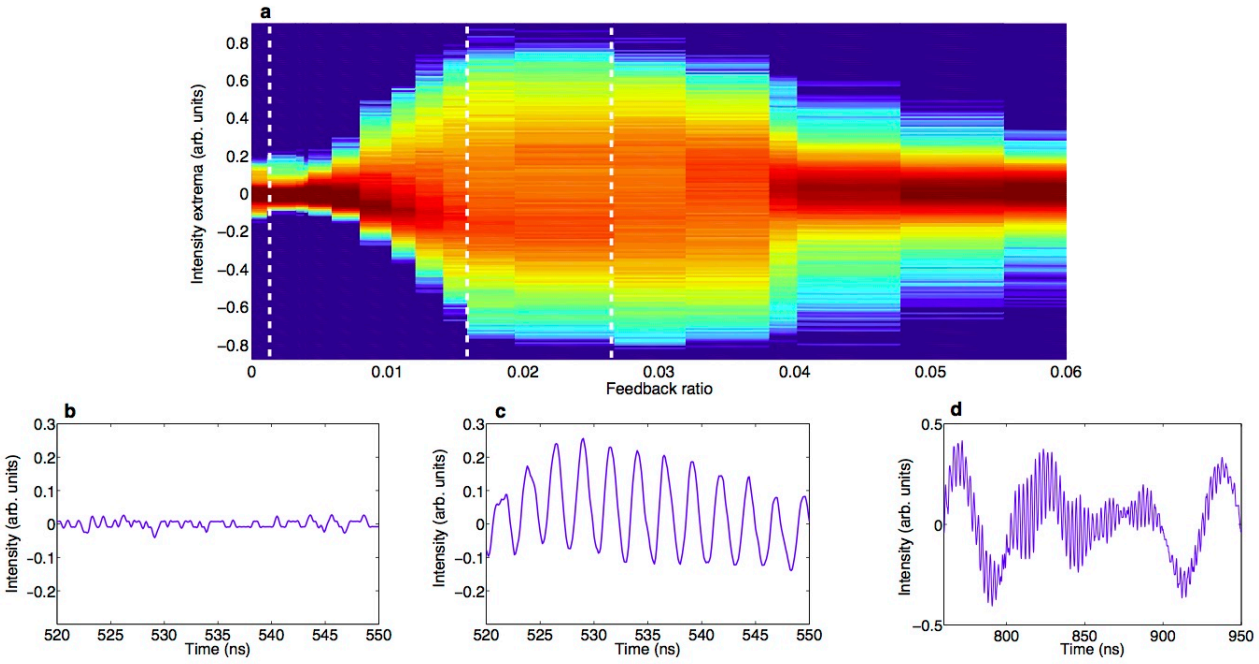

Figure 4.21: Experimental bifurcation diagram for $P = 0.02$ and $L_{ext} = 35$ cm, and associated time series. a) Experimental bifurcation diagram, the white dashed lines correspond to the feedback ratios at which the time series were recorded. b) Time trace for $f_{ext} = 0.11\%$, showing stable signal. c) Time trace for $f_{ext} = 1.58\%$, showing oscillations at the external cavity frequency. d) Time trace for $f_{ext} = 2.66\%$, showing both LFF and oscillations at the external cavity frequency.

A careful sweep of the feedback ratio at fixed external cavity length $L_{ext} = 35$ cm and fixed bias current $P = 0.02$ allows the mapping of the bifurcation diagram of the QCL under optical feedback. In particular, the Hopf bifurcation at which the laser starts to oscillate is measured at $f_{ext} = 0.59\%$. The study of the time traces before and after the Hopf bifurcation presents a route to chaos different to that commonly observed in semiconductor lasers. For very low feedback ratios, the QCL is stable, the only fluctuations in the time traces originate from noise. At the Hopf bifurcation, the laser starts to oscillate at the external

cavity frequency. Afterwards, for $f_{ext} \geq 2.66\%$, the LFF superimpose on the external cavity frequency oscillations, the QCL enters into a chaotic regime. Finally, around $f_{ext} = 4\%$, the laser re-stabilizes and remains on this stable external cavity mode up to the highest achievable feedback ratios.

When increasing the external cavity length from 25 to 35 to 45 cm at a fixed bias P = 0.02, the feedback ratio at which the Hopf bifurcation occurs remains constant with an oscillation frequency changing according to the cavity length, whereas the LFF area appears earlier, at 3.18%, 2.66% and 2.40% respectively. This tendency is in qualitative agreement with the cartography previously measured by studying the optical spectra, although the values can not be directly compared due to the different operating points. Furthermore, for a fixed cavity length of 25 cm, the Hopf bifurcation and appearance of LFF occur at 0.59% and 3.18% respectively at a bias of P = 0.02, and it rapidly varies with the pump. For P = 0.10, these two remarkable points occur at feedback ratios as high as 7.1% and 11.1%, respectively.

This route to chaos is unusual for a semiconductor laser. First, no oscillations at the relaxation oscillation frequency appear in the dynamics. However, as already mentioned in the first chapter, there are no relaxation oscillations in QCLs due to the very high damping. This point therefore does not prove an atypical behavior of the QCL under optical feedback. Thus, the main argument for an unusual route to chaos for the QCL is the appearance of oscillations at the external cavity frequency before the chaotic area. In interband semiconductor lasers, the external cavity frequency does appear but only for feedback ratios above the limits of the bubble of chaos. On the contrary, for class A gas lasers subject to optical feedback, the route to chaos is exactly the one described here, with first oscillations at the external cavity frequency and then chaos. Furthermore, the shape of the LFF for the QCL, i.e. a progressive power drop-out followed by a fast recovery as shown in Figure 4.19 a and b, resembles the one in gas lasers rather than the one in other semiconductor lasers, where the power drop-out is sudden and the recovery progressive. All these arguments are in favor of a class A-like behavior of the QCLs under optical feedback.

Moreover, the strong similarities between the consecutive time traces as shown in Figure 7.14 suggest a low sensitivity of the chaotic trajectories to changes in the initial condi-

tions, and therefore a low-dimension chaos. However, a careful analysis of the chaos complexity and the calculation of the Lyapunov exponents [65], defined as the deviation with respect to the initial condition, which is positive in case of chaos, would be necessary to conclude on this point, which is not feasible here due to the limited resolution of the experimental time traces.

4.7.4 Numerical bifurcation diagram

To confirm the experimental observations and verify whether the absence of the relaxation oscillations in the experimental bifurcation diagram of QCLs under feedback really is a property of such devices or is only due to a lack of available high-bandwidth detectors, the numerical bifurcation diagram is calculated. Due to the complex resolution of the differential delayed equations composing the rate equations of the QCL under optical feedback, it was decided to base the study on the classical rate equations of a semiconductor laser under optical feedback as defined by Lang and Kobayashi, for which resolution algorithms are already implemented and efficient, but inserting the parameters that correspond to the QCL case.

$$\frac{dY}{ds} = (1 + i\alpha)\, Z\, Y \; + \; \eta \; exp(-i\Omega_0\theta)\, Y(s - \theta) \tag{4.24}$$

$$T\,\frac{dZ}{ds} = P - Z - (1 + 2Z)\; |Y|^2 \tag{4.25}$$

In the Lang and Kobayashi equations recalled above, the carrier to photon lifetime ratio is $T = 0.265$, the normalized bias current is $P = 0.02$, the normalized cavity roundtrip time is $\theta = 492$ and the linewidth enhancement factor is $\alpha = 1.7$, value that best fits the experimental results. The feedback phase $\Omega_0\theta = -atan(\alpha)$ is chosen to an arbitrary value. Noise is integrated in the resolution by adding a random less than unity term multiplied by a noise coefficient, at each iteration both on the real and imaginary parts of the complex field. This noise coefficient was varied between 10^{-14} (no noise) and 10^{-7} (noisy experiment) without any significant change in the bifurcation diagram.

The characteristic frequency and damping rate from the laser modulation response can be obtained from the Lang and Kobayashi equations without optical feedback. Indeed, by writing $Y = \sqrt{A}e^{i\phi}$, eq. 7.16 in the absence of feedback can be written as:

$$\frac{dY}{ds} = \frac{1}{2}\frac{1}{\sqrt{A}}\frac{dA}{ds}e^{i\phi} + i\sqrt{A}e^{i\phi}\frac{d\phi}{ds} = (1 + i\alpha)\, Z\, \sqrt{A}e^{i\phi} \tag{4.26}$$

And therefore, by separating real and imaginary part, the normalized rate equations in absence of feedback become:

$$\frac{dA}{ds} = 2ZA \tag{4.27}$$

$$\frac{d\phi}{ds} = \alpha ZA \tag{4.28}$$

$$T\,\frac{dZ}{ds} = P - Z - (1 + 2Z)\, A \tag{4.29}$$

The steady-state of eq. 4.27 to 4.29, are given by:

$$0 = 2Z_s A_s \tag{4.30}$$

$$0 = P - Z_s - (1 + 2Z_s)\, A_s \tag{4.31}$$

and since the laser is on under steady-state ($A_s \neq 0$), this leads to $Z_s = 0$ and $A_s = P$. The small-signal analysis consists in considering perturbed steady-states with $A = A_s + \delta A$ and $Z = Z_s + \delta Z$. Eq. 4.27 becomes:

$$\frac{d\delta A}{ds} = 2(Z_s + \delta Z)(A_s + \delta A) = 2P\delta Z \tag{4.32}$$

$$T\frac{d\delta Z}{ds} = P - Z_s - \delta Z - (1 + 2Z_s + 2\delta Z)(A_s + \delta A) = -(1 + 2P)\delta Z - \delta A \tag{4.33}$$

The Jacobian matrix M of this system can be written from:

$$\begin{pmatrix} \delta A \\ \delta Z \end{pmatrix} = \begin{pmatrix} 0 & 2P \\ -\frac{1}{T} & -\frac{1+2P}{T} \end{pmatrix} \begin{pmatrix} \delta A \\ \delta Z \end{pmatrix} \tag{4.34}$$

Solving the equation $det(M - \lambda I) = 0$ leads to the eigenvalues of the perturbed sytem

$\lambda_{\pm} = -\Gamma_{norm} \pm \sqrt{\Gamma_{norm}^2 - \Omega^2}$ with:

$$\Omega = \sqrt{\frac{2P}{T}} \tag{4.35}$$

$$\Gamma_{norm} = \frac{1+2P}{2T} \tag{4.36}$$

which, after de-normalization gives the characteristic frequency and damping rate of the laser:

$$f_r = \sqrt{\frac{2P}{T}} \frac{1}{2\pi\tau_p} \tag{4.37}$$

$$\Gamma = \frac{1+2P}{2T} \frac{1}{\tau_p} \tag{4.38}$$

Very close to threshold with $P = 0.02$, these parameters take values as high as $f_r = 13$ GHz and $\Gamma = 419$ GHz, the latter being about thirty times higher than the characteristic frequency, thus confirming the absence of relaxation oscillations in the studied QCL.

The numerical bifurcation diagram is in good agreement with the experimental one. The stable solution appearing for low feedback ratios destabilizes at the Hopf point $f_{ext} = 2.14\%$ and the route to chaos does not involve any oscillations at the characteristic frequency, only oscillations at the external cavity frequency. The bubble of chaos that occurs between $f_{ext} = 2.69\%$ and $f_{ext} = 2.91\%$ takes the form of LFF that are superimposed on the external cavity frequency oscillations. Finally, at high feedback ratios, the QCL is stable again on a different external cavity mode with larger output power. Running the simulation by decreasing the feedback ratio instead of increasing it gives another solution of successive stable external cavity modes, which coexist with the periodic and chaotic solution found previously. This multistability is difficult to observe experimentally since it requires a very fine tuning of the feedback ratio. Moreover, since the basin of attraction of the LFF dynamics is large, as shown numerically, it captures most of the system trajectories in phase space.

The numerical bifurcation diagram therefore confirms the class A-like scenario in the QCL under optical feedback, without any oscillations at the laser characteristic frequency.

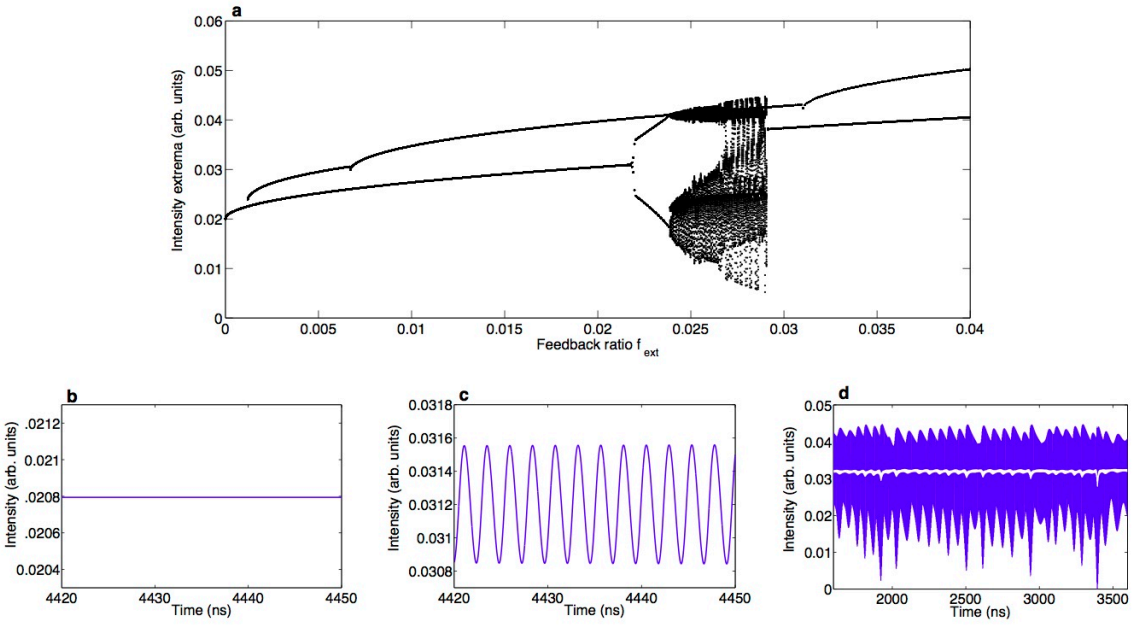

Figure 4.22: Numerical bifurcation diagram for $P = 0.02$ and $L_{ext} = 35$ cm, and associated time series. a) Numerical bifurcation diagram. b) Time trace for $f_{ext} = 0.11\%$, showing stable signal. c) Time trace for $f_{ext} = 2.14\%$, showing oscillations at the external cavity frequency. d) Time trace for $f_{ext} = 2.59\%$, showing both LFF and oscillations at the external cavity frequency.

The value $\alpha = 1.7$ was determined to best fit the experimental results within the range of values measured previously in CW operation. Although the dynamical response of the laser to optical feedback is equivalent to a modulation, which can lead to a change in the LEF value due to e.g. thermal effects or gain compression, the α-factor can be considered as quasi-static in this case. The typical frequency above which the modulation response of a QCL reaches a plateau corresponding to a quasi-static LEF is indeed below 100 MHz close to threshold [143], well below the external cavity frequency which arise in the system under optical feedback. Furthermore, the occurrence of LFF and chaos can no longer be analyzed using the small-signal modulation approximation, and the dependency of the α-factor on the modulation frequency no longer applies. Therefore, the LEF can be considered as quasi-static for the whole set of feedback conditions, and the choice of $\alpha = 1.7$ is justified.

As shown in Figure 4.23, the destabilization of the QCL under optical feedback still occurs for lower values of α-factor, and the bifurcation scenario remains the same, involving

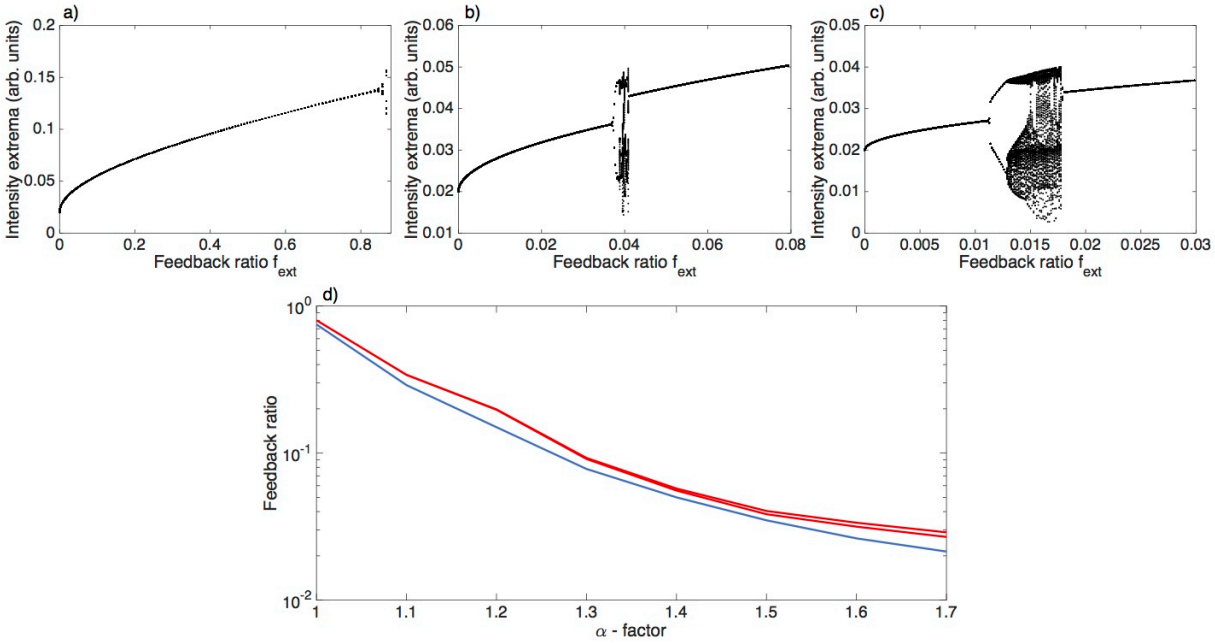

Figure 4.23: Influence of the α-factor on the bifurcation diagram for $P = 0.02$ and $L_{ext} = 35$ cm. a) Numerical bifurcation diagram for $\alpha = 1$. b) Numerical bifurcation diagram for $\alpha = 1.5$. c) Numerical bifurcation diagram for $\alpha = 2$. d) Evolution of the Hopf point (in blue) and of the lower and upper limits of the LFF area (in red) as a function of the α-factor.

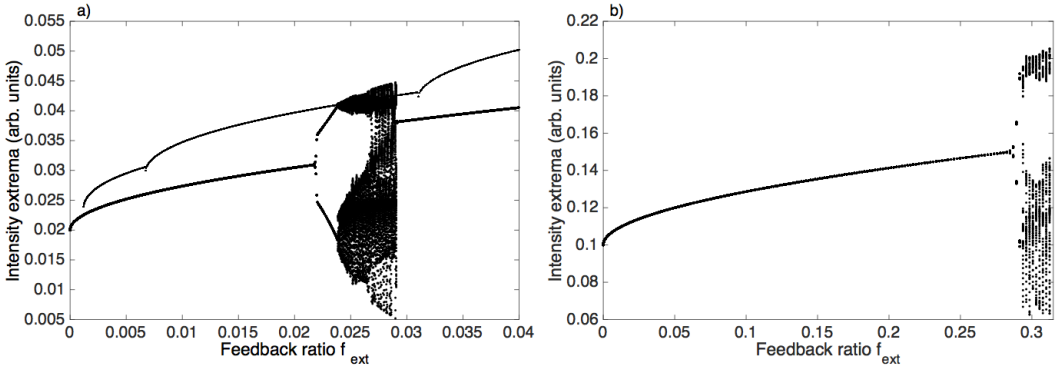

Figure 4.24: Influence of the bias parameter P on the bifurcation diagram for $L_{ext} = 35$ cm and $\alpha = 1.7$. a) Numerical bifurcation diagram for $P = 0.02$. b) Numerical bifurcation diagram for $P = 0.10$.

oscillations at the external cavity frequency and low frequency fluctuations. However, the feedback ratio at which the first Hopf bifurcation occurs increases drastically for smaller LEF, and the amplitude of the LFF area is strongly reduced. For instance, when $\alpha = 1$, with the same parameters $P = 0.02$ and $L_{ext} = 35$ cm, the Hopf bifurcation takes place at $f_{ext} = 75\%$ and the LFF, which appear around $f_{ext} = 80\%$, disappear after an increase in feedback ratio of only 0.05%. Such high values of feedback ratios are obviously unreachable experimentally. In THz QCLs, for which α-factor values much lower that 1 were reported, there will probably be no occurrence of chaos.

As expected from the study in interband lasers, the appearance of LFF depends strongly on the bias current, and they are rapidly displaced towards high feedback ratios as the pump parameter P increases. For $L_{ext} = 35$ cm and $\alpha = 1.7$, the first Hopf bifurcation occurs at $f_{ext} = 2.14\%$ at $P = 0.02$ and at $f_{ext} = 26.44\%$ for $P = 0.10$, whereas the LFF appear at $f_{ext} = 2.69\%$ and $f_{ext} = 29.34\%$ respectively, as shown in Figure 4.24.

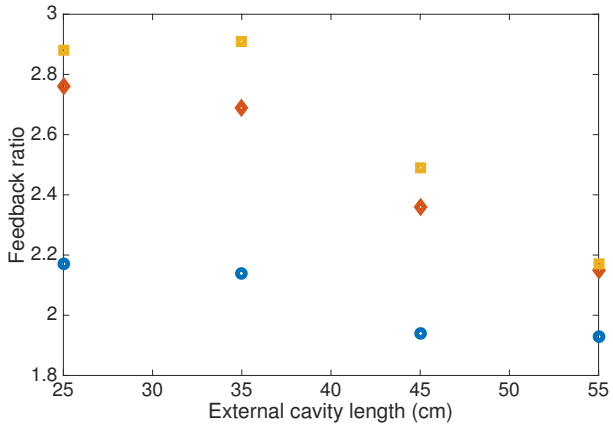

Figure 4.25: Influence of the external cavity length L_{ext} on the bifurcation diagram for P = 0.02 and $\alpha = 1.7$. In blue circles, occurence of the first Hopf bifurcation. In red diamonds, appearance of the LFF. In yellow squares, restabilization.

The evolution of the bifurcation diagram with the external cavity length follows the same trend as the one observed experimentally. As presented in Figure 4.25, the feedback ratio at which the Hopf point occurs shows only a small variation when increasing the external cavity

length from 25 to 55 cm (blue circles), whereas the LFF begin at a significantly lower feedback ratio (2.15% for 55 cm instead of 2.76% for 25 cm, red diamonds), and the amplitude of the LFF area also decreases (yellow squares representing the limit of restabilization). This trend is also similar to that obtained from the analysis of the optical spectra, where the extend of the fourth regime, which is supposed to correspond to instabilities and chaos, decreases rapidly with the external cavity length, although its starting point remains roughly the same.

Finally, for some configurations, a second destabilization was observed numerically for high feedback ratios (higher that what is experimentally achievable), resulting in periodic or multi-periodic oscillations. However, no second chaotic bubble was obtained with the considered parameters.

The same conclusions on the class A-like dynamics of QCLs subject to optical feedback, with chaos that may appear very close to threshold, have been recently obtained by analytic resolution of the full set of equations of a QCL under optical feedback [144].

4.7.5 Consequences of the possible chaotic operation of a QCL

This first observation of temporal chaos in a QCL under optical feedback have several consequences for the everyday use of the QCLs. Parasitic feedback must indeed be avoided in experimental setups. It is therefore necessary to develop compact and low-cost mid-infrared optical isolators, that could be integrated in QCL packages. Until now, although some companies such as Thorlabs, for wavelengths below 5 μm, or Innvation Photonics offer mid-infrared isolators, they remain custom-made, cumbersome, expensive and not suitable for systematic use. Furthermore, the fabrication of mid-infrared optical fibers must be carefully controlled to limit parasitic reflections and Rayleigh backscattering, similarly to near-infrared fibers.

On the other hand, a chaotic light source at mid-infrared wavelength could lead to new applications of QCLs, as for interband laser diodes. Chaotic QCLs could be efficient for optical countermeasures as they offer unpredictable sources. One could also imagine chaotic mid-infrared LIDAR that would provide high-resolution and jamming-resistant sensors. For cryptography in the mid-infrared range, chaotic QCLs could provide random bit generation

or secured communications using chaos modulation for the message encryption and synchronized chaos for the message transmission.

4.8 Conclusion

Both static and dynamical studies have shown that quantum cascade lasers are sensitive to optical feedback, although they are more resistant than interband laser diodes. Five feedback regimes either stable, bistable or chaotic appear depending on the feedback ratio, resembling to what happens in class B semiconductor lasers. However, the transition between stable and chaotic behaviors occurs through oscillations at the external cavity frequency, without involving the relaxation oscillations, a route to chaos similar to that observed in class A gas lasers.

Chapter 5

Beam shaping in broad-area quantum cascade lasers using optical feedback

QCLs with extremely high power and luminance are required to address demanding applications such as very high precision spectroscopy, selective surgery or infrared countermeasures, A straightforward idea to increase the power of a laser diode is to enlarge the active region, and especially the laser width. Hence, QCLs as broad as 400 μm have shown record-breaking output peak powers as high as 120 W [145].

5.1 Motivations

Broad-area (BA) QCLs are strongly affected by both thermal and optical issues hence showing rather poor beam quality performance. Indeed, even if the thermal resistance decreases with the ridge width, the thermal load becomes too important to be dissipated efficiently. Then, the laser needs to be operated with very short pulses to avoid thermally degraded performances, and even device destruction, which limits the mean optical power. Furthermore, a larger cavity will support numerous transverse modes. Thereby, the lasing transverse mode is no longer the fundamental mode and the far-field pattern is typically bi-lobe. In this respect, several solutions have been proposed to improve the beam quality of BA devices. QCLs with photonic cristals etched on top of the active region with diffraction-limited single-lobe far-field have been studied [146] and reported at 4.36 μm [147], 4.75 μm [148] and 7.8 μm [149]. Moreover, architectures with a tilted facet have shown an improved far-field [150, 151, 152]. Likewise, even if they present a smaller gain region compared to BA QCLs, tapered QCLs

are an interesting trade-off between large effective active region, high power, and good beam quality [153, 154]. Another approach to solve both thermal and optical drawbacks of BA QCLs is to split the ridge into an array of micro-stripes optically coupled to each other to achieve a stable optical supermode. The far-field is typically two-lobed in the case of evanescent coupling [155, 156], but single-lobe emission has been achieved by coupling the stripes by antiguiding [157].

Nevertheless, all these solutions require monolithic integration, and are therefore highly depending on the fabrication steps repeatability and quality, lacking flexibility and requiring costly additional processes such as electronic lithography or semiconductor regrowth.

In interband semiconductor BA lasers, inducing external perturbations such as optical feedback or optical injection is an efficient technique to control the beam quality and dynamical stability, without resorting to integrated solutions [36, 158, 159, 160]. For instance, applying optical feedback enhances the beam quality by reducing substantially the filamentation, which is one of the main issues of BA laser diodes. The latter corresponds to fast spatio-temporal oscillations, due to diffraction of light, self-focusing and spatial hole-burning, whose position along the laser cavity fluctuates with time. Even though the origin of filamentation is not fully understood yet, it leads to the excitation of higher spatial modes, with different phase velocities, hence deteriorating significantly the laser coherence and the beam quality. Moreover, the appearance of filamentation in a BA laser is related to the linewidth enhancement factor (LEF) value of the device [161]. The higher the LEF, the more the laser beam quality will be impacted by filamentation. Optical feedback can be used to counter the filamentation-induced drawbacks, without altering other performance of the laser. Furthermore, the dynamics ruling a BA semiconductor laser are complex, originating from the competition between the many transverse modes that coexist in the cavity. Strong instabilities or even chaos may appear in the emitted signal of a free-running BA laser diode, which can also be compensated using optical feedback.

The impact of optical feedback on the near-field profile and dynamical behavior of a BA semiconductor laser is ruled by three main parameters. The first one is the sign of the population-inversion induced index change, i.e. whether the laser design is based on gain-

guiding (positive index variation) or index-guiding (negative index variation). Studies have shown that total stabilization of the emission pattern, where optical feedback forces the laser to operate on the fundamental transverse mode, can only be achieved in the case of negative population-induced index change [162]. Furthermore, the two other key parameters are the feedback conditions: depending on the feedback ratio and the external cavity length, higher spatial modes will be either excited or suppressed [159, 160]. As the number of excited modes increases, the dynamical behavior will switch from stable emission, to pulse package fluctuations and finally to fully developed chaotic state [158].

Spatially-filtered optical feedback can further improve the near-field profile of the laser emission. Reinjecting only the central part of the emitted beam will indeed favor the lower order modes, leading to a high quality beam profile close to the single-transverse mode behavior [160].

As shown previously, QCLs have a low linewidth enhancement factor, hence reducing the risk for filamentation. However, applying optical feedback could improve the beam quality of BA QCLs and make them suitable sources for high power mid-infrared applications.

In this chapter, after a preliminary study that underlines the importance of the mirror angle control when studying the response of a BA QCL to optical feedback, conventional and spatially-filtered optical feedback will be applied to a 32 μm-wide QCL. The high performances of this QCL emitting around 4.6 μm will first be detailed. In particular, we will report that this laser presents high mean and peak powers, efficient heat dissipation allowing operation at high duty cycle, as well as high quality far-field over the whole range of operation. In a second part, the impact of optical feedback on the laser near-field as a function of the feedback mirror angle will be studied, showing significant modification of the near-field pattern. Strong amelioration of the profile is achieved in the case of centered feedback using spatial filtering. Furthermore, the response of a QCL with poor far-field quality to feedback will be investigated, as well as the influence of the laser width by comparing to 14 μm-wide devices.

5.2 Preliminary study

A preliminary study was realized in collaboration with the US Air Force Research Laboratories, on BA QCLs grown at Northwestern University. The lasers are 40 μm wide, 3 mm long, with a threshold current of 1.7 A and emitting around 4.6 μm.

5.2.1 Experimental setup

In order to characterize the QCL behavior under external optical feedback, we consider the experimental setup described in Figure 5.1. The emitted light is collected at the output of the laser and split into a feedback path and a detection path using a 60/40 beam splitter. On the feedback path, part of the light is reinjected into the laser after reflection on a rotating mirror, with an external cavity length of about 24 cm. On the detection path, the very short focal length $f = 1.87$ mm of the lens enables imaging the near-field of the QCL on a camera.

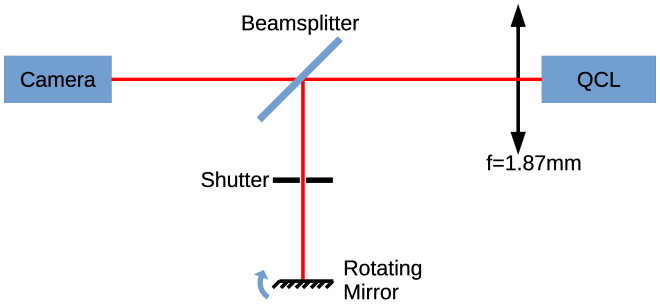

Figure 5.1: Experimental setup for BA-QCLs.

5.2.2 Beam shaping with optical feedback

As shown in Figure 5.2, when varying the angle of the feedback mirror, the shape of the QCL near-field is significantly impacted by optical feedback. In each configuration, the profile is calculated by summing the intensities on each pixel column, and the inset presents directly the near-field recorded on the camera. Compared to the free-running case, an intensity peak can appear either centered or off-centered on the beam profile, or the near-field can be completely evened.

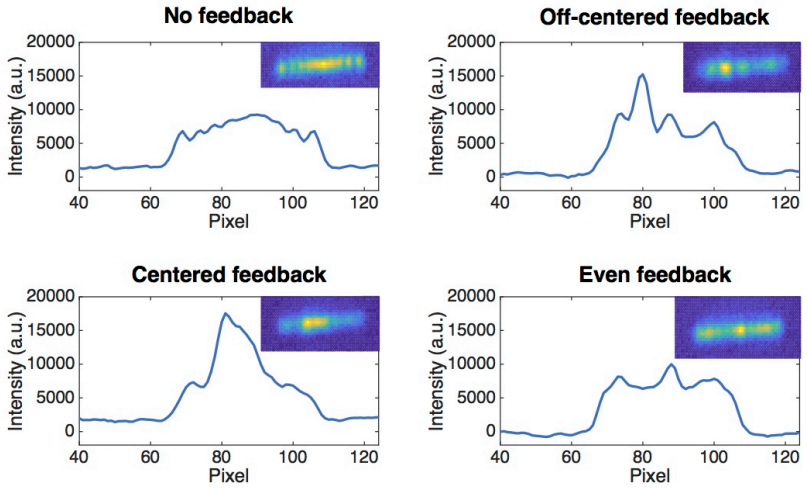

Figure 5.2: Near-field at the laser facet for several feedback angle. Plots in inset correspond to the near-field recorded on the camera.

The dependency of the near-field depending on the feedback mirror can be understood by considering the rate equations of the BA QCL under optical feedback. The equation governing the complex electric field of the QCL subject to optical feedback is indeed given by [159]:

$$\begin{aligned}\frac{\partial E(x,t)}{\partial t} = \frac{i\pi c^2}{\omega_0 n_{eff}^2}\frac{\partial^2 E(x,t)}{\partial x^2} + \frac{1+i\alpha}{2}\left(N_{pd}G_0\Delta N(x,t) - \frac{1}{\tau_p}\right)E(x,t) \\ + kE(x-\Delta x, t-\tau_{ext})\exp(-i\omega_0\tau_{ext})\end{aligned} \tag{5.1}$$

where c is the light velocity, ω_0 the free-running angular frequency, n_{eff} the effective refractive index, τ_p the photon lifetime inside the laser cavity. G_0 corresponds to the net modal gain for one period, N_{pd} to the number of periods, α to the linewidth enhancement factor and τ_{ext} to the external cavity roundtrip time. ΔN is the carrier density difference between the upper and the lower lasing states. Finally, k is the feedback coefficient, defined in the case of Fabry-Perot lasers as:

$$k = \frac{1}{\tau_{in}}\frac{1-R_2}{\sqrt{R_2}}\sqrt{f_{ext}} \tag{5.2}$$

with τ_{in} the internal cavity roundtrip time, R_2 the front facet reflectivity (here $R_2 = 0.3$) and f_{ext} the feedback ratio, i.e. the ratio between reinjected and emitted light.

In BA lasers, the dependency of the field and carrier densities on the spatial variable x becomes very important, as underlined by the diffraction term in the complex field rate equation 7.4. A diffusion term D_n furthermore exists in the carrier rate equation, and for an interband laser under optical feedback, it can be written as [163],:

$$\frac{\partial N(x,t)}{\partial t} = D_n \frac{\partial^2 N(x,t)}{\partial x^2} + \frac{I}{q} - \frac{N(x,t)}{\tau_c} - G(N(x,t))|E|^2 \tag{5.3}$$

In a QCL, several diffusion coefficients corresponding to the several carrier rate equations have to be considered. Moreover, when applying optical feedback, the reinjected mode is not necessarily superimposed on the corresponding emitted mode, it can be shifted by a quantity Δx. It will therefore be crucial to control precisely the angle of the mirror when applying optical feedback to BA QCLs.

5.2.3 Temporal evolution with optical feedback

Replacing the camera with a fast MCT detector in the experimental setup enables to observe the effect of optical feedback on the temporal response of the QCL.

As shown in Figure 5.3, varying the feedback mirror angle also impacts the temporal response of the laser. Compared to the free-running scenario, an increase or decrease of the power may appear, either on the totality or on only part of the temporal peak power during the pulse. Since no precise position was recorded during the near-field measurement, it is not at this stage possible to link these temporal response with a mirror position and near-field profile. Qualitatively, the maximum peak power is obtained for centered optical feedback, with an intensity peak at the center of the beam profile.

Furthermore, some oscillations seem to appear for some angles of the feedback mirror, but the measurements here are limited by the resolution of the oscilloscope, and no period could be extracted. It would be necessary to repeat these measurements with higher resolution equipment, to conclude on whether these oscillations occur at the external cavity frequency, as in the case of narrow-ridge QCLs.

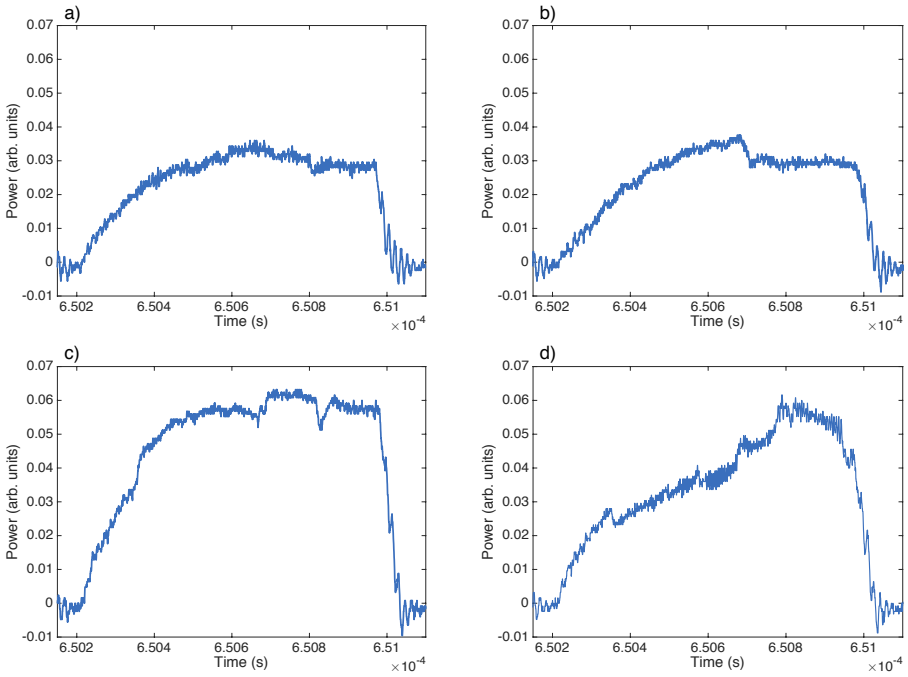

Figure 5.3: Temporal power evolution with optical feedback. a) Free-running scenario. b) Decrease of the power. c) Increase of the power. d) Appearance of oscillations.

5.3 Case of a high-performance 32 μm-wide QCL

The experiment is repeated with a high-performance 32 μm-wide QCL from mirSense, in order to further investigate the impact of optical feedback on the near-field beam profile.

5.3.1 Design and processing

A 2.5 μm thick n-doped InP layer ($n = 10^{17}$ cm^{-3}), acting as the bottom optical cladding layer, is grown by MBE, followed by a 200 nm $Ga_{0.47}In_{0.53}As$ layer ($n = 6\times10^{16}$ cm^{-3}), which plays the role of a large optical cavity (LOC). Finally, we grow the 30 period active region and another similar LOC. The QCL active region design is derived from the shallow-well structure previously published [18], and adapted to have a gain centered around 4.6 μm. The specificity of this structure is the InP:Fe regrowth by low pressure hydride vapor phase epitaxy (HVPE) on the sides of the ridges. The studied device is 4 μm-long, gold HR-coated

on the back facet and mounted epi-side down onto an AlN submount. The mounted device is shown on Figure 5.4.

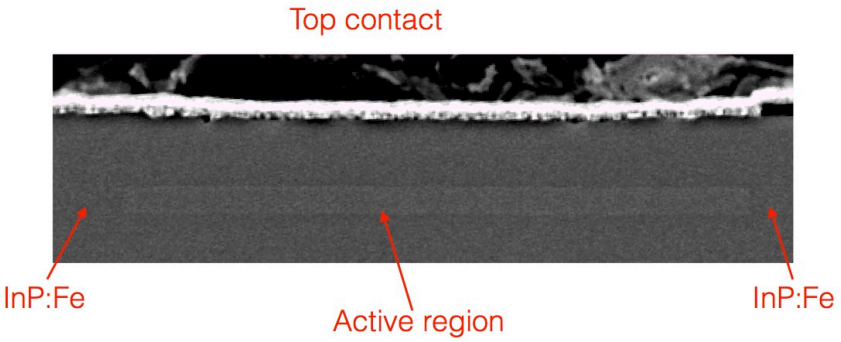

Figure 5.4: SEM picture of the device facet mounted epi-side down. The 32 μm active region (in lighter gray) is surrounded by InP:Fe and sandwiched between two n-doped InP cladding layers.

5.3.2 Laser performances

Standard voltage vs current and power vs current (L-I-V) curves are measured at temperatures ranging from 10°C to 40°C. The laser submount is set on a copper heat sink which temperature is controlled with a Peltier cooler. The duty cycle is 3%, the pulses lasting 600 ns. The mean power is measured behind an aspherical lens ($f = 1.87$ mm, $NA = 0.87$). The collection factor was evaluated to be 0.8 by comparing the maximum optical power with this setup with the one read from a second power-meter with high aperture angle placed right after the laser facet. Results are shown in Figure 5.5 a. The threshold current density is 1.51 kA/cm^2 at 10°C, and 1.69 kA/cm^2 at 40°C, which yields a characteristic temperature of $T_0 = 266$ K in the temperature range 10° to 40°C. This value is in accordance with previously published results for QCLs with the same design [18]. The low values of the current densities show that the current leakage through the InP:Fe is negligible, and thus the quality of the HVPE regrowth. At 10°C, the mean power is 254 mW and the peak power is 11.5 W.

Furthermore, the evolution of the mean power with the duty cycle was measured, as represented in Figure 5.5 b. Our current source was limited to 26% of duty cycle, which was below the thermal roll-over both at 20°C and 40°C. It shows the heat load is efficiently

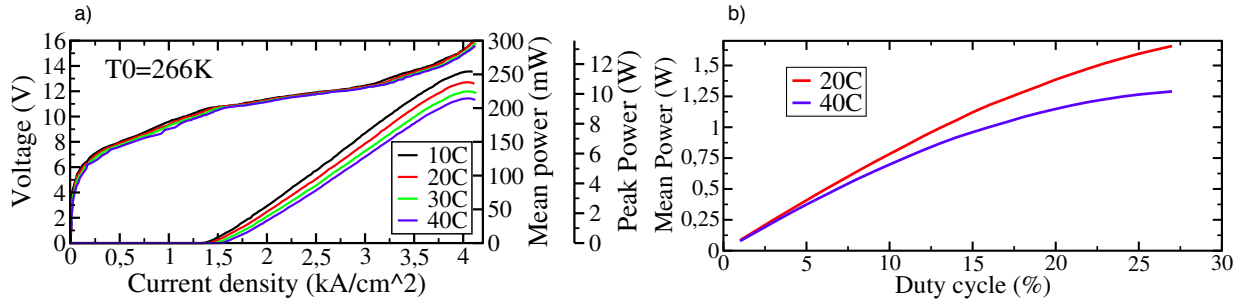

Figure 5.5: a) LIV curves at 3% duty cycle for temperatures from 10°C to 40°C. b) Evolution of the mean power with duty cycle at 20°C and 40°C

dissipated through the laser top contact and the InP:Fe on its sides. At a duty cycle of 26%, the maximum mean power exceeds 1.6 W.

We measure the far-field by placing the power-meter on an automated two-axis rotating stage. The scanning speed is around 0.6 degree per second. We use the same current source and average power-meter as for the PIV experiments. A background scan is performed with the laser turned off to suppress the thermal background. Both horizontal and vertical far-fields are shown in Figure 5.6. As for typical QCL, the vertical divergence is large [13], the full-width at half-maximum (FWHM) is 45.5° at 14 V, but is weakly depending on the operating point. However, the horizontal far-field remains single-lobed up to a 12 V bias and is only affected by a shoulder afterwards, whereas BA QCLs usually experience multi-lobed far-fields significantly degrading with increasing current.

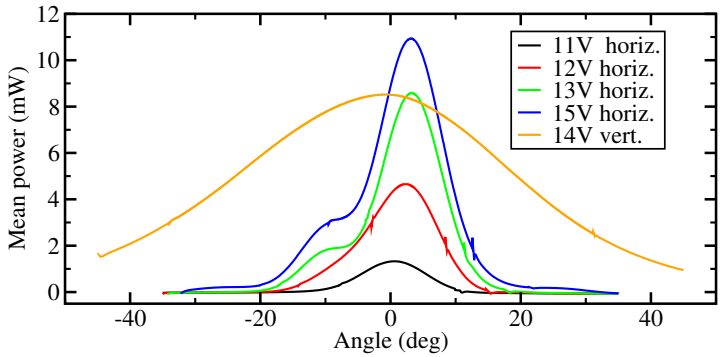

Figure 5.6: Horizontal and vertical far-fields at different bias currents.

The transverse optical modes that can exist in the cavity have been estimated by solving Maxwell's equations using a 2D solver. For the simulation, the refractive indices are chosen to be 3.19 for the active region, 1 for the SiO_2 forming the passivation layer, 3.09 for the InP:Fe. The LOCs and the cladding layers are modeled by Drude model with a high frequency permittivity of $\epsilon_\infty = 9.61$, an effective electron mass to free electron mass ratio of $m^\star/m_0 = 0.08$ and an electron scattering time of $\tau_{scat} = 0.1$ ps. Resulting fundamental and highest order modes, TM0 and TM5, are shown in Figure 5.7.

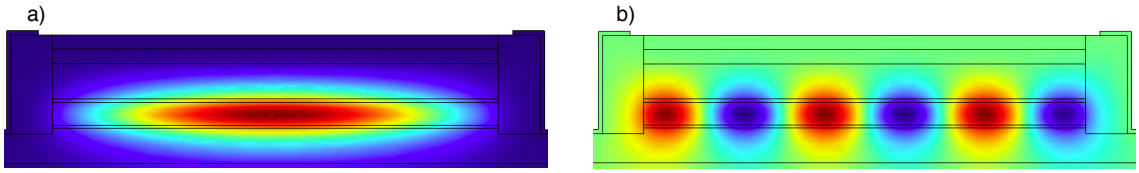

Figure 5.7: Simulated TM0 (a) and TM5 (b) electric field intensities.

Mode order	Overlap with the active region (%)	Effective refractive index
TM0	58.58	3.1305
TM1	58.38	3.1284
TM2	58.03	3.1248
TM3	57.51	3.1199
TM4	56.73	3.1136
TM5	55.51	3.1059

Table 5.1: Model parameters for InP substrate, SiO_2, Si_3N_4, TiO_2.

The overlaps of the modes with the active region and their calculated effective refractive index are summarized in Table 5.1. The higher the mode order, the more it spills into the InP:Fe spacers. In comparison, in the case of a standard double trench (DT) device, the overlap difference is lower between the modes as they are all strongly confined by the dielectric layer [56]. In the case of the studied device, the overlap difference between TM0 and TM5 is $\Delta\Gamma = 3.1\%$ whereas it is only $\Delta\Gamma_{DT} = 0.87\%$ for a 32 μm DT device. Thus, the InP:Fe spacers are acting as a high-order mode filter.

In addition, the effective refractive index of TM0 is 3.1305, which is below the active region refractive index. Therefore, the refractive index variation is negative, and in accordance with the results in near-IR mentioned previously we expect to be able to change the energy distribution between the modes in order to favor the fundamental one, by using optical feedback.

5.3.3 Beam steering effect

In the far-field of Figure 5.7, the measured horizontal FWHM increases with the bias current, ranging from 11° to 13.1°. As the bias is increasing, the peak horizontal emission is right-shifted from 0.5° to 3.2° and a shoulder appears on one side of the far-field profile. This evolution of the far-field with the bias current is due to beam steering. It is attributed to beating between the lowest order transverse modes, their effective refractive indices being close to each other, as shown in Table 5.1.

Generally speaking, beam steering is due to the large nonlinear susceptibility $\chi^{(3)}$ in QCLs [164], which induces nonlinear coupling between the transverse modes and leads to four-wave mixing interactions and phase coherence [165], as depicted in Figure 5.8 a and b. The electric field is indeed expressed as:

$$E(x) = \sum_i \alpha_i E_i(x) \tag{5.4}$$

where $E_i(x)$ is the complex electric field of the ith transverse mode and α_i a coupling coefficient.

When considering only the two lowest-order transverse modes, the beam steering only results in an off-axis far-field, depending on the phase difference between the complex electric fields of the two modes (see Figure 5.8 c and [166]). However, when more modes are interacting, the far-field is often significantly deteriorated, as shown in Figure 5.8 b: when increasing the bias current, more and more modes are involved and the far-field profile is degraded.

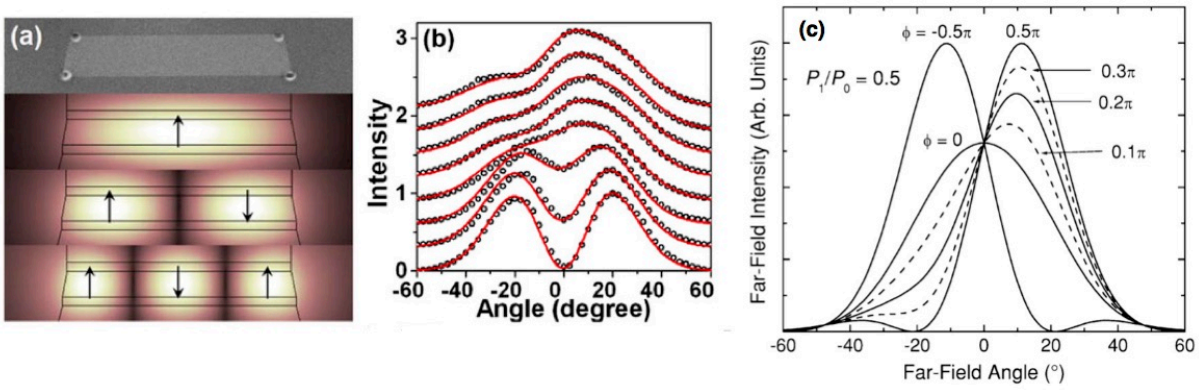

Figure 5.8: a) SEM picture of the laser facet and simulated TM0, TM1 and TM2. b) Measured (black dots) and fitted (red lines) far-fields at different bias currents. Courtesy of [165]. c) Simulated far-field in case of equal power coupling between TM0 and TM1 for various phase difference (courtesy of [166]).

5.3.4 Modifications on the optical feedback experimental setup

This laser is inserted in a similar setup as described in Figure 5.1, but this time the feedback mirror is mounted on a precision rotation stage with vernier scale to control the angle of feedback. Furthermore, the external cavity length is carefully chosen: the camera is at the same distance from the laser as the feedback mirror. The beam is therefore focused at the same time on the camera and on the mirror, and what is reinjected into the QCL is an image of its near-field. The external cavity length is chosen to be $L_{ext} = 29$ cm, but longer cavities were also considered and led to similar results, as long as the laser beam remains focused on the feedback mirror.

With the described experimental setup, it is not possible to measure exactly this feedback ratio. However, the observed threshold fluctuations of less than ± 1% suggest that only a small amount of light is reinjected into the cavity, corresponding to feedback ratios of less than 5%. This small quantity of optical feedback should however lead to an amelioration of the beam profile, whereas higher amount of reinjection would tend to destabilize the laser [158].

In this section, the influence of the spatial position of the reinjected beam will be studied, and the angle of the feedback mirror θ can therefore be adjusted in order to sweep the

feedback over the whole active area. Furthermore, a shutter on the feedback path enables spatial filtering of the reinjection, by choosing which part of the beam is fed-back into the laser cavity.

5.3.5 Conventional optical feedback

Figure 7.17 presents the near-field profiles of the QCL previously described operated close to threshold (at 11.19 V with a 3% duty cycle) when subjected to conventional optical feedback. The nine curves correspond to different feedback mirror angles, as indicated above the plots. The first and last curves are the free-running cases, where the reinjected beam does not enter the laser cavity. When changing the feedback angle, the impact of optical feedback is shown to be perfectly symmetrical with respect to the central position, corresponding to $\Delta x = 0$.

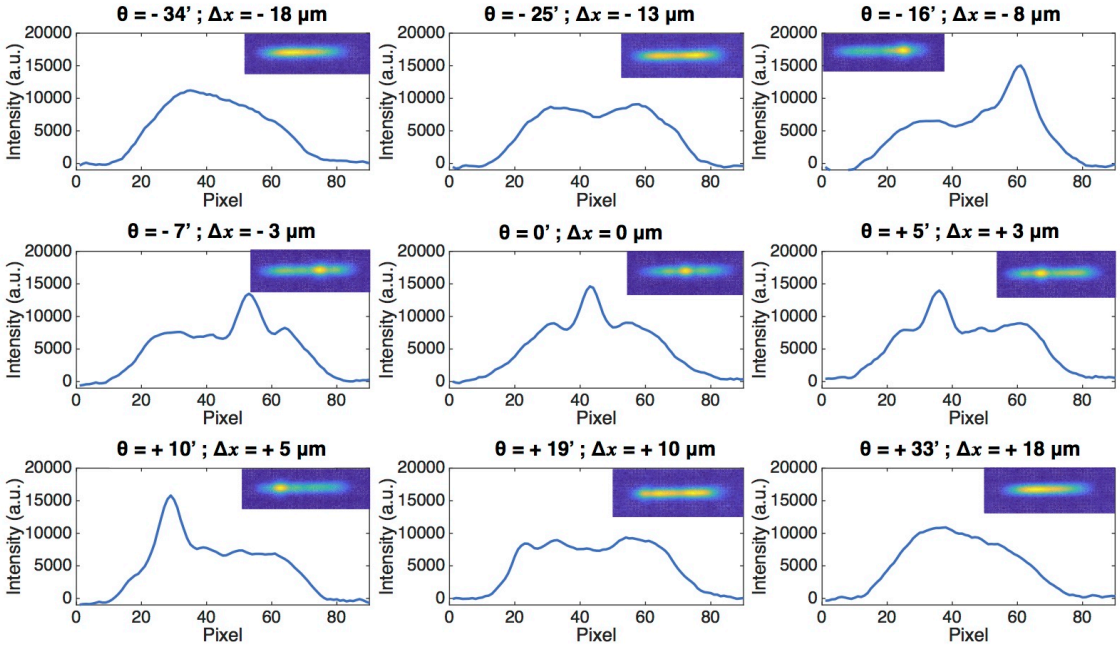

Figure 5.9: Near-field at the laser facet for different feedback angle, expressed both in arc-minute and in displacement on the laser facet with respect to the central position. The shutter is open and has no impact on the feedback. Figures in inset correspond to the near-field recorded on the camera.

Under free-running operation ($\theta = -34'$ and $+33'$), the QCL near-field is not completely symmetric, there is more power on the left-hand side of the profile. This originates from beam steering effect, which has been often observed in BA QCLs [166]. This beam steering

can be compensated by reinjecting a small amount of optical feedback on one side of the cavity. In that case, the power distribution becomes almost homogeneous over the near-field profile ($\theta = -25'$ and $+19'$). Afterwards, when directing the feedback closer to the center of the cavity, a peak appears on the near-field profiles, corresponding to the position where the light is reinjected, and this peak is shifted continuously along the near-field when changing the mirror angle (from $\theta = -16'$ to $+10'$). In particular, the transverse mode with three maxima TM2 becomes preponderant for centered optical feedback ($\theta = 0'$). It is however important to stress that, although the power distribution between the several modes is strongly modified by optical feedback, the total emitted power is hardly affected, whatever the position of the reinjected beam.

5.3.6 Spatially-filtered optical feedback

On this central position where the TM2 mode is predominant, a shutter is added on the feedback path close to the beam-splitter in order to spatially filter the central peak of the reinjected mode. As shown in Figure 7.18, when the shutter is fully open, the TM2 mode appears, where the less pronounced peaks can be explained by a different contrast on the camera. Finally, when the shutter is partially closed to let through only the central peak, a spatial profile closer to the fundamental transverse mode TM0 is obtained. This is consistent with studies of optical feedback on BA laser diodes, that have shown that spatial filtering of the feedback will lead to the excitation of lower order transverse modes [160].

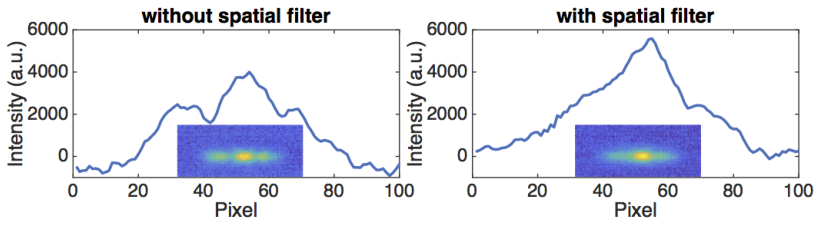

Figure 5.10: Near-fields at the laser facet with centered optical feedback and two shutter apertures. The shutter is fully open (a) and partially closed to filter the central lobe (b).

5.3.7 Feedback response of a QCL with multi-lobe far-field

A second QCL is considered, which has the same design and same width as the first one. Although the power performances are similar, the horizontal far-field shows many lobes even at low bias voltage, as represented in Figure 5.11 b. These deteriorated performances can be understood by observing the facet, as shown in Figure 5.11 a. A crack is indeed observed on the right-hand side of the facet. This defect breaks the symmetry of the device, which leads to an inhomogeneous gain. Some nonlinear effects will be enhanced, such as strong spatial hole burning, which is responsible for the multi-lobe far-field.

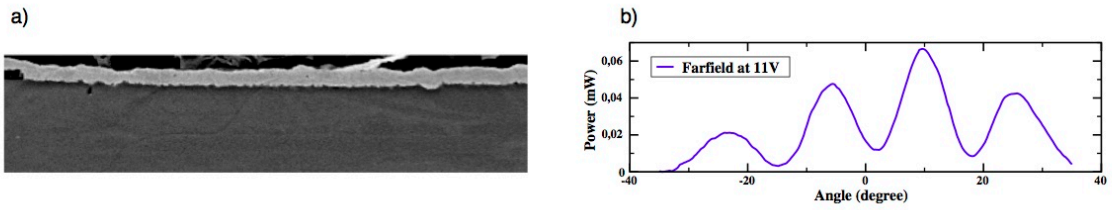

Figure 5.11: a) SEM picture of the laser with a defect facet. b) Horizontal far-field at 11 V.

When subjecting this QCL to optical feedback, a response very different from the previous laser is observed, as depicted in Fig. 5.12. The near-field patterns are no longer symmetrical with respect to the centered feedback case, and here only the most interesting half of the way is shown, from the free-running to the case where $\Delta x = 0$. When changing the feedback angle towards the center of the cavity, more and more transverse modes are excited. The succession of TM1 ($\theta = +19'$), TM2 ($\theta = +15'$), TM3 ($\theta = +11'$) and TM4 ($\theta = +7'$) are observed. Finally, for centered optical feedback, TM5 is excited ($\theta = 0'$), although the extinction between the lobes is not very clear. These observations are consistent with the conducted simulations showing that a maximum of six transverse modes can co-exist in the 32 μm cavity.

Furthermore, these near-field patterns where higher order transverse modes appear in the case of optical feedback resemble the situation described in BA laser diode very sensitive to spatial hole burning [159]. This might suggest the appearance of filamentation in this BA QCL presenting a defect on the facet, although a temporal study would be necessary in order

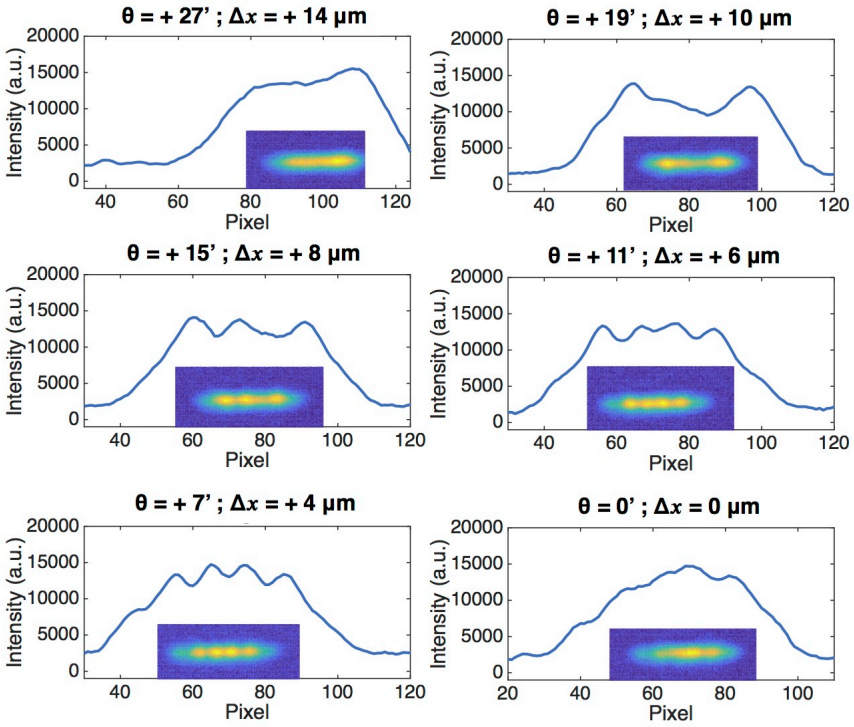

Figure 5.12: Near-field at the facet for the 32 μm-wide QCL presenting a defect, for different feedback angle.

to conclude on this point. Similar field distributions and response to optical feedback should be expected in the case of any BA QCL presenting an asymmetry or an inhomogeneous gain, leading to a multi-lobe far-fied.

5.3.8 Comparison with a 14 μm-wide laser

In order to evaluate the impact of the QCL width on its response to optical feedback, an additional measurement was performed on a 14 μm-wide QCL. This laser has the same active region design as the one described previously, and was processed using a standard double-trench technique. According to the simulations, three modes can exist in this cavity, but the beam profile of the free-running laser is gaussian, as shown in the first plot of Figure 5.13. This QCL can no longer be considered as a BA laser, and its response to centered optical feedback is indeed the one of a narrow-ridge laser, with an increase of the output power and a narrowing of the near-field profile.

However, when rotating the feedback angle, the higher order mode TM1 can be excited

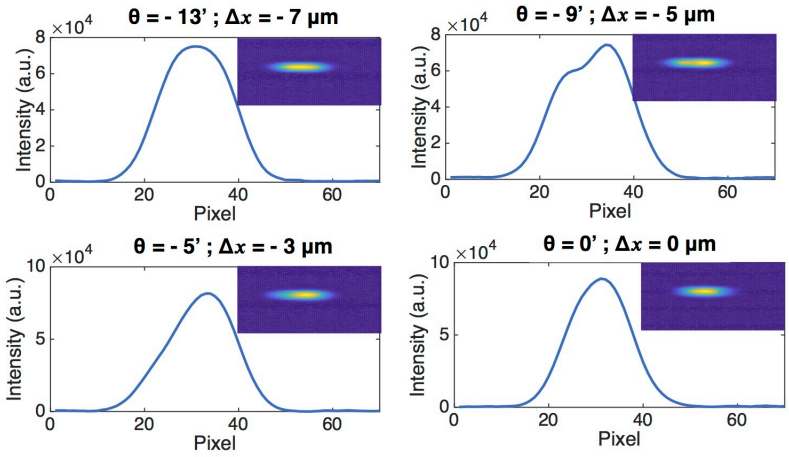

Figure 5.13: Near-field at the facet for the 14 μm QCL based on the previously described design, for different feedback angle.

($\theta = -9'$ and $-5'$), as depicted in Figure 5.13. We observe the same tendency as in the case of BA QCL under feedback, with a limited displacement of the feedback peak due to the smaller width of the cavity and the limited number of modes that can get excited. Therefore, this study on a 14 μm QCL can be considered as the limit case where the spatial dimension x of optical feedback must be taken into account.

5.4 Beam steering suppression with optical feedback

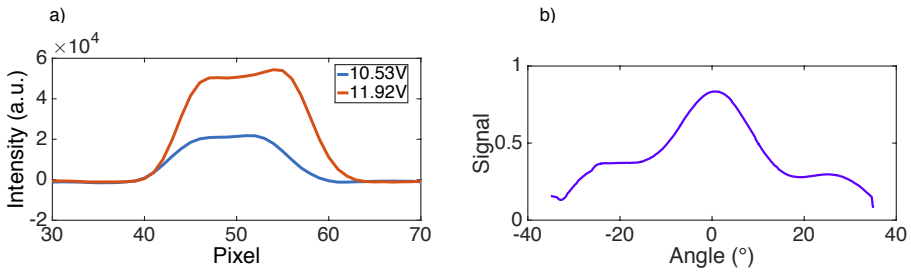

Figure 5.14: a) Evolution of the near-field profile with the bias voltage of a 14 μm QCL based on a different design, evidencing strong beam steering. b) Deteriorated far-field of the laser at high bias current.

Some 14 μm-wide QCLs based on a different design are already sensitive to multimode

interactions within the laser cavity, which results for instance in strong beam steering of the free-running laser. This is the case for the QCL studied in this section, also emitting around 4.6 μm. As depicted in Figure 5.14, the near-field profile of this laser indeed becomes more and more distorted when increasing the bias voltage.

As shown in Figure 7.19, when applying off-centered optical feedback on this laser, two well-separated maxima appear on the near-field profile, corresponding to a predominant first order transverse mode TM1. However, when the feedback beam is reinjected in the center of the laser cavity, the beam steering is totally suppressed, and the obtained near-field profile is perfectly single-lobe, corresponding to TM0.

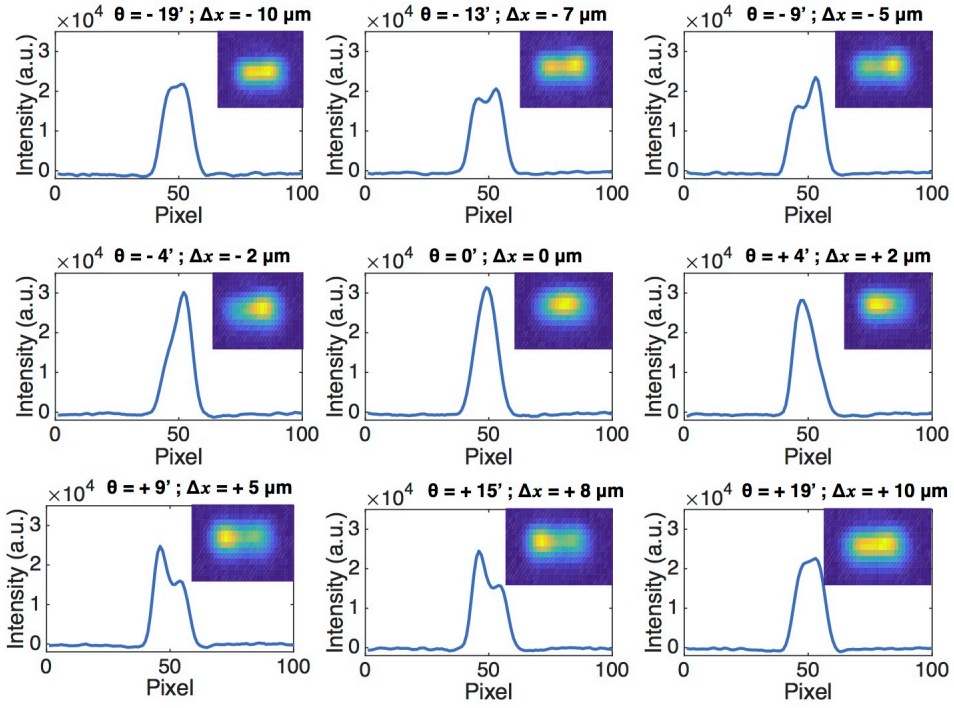

Figure 5.15: Impact of optical feedback on a 14 μm QCL based on a different design presenting strong beam steering.

5.5 Conclusions

This study shows the possibility to engineer the emission pattern of BA QCLs using a non-linear external control with and without spatial filtering. Tailoring the near-field emission

pattern becomes possible, even with a small amount of off-centered reinjected light which avoids complex monolithic integration and is therefore much easier to implement. It can be changed either to a more homogeneous distribution or to a near-field that presents an intensity peak following the mirror displacement for a QCL emitting on a single lobe. Spatially-filtered optical feedback is used to further enhance the near-field profile quality. In the case of a BA QCL with a multi-lobe far-field, all the cavity transverse modes are sequentially excited while changing the feedback mirror angle. The comparison with a narrower device points out the impact of the number of cavity modes on the feedback response. Moreover, even for smaller cavities, optical feedback can efficiently be used in order to suppress the beam steering that may occur.

Further works will investigate the dynamical behavior of QCLs under optical feedback. As a matter of fact, depending on the QCL structure quality, strong spatial hole burning can arise, which might lead to filamentation. Optical feedback can be used as an efficient solution to stabilize the QCL dynamics, as for BA near-infrared laser diodes. Furthermore, the design of the spatial filters should be optimized to reach a better control of the reinjected beam, and therefore, on the device far-field pattern. In addition, further experiments will be performed in order to explore the impact the optical feedback has on BA devices of several hundreds of microns. Such QCLs are indeed of interest because they produce extremely high output powers but, due to the existence of many transverse modes in the cavity, they present very poor beam quality, which should be improved by applying optical feedback.

Chapter 6

Impact of optical injection on quantum cascade lasers

Optical injection consists in injecting part of the light emitted by a first laser, or master laser, into a second laser, called slave laser. It can improve the emission properties of the slave laser, similarly to optical feedback, but the impact of optical injection is much more significant.

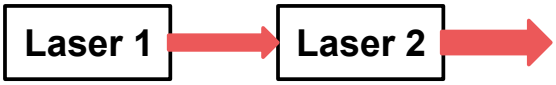

Figure 6.1: Principle of optical injection.

When injecting light into the laser and increasing progressively the injected power at fixed master laser wavelength, the wavelength of the slave laser will be pushed away from that of the master laser (Figure 6.2 a). On the other hand when increasing progressively the master wavelength at fixed injected power, the wavelength of the slave laser will be pulled towards that of the master laser (Figure 6.2 b). In the particular case when the frequency of the master laser is close enough to the slave laser frequency and the master laser power is high enough, the slave laser will operate at the master laser frequency. This phenomenon, called injection locking, is well-known in physical systems. In the 17^{th} century, Huygens observed that two pendulums of clocks mounted on the same wall would synchronize and oscillate at the same frequency, due to the propagation of vibrations through the wall. Injection locking was later applied to electrical oscillators [167], to lasers under electrical injection [168] and

finally to lasers subject to optical injection [169].

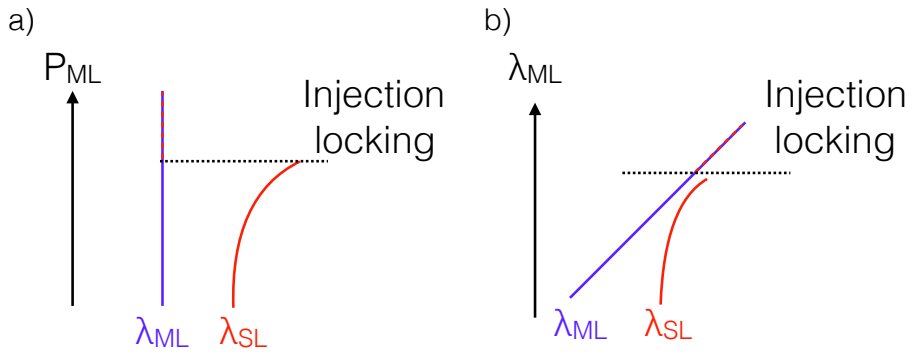

Figure 6.2: Schematic of injection locking. a) Evolution of the slave wavelength λ_{SL} as a function of the injected power. b) Evolution of the slave wavelength λ_{SL} as a function of the master wavelength λ_{ML}.

In the optical injection experimental setup, an optical isolator between the master and slave lasers is a key element to avoid optical feedback of the master after reflection on the slave facet, or optical injection of the slave inside the master. Without isolator, the two lasers impact each other, it corresponds to mutually coupled lasers, which also experience complex dynamics [170, 171], but will not be studied here.

After a brief review of the effects of optical injection on a laser diode both in and outside the locking range, this chapter will present a overview of the state of the art on optical injection in QCLs, as well as a numerical study applied to the QCL structure described in the second chapter.

6.1 Impact of optical injection on interband laser diodes

Optical injection in interband semiconductor lasers has been studied since the early eighties, both experimentally and numerically.

6.1.1 Locking map

The rate equations of a laser diode under an electric field $E = \sqrt{S}e^{i\phi_0}$ subject to optical injection $E_{inj} = \sqrt{S_{inj}}$ can be expressed as [172, 173]:

$$\frac{dN}{dt} = \frac{I}{q} - \frac{N}{\tau_c} - G(N)S \tag{6.1}$$

$$\frac{dS}{dt} = \left(G(N) - \frac{1}{\tau_p}\right)S + 2k\sqrt{S_{inj}S}\,\cos(\phi_0) \tag{6.2}$$

$$\frac{d\phi}{dt} = \frac{\alpha}{2}\left(G(N) - \frac{1}{\tau_p}\right) - k\sqrt{\frac{S_{inj}}{S}}\,\sin(\phi_0) - \Delta\omega \tag{6.3}$$

where N is the carrier density of the slave laser, I is the slave bias current, q the electron charge, τ_c the slave carrier lifetime, τ_p the slave photon lifetime, $G(N)$ the slave gain per unit time and α the slave linewidth enhancement factor. The frequency detuning is defined as $\Delta\omega = \omega_{ML} - \omega_{SL}$, with ω_{ML} and ω_{SL} the frequencies of the master and slave lasers, respectively. Finally, the injection coupling coefficient k can be written as:

$$k = \frac{1}{\tau_{in}}2C_l \tag{6.4}$$

with τ_{in} the slave internal cavity roundtrip time and C_l the external coupling coefficient defined as in the case of optical feedback (see eq. 7.7 for a Fabry-Perot laser and eq. 3.8 for a DFB laser).

The analytical conditions for stable injection locking in a laser diode have been given by Morgensen *et al.* [174]. Under steady-state, with $G(N) = 1/\tau_p + G_N(N - N_{th})$ and $N - N_{th} = \Delta N$, eq. 6.1 to 6.3 indeed lead to [175]:

$$\Delta\omega = -k\sqrt{1+\alpha^2}\sqrt{K}\,\sin(\phi_0 + atan\,\alpha) \tag{6.5}$$

$$\Delta N = \frac{2}{G_N}k\cos(\phi_0)\sqrt{K} \tag{6.6}$$

with $K = S_{inj}/S$ the injection ratio. Since $-1 \leq sin(\phi_0 + atan\,\alpha) \leq 1$, eq. 6.5 gives the

boundaries of the locking range:

$$-k\sqrt{K}\sqrt{1+\alpha^2} < \Delta\omega < k\sqrt{K}\sqrt{1+\alpha^2} \tag{6.7}$$

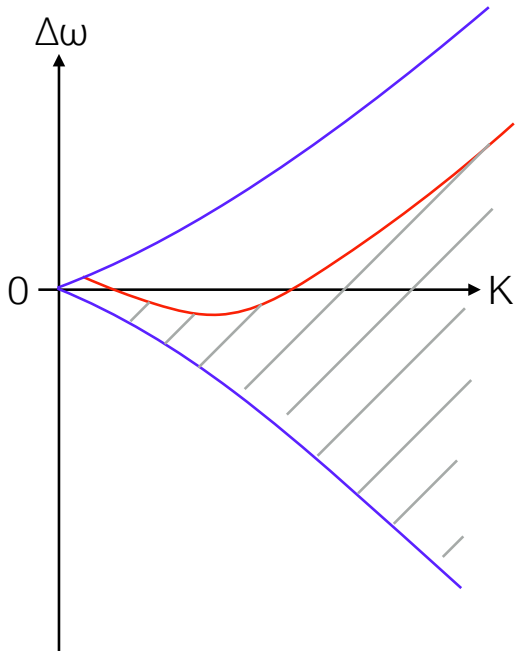

Figure 6.3: Typical locking map of a laser diode. In blue, Saddle-Node bifurcations. In red, Hopf bifurcation. In dashed gray, stable locking region.

These boundaries correspond to Saddle-Node bifurcations, represented in blue in Figure 6.3. Another stability boundary was given later by Gavrielides *et al.* [176], which can be expressed as [43]:

$$\left(\frac{\Delta\omega}{\omega_r}\right)^2 = \frac{K^2(2K^2+1-\alpha^2)^2}{\alpha^2+(2K^2+1)} \tag{6.8}$$

with ω_r the relaxation oscillation angular frequency. It corresponds to a Hopf bifurcation, leading to an unstable locking at zero detuning for small injection ratios, as represented in red in Figure 6.3. The stable locking area is located between the Hopf curve and the Saddle-Node at negative detuning, as shown in dashed gray in Figure 6.3.

6.1.2 Improved laser properties in the stable locking region

In the stable locking region, the emission properties of the slave laser are ameliorated. By definition, the injection locked slave laser will operate at the master laser frequency, with a strong suppression of the Fabry-Perot side-modes when increasing the injection ratio [172], as shown in Figure 6.4. Furthermore, the optical linewidth of the slave laser under stable injection locking is strongly reduced. Typically, Morgensen *et al.* [177] demonstrated an injection-locked linewidth of 5.84 MHz when the free-running linewidth was 87.5 MHz, based on FM noise calculations.

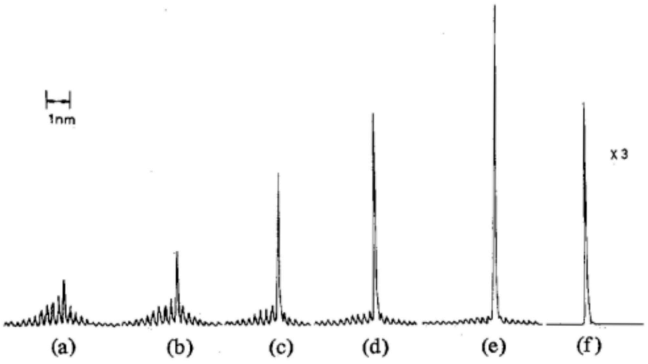

Figure 6.4: Optical spectra of a laser diode as a function of the injected power (courtesy of [172]). a) Free-running case. b) $P_{inj} = -$ 49.5 dBm. c) $P_{inj} = -$ 42.5 dBm. d) $P_{inj} = -$ 39.5 dBm. e) $P_{inj} = -$ 29.5 dBm. f) $P_{inj} = -$ 22.5 dBm.

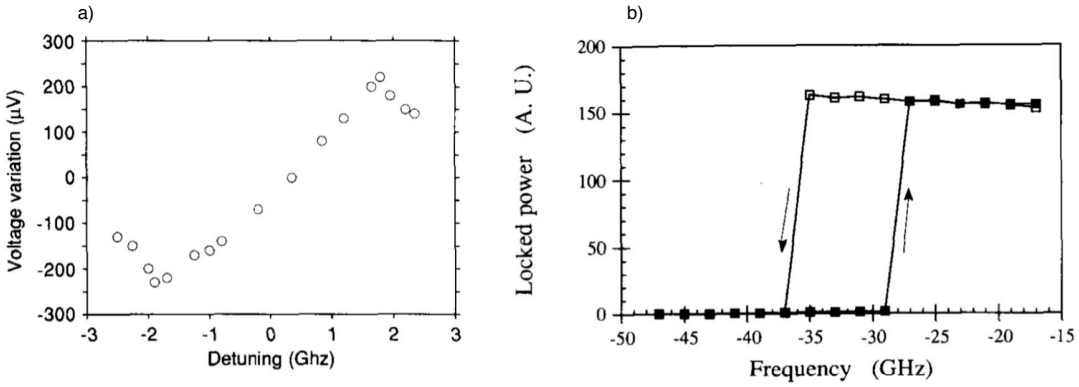

Figure 6.5: a) Voltage evolution with the detuning, showing the locking range. b) Influence of the detuning on the optical power at constant injection strength. (Courtesy of [178]).

Stable injection locking also impacts the voltage and output power of the slave laser [178, 179, 180]. As shown in Figure 6.5 a, the bias voltage will increase linearly in the locking range when increasing the detuning. From this voltage variation compared to free-running versus detuning curve, van Exter *et al.* [179] proposed a new technique to measure the α-factor. If ν_0 is the detuning at which the bias voltage is equal to the free-running value, and ν_m is the half-width of the locking range, the LEF can be written as:

$$\alpha = \sqrt{\left(\frac{\nu_m}{\nu_0}\right)^2 - 1} \tag{6.9}$$

The optical power also increases significantly when the laser in under stable injection locking, as depicted in Figure 6.5 b. Furthermore, a strong bistability appears on the measurement depending on whether the detuning is increased or increased.

Spano *et al.* [181] studied the evolution of the intensity and frequency noise of a semiconductor laser under optical injection. They proved numerically and experimentally that the slave laser noise will tend to reproduce the master laser noise when the detuning is close enough to 0, both for intensity and frequency noise. Therefore, if the purity of the master laser is high, the noise of the slave laser will be significantly reduced.

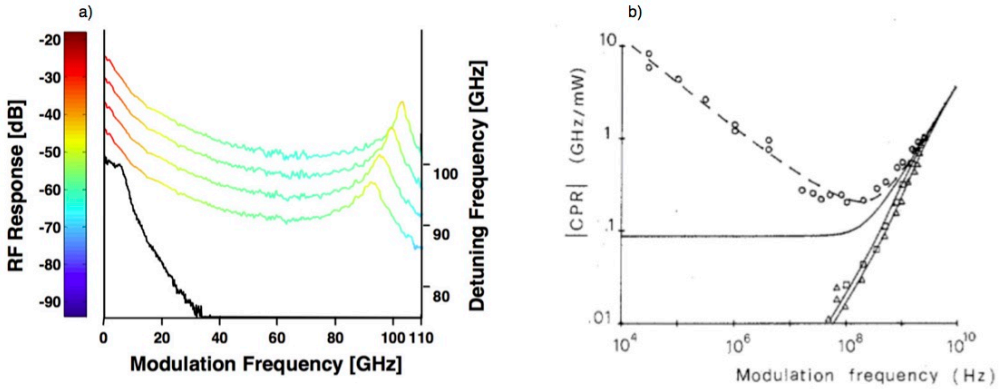

Figure 6.6: a) Improvement of the modulation bandwidth with optical injection, compared to the free-running case in black (courtesy of [182]). b) Chirp reduction with optical injection, compared to the free-running represented by circles (courtesy of [183]).

The modulation response of a laser diode under stable injection locking is also drastically improved. As shown in Figure 6.6 a, the -3 dB modulation bandwidth of a VCSEL

can be enhanced when increasing the injection ratio, and values over 80 GHz have been reported [182].

Furthermore, the low frequency chirp is also reduced, as depicted in Figure 6.6 b. Under optical injection, the chirp to power ratio (CPR), defined as the ratio between frequency and power deviations CPR $= \Delta\nu/\Delta P_{opt}$, keeps decreasing linearly when decreasing the modulation frequency, whereas the free-running CPR reaches a plateau at low frequency [183]. A laser with no chirp was even reported, by zeroing the α-factor through optical injection [184].

Under stable injection locking, the slave laser diode properties are therefore significantly enhanced, and tend to reproduce the characteristics of the master laser.

6.1.3 Instabilities and chaos outside the stable locking region

On the other hand, when the laser is injected outside the stable locking range, complex dynamical behaviors may appear [185, 186]. Similarly to the case of optical feedback, period 1, period 2, higher harmonics and chaos will arise. However, at zero detuning, the laser is not always stable at low injection ratio [187]: depending on the slave parameters, when increasing the injection ratio, the laser may start stable, become periodic and restabilize, or it may first be chaotic, then enter period 2, period 1 and finally stabilize (see Figure 6.7).

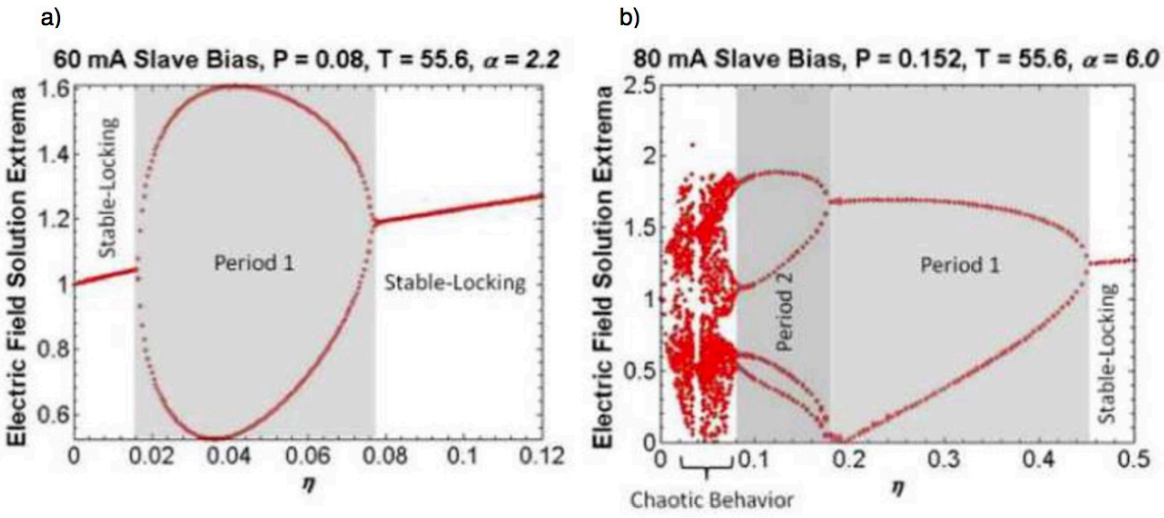

Figure 6.7: Examples of bifurcation diagrams depending on the slave laser parameters. Here the normalized parameters have the same definition as for optical feedback (courtesy of [187]).

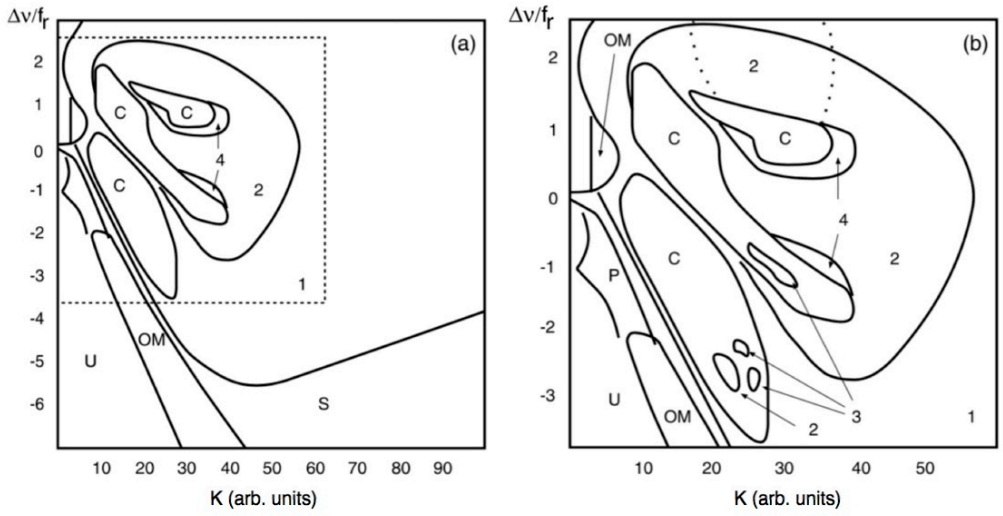

Figure 6.8: Experimental locking map, presenting the complex dynamics of a laser subject to optical injection. The dashed area in a) is represented in b) (courtesy of [188]).

Figure 6.8 a presents an example of the complete locking map of a semiconductor laser under optical injection [188]. The stable injection locking region is marked by 'S', and the unlocked region by 'U'. 'OM' indicates that the laser operates on other longitudinal modes. A zoom on the unstable locking region is presented in Figure 6.8 b. In this area, the laser dynamics are very complex. Three islands of chaos can be observed, marked with 'C'. Some periodic oscillations appear, they are marked with a number on the graph ('1' for period 1, '2' for period 2, etc.). Bubbles of periodic oscillations even occur within a chaotic island. Finally, the region labelled 'P' corresponds to frequency pulling, where the slave laser frequency is pulled towards the master frequency, but the injection ratio is not high enough, and the laser does not lock.

The dynamics that occur in a laser diode outside the stable locking range are therefore very complex, and depend both on the intrinsic parameters of the slave laser and on the injection conditions.

6.2 Previous studies of optical injection in quantum cascade lasers

Taubman *et al.* [189] were the first to report injection locking of a DFB QCL into a second

DFB QCL. By gradually increasing the master laser power, they observed an increase of the locking range, up to ± 500 MHz for the maximum achievable injection ratio of 3%.

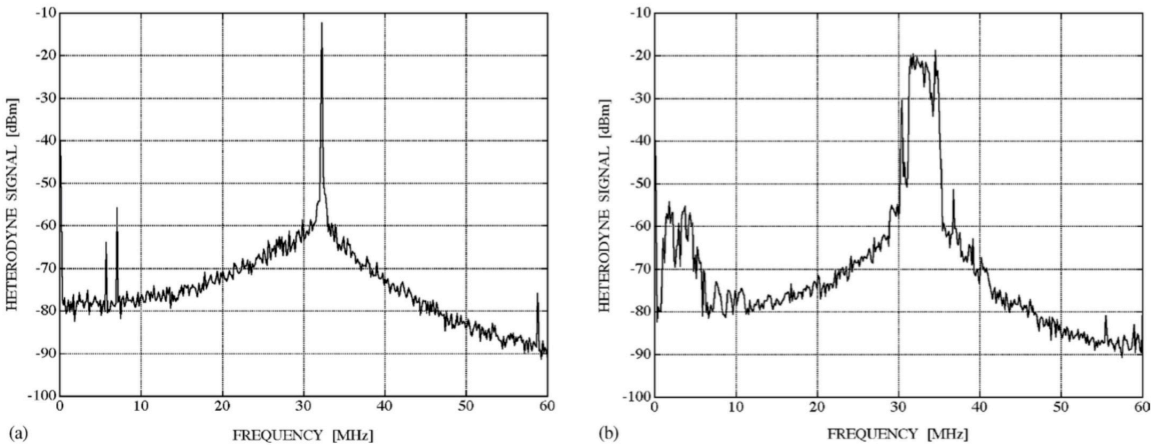

Figure 6.9: Heterodyne beating between the master QCL and the slave QCL. a) Case of injection locking. b) Free-running slave laser. (Courtesy of [189]).

Furthermore, an asymmetry appeared on the locking map, which was attributed to a non-zero α-factor: the extracted LEF was $\alpha = 0.26 \pm 0.1$. By studying the heterodyne beating between the slave and master lasers, a clear reduction of the slave linewidth was also observed, as shown in Figure 6.9. Finally, optical injection locking was used to suppress residual amplitude modulation (RAM). Direct modulation of the bias current of a QCL indeed produces both frequency (FM) and amplitude modulations (AM), the latter being a source of noise in the case of FM spectroscopy. Under optical injection locking, the RAM was reduced by 49 dB and can even be totally suppressed by applying an additional modulation on the slave bias current, out of phase with the one applied on the master laser. The RAM reduction using optical injection was also studied numerically by Yong *et al.* [190].

Optical injection locking can also be exploited to reduce the noise of a QCL. By injecting a DFB QCL into another one, the RIN at low frequency can be reduced by 20 dB/Hz [191], as shown in Figure 6.10 a. Experimentally, under the same conditions, a maximum RIN decrease of around 10 dB/Hz was observed [60]. As presented in Figure 6.10 b, when tuning the master laser frequency over the whole slave laser range, the otherwise well-suppressed side-modes of the slave QCL will lock successively, inducing RIN reduction and output power increase. However, the efficiency and locking range will depend on the enhanced side-mode, it

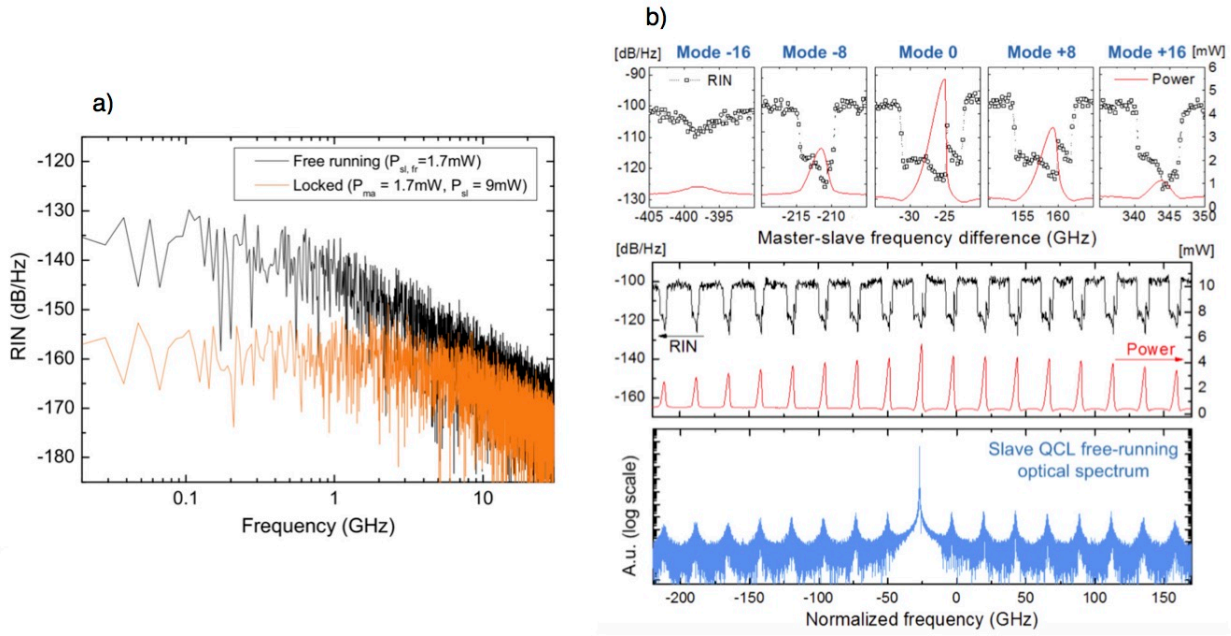

Figure 6.10: a) Numerical RIN reduction with optical injection (courtesy of [191]). b) Experimental RIN and power evolution with the frequency detuning: when one of the slave laser mode is locked on the master frequency, the RIN is reduced and the power increased (courtesy of [60]).

reaches a maximum range of 8 GHz on the central mode. By injecting a frequency comb into a Fabry-Perot QCL, the low-frequency frequency noise was also significantly reduced [192]. Up to 100 kHz, the slave QCL will reproduce the behavior of the master, and therefore decrease its frequency noise by 3 to 4 orders of magnitude. As a consequence, the linewidth of the laser is also reduced from a few MHz down to 20 kHz.

A few theoretical studies based on the QCL rate equations, also focused on the modulation properties of a QCL under optical injection [193, 194]. For instance, Wang *et al.* [195] demonstrated an increase up to 30 GHz of the -3 dB modulation bandwidth. Furthermore, all these studies concluded that no unstable locking region would exist in QCLs, due to the ultra-fast carrier lifetime. However, no experimental studies on the modulation of a QCL under optical injection locking have been performed so far to verify these predictions, although the modulation bandwidth has been significantly improved up to 14 GHz in a QCL under radio-frequency (RF) injection locking [196].

6.3 Numerical analysis of injection locking in quantum cascade lasers

6.3.1 Rate equations under optical injection

Similarly to the case of optical feedback, when neglecting spontaneous emission, if the slave QCL is under an electric field $E = \sqrt{S}e^{i\phi}e^{i\omega_{SL}t}$ and $E_{inj} = \sqrt{S_{inj}}e^{i\omega_{ML}t}$ is the electric field of the master laser, the rate equations of the QCL subject to optical injection can be written as:

$$\frac{dN_3}{dt} = \eta\frac{I}{q} - \frac{N_3}{\tau_{32}} - \frac{N_3}{\tau_{31}} - G_0\Delta NS \tag{6.10}$$

$$\frac{dN_2}{dt} = \frac{N_3}{\tau_{32}} - \frac{N_2}{\tau_{21}} + G_0\Delta NS \tag{6.11}$$

$$\frac{dN_1}{dt} = \frac{N_3}{\tau_{31}} + \frac{N_2}{\tau_{21}} - \frac{N_1}{\tau_{out}} \tag{6.12}$$

$$\frac{dS}{dt} = \left(N_{pd}G_0\Delta N - \frac{1}{\tau_p}\right)S + 2k\sqrt{S_{inj}S}\cos(\phi) \tag{6.13}$$

$$\frac{d\phi}{dt} = \frac{\alpha}{2}\left(N_{pd}G_0\Delta N - \frac{1}{\tau_p}\right) - \Delta\omega - k\sqrt{\frac{S_{inj}}{S}}\sin(\phi) \tag{6.14}$$

where N_j is the carrier density of level j, with $\Delta N = N_3 - N_2$, η is the conversion efficiency, I is the bias current. τ_{ij} corresponds to the carrier lifetime from level i to level j, τ_{out} is the characteristic time for the electron to tunnel into the injector, τ_p is the photon lifetime inside the laser cavity. G_0 corresponds to the net modal gain for one period, N_{pd} to the number of periods and α to the linewidth enhancement factor. $\Delta\omega$ is the frequency detuning, defined as $\Delta\omega = \omega_{ML} - \omega_{SL}$. Finally, k is the injection coefficient, defined as:

$$k = \frac{1}{\tau_{in}}2C_l \tag{6.15}$$

where τ_{in} is the internal cavity roundtrip time and C_l is the external coupling coefficient as defined in Eq. 7.7 or 3.8.

6.3.2 Analytical model

From eq. 7.18 to 7.22, the analytical model for a QCL under optical injection has been developed by Erneux *et al.* [197].

The rate equations are normalized with respect to the photon lifetime τ_p, with $s = t/\tau_p$ the normalized time, and defining the new set of variables (Y, Y_{inj}, Z, V), with Y and Y_{inj} the normalized amplitude of the slave and master laser electric fields, respectively, Z the normalized carrier density difference, and V the normalized carrier density of level $|2\rangle$, by:

$$\begin{aligned} Y &= G_0\tau_{32}S \\ Y_{inj} &= G_0\tau_{32}S_{inj} \\ \Delta N &= \frac{1+2Z}{N_{pd}G_0\tau_p} \\ N_2 &= \frac{1}{N_{pd}G_0\tau_p}\frac{1+V}{\frac{\tau_{32}}{\tau_{21}}-1} \end{aligned}$$

Other parameters, such as the normalized lifetimes γ_1, γ_2, γ_3 and γ_4, the normalized bias current P, the normalized injected power γ and the normalized detuning Ω are expressed as:

$$\begin{aligned} \gamma_1 &= \frac{\tau_p}{\tau_{32}} \\ \gamma_2 &= \left(\frac{\tau_{32}}{\tau_{21}}-1\right)\frac{\tau_p}{\tau_{32}} \\ \gamma_3 &= \left(\frac{\tau_{32}}{2\tau_{21}}-1-\frac{\tau_{32}}{2\tau_{31}}\right)\frac{1}{\frac{\tau_{32}}{\tau_{21}}-1} \\ \gamma_4 &= 2\left(1+\frac{\tau_{32}}{2\tau_{31}}\right) \\ P &= \frac{N_{pd}G_0\tau_p\tau_{32}}{2}\,\frac{\eta(I-I_{th})}{q} \\ \gamma &= k\tau_p\sqrt{Y_{inj}} \\ \Omega &= \Delta\omega\tau_p \end{aligned}$$

It is worth noting that the conversion efficiency η was not included in the normalized pump parameter P in the work of [197], but impacts significantly the resulting locking map. Injecting these normalized parameters into the rate equations 7.18 to 7.22 leads to (the

detailed calculation can be found in Ref. [197]):

$$\frac{dZ}{ds} = \gamma_1 \left[P + \gamma_3 V - \gamma_4 Z - (1 + 2Z)Y \right] \tag{6.16}$$

$$\frac{dV}{ds} = \gamma_2 \left[2Z - V + (1 + 2Z)Y \right] \tag{6.17}$$

$$\frac{dY}{ds} = 2YZ + 2\gamma\sqrt{Y}\cos(\phi) \tag{6.18}$$

$$\frac{d\phi}{ds} = \alpha Z - \Omega - \gamma\sqrt{\frac{1}{Y}}\sin(\phi) \tag{6.19}$$

At this stage, an approximation can be made: the values for γ_2 extracted from the literature suggest to eliminate adiabatically V using $V = 2Z + (1 + 2Z)Y$, i.e. the steady-state value of eq. 6.17. By writing $\gamma_{41} = \gamma_4 - 1$, the rate equations 6.16 to 6.19 become:

$$\frac{dZ}{ds} = \gamma_1 \left[P - \gamma_{41} Z - (1 + 2Z)\frac{Y}{2} \right] \tag{6.20}$$

$$\frac{dY}{ds} = 2YZ + 2\gamma\sqrt{Y}\cos(\phi) \tag{6.21}$$

$$\frac{d\phi}{ds} = \alpha Z - \Omega - \gamma\sqrt{\frac{1}{Y}}\sin(\phi) \tag{6.22}$$

Under steady-state, the parametric equations expressing Y and the injection strength γ as a function of Z, with $-1/2 < Z < P/\gamma_{41}$, are given by:

$$Y = \frac{2(P - \gamma_{41} Z)}{1 + 2Z} \tag{6.23}$$

$$\gamma^2 = \left[Z^2 + (\alpha Z - \Omega)^2 \right] \frac{2(P - \gamma_{41} Z)}{1 + 2Z} \tag{6.24}$$

The stability boundaries of the QCL under optical injection can be extracted from the Jacobian matrix resulting from eq. 6.20 to 6.22 (see Ref. [197] for the detailed calculation). The Saddle-Node bifurcation, corresponding to the locking condition with one zero root, is obtained by solving:

$$-\frac{\gamma_{41} + 2P}{1 + 2Z}\left[Z^2 + (\alpha Z - \Omega)^2 \right] + 2(P - \gamma_{41} Z)\left[Z + \alpha(\alpha Z - \Omega) \right] = 0 \tag{6.25}$$

The two Hopf bifurcations, with two purely imaginary roots, verify:

$$2Z\left[-2\gamma_1\frac{\gamma_{41}+2P}{1+2Z}+Z^2+(\alpha Z-\Omega)^2\right]-2\gamma_1^2\frac{\gamma_{41}+2P}{1+2Z}\left[-\frac{\gamma_{41}+2P}{1+2Z}Z+P-\gamma_{41}Z\right] \\ -2\gamma_1(P-\gamma_{41}Z)\left[Z+\alpha(\alpha Z-\Omega)\right]=0 \tag{6.26}$$

$$2\gamma_1\frac{\gamma_{41}+2P}{1+2Z}Z+2\gamma_1(P-\gamma_{41}Z)+Z^2+(\alpha Z-\Omega)^2>0 \tag{6.27}$$

Figure 7.20 presents the analytical locking maps obtained from eq. 6.25 to 6.27 for different α-factors and bias currents. The other parameters of the simulation correspond to the 4 mm $\times$ 12 μm Fabry-Perot QCL described in the second chapter, with a threshold current of 1.2 A. On the graph, the blue curve corresponds to the Saddle-Node solution, and the two red curves to the Hopf solutions.

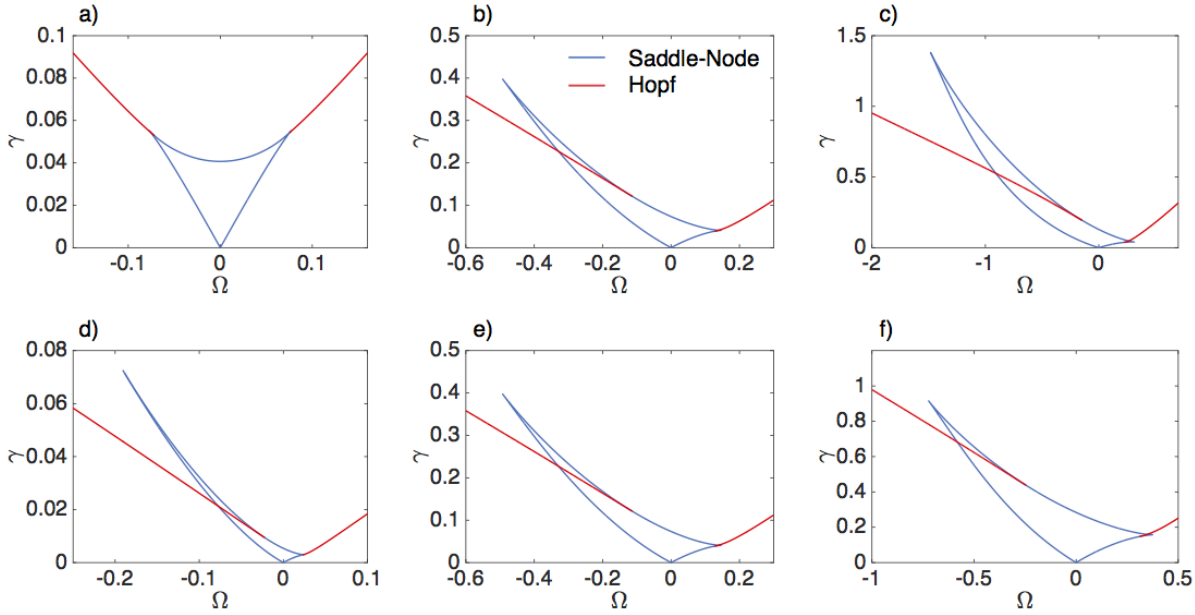

Figure 6.11: Analytical simulations of the 12 μm Fabry-Perot QCL subject to optical injection. First row: constant bias current $I = 1.5$ A with a) $\alpha = 0$, b) $\alpha = 1.5$ and c) $\alpha = 3$. Second row: fixed $\alpha = 1.5$ and d) $I = 1.25$ A, e) $I = 1.5$ A, f) $I = 2$ A.

The shape of the QCL locking map is very different from the one usually observed in interband lasers, for instance represented in Figures 6.3 and 6.8. However, it resembles the one typically obtained for class A lasers [198] or numerically for highly damped class B lasers

such as quantum dot lasers [199], although it was never observed experimentally in this last case. The main difference is that in QCLs and class A lasers, the laser will always be locked at zero detuning, even for low injection ratios. Furthermore, no unstable locking region will appear in a QCL, and hence no chaos. Destabilization of the slave laser will only occur in the upper left and lower right parts of the curves, beyond the Hopf lines but within the limits of the Saddle-Node region. In this range, the QCL should experience phase-locked bistability [199], either between two stable solutions or between a stable and a periodic solution [198].

In Figure 7.20, the first row corresponds to a fixed bias current $I = 1.5$ A, but three values of the linewidth enhancement factor. On each plot, the scales are modified in order to observe the complete locking map. When $\alpha = 0$, the Saddle-Node and Hopf curves are perfectly symmetrical with respect to the zero detuning case. When increasing progressively the α-factor, an asymmetry arises: the locking region at negative detuning becomes larger than the locking range at positive detuning. Furthermore, both the locking range and the bistable region between the Hopf bifurcation and the upper Saddle-Node curve also increase with the LEF.

The second row of Figure 7.20 presents the evolution of the locking map with the bias current, at constant LEF $\alpha = 1.5$. It shows that the locking range increases with the bias current. Very close to threshold, the Hopf bifurcation will moreover arise for lower injection strength, but the bistable region is narrower compared to the high bias scenario.

6.3.3 Numerical locking map

The second simulation method is also based on the rate equations of the QCL under optical injection (eq. 7.18 to 7.22). In this case, the perturbed electric field of the slave laser is calculated for each point of the locking map, and the locking range corresponds to the situation where the slave response is stable. In presence of injected light outside the stable locking range, both the amplitude and phase of the slave electric field will indeed oscillate due to the $\cos(\phi)$ and $\sin(\phi)$ terms in eq. 7.21 and 7.22, also inducing an oscillation on the carriers.

The starting point of the numerical simulations are the rate equations of the laser with-

out optical injection. In order to obtain the free-running characteristics, the spontaneous emission term $\beta N_3/\tau_{sp}$ is added to the rate equations on N_2 and S, and substracted to the equation on N_3, where β is the spontaneous emission coefficient and τ_{sp} the spontaneous emission lifetime. Since the spontaneous emission is very weak in QCLs, values as low as $\beta = 10^{-6}$ [45] and as fast as $\tau_{sp} = 1$ ns were considered. Varying these values does not impact significantly the laser behavior, as long as $\tau_{sp} \gg \tau_{32}$. However, it is necessary to consider even a small amount of spontaneous emission to start the stimulated emission.

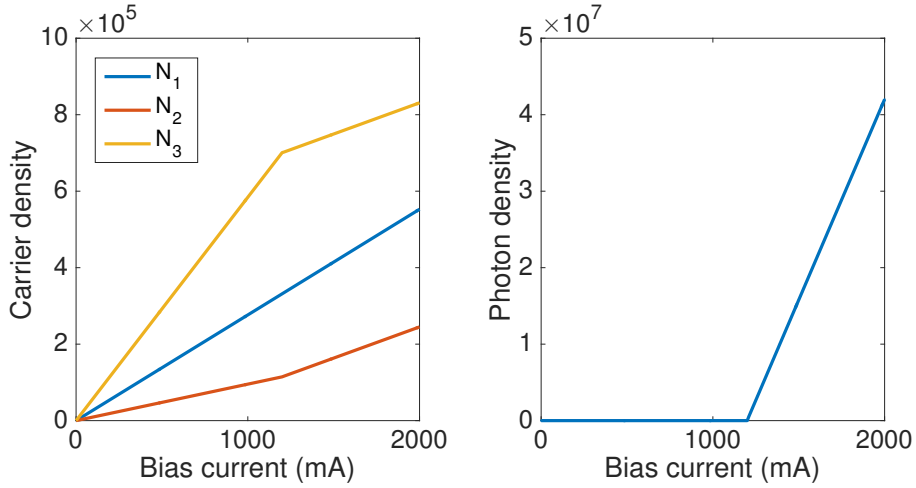

Figure 6.12: Simulated carrier and photon densities of the free-running QCL as a function of the bias current.

Figure 6.12 shows the carrier and photon densities as a function of the bias current. The coefficient η of eq. 7.18 was determined in order to correspond to the 12 μm-wide Fabry-Perot QCL, which threshold is located at $I = 1.2$ A. A value of $\eta = 0.082$ fits well to this laser, and the simulated threshold on the photon density curve is indeed at $I = 1.2$ A. Furthermore, it is interesting to note on the carrier densities plot that, contrary to the case of interband laser diodes, the carrier densities are not clamped above threshold. Only the gain, and therefore the carrier density difference $\Delta N = N_3 - N_2$ is clamped, which is consistent with all numerical studies in QCLs (see e.g. [52]).

Figure 7.21 presents the numerical simulations of the 12 μm Fabry-Perot QCL. The locking map is obtained by plotting the difference between the intensity extrema of the

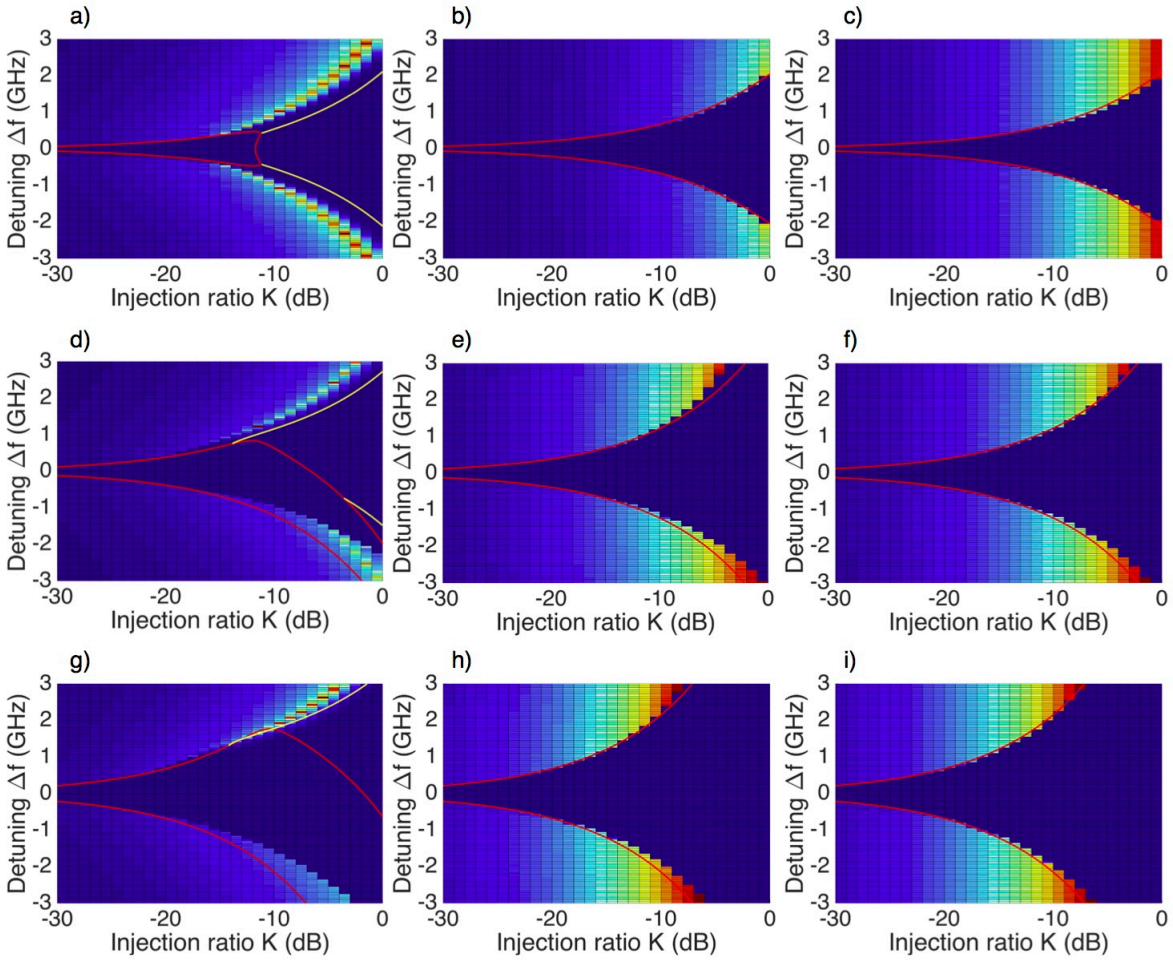

Figure 6.13: Numerical simulations of the signal intensity as a function of the injection ratio and detuning, superimposed on the analytical solutions (red for Saddle-Node and yellow for Hopf curves) for the 12 μm Fabry-Perot QCL subject to optical injection. First row: $\alpha = 0$ with a) $I = 1.25$ A, b) $I = 1.5$ A, c) $I = 2$ A. Second row: $\alpha = 1.5$ with d) $I = 1.25$ A, e) $I = 1.5$ A, f) $I = 2$ A. Third row: $\alpha = 3$ with g) $I = 1.25$ A, h) $I = 1.5$ A, i) $I = 2$ A.

temporal response as a function of the injection ratio and detuning. The results are analyzed for several α-factors and bias currents, superimposed with the analytical results. Both simulations give the same results in the case $\alpha = 0$ (first row). However, when increasing the α-factor, the two simulations slightly diverge from one another. This is probably linked to the approximations made for the analytical calculations (see Ref. [197]). As expected, the QCL is nevertheless always locked at zero detuning.

Furthermore, some interesting behaviors occur close to threshold, as shown in the first column of Figure 7.21, with $I = 1.25$ A. At this bias, the Hopf curves from the analytical simulations appear in a range of parameters reasonably achievable in the experiments. In the numerical simulations, it corresponds to the occurrence of new dynamics. Beyond the Hopf bifurcation, sinusoidal oscillations appear. These period one dynamics occur for instance on both sides for $\alpha = 0$ (Figure 7.21 a), and in the case of positive detuning for $\alpha = 1.5$ (Figure 7.21 d) and $\alpha = 3$ (Figure 7.21 g), with a period depending on injection parameters.

Moreover, still considering the case very close to threshold, some high-intensity events appear punctually along the limit of the locking region when the Hopf bifurcation is located beyond the Saddle-Node curve (see on both sides of Figures 7.21 a and d, and for positive detuning of Figure 7.21 g). The nature of these events remains unclear, but QCLs subject to optical injection could potentially be used as extreme events generators [200].

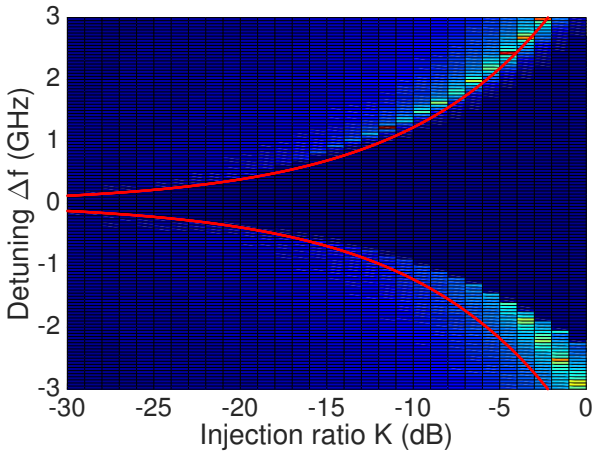

Figure 6.14: Influence of η on the locking map for the 12 μm QCL with $I = 1.25$ A and $\alpha = 1.5$. The conversion efficiency is taken into account in the numerical calculation but taken to $\eta = 1$ in the analytial curves.

These new dynamics are clearly linked to the existence of the Hopf curve within a reasonable range of parameters. If considering $\eta = 1$ in the analytical model, as is the case in Ref [197] and as shown in Figure 6.14, no Hopf curve should appear, and the dynamics outside the locking range should resemble that at higher bias currents, which is obviously not the case, as obtained from the numerical simulation.

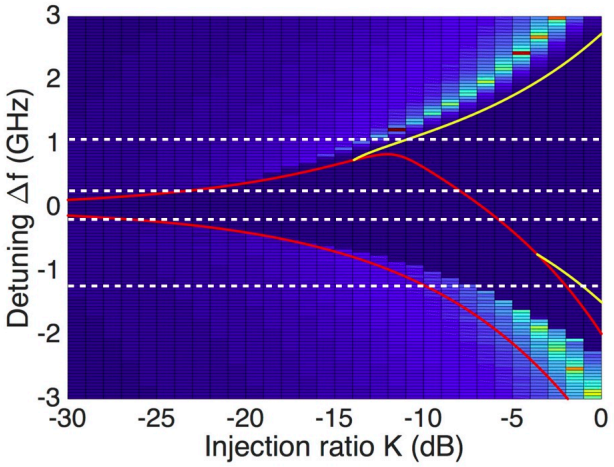

Figure 6.15: Measurement points (in dashed lines) for the numerical time traces of the 12μm QCL under optical injection represented in Figure 7.22 for $\alpha = 1.5$ and $I = 1.25$ A.

Figure 7.22 shows the evolution of the photon density time traces with the injection ratio K at several detuning values, calculated using the numerical simulations for $\alpha = 1.5$ and $I = 1.25$ A (see Figure 6.15, where the dashed lines indicates the measurement points). The α-factor value of 1.5 was chosen to best correspond to the QCLs, as measured previously and the bias current was set to observe the richest dynamics, present both Saddle-Node and Hopf curves at positive detuning and Saddle-Node curve with extreme events at negative detuning.

For all the measurement points located inside the locking range (Figures 7.22 c, f, i and l), the laser remains stable, with constant intensity after a short transient regime. There is therefore no unstable locking region, which is consistent with the previous analytical simulations.

Furthermore, the first row of Figure 7.22, corresponding to $\Delta f = +1.05$ GHz, describes

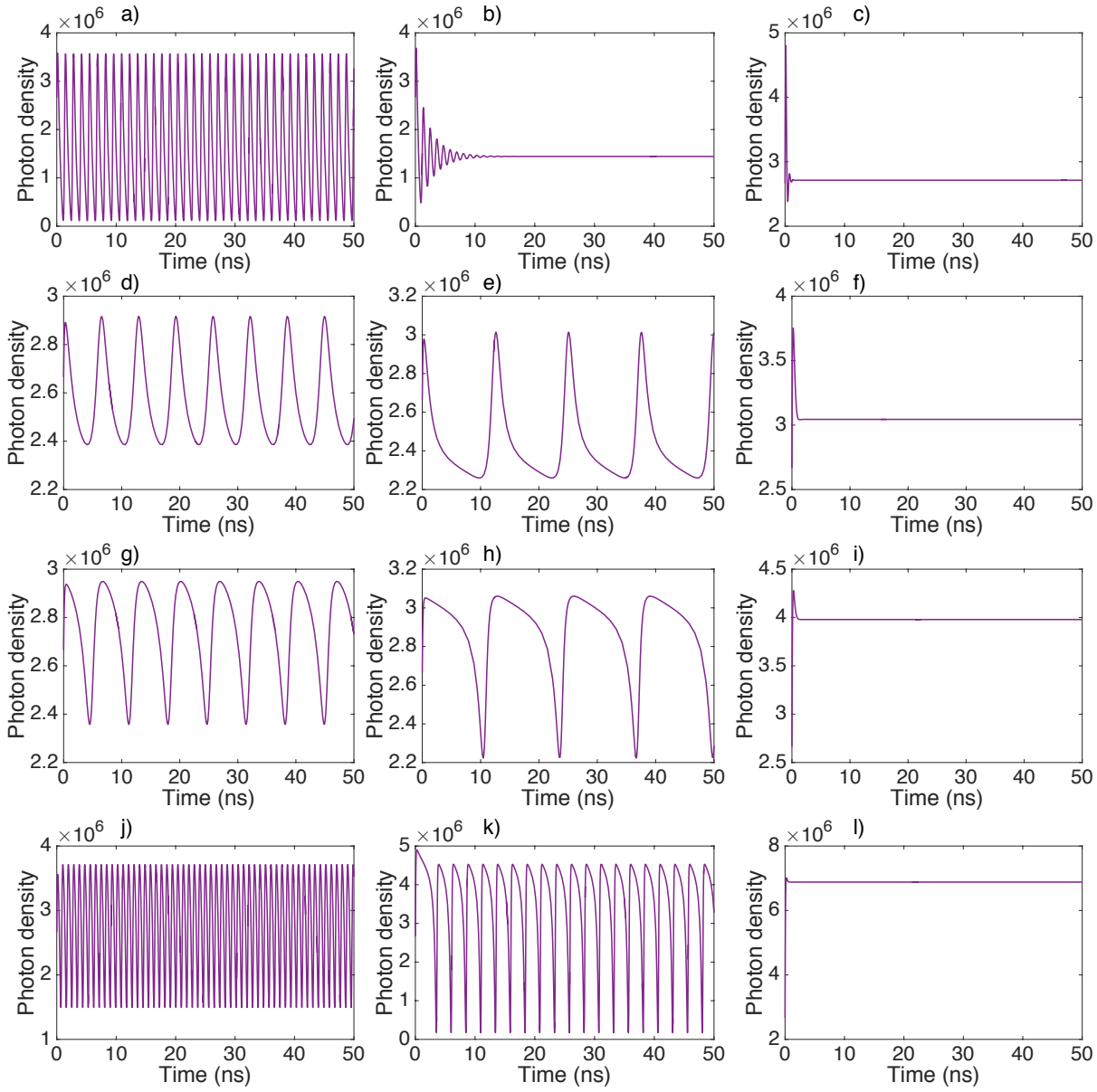

Figure 6.16: Numerical time traces of the photon density for the 12 μm Fabry-Perot QCL subject to optical injection, with $\alpha = 1.5$ and $I = 1.25$ A . First row: $\Delta f = +1.05$ GHz with a) $K = -14$ dB, b) $K = -13$ dB, c) $K = -6$ dB. Second row: $\Delta f = +0.2$ GHz with d) $K = -30$ dB, e) $K = -27$ dB, f) $K = -15$ dB. Third row: $\Delta f = -0.2$ GHz with g) $K = -29$ dB, h) $K = -26$ dB, i) $K = -12$ dB. Fourth row: $\Delta f = -1.2$ GHz with j) $K = -15$ dB, k) $K = -8$ dB, l) $K = -2$ dB.

the behavior along the Hopf curve: the unlocking of the laser occurs through the undamping of periodic sinusoidal oscillations at the detuning frequency (Figure 7.22 a). By adjusting the detuning in this case, it should therefore be possible to adjust the oscillation frequency, and QCLs under optical injection at low bias current and high positive detuning could thus be used as tunable photonic oscillators in the mid-infrared range.

On the other hand, for all other detuning values, the limit of the locking range corresponds to a Saddle-Node bifurcation. The second row corresponds to $\Delta f = +0.2$ GHz, the third row to $\Delta f = -0.2$ GHz and the last one to $\Delta f = -1.2$ GHz. In these cases, the unlocking is characterized by the appearance of small-amplitude periodic fluctuation, whose shape depends on the detuning and injection ratio. For very small injection ratios, these oscillations are sinusoidal, but closer to the limit of the locking range they are peaked on one side, depending on the detuning sign (see e.g. Figure 7.22 e for positive detuning compared to Figure 7.22 h for negative detuning). Moreover, the frequency of the oscillations also depends on the injection parameters since it corresponds to the detuning frequency. The extreme events appearing on this side of the present the same shape and frequency, but with very high intensity and minima close to zero (see Figure 7.22 k).

6.4 Conclusions

According to the numerical simulations and analytical expressions, QCLs can exhibit rich nonlinear dynamics when subjected to optical injection. Furthermore, the dynamical state can be precisely controled by adjusting the laser and injection parameters. It would be interesting to verify these predictions experimentally. Within the locking range, effects similar to that observed in interband lasers are expected, such as sharp linewidth, noise reduction or increase of the modulation bandwidth. However, the master and slave QCLs should be chosen carefully since the locking range is relatively narrow: $\pm$ 3 GHz as obtained typically around $K = -5$ dB corresponds only to $\pm$ 0.1 cm^{-1}.

Furthermore, some period 1 oscillations appear outside the locking range for positive detuning at very low bias currents. These oscillations occur at the detuning frequency, and QCLs under optical injection could therefore be used as tunable photonic oscillators.

Extreme event generation also seem to occur close to the limit of the locking range at low bias current.

Further investigations will conclude on whether a certain range of parameters exists for which some specific microwave oscillations points can be insensitive to the detuning frequency. This has been already proved to be of great importance in diode laser systems where these oscillations points can stabilize the microwave frequency against fluctuations in the detuning frequency. [201, 202].

Chapter 7

Conclusions and perspectives

The studies presented in this thesis have shown that QCLs are sensitive to external perturbations such as optical feedback. As in interband lasers, depending on the external cavity length and the feedback ratio, the output power of both Fabry-Perot and DFB QCLs emitting around 5.6 μm can be increased and the threshold current significantly reduced. Furthermore, when increasing the feedback ratio at fixed external cavity length, the QCL undergoes five regimes characterized by their optical spectra: the QCL emission will evolve from stable and single-mode to a beating between two modes, and then to a single-mode regime again but where the QCL operates on a mode different from the free-running one. Afterwards, the QCL enters an unstable regime, recognized on the optical spectra by an strong increase of the pedestal and a rise of the side-modes. Finally, at very high feedback ratios, the QCL is stable and single-mode again. These regimes are similar to that observed in laser diodes, but they appear at much higher feedback ratios, and the fourth unstable regime is narrower, the QCLs are therefore much more resistant to optical feedback.

From a dynamical viewpoint, both the experimental bifurcation diagram and the numerical verification using the Lang and Kobayashi rate equations prove that the QCL can oscillate periodically at the external cavity frequency and even become chaotic under some feedback conditions. The observed chaos, which takes the shape of low-frequency fluctuations, and the absence of dynamical features at the relaxation oscillation frequency, consistent with the absence of such oscillations in the modulation response of QCLs, leads to the conclusion that the QCLs experience a class A-like dynamical scenario when subjected to optical feedback, i.e. a scenario that was only observed in gas lasers before.

Although these low frequency fluctuations can only be observed close above threshold at reasonable feedback ratios that can be achieved experimentally, the fact that chaos may occur in QCLs under optical feedback furthermore proves that the above-threshold room-temperature α-factor of mid-infrared QCLs is not zero, contrary to what was predicted theoretically. This important parameter was measured using two techniques based on optical feedback, self-mixing interferometry and wavelength evolution at low feedback ratios, resulting in values ranging from 0.8 to 2.9 strongly dependent on the bias current. Values of α-factor around 1.5 relatively close to threshold result in an excellent agreement between experiments and simulations. These effective α-factor values are consistent with other measurements realized above threshold and at room temperature, and the threshold limit of $\alpha_0 = 0.4$ is consistent with the material α-factor measurements performed with other methods on similar structures. The strong dependence with the bias current moreover leads to a very high value of the gain compression coefficient for the studied QCL structure of $\epsilon_S = 4.5 \times 10^{-15}$ cm^3, which would be consistent with the very high spatial hole burning reported in mid-infrared QCLs but needs to be confirmed by other methods.

Optical feedback was also applied to 32 μm-wide BA QCLs emitting around 4.6 μm, which present excellent performances in terms of both output power and heat-load dissipation. In this case, the position of the reinjected beam along the laser facet becomes an important parameter. Depending on the feedback mirror angle, the beam profile of the laser can be strongly improved, in particular with the suppression of spatial nonlinear effects such as beam steering and a tendency to operate on the fundamental transverse mode, enhanced by the use of spatial filtering. On the other hand, optical feedback can also excite higher order modes, suggesting the appearance of filamentation in QCLs with lower quality of fabrication. However, a dynamical study remains necessary in order to fully understand the impact of optical feedback on BA QCLs.

The consequences of the sensitivity of QCLs to optical feedback is twofold. First, unwanted optical feedback originating from parasitic reflections on the experimental setup can deteriorate the emission purity and must be avoided, especially for applications such as gas spectroscopy. In particular, it has been shown that vertically-cleaved mid-infrared chalco-

genide fibers can result in feedback ratios as high as 15%. To prevent this parasitic optical feedback, the development of low-cost and compact mid-infrared optical isolators that could be included in QCL packages is necessary.

However, studying optical feedback can lead to a better understanding of the QCLs. Applying optical feedback indeed enables to extract key laser parameters such as the α-factor or the gain compression coefficient ϵ_S. In order to fully validate these measurements, it would be important to retrieve the α-factor of one single laser using all possible methods (Hakki-Paoli, FM-AM ratio...). A collaboration recently started with the Materials and Engineering Research Institute of Sheffield Hallam University to model the α-factor of QCLs by calculating the Green functions, in order to better understand its non-zero value. For the gain compression coefficient, finding another method, either experimental or numerical, would be necessary to validate the obtained value, which could not be verified.

Furthermore, the next step in this work will be to study the impact of optical feedback on other mid-infrared QCL structures. According to previous experiments realized on interband lasers, the response of the laser to optical feedback varies significantly with the device parameters, such as design, wavelength, dimensions, DFB grating parameters... The impact of optical feedback on the QCL linewidth and modulation response will also be investigated, where a significant linewidth reduction in regimes I and III, as well as increase of the cut-off frequency of the QCL under modulation are expected. This study will lead to a better understanding of optical feedback, but also of the QCLs themselves, and eventually will lead to selection rules for designing feedback-resistant QCLs.

Afterwards, when this phenomenon is fully understood, QCLs under optical feedback could be used for practical applications. It has been shown that a controlled use of optical feedback can greatly improve the QCL properties and for instance, BA QCLs with good beam quality would be of interest for applications requiring high output power. Future work on this topic would include dynamical studies of BA QCLs under optical feedback, far-field measurements, as well as shaping of the spatial filter in order to further optimize the beam profile.

Using Fourier or Talbot cavities, with optical feedback originating from partial reflection of the light emitted by a laser array on either a lens or a tilted mirror, has proven useful

to phase-lock the lasers, and achieve coherent light emission from a laser array, with good beam quality and very high output power [203]. This technique could be applied to QCL arrays in order to obtain high performances at mid-infrared wavelength.

The possibility of chaotic operation in QCLs furthermore suggests new applications for these devices, such as chaotic LIDAR, unpredictable optical countermeasures or secured free-space communications. For the latter, the possibility of chaos synchronization will first have to be demonstrated, before applying it to secured transmission of information. Further development would also include integrated solutions where a QCL and a feedback mirror will be aligned in a single package, or even monolithic sources with careful control of the feedback ratio, to provide performant mid-infrared sources ready to be used in these applications.

It would moreover be interesting to investigate experimentally the impact of optical injection on QCLs. According to the simulations, mid-infrared QCLs are sensitive to optical injection as well, and can be locked over a wide range of frequencies. In the locking range, if the response of QCLs to optical injection is similar to that of near-infrared laser diodes, which should be the case, the slave QCL properties should be significantly enhanced. In particular, a tremendous increase of the modulation bandwidth would be expected. Furthermore, the dynamics predicted outside the locking range, with periodic oscillations whose frequency can be controlled by adjusting the injection parameters, and high intensity events occurring alongside the Hopf bifurcation, would lead to new QCL applications. For instance, one can imagine a tunable photonic oscillator in the mid-infrared based on a periodically oscillating QCL, or extreme events generation. A preliminary study equivalent to that described in this thesis for optical feedback should therefore be performed in the case QCLs of subjected to optical injection.

Furthermore, optical injection can be used to generate four-wave mixing in laser diodes [40]. Since the third-order nonlinear susceptibility is large in QCLs (typically $\chi^{(3)} \sim 10^{-16}$ cm^2/V^2 in [164]), the four-wave mixing mechanism occurs over a wide range of wavelengths, and can be used for phase locking or ultra-fast wavelength conversion.

Optical injection can also be used to control the pulses and limit the temporal jitter in mode-locked semiconductor lasers [204]. The interest for mode-locked QCLs is growing [205],

for applications such as stable ultra-fast pulses or frequency comb generation, and optical injection could be of interest for these structures as well.

Moreover, mutually-coupled QCLs could lead to complex dynamics, and might result to similar behaviors as optical injection. Although this coupling of both lasers into one another is difficult to model and to fully understand, it is much easier to implement experimentally, since no optical isolator is required.

Finally, THz QCLs present a faster upper-state lifetime and a lower α-factor, resulting in dynamics different from the ones observed in mid-infrared structures, such as modelocking or ultrafast pulse generation [206]. Furthermore, novel QCL-based devices have recently been proposed, with the first demonstration of QCL on silicon [207] for monolithic integration, or with numerical studies on quantum-dot QCLs, which would present much lower threshold current densities [208] or would lead to THz QCLs operating at room-temperature [209]. These structures may lead to new dynamics when subjected to optical feedback or optical injection, that do not appear in standard mid-infrared QCL devices, and result in novel applications.

Bibliography

[1] A. Kosterev, G. Wysocki, Y. Bakhirkin, S. So, R. Lewicki, M. Fraser, F. Tittel, and R. Curl, "Application of quantum cascade lasers to trace gas analysis," *Appl. Phys. B*, vol. 90, no. 2, pp. 165–176, 2008.

[2] A. Majumdar and J. Ricklin, *Free-Space Laser Communications: Principles and Advances*. Springer, 2010.

[3] C. K. N. Patel, "Interpretation of CO_2 optical maser experiments," *Phys. Rev. Lett.*, vol. 12, no. 21, pp. 588–590, 1964.

[4] S. Sanders, R. J. Lang, L. E. Myers, M. M. Fejer, and R. L. Byer, "Broadly tunable mid-IR radiation source based on difference frequency mixing of high power wavelength-tunable laser diodes in bulk periodically poled $LiNbO_3$," *Electron. Lett.*, vol. 32, no. 3, pp. 218–219, 1996.

[5] M. M. J. W. van Herpend, S. E. Bisson, A. K. Y. Ngai, and F. J. M. Harren, "Combined wide pump tuning and high power of a continuous-wave, singly resonant optical parametric oscillator," *Appl. Phys. B*, vol. 78, pp. 281–286, 2004.

[6] D. L. Partin, "Lead salt quantum effect structures," *IEEE J. Quantum Electron.*, vol. 24, no. 8, pp. 1716–1726, 1988.

[7] M. Tacke, "Lead-salt lasers," *Phil. Trans. R. Soc. Lond. A*, vol. 359, pp. 547–566, 2001.

[8] J. G. Kim, L. Shterengas, R. U. Martinelli, and G. L. Belenky, "High-power room-temperature continuous wave operation of 2.7 and 2.8 μm In(Al)GaAsSb/GaSb diode lasers," *Appl. Phys. Lett.*, vol. 83, no. 10, pp. 1926–1928, 2003.

[9] C. L. Canedy, W. W. Bewley, J. R. Lindle, I. Vurgaftman, C. S. Kim, M. Kim, and J. R. Meyer, "High-power continuous-wave midinfrared type-II "W" diode lasers," *Appl. Phys. Lett.*, vol. 86, p. 211105, 2005.

[10] C. H. Lin, R. Q. Yang, D. Zhang, S. J. Murry, S. S. Pei, A. A. Allerman, and S. R. Kurtz, "Type-II interband quantum cascade laser at 3.8 μm," *Electron. Lett.*, vol. 33, no. 7, pp. 598–599, 1997.

[11] R. Q. Yang, "Infrared laser based on intersubband transitions in quantum wells," *Superlatt. Microstruct.*, vol. 17, no. 1, pp. 77–83, 1995.

[12] C. Li, L. Dong, C. Zheng, and F. K. Tittel, "Compact TDLAS based optical sensor for ppb-level ethane detection by use of a 3.34 μm room-temperature CW interband cascade laser," *Sensor. Actuat. B-Chem.*, vol. 232, pp. 188–194, 2016.

[13] J. Faist, *Quantum Cascade Lasers.* Oxford University Press, 2013.

[14] R. F. Kazarinov and R. A. Suris, "Possibility of the amplification of electromagnetic waves in a semiconductor with a superlattice," *Sov. Phys. Semicond.*, vol. 5, no. 4, pp. 707–709, 1971.

[15] J. Faist, F. Capasso, D. L. Sivco, C. Sirtori, A. L.Hutchinson, and A. Y. Cho, "Quantum Cascade Laser," *Science*, vol. 264, no. 5158, pp. 553–556, 1994.

[16] M. Beck, D. Hofstetter, T. Aellen, J. Faist, U. Oesterle, M. Ilegems, E. Gini, and H. Melchior, "Continuous wave operation of a mid-infrared semiconductor laser at room temperature," *Science*, vol. 295, pp. 301–305, 2002.

[17] M. Razeghi, S. Slivken, Y. Bai, B. Gokden, and S. R. Darvish, "High power quantum cascade lasers," *New Journal of Physics*, vol. 11, no. 12, p. 125017, 2009.

[18] Y. Bai, N. Bandyopadhyay, S. Tsao, S. Slivken, and M. Razeghi, "Room temperature quantum cascade lasers with 27% wall plug efficiency," *Appl. Phys. Lett.*, vol. 98, p. 181102, 2011.

[19] M. S. Vitiello, G. Scalari, B. Williams, and P. D. Natale, "Quantum cascade lasers: 20 years of challenges," *Opt. Express*, vol. 23, no. 4, pp. 5167–5182, 2015.

[20] R. Koehler, A. Tredicucci, F. Beltram, H. E. Beere, E. Linfield, A. Davies, D. Ritchie, R. Iotti, and F. Rossi, "Terahertz semiconductor-heterostructure laser," vol. 417, pp. 156–159, 2002.

[21] A. Wade, G. Fedorov, D. Smirnov, S. Kumar, B. S. Williams, Q. Hu, and J. L. Reno, "Magnetic-field-assisted terahertz quantum cascade laser operating up to 225 K," *Nat. Photon.*, vol. 3, pp. 41–45, 2009.

[22] M. Belkin, F. Capasso, F. Xie, A. Belyanin, M. Fischer, A. Wittmann, and J. Faist, "Room temperature terahertz quantum cascade laser source based on intracavity difference frequency generation," *Appl. Phys. Lett.*, vol. 92, no. 201101, 2008.

[23] J. Devenson, O. Cathabard, R. Tessier, and A. N. Baranov, "InAs/AlSb quantum cascade laser emitting at 2.75 -2.97 μm," *Appl. Phys. Lett.*, vol. 91, p. 251102, 2007.

[24] C. Gmachl, F. Capasso, D. L. Sivco, and A. Y. Cho, "Recent progress in quantum cascade lasers and applications," *Rep. Prog. Phys.*, vol. 64, no. 11, p. 1533, 2001.

[25] G. Bastard, *Wave mechanics applied to semiconductor heterostructures.* Les éditions de physique, Paris, 1990.

[26] R. Maulini, "Broadly tunable mid-infrared quantum cascade laser for spectroscopic applications," Ph.D. dissertation, Université de Neuchâtel, 2006.

[27] G. Maisons, "Réalisation de sources lasers monomodes innovantes émettant dans le moyen infrarouge. Application à la spectroscopie." Ph.D. dissertation, Université de Grenoble, 2010.

[28] Y. Petitjean, F. Destic, J. C. Mollier, and C. Sirtori, "Dynamic modeling of terahertz quantum cascade lasers," *IEEE J. Sel. Top. Quantum Electron.*, vol. 17, no. 1, pp. 22–29, 2011.

[29] G. Agrawal, *Long-wavelength semiconductor lasers*, ser. Van Nostrand Reinhold Electrical/Computer Science and Engineering Series. Springer Netherlands, 1986.

[30] F. Rana and R. J. Ram, "Current noise and photon noise in quantum cascade lasers," *Phys. Rev. B*, vol. 65, pp. 125 313–125 342, 2002.

[31] R. Paiella, R. Martini, F. Capasso, C. Gmachl, H. Y. Hwang, D. L. Sivco, J. N. Baillargeon, A. Y. Cho, E. A. Whittaker, and H. C. Liu, "High-frequency modulation without the relaxation oscillation resonance in quantum cascade lasers," *Appl. Phys. Lett.*, vol. 79, no. 16, pp. 2526–2528, 2001.

[32] A. L. Schawlow and C. H. Townes, "Infrared and optical masers," *Phys. Rev.*, vol. 112, no. 6, pp. 1940–1949, 1958.

[33] M. Lax, "Quantum noise. X. Density-matrix treatment of field of population difference fluctuations," *Phys. Rev.*, vol. 157, no. 2, pp. 213–231, 1967.

[34] H. Haug and H. Haken, "Theory of noise in semiconductor laser emission," *Z. Phys.*, vol. 204, pp. 262–275, 1967.

[35] C. H. Henry, "Theory of the linewidth of semiconductor lasers," *IEEE J. Quantum Electron.*, vol. 18, pp. 259–264, 1982.

[36] J. R. Marciante and G. P. Agrawal, "Nonlinear mechanisms of filamentation in broad-area semiconductor lasers," *IEEE J. Quantum Electron.*, vol. 32, no. 4, pp. 590–596, 1996.

[37] M. Osinski and J. Buus, "Linewidth broadening factor in semiconductor lasers - an overview," *IEEE J. Quantum Electron.*, vol. 23, no. 1, pp. 9–29, 1987.

[38] B. W. Hakki and T. L. Paoli, "Gain spectra in GaAs double heterostructure injection lasers," *J. Appl. Phys.*, vol. 46, no. 3, pp. 1299–1306, 1975.

[39] I. D. Henning and J. Collins, "Measurement of the semiconductor linewidth broadening factor," *Electron. Lett.*, vol. 19, no. 22, pp. 927–929, 1983.

[40] H. Huang, K. Schires, P. J. Poole, and F. Grillot, "Non-degenerate four-wave mixing in an optically injection-locked InAs/InP quantum dot Fabry-Perot laser," *Appl. Phys. Lett.*, vol. 106, p. 143501, 2015.

[41] T. C. Newell, D. J. Bossert, A. Stintz, B. Fuchs, K. J. Malloy, and L. F. Lester, "Gain and linewidth enhancement factor in InAs quantum-dot laser diodes," *IEEE Photon. Technol. Lett.*, vol. 11, no. 12, pp. 1527–1529, 1999.

[42] J. G. Provost and F. Grillot, "Measuring the chirp and the linewidth enhancement factor of optoelectronic devices with a Mach-Zehnder interferometer," *IEEE Photon. J.*, vol. 3, no. 3, pp. 476–488, June 2011.

[43] K. E. Chlouverakis, K. M. Al-Aswad, I. D. Henning, and M. J. Adams, "Determining laser linewidth parameter from hopf bifurcation minimum in lasers subject to optical injectio," *Electron. Lett.*, vol. 39, no. 16, pp. 1185–1187, 2003.

[44] C. Wang, K. Schires, M. Osinski, P. J. Poole, and F. Grillot, "Thermally insensitive determination of the linewidth broadening factor in nanostructured semiconductor lasers using optical injection locking," *Sci. Rep.*, vol. 6, p. 27825, 2016.

[45] C. Wang, "Modulation dynamics of InP-based nanostructure laser and quantum cascade laser," Ph.D. dissertation, INSA Rennes, 2015.

[46] B. Dagens, A. Markus, J. X. Chen, J.-G. Provost, D. Make, O. L. Gouezigou, J. landreau, A. Fiore, and B. Thedrez, "Giant linewidth enhancement factor and purely frequency modulated emission from quantum dot laser," *Electron. Lett.*, vol. 41, no. 6, pp. 323–324, 2005.

[47] M. Lerttamrab, S. L. Chuang, C. Gmachl, D. L. Sivco, F. Capasso, and A. Y. Cho, "Linewidth enhancement factor of a type-I quantum cascade laser," *J. Appl. Phys.*, vol. 94, no. 8, pp. 5426–5428, 2003.

[48] J. Kim, M. Lerttamrab, S. L. Chuang, C. Gmachl, D. L. Sivco, F. Capasso, and A. Y. Cho, "Theoretical and experimental study of optical gain and linewidth enhancement factor of type I quantum cascade lasers," *IEEE J. Quantum Electron.*, vol. 40, no. 12, pp. 1663–1674, 2004.

[49] T. Liu, K. E. Lee, and Q. J. Wang, "Importance of the microscopic effects on the linewidth enhancement factor of quantum cascade lasers," *Opt. Express*, vol. 21, no. 23, pp. 27 804–27 815, 2013.

[50] A. Gordon, C. Y. Wang, L. Diehl, F. X. Kärtner, A. Belyanin, D. Bour, S. Corzine, G. Höfler, H. C. Liu, H. Scneider, T. Maier, M. Troccoli, J. Faist, and F. Capasso, "Multimode regimes in quantum cascade lasers: From coherent instabilities to spatial hole burning," *Phys. Rev. A*, vol. 77, p. 053804, 2008.

[51] A. Hangauer and G. Wysocki, "Gain compression and linewidth enhancement factor in mid-IR quantum cascade lasers," *IEEE J. Sel. Top. Quantum Electron.*, vol. 21, no. 6, p. 1200411, 2015.

[52] J. von Staden, T. Gensty, M. Peil, W. Elsässer, G. Giuliani, and C. Mann, "Measurements of the α factor of a distributed-feedback quantum cascade laser by an optical feedback self-mixing technique," *Opt. Lett.*, vol. 31, no. 17, pp. 2574–2576, 2006.

[53] T. Aellen, R. Maulini, R. Terazzi, N. Hoyler, M. Giovannini, J. Faist, S. Blaser, and L. Hvozdara, "Direct measurement of the linewidth enhancement factor by optical heterodyning of an amplitude-modulated quantum cascade laser," *Appl. Phys. Lett.*, vol. 89, p. 091121, 2006.

[54] A. Evans, J. S. Yu, J. David, L. Doris, K. Mi, S. Slivken, and M. Razeghi, "High-temperature, high-power, continuous-wave operation of buried heterostructure quantum-cascade lasers," *Appl. Phys. Lett.*, vol. 84, no. 3, pp. 314–316, 2004.

[55] M. Carras, G. Maisons, B. Simozrag, M. Garcia, O. Parillaud, J. Massies, and X. Marcadet, "Room-temperature continuous-wave metal grating distributed feedback quantum cascade lasers," *Appl. Phys. Lett.*, vol. 96, no. 16, p. 161105, 2010.

[56] A. Szerling, P. Karbownik, K. Kosiel, J. Kubacka-Traczyk, E. Pruszynska-Karbownik, M. Pluska, and M. Bugajski, "Mid-infrared GaAs/AlGaAs quantum cascade lasers technology," *Acta Phys. Pol. A*, vol. 116, pp. S45 – S48, 2009.

[57] V. Trinité, E. Ouerghemmi, V. Guériaux, M. Carras, A. Nedelcu, E. Costard, and J. Nagle, "Modelling of electronic transport in quantum well infrared photodetectors," *Infrared Phys. Techn.*, vol. 54, no. 3, pp. 204 – 208, 2011.

[58] E. Benveniste, S. Laurent, A. Vasanelli, C. Manquest, C. Sirtori, F. Teulon, M. Carras, and X. Marcadet, "Measurement of gain and losses of a mid-infrared quantum cascade laser by wavelength chirping spectroscopy," *Appl. Phys. Lett.*, vol. 94, p. 081110, 2009.

[59] K. Petermann, *Laser diode modulation and Noise*. Springer, 1988.

[60] C. Juretzka, H. Simos, A. Bogris, D. Syvridis, W. Elsaber, and M. Carras, "Intensity noise properties of mid-infrared injection locked quantum cascade lasers: II. Experiments," *IEEE J. Quantum Electron.*, vol. 51, no. 1, pp. 1–8, 2015.

[61] R. F. Broom, E. Mohn, C. Risch, and R. Salathe, "Microwave self-modulation of a diode laser coupled to an external cavity," *IEEE J. Quantum Electron.*, vol. 6, no. 6, pp. 328–334, 1970.

[62] I. Ikushima and M. Maeda, "Self-coupled phenomena of semiconductor lasers caused by an optical fiber," *IEEE J. Quantum Electron.*, vol. 14, no. 5, pp. 331–332, 1978.

[63] D. M. Kane and K. A. Shore, *Unlocking dynamical diversity : Optical feedback effects on semiconductor lasers*. Wiley Chichester, 2005.

[64] T. H. Maiman, R. H. Hoskins, I. J. D'Haenens, C. K. Asawa, and V. Evtuhov, "Stimulated optical emission in fluorescent solids. II. Spectroscopy and stimulated emission in ruby," *Phys. Rev.*, vol. 123, p. 1151, 1961.

[65] S. H. Strogatz, *Nonlinear dynamics and chaos*. Perseus Books, 1994.

[66] E. Rosencher and B. Vinter, *Optoelectronics*. Cambridge University Press, 2002.

[67] F. T. Arecchi, G. L. Lippi, G. P. Puccioni, and J. R. Tredicce, "Deterministic chaos in lasers with injected signal," *Opt. Commun.*, vol. 51, no. 5, pp. 308–314, Oct 1984.

[68] C. O. Weiss, W. Klische, P. S. Ering, and M. Cooper, "Instabilities and chaos of a single mode NH_3 ring laser," *Opt. Commun.*, vol. 52, no. 6, pp. 405–408, 1985.

[69] F. T. Arecchi, R. Meucci, G. Puccioni, and J. Tredicce, "Experimental evidence of subharmonic bifurcations, multistability and turbulence in a Q-switched gas laser," *Phys. Rev. Lett.*, vol. 49, no. 17, pp. 1217–1220, 1982.

[70] M. Vitre, K. Panajotov, H. Thienpont, and M. Sciamanna, "Deterministic polarization chaos in a laser diode," *Nat. Photon.*, vol. 7, no. 1, pp. 60–65, 2013.

[71] C. O. Weiss, A. Godone, and A. Olafsson, "Routes to chaotic emission in a cw He-Ne laser," *Phys. Rev. A*, vol. 28, no. 2, pp. 892–895, 1983.

[72] F. Favre, D. L. Guen, and J.-C. Simon, "Optical feedback effects upon laser diode oscillation field spectrum," *IEEE T. Microw. Theory*, vol. 30, no. 10, pp. 1700–1705, 1982.

[73] L. Goldberg, H. F. Taylor, A. Dandridge, J. F. Weller, and R. Miles, "Spectral characteristics of semiconductor lasers with optical feedback," *IEEE J. Quantum Electron.*, vol. 18, no. 4, pp. 555–564, 1982.

[74] R. W. Tkach and A. R. Chraplyvy, "Regimes of feedback effects in 1.5 μm distributed feedback lasers," *J. Lightwave Technol.*, vol. 4, no. 11, pp. 1655–1661, 1986.

[75] Y. C. Chung and Y. H. Lee, "Spectral characteristics of vertical-cavity surface-emitting lasers with external optical feedback," *IEEE Photon. Technol. Lett.*, vol. 3, no. 7, pp. 597–599, 1991.

[76] S. Donati and R. H. Hong, "The diagram of feedback regimes revisited," *IEEE J. Sel. Top. Quantum Electron.*, vol. 19, no. 4, p. 1500309, 2013.

[77] J. S. Lawrence, D. M. Kane, and P. S. Spencer, "Suppression of coherence collapse in semiconductor diode lasers with short external cavities," in *Advanced Semiconductor Lasers and Their Applications*, no. 67. OSA Trends in Optics and Photonics, 1999.

[78] R. Lang and K. Kobayashi, "External optical feedback effects on semiconductor injection laser properties," *IEEE J. Quantum Electron.*, vol. 16, no. 3, pp. 347–355, 1980.

[79] F. Grillot, "On the effects of an antireflection coating impairment on the sensitivity to optical feedback of AR/HR semiconductor DFB lasers," *IEEE J. Quantum Electron.*, vol. 45, no. 6, pp. 720–729, 2009.

[80] H. Olesen, J. H. Osmundsen, and B. Tromborg, "Nonlinear dynamics and spectral behavior for an external cavity laser," *IEEE J. Quantum Electron.*, vol. 22, no. 6, pp. 762–773, 1986.

[81] J. Mork, M. Semkow, and B. Tromborg, "Measurement and theory of mode hopping in external cavity lasers," *Electron. Lett.*, vol. 26, no. 9, pp. 609–610, 1990.

[82] J. Osmundsen and N. Gade, "Influence of optical feedback on laser frequency spectrum and threshold conditions," *IEEE J. Quantum Electron.*, vol. 19, no. 3, pp. 465–469, 1983.

[83] G. P. Agrawal, "Line narrowing in a single-mode injection laser due to external optical feedback," *IEEE J. Quantum Electron.*, vol. 20, no. 5, pp. 468–471, 1984.

[84] K. Petermann, "External optical feedback phenomena in semiconductor lasers," *IEEE J. Sel. Top. Quantum Electron.*, vol. 1, no. 2, pp. 480–489, 1995.

[85] N. Schunk and K. Petermann, "Numerical analysis of the feedback regimes for a single-mode semiconductor laser with external feedback," *IEEE J. Quantum Electron.*, vol. 24, no. 7, pp. 1242–1247, 1988.

[86] C. H. Henry and R. F. Kazarinov, "Instability of semiconductor lasers due to optical feedback from distant reflectors," *IEEE J. Quantum Electron.*, vol. 22, no. 2, pp. 294–301, 1986.

[87] A. M. Levine, G. H. M. van Tartwijk, D. Lenstra, and T. Erneux, "Diode lasers with optical feedback: Stability of the maximum gain mode," *Phys. Rev. A*, vol. 52, no. 5, pp. R3436–R3439, 1995.

[88] D. Lenstra, B. Verbeek, and A. D. Boef, "Coherence collapse in single-mode semiconductor lasers due to optical feedback," *IEEE J. Quantum Electron.*, vol. 21, no. 6, pp. 674–679, 1985.

[89] H. Kakiuchida and J. Ohtsubo, "Characteristics of a semiconductor laser with external feedback," *IEEE J. Quantum Electron.*, vol. 30, no. 9, pp. 2087–2097, 1994.

[90] P. M. Alsing, V. Kovanis, A. Gavrielides, and T. Erneux, "Lang and Kobayashi phase equation," *Phys. Rev. A*, vol. 53, no. 6, pp. 4429–4434, 1996.

[91] A. Hohl and A. Gavrielides, "Bifurcation cascade in a semiconductor laser subject to optical feedback," *Phys. Rev. Lett.*, vol. 82, pp. 1148–1151, 1999.

[92] A. T. Ryan, G. P. Agrawal, G. R. Gray, and E. C. Gage, "Optical-feedback-induced chaos and its control in multimode semiconductor lasers," *IEEE J. Quantum Electron.*, vol. 30, no. 3, pp. 668–679, 1994.

[93] J. Y. Law and G. P. Agrawal, "Effect of optical feedback on static and dynamic characteristics of vertical-cavity surface-emitting lasers," *IEEE J. Sel. Top. Quantum Electron.*, vol. 3, no. 2, pp. 353–358, 1997.

[94] J. Mork, B. Tromborg, and J. Mark, "Chaos in semiconductor lasers with optical feedback: Theory and experiment," *IEEE J. Quantum Electron.*, vol. 28, no. 1, pp. 93–108, 1992.

[95] T. Mukai and K. Otsuka, "New route to optical chaos: successive-subharmonic-oscillation cascade in a semiconductor laser coupled to an external cavity," *Phys. Rev. Lett.*, vol. 55, no. 17, pp. 1711–1714, 1985.

[96] T. Heil, I. Fischer, and W. Elsässer, "Dynamics of semiconductor lasers subject to delayed optical feedback: The short cavity regime," *Phys. Rev. Lett.*, vol. 87, no. 24, p. 243901, 2001.

[97] R. J. Jones, P. S. Spencer, J. Lawrence, and D. M. Kane, "Influence of external cavity length on the coherence collapse regime in laser diodes subject to optical feedback," *Optoelectronics, IEE Proceedings*, vol. 148, no. 1, pp. 7–12, 2001.

[98] O. Ushakov, S. Bauer, O. Brox, H. J. Wünsche, and F. Henneberger, "Dynamics of lasers with ultra-short optical feedback," *Proc. SPIE*, vol. 5349, p. 348, 2004.

[99] M. Sciamanna, P. Mégret, and M. Blondel, "Hopf bifurcation cascade in small-α laser diodes subject to optical feedback," *Phys. Rev. E*, vol. 69, p. 046209, 2004.

[100] J. Ohtsubo, "Feedback induced instability and chaos in semiconductor lasers and their applications," *Opt. Rev.*, vol. 6, no. 1, pp. 1–15, 1999.

[101] G. C. Dente, P. S. Durkin, K. A. Wilson, and C. E. Moeller, "Chaos in the coherence collapse of semiconductor lasers," *IEEE J. Quantum Electron.*, vol. 24, no. 12, pp. 2441–2447, 1988.

[102] F. Grillot, N. A. Naderi, M. Pochet, C. Y. Lin, and L. F. Lester, *Semiconductor Technologies*. InTech, 2010, ch. The critical feedback level in nanostructure-based semiconductor lasers.

[103] T. Heil, I. Fischer, and W. Elsässer, "Coexistence of low-frequency fluctuations and stable emission on a single high-gain mode in semiconductor lasers with external optical feedback," *Phys. Rev. A*, vol. 58, no. 4, p. R2672, 1998.

[104] J. Mork, B. Tromborg, and P. L. Christiansen, "Bistability and low-frequency fluctuations in semiconductor lasers with optical feedback: A theoretical analysis," *IEEE J. Quantum Electron.*, vol. 24, no. 2, pp. 123–133, 1988.

[105] T. Sano, "Antimode dynamics and chaotic itinerancy in the coherence collapse of semiconductor lasers with optical feedback," *Phys. Rev. A*, vol. 50, no. 3, pp. 2719–2726, 1994.

[106] D. W. Sukow, J. R. Gardner, and D. J. Gauthier, "Statistics of power-dropout events in semiconductor lasers with time-delayed optical feedback," *Phys. Rev. A*, vol. 56, pp. R3370–R3373, 1997.

[107] P. Besnard, B. Meziane, and G. Stephan, "Feedback phenomena in a semiconductor laser induced by distant reflectors," *IEEE J. Quantum Electron.*, vol. 29, no. 5, pp. 1271–1284, 1993.

[108] J. Sacher, W. Elsässer, and E. O. Göbel, "Intermittency in coherence collapse of a semiconductor laser with external feedback," *Phys. Rev. Lett.*, vol. 63, no. 20, pp. 2224–2227, 1989.

[109] M. C. Eguia and G. B. Mindlin, "Semiconductor laser with optical feedback: From excitable to deterministic low-frequency fluctuations," *Phys. Rev. E*, vol. 60, pp. 1551–1557, 1999.

[110] K. Panajotov, M. Sciamanna, M. A. Arteaga, and H. Thienpont, "Optical feedback in Vertical-Cavity Surface-Emitting Lasers," *J. Sel. Top. Quantum Electron.*, vol. 19, no. 4, p. 1700312, 2013.

[111] F. Kuwashima, T. Ichikawa, I. Kitazima, and H. Iwasawa, "Chaotic oscillations in single-mode class A He-Ne Laser (6328A) II," *Jpn. J. Appl. Phys.*, vol. 38, no. 11, pp. 6321–6326, 1999.

[112] F. Kuwashima, I. Kitazima, and H. Iwasawa, "Theory of chaotic dynamics on class A laser with optical delayed feedback," *Jpn. J. Appl. Phys.*, vol. 40, no. 2R, p. 601, 2001.

[113] D. Pieroux and P. Mandel, "Bifurcation diagram of a complex delay-differential equation with cubic nonlinearity," *Phys. Rev. E*, vol. 67, p. 056213, 2003.

[114] D. O'Brien, S. P. Hegarty, and G. Huyet, "Sensitivity of quantum-dot semiconductor lasers to optical feedback," *Opt. Lett.*, vol. 29, no. 10, pp. 1072–1074, 2004.

[115] C. Otto, K. Lüdge, E. Viktorov, and T. Erneux, *Nonlinear laser dynamics - From quantums dots to cryptography.* Wiley, 2011, ch. Quantum dot laser tolerance to optical feedback.

[116] K. D. LaViolette, "The impact of Rayleigh backscatter induced noise on QPSK transmission with Fabry-Perot lasers," *IEEE Photon. Technol. Lett.*, vol. 8, pp. 706–708, 1996.

[117] A. Uchida, *Optical communication with chaotic lasers.* Wiley, 2012.

[118] M. Sciamanna and K. A. Shore, "Physics and applications of laser diode chaos," *Nat. Photon.*, vol. 9, pp. 151–162, 2015.

[119] F.-Y. Lin and J.-M. Liu, "Chaotic lidar," *IEEE J. Sel. Top. Quantum Electron.*, vol. 10, no. 5, pp. 991–997, 2004.

[120] ——, "Chaotic radar using nonlinear laser dynamics," *IEEE J. Quantum Electron.*, vol. 40, no. 6, pp. 815–820, 2004.

[121] G. D. VanWiggeren and R. Roy, "Communication with chaotic lasers," *Science*, vol. 279, pp. 1198–1200, 1998.

[122] A. Uchida, K. Amano, M. Inoue, K. Hirano, S. Naito, H. Someya, I. Oowada, T. Kurashige, M. Shiki, S. Yoshimori, K. Yoshimura, and P. Davis, "Fast physical random bit generation with chaotic semiconductor lasers," *Nat. Photon.*, vol. 2, no. 728-732, 2008.

[123] M. C. Soriano, J. Garcia-Ojalvo, C. R. Mirasso, and I. Fischer, "Complex photonics: Dynamics and applications of delay-coupled semiconductor lasers," *Rev. Mod. Phys.*, vol. 85, no. 1, pp. 421–470, 2013.

[124] A. Dejonckheere, F. Duport, A. Smerieri, L. Fang, J.-L. Oudar, M. Haelterman, and S. Massar, "All-optical reservoir computer based on saturation of absorption," *Opt. Express*, vol. 22, no. 9, pp. 10 868–10 881, 2014.

[125] K. Vandoorne, P. Mechet, T. V. Vaerenbergh, M. Fiers, G. Morthier, D. Verstraeten, B. Schrauwen, J. Dambre, and P. Bienstman, "Experimental demonstration of reservoir computing on a silicon photonics chip," *Nat. Commun.*, vol. 5, no. 3541, 2014.

[126] J. Nakayama, K. Kanno, and A. Uchida, "Laser dynamical reservoir computing with consistency: An approach of a chaos mask signal," *Opt. Express*, vol. 24, no. 8, pp. 8679–8692, 2016.

[127] A. Hugi, R. Maulini, and J. Faist, "External cavity quantum cascade laser," *Semicond. Sci. Tech.*, vol. 25, no. 8, p. 083001, 2010.

[128] C. Juretzka, S. Breuer, L. Drzewietzki, F. Schad, M. Carras, and W. Elsässer, "9.5 dB relative intensity noise reduction in quantum cascade laser by detuned loading," *Electron. Lett.*, vol. 49, no. 24, pp. 1548–1550, 2013.

[129] D. Weidmann, K. Smith, and B. Ellison, "Experimental investigation of high-frequency noise and optical feedback effects using a 9.7 μm continuous-wave distributed-feedback quantum-cascade laser," *Appl. Optics*, vol. 46, no. 6, pp. 947–953, 2007.

[130] F. P. Mezzapesa, L. L. Columbo, M. Brambilla, M. Dabbicco, S. Borri, M. S. Vitiello, H. E. Beere, D. A. Ritchie, and G. Scamarcio, "Intrinsic stability of quantum cascade lasers against optical feedback," *Opt. Express*, vol. 21, no. 11, pp. 13 748–13 757, 2013.

[131] L. L. Columbo and M. Brambilla, "Multimode regimes in quantum cascade lasers with optical feedback," *Opt. Express*, vol. 22, no. 9, pp. 10 105–10 118, 2014.

[132] C. Gmachl, F. Capasso, E. E. Narimanov, J. U. Nöckel, A. D. Stone, J. Faist, D. L. Sivco, and A. Y. Cho, "High-power directional emission from microlasers with chaotic resonators," *Science*, vol. 280, no. 5369, pp. 1556–1564, 1998.

[133] L. L. Bonilla and H. T. Grahn, "Non-linear dynamics of semiconductor superlattices," *Rep. Prog. Phys.*, vol. 68, pp. 577–683, 2005.

[134] S. Donati, "Laser interferometry by induced modulation of the cavity field," *J. Appl. Phys.*, vol. 49, no. 2, pp. 495–497, 1978.

[135] G. Giuliani, M. Norgia, S. Donati, and T. Bosch, "Laser diode self-mixing technique for sensing applications," *J. Opt. A : Pure Appl. Opt.*, vol. 4, pp. 283–294, 2002.

[136] Y. Yu, G. Giuliani, and S. Donati, "Measurement of the linewidth enhancement factor of semiconductor lasers based on the optical feedback self-mixing effect," *IEEE Photon. Technol. Lett.*, vol. 16, no. 4, pp. 990–992, 2004.

[137] J. Huang and L. W. Casperson, "Gain and saturation in semiconductor lasers," *Opt. Quant. Electron.*, vol. 25, pp. 369–390, 1993.

[138] F. Grillot, B. Dagens, J.-G. Provost, H. Su, and L. F. Lester, "Gain compression and above-threshold linewidth enhancement factor in 1.3 μm InAs-GaAs quantum-dot lasers," *IEEE J. Quantum Electron.*, vol. 44, no. 10, pp. 946–951, 2008.

[139] F. Girardin, G. H. Duan, and P. Gallion, "Linewidth rebroadening due to nonlinear gain and index induced by carrier heating in strained quantum-well lasers," *IEEE Photon. Technol. Lett.*, vol. 8, no. 3, pp. 334–336, 1996.

[140] L. A. Coldren, S. W. Corzine, and M. L. Mashanovitch, *Diode lasers and photonic integrated circuits*. Wiley, 2012.

[141] J. Troles, Q. Coulombier, G. Canat, M. Duhant, W. Renard, P. Toupin, L. Calvez, G. Renversez, F. Smektala, M. E. Amraoui, J. L. Adam, T. Chartier, D. Mechin, and L. Brilland, "Low loss microstructured chalcogenide fibers for large non linear effects at 1995 nm," *Opt. Express*, vol. 18, pp. 26 647–26 654, 2010.

[142] P. Toupin, L. Brilland, G. Renversez, and J. Troles, "All-solid all-chalcogenide microstructured optical fiber," *Opt. Express*, vol. 21, pp. 14 643–14 648, 2013.

[143] A. Hangauer, G. Spinner, M. Nikodem, and G. Wysocki, "High frequency modulation capabilities and quasi single-sideband emission from a quantum cascade laser," *Opt. Express*, vol. 22, no. 19, pp. 23 439–23 455, 2014.

[144] G. Friart, G. van der Sande, G. Verschaffelt, and T. Erneux, "Analytical stability boundaries for quantum cascade lasers subject to optical feedback," *Phys. Rev. E*, vol. 93, no. 5, p. 052201, 2016.

[145] Y. Bai, S. Slivken, S. Darvish, A. Haddadi, B. Gokden, and M. Razeghi, "High power broad area quantum cascade lasers," *Appl. Phys. Lett.*, vol. 95, no. 22, p. 221104, 2009.

[146] I. Vurgaftman and J. R. Meyer, "Photonic-crystal distributed-feedback quantum cascade lasers," *IEEE J. Quantum Electron.*, vol. 38, no. 6, pp. 592–602, 2002.

[147] B. Gökden, Y. Bai, N. Bandyopadhyay, S. Slivken, and M. Razeghi, "Broad area photonic crystal distributed feedback quantum cascade lasers emitting 34 W at $\lambda \sim 4.36$ μm," *Appl. Phys. Lett.*, vol. 97, no. 13, p. 1112, 2010.

[148] Y. Bai, S. Darvish, S. Slivken, P. Sung, J. Nguyen, A. Evans, W. Zhang, and M. Razeghi, "Electrically pumped photonic crystal distributed feedback quantum cascade lasers," *Appl. Phys. Lett.*, vol. 91, no. 14, p. 141123, 2007.

[149] Q. Lu, W. Zhang, L. Wang, F. Liu, and Z. Wang, "Photonic crystal distributed feedback quantum cascade laser fabricated with holographic technique," *Electron. Lett.*, vol. 45, no. 1, p. 1, 2009.

[150] Y. Bai, S. Slivken, Q. Lu, N. Bandyopadhyay, and M. Razeghi, "Angled cavity broad area quantum cascade lasers," *Appl. Phys. Lett.*, vol. 101, no. 8, p. 081106, 2012.

[151] S. Ahn, C. Schwarzer, T. Zederbauer, D. C. MacFarland, H. Detz, A. M. Andrews, W. Schrenk, and G. Strasser, "High-power, low-lateral divergence broad area quantum cascade lasers with a tilted front facet," *Appl. Phys. Lett.*, vol. 104, no. 5, p. 051101, 2014.

[152] D. Heydari, Y. Bai, N. Bandyopadhyay, S. Slivken, and M. Razeghi, "High brightness angled cavity quantum cascade lasers," *Appl. Phys. Lett.*, vol. 106, no. 9, p. 091105, 2015.

[153] S. Menzel, L. Diehl, C. Pflügl, A. Goyal, C. Wang, A. Sanchez, G. Turner, and F. Capasso, "Quantum cascade laser master-oscillator power-amplifier with 1.5 W output power at 300 K," *Opt. Express*, vol. 19, no. 17, pp. 16 229–16 235, 2011.

[154] A. Lyakh, R. Maulini, A. Tsekoun, R. Go, and C. K. N. Patel, "Tapered 4.7 μm quantum cascade lasers with highly strained active region composition delivering over 4.5 watts of continuous wave optical power," *Opt. Express*, vol. 20, no. 4, pp. 4382–4388, 2012.

[155] G. De Naurois, M. Carras, B. Simozrag, O. Patard, F. Alexandre, and X. Marcadet, "Coherent quantum cascade laser micro-stripe arrays," *AIP Adv.*, vol. 1, no. 3, p. 032165, 2011.

[156] S. Lourdudoss, W. Metaferia, C. Junesand, B. Manavaimaran, S. Ferré, B. Simozrag, M. Carras, R. Peretti, V. Liverini, M. Beck *et al.*, "Hydride vapour phase epitaxy assisted buried heterostructure quantum cascade lasers for sensing applications," in *SPIE OPTO*. International Society for Optics and Photonics, 2015, pp. 93 700D–93 700D.

[157] J. Kirch, C.-C. Chang, C. Boyle, L. Mawst, D. Lindberg III, T. Earles, and D. Botez, "5.5 W near-diffraction-limited power from resonant leaky-wave coupled phase-locked arrays of quantum cascade lasers," *Appl. Phys. Lett.*, vol. 106, no. 6, p. 061113, 2015.

[158] S. K. Mandre, I. Fischer, and W. Elsässer, "Spatiotemporal emission dynamics of a broad-area semiconductor laser in an external cavity: Stabilization and feedback-induced instabilities," *Opt. Commun.*, vol. 244, pp. 355–365, 2005.

[159] T. Tachikawa, S. Takimoto, R. Shogenji, and J. Ohtsubo, "Dynamics of broad-area semiconductor lasers with short optical feedback," *IEEE J. Quantum Electron.*, vol. 46, no. 2, pp. 140–149, 2010.

[160] A. Takeda, R. Shogenji, and J. Ohtsubo, "Spatial-mode analysis in broad-area semiconductor lasers subjected to optical feedback," *Opt. Rev.*, vol. 20, no. 4, pp. 308–313, 2013.

[161] G. C. Dente, "Low confinement factors for suppressed filaments in semiconductor lasers," *IEEE J. Quantum Electron.*, vol. 37, no. 12, pp. 1650–1653, 2001.

[162] J. Martin-Regalado, G. H. M. van Tartwijk, S. Balle, and M. san Miguel, "Mode control and pattern stabilization in broad-area lasers by optical feedback," *Phys. Rev. A*, vol. 54, no. 6, pp. 5386–5393, 1996.

[163] E. Wolf, Ed., *Progress in Optics*. Elsevier, 2002, vol. 44.

[164] P. Friedli, H. Sigg, B. Hinkov, A. Hugi, S. Riedi, M. Beck, and J. Faist, "Four-wave mixing in a quantum cascade laser amplifier," *Appl. Phys. Lett.*, vol. 102, p. 222104, 2013.

[165] N. Yu, L. Diehl, E. Cubukcu, D. Bour, S. Corzine, G. Höfler, A. K. Wojcik, K. B. Crozier, A. Belyanin, and F. Capasso, "Coherent coupling of multiple transverse modes in quantum cascade lasers," *Phys. Rev. Lett.*, vol. 102, no. 1, p. 013901, 2009.

[166] W. W. Bewley, J. R. Lindle, C. S. Kim, I. Vurgaftman, J. R. Meyer, A. J. Evans, J. S. Yu, S. Slivken, and M. Razeghi, "Beam steering in high-power CW quantum cascade lasers," *IEEE J. Quantum Electron.*, vol. 41, no. 6, pp. 833–841, 2005.

[167] R. Adler, "A study of locking phenomena in oscillators," *Proceedings of IRE*, vol. 53, pp. 351–7, 1946.

[168] R. H. Pantell, "The laser oscillator with an external signal," *Proceedings of the IEEE*, vol. 53, pp. 474–477, 1965.

[169] H. L. Stover and W. H. Steier, "Locking of laser oscillators by light injection," *Appl. Phys. Lett.*, vol. 8, pp. 91–93, 1966.

[170] H. Erzgräber, D. Lenstra, B. Krauskopf, E. Wille, M. Peil, I. Fischer, and W. Elsässer, "Mutually delay-coupled semiconductor lasers: Mode bifurcation scenarios," *Opt. Commun.*, vol. 255, pp. 286–296, 2005.

[171] P. Kumar and F. Grillot, "Control of dynamical instability in semiconductor quantum nanostructures diodes laser: Role of phase amplitude coupling," *Eur. Phys. J.-Appl. Phys.*, vol. 222, p. 813, 2013.

[172] S. Kobayashi and T. Kimura, "Injection locking in AlGaAs semiconductor laser," *IEEE J. Quantum Electron.*, vol. 17, no. 5, pp. 681–689, 1981.

[173] R. Lang, "Injection locking properties of a semiconductor laser," *IEEE J. Quantum Electron.*, vol. 18, no. 6, pp. 976–983, 1982.

[174] F. Morgensen, H. Olesen, and G. Jacobsen, "Locking conditions and stability properties for a semiconductor laser with external light injection," *IEEE J. Quantum Electron.*, vol. 21, no. 7, pp. 784–793, 1985.

[175] N. A. Naderi, "External control of semiconductor nanostructure lasers," Ph.D. dissertation, University of New Mexico, 2011.

[176] A. Gavrielides, V. Kovanis, and T. Erneux, "Analytical stability boundaries for a semiconductor laser subject to optical injection," *Opt. Commun.*, vol. 136, pp. 253–256, 1997.

[177] F. Morgensen, H. Olesen, and G. Jacobsen, "FM noise suppression and linewidth reduction in an injection-locked semiconductor laser," *Electron. Lett.*, vol. 21, no. 16, pp. 696–697, 1985.

[178] R. Hui, A. D'Ottavi, A. Mecozzi, and P. Spano, "Injection locking in distributed feedback semiconductor lasers," *IEEE J. Quantum Electron.*, vol. 27, no. 6, pp. 1688–1695, 1991.

[179] M. P. van Exter, C. Biever, and J. P. Woerdman, "Effect of optical injection on bias voltage and spectrum of a semiconductor laser," *IEEE J. Quantum Electron.*, vol. 29, no. 11, pp. 2771–2779, 1993.

[180] L. Li, "Static and dynamic properties of injection-locked semiconductor lasers," *IEEE J. Quantum Electron.*, vol. 30, no. 8, pp. 1701–1708, 1994.

[181] P. Spano, S. Piazzolla, and M. Tamburrini, "Frequency and intensity noise in injection-locked semiconductor lasers: Theory and experiments," *IEEE J. Quantum Electron.*, vol. 22, no. 3, pp. 427–435, 1986.

[182] E. K. Lau, X. Zhao, H.-K. Sung, D. Parekh, C. Chang-Hasnain, and M. C. Wu, "Strong optical injection-locked semiconductor lasers demonstrating >100 GHz resonance frequencies and 80 GHz intrinsic bandwidth," *Opt. Express*, vol. 16, no. 9, pp. 6609–6618, 2008.

[183] S. Piazzolla, P. Spano, and M. Tamburrini, "Small signal analysis of frequency chirping in injection-locked semiconductor lasers," *IEEE J. Quantum Electron.*, vol. 22, no. 12, pp. 2219–2223, 1986.

[184] L. F. Lester, N. A. Naderi, F. Grillot, R. Raghunathan, and V. Kovanis, "Strong optical injection and the differential gain in a quantum dash laser," *Opt. Express*, vol. 22, pp. 7222–7228, 2014.

[185] K. Panajotov, M. Sciamanna, I. Gatare, M. Arteaga, and H. Thien, "Nonlinear dynamics of Vertical-Cavity Surface-Emitting Lasers," *Advances in Optical Technologies*, vol. 2011, no. 469627, 2011.

[186] S. Wieczorek, B. Krauskopf, T. B. Simpson, and D. Lenstra, "The dynamical complexity of optically injected semiconductor lasers," *Phys. Rep.*, vol. 416, pp. 1–128, 2005.

[187] M. Pochet, N. A. Naderi, N. Terry, V. Kovanis, and L. F. Lester, "Dynamic behavior of an injection-locked quantum-dash Fabry-Perot laser at zero detuning," *Opt. Express*, vol. 17, no. 23, pp. 20 623–20 630, 2009.

[188] S. Eriksson, "Dependence of the experimental stability diagram of an optically injected semiconductor laser on the laser current," *Opt. Commun.*, vol. 210, pp. 343–353, 2002.

[189] M. S. Taubman, T. L. Myers, B. D. Cannon, and R. M. Williams, "Stabilization, injection and control of quantum cascade lasers, and their application to chemical sensing in the infrared," *Spectrochim. Acta A*, vol. 60, no. 14, pp. 3457 – 3468, 2004.

[190] K. S. C. Yong, M. K. Haldar, and J. F. Webb, "Theory of reduction of residual amplitude modulation in mid-infrared wavelength modulation spectroscopy by injection locking of quantum cascade lasers," *IEEE J. Sel. Top. Quantum Electron.*, vol. 21, no. 6, p. 1701210, 2015.

[191] H. Simos, A. Bogris, D. Syvridis, and W. Elsasser, "Intensity noise properties of mid-infrared injection locked quantum cascade lasers: I. Modeling," *IEEE J. Quantum Electron.*, vol. 50, no. 2, pp. 98–105, Feb 2014.

[192] S. Borri, I. Galli, F. Cappelli, A. Bismuto, S. Bartalini, P. Cancio, G. Giusfredi, D. Mazzotti, J. Faist, and P. D. Natale, "Direct link of a mid-infrared qcl to a frequency comb by optical injection," *Opt. Lett.*, vol. 37, no. 6, pp. 1011–1013, 2012.

[193] B. Meng and Q. J. Wang, "Theoretical investigation of injection-locked high modulation bandwidth quantum cascade lasers," *Opt. Express*, vol. 20, no. 2, pp. 1450–1464, 2012.

[194] C. Wang, F. Grillot, V. Kovanis, and J. Even, "Rate equation analysis of injection-locked quantum cascade lasers," *J. Appl. Phys.*, vol. 113, p. 063104, 2013.

[195] C. Wang, F. Grillot, V. I. Kovanis, J. D. Bodyfelt, and J. Even, "Modulation properties of optically injection-locked quantum cascade lasers," *Opt. Lett.*, vol. 38, no. 11, pp. 1975–1977, 2013.

[196] M. Renaudat St-Jean, M. I. Amanti, A. Bernard, A. Calvar, A. Bismuto, E. Gini, M. Beck, J. Faist, H. C. Liu, and C. Sirtori, "Injection locking of mid-infrared quantum cascade laser at 14 GHz, by direct microwave modulation," *Laser Photonics Rev.*, vol. 8, no. 3, pp. 443–449, 2014.

[197] T. Erneux, V. Kovanis, and A. Gavrielides, "Nonlinear dynamics of an injected quantum cascade laser," *Phys. Rev. E*, vol. 88, p. 032907, 2013.

[198] C. Mayol, R. Toral, C. R. Mirasso, and M. A. Natiello, "Class-A lasers with injected signal: Bifurcation set and Lyapunov-potential function," *Phys. Rev. A*, vol. 66, no. 1, p. 013808, 2002.

[199] B. Kelleher, S. P. Hegarty, and G. Huyet, "Optically injected lasers: The transition from class B to class A lasers," *Phys. Rev. E*, vol. 86, no. 6, p. 066206, 2012.

[200] N. Akhmediev, B. Kibler, F. Baronio, M. Belic, W.-P. Zhong, Y. Zhang, W. Chang, J. M. Soto-Crespo, P. Vouzas, P. Grelu, C. Lecaplain, K. Hammani, S. Rica, A. Picozzi, M. Tlidi, K. Panajotov, A. Mussot, A. Bendahmane, P. Szriftigiser, G. Genty, J. Dudley, A. Kudlinski, A. Demircan, U. Morgner, C. Masoller, N. G. R. Broderick, A. F. J. Runge, M. Erkintalo, S. Residori, U. Bortolozzo, F. T. Arecchi, S. Wabnitz, C. G. Tiofack, S. Coulibably, and M. Taki, "Roadmap on optical rogue waves and extreme events," *J. Opt.*, vol. 18, no. 063001, 2016.

[201] T. B. Simpson, J.-M. Liu, M. AlMulla, N. G. Usechak, and V. Kovanis, "Tunable oscillations in optically injected semiconductor lasers with reduced sensitivity to perturbations," *J. Lightwave Technol.*, vol. 32, no. 20, pp. 3749–3758, 2014.

[202] C. Wang, R. Raghunathan, K. Schires, S.-C. Chan, L. F. Lester, and F. Grillot, "Optically injected InAs/GaAs quantum dot laser for tunable photonic microwave generation," *Opt. Lett.*, vol. 41, no. 6, pp. 1153–1156, 2016.

[203] D. Paboeuf, "Combinaison cohérente de diodes laser de luminance élevée en cavité externe," Ph.D. dissertation, Université Paris Sud XI, 2009.

[204] T. Habuseva, S. O'Donoghue, N. Rebrova, S. P. Hegarty, D. Rachinskii, and G. Huyet, "Single and dual-mode injection locked quantum-dot mode-locked lasers," in *Conference on Lasers and Electro-Optics*, 2009.

[205] D. G. Revin, M. Hemingway, Y. Wanf, J. W. Cockburn, and A. Belyanin, "Active mode locking of quantum cascade lasers in an external ring cavity," *Nat. Commun.*, vol. 7, no. 11440, 2016.

[206] F. Wang, K. Maussang, S. Moumdji, R. Colombelli, J. R. Freeman, I. Kundu, L. Li, E. H. Linfield, A. G. Davies, J. Mangeney, J. Tignon, and S. S. Dhillon, "Generation ultrafast pulses of light from quantum cascade lasers," *Optica*, vol. 2, no. 11, pp. 944–949, 2015.

[207] A. Spott, J. Peters, M. L. Davenport, E. J. Stanton, C. D. Merritt, W. W. Bewley, I. Vurgaftman, C. S. Kim, J. R. Meyer, J. Kirch, L. J. Mawst, D. Botez, and J. E. Bowers, "Quantum cascade laser on silicon," *Optica*, vol. 3, no. 5, pp. 545–551, 2016.

[208] S. Michael, W. W. Chow, and H. C. Schneider, "Mid-infrared quantum-dot quantum cascade lasers: A theoretical feasibility study," *Photonics*, vol. 3, no. 29, 2016.

[209] E. A. Zibik, T. Grange, B. A. Carpenter, N. E. Porter, R. Ferreira, G. Bastard, D. Stehr, S. Winnerl, M. Helm, H. Y. Liu, M. S. Skolnick, and L. R. Wilson, "Long

lifetimes of quantum-dot intersublevel transitions in the terahertz range," *Nat. Mater.*, vol. 8, pp. 803–807, 2009.

List of publications

Journal publications

1. **L. Jumpertz**, M. Carras, K. Schires and F. Grillot, "Regimes of external optical feedback in 5.6 μm distributed feedback mid-infrared quantum cascade lasers". *Appl. Phys. Lett.*, vol. 105, p. 131112, 2014.

2. **L. Jumpertz**, F. Michel, R. Pawlus, W. Elsässer, K. Schires, M. Carras and F. Grillot, "Measurements of the linewidth enhancement factor of mid-infrared quantum cascade lasers by different optical feedback techniques". *AIP Adv.*, vol. 6, no. 1, p. 015212, 2016.

3. **L. Jumpertz**, K. Schires, M. Carras, M. Sciamanna and F. Grillot, "Chaotic light at mid-infrared wavelength". *Light Sci. Appl.*, vol. 5, p. e16088, 2016.

4. **L. Jumpertz**, C. Caillaud, C. Gilles, S. Ferré, K. Schires, L. Brilland, J. Troles, M. Carras and F. Grillot, "Estimating optical feedback from a chalcogenide fiber in mid-infrared quantum cascade lasers". *AIP Adv.*, vol. 6, no. 10, p. 105201, 2016.

Invited conference presentations

1. **L. Jumpertz**, F. Michel, R. Pawlus, W. Elsässer, M. Carras and F. Grillot, "Linewidth broadening factor and gain compression in quantum cascade lasers". SPIE Photonics West, 2016.

2. F. Grillot, **L. Jumpertz**, K. Schires, M. Carras and M. Sciamanna, "Deterministic

temporal chaos from a mid-infrared external cavity quantum cascade laser". SPIE Photonics West, 2016.

3. **L. Jumpertz**, K. Schires, M. Carras and F. Grillot, "Première observation de l'effet papillon dans un laser à cascade quantique émettant dans le moyen infra-rouge". Journée Nationales d'Optique Guidée (JNOG), 2016.

Conference presentations

1. V. Trinité, S. Ferré, **L. Jumpertz**, G. Maisons, M. Carras, G.-M. De Naurois, T. Mansipur and F. Capasso, "Experimental and theoretical study of the gain saturation in MIR QCL". International Quantum Cascade Laser School and Workshop (IQCLSW), 2014: poster presentation.

2. **L. Jumpertz**, M. Carras, K. Schires and F. Grillot, "Regimes of feedback effects in mid-infrared distributed feedback quantum cascade lasers". International Symposium on Physics and Applications of Laser Dynamics (IS-PALD), 2014: oral presentation.

3. **L. Jumpertz**, M. Carras and F. Grillot, "First experimental observation of external optical feedback regimes in mid-infrared quantum cascade lasers". Mid-Infrared Optoelectronics: Materials and Devices (MIOMD), 2014: oral presentation.

4. V. Trinité, S. Ferré, **L. Jumpertz**, G. Maisons, M. Carras, G.-M. De Naurois, T. Mansipur and F. Capasso, "Experimental and theoretical study of the gain saturation in MIR QCL". Mid-Infrared Optoelectronics: Materials and Devices (MIOMD), 2014: oral presentation.

5. **L. Jumpertz**, M. Carras, K. Schires and F. Grillot, "Etude expérimentale des régimes d'auto-injection optique dans les lasers à cascade quantique". Journée Nationales d'Optique Guidée (JNOG), 2014: oral presentation.

6. **L. Jumpertz**, S. Ferré, K. Schires, M. Carras and F. Grillot, "Nonlinear dynamics of quantum cascade lasers with optical feedback". SPIE Photonics West, 2015: oral presentation.

7. L. Brilland, L. Provino, S. Venck, D. Méchin, C. Caillaud, S. Ferré, C. Gilles, **L. Jumpertz**, M. Carras and J. Troles, "Optical characterization of a single mode mid infrared microstructured optical fiber up to 10 μm: Potential for supercontinuum generation and applications for QCLs based sensors". Conference on Lasers and Electro-Optics (CLEO) Europe, 2015: oral presentation.

8. **L. Jumpertz**, F. Michel, R. Pawlus, W. Elsässer, M. Carras and F. Grillot, "Etude expérimentale du facteur de couplage phase-amplitude dans un laser à cascade quantique émettant dans le moyen infra-rouge". Journée Nationales d'Optique Guidée (JNOG), 2015: oral presentation.

9. **L. Jumpertz**, F. Michel, R. Pawlus, W. Elsässer, K. Schires, M. Carras and F. Grillot, "Experimental investigation of the above-threshold linewidth broadening factor of a mid-infrared quantum cascade laser". IEEE International Photonics Conference (IPC), 2015: oral presentation.

10. **L. Jumpertz**, K. Schires M. Carras, M. Sciamanna and F. Grillot, "Chaotic pulsing in quantum cascade lasers subject to optical feedback". International Symposium on Physics and Applications of Laser Dynamics (IS-PALD), 2015: oral presentation.

11. J. Troles, C. Caillaud, C. Gilles, L. Provino, L. Brilland, **L. Jumpertz**, S. Ferré, M. Carras, M. Brun and J.-L. Adam, "Elaboration of a chalocogenide microstructured optical fiber presenting high birefringence". American Ceramic Society Glass and Optical Material Division (GOMD), 2016: oral presentation.

12. M. F. Pereira, D. Winge, A. Wacker, **L. Jumpertz**, W. Elsässer, M. Carras and F. Grillot, "The Linewidth Enhancement Factor of QCLs". International Quantum Cascade Laser School and Workshop (IQCLSW), 2016: poster presentation.

13. M. F. Pereira, D. O. Winge, A. Wacker, **L. Jumpertz**, F. Michel, R. Pawlus, W. Elsässer, K. Schires, M. Carras and F. Grillot, "Nonequilibrium Green's functions theory for the alpha factor of quantum cascade lasers". SPIE Nanoscience + Engineering, 2016: oral presentation.

14. T. Newell, **L. Jumpertz**, F. Grillot, C. Lu and R. Kaspi, "Investigation of a broad-area quantum cascade laser with external cavity feedback". International Symposium on Physics and Applications of Laser Dynamics (IS-PALD), 2016: oral presentation.

15. S. Ferré, **L. Jumpertz**, M. Carras and F. Grillot, "Mode control and pattern stabilization in broad area quantum cascade laser by optical feedback". International Symposium on Physics and Applications of Laser Dynamics (IS-PALD), 2016: oral presentation.

Annex A: Résumé en français

Introduction

Les lasers à cascade quantique

Les lasers à cascade quantiques (LCQ) sont des sources semi-conductrices basées sur des transitions inter-sous-bandes au sein de la bande de conduction [13]. Contrairement aux diodes lasers, dans lesquelles la transition radiative a lieu entre la bande de conduction et la bande de valence, la longueur d'onde d'émission des LCQ n'est pas fixée par le gap intrinsèque au matériau utilisé. Selon l'ingénierie quantique de la zone active, la longueur d'onde d'émission peut aller du moyen infrarouge ($3 - 12\ \mu$m) au domaine terahertz ($50 - 250\ \mu$m), selon la largeur des puits quantiques. De plus, un effet de cascade, où chaque électron va traverser plusieurs zones actives et fournir plusieurs photons, permet d'obtenir un meilleur rendement, comme représenté sur la Figure 7.1.

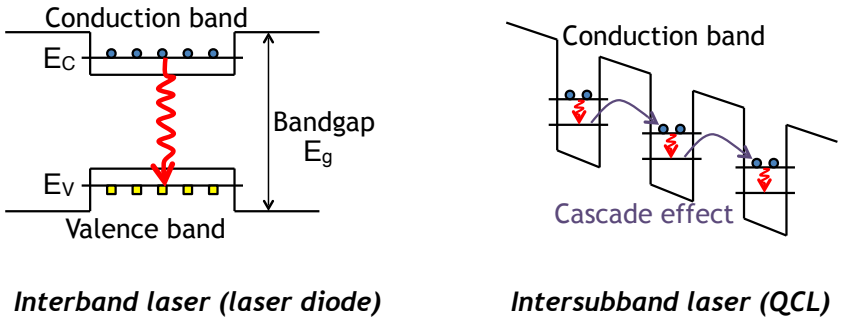

Figure 7.1: Transitions inter-sous-bande et effet de cascade dans les lasers à cascade quantique.

Depuis leur invention en 1994 [15], la technologie des LCQ moyen infrarouges a rapidement progressé, et ceux-ci fonctionnent désormais en impulsionnel ou en continu, en régime multimode ou monomode, et peuvent émettre jusqu'à quelques watts à température ambiante avec uniquement un refroidissement thermo-électrique.

Applications moyen infra-rouges

Grâce à leurs excellentes performances, les LCQ sont devenues des sources privilégiées pour de nombreuses applications moyen infrarouges.

Tout d'abord, la spectroscopie de gaz exploite principalement le moyen infrarouge car la plupart des molécules d'intérêt (drogues, explosifs, polluants, glucose...) absorbent à ces longueurs d'onde, comme présenté en Figure 7.2. Pour détecter et quantifier la présence d'un molécule dans un milieu, on l'illumine avec une source moyen-infrarouge et on analyse soit directement le spectre d'absorption en sortie du milieu, soit les vibrations du milieu à l'aide d'un haut-parleur : il s'agit alors de détection photo-acoustique [1].

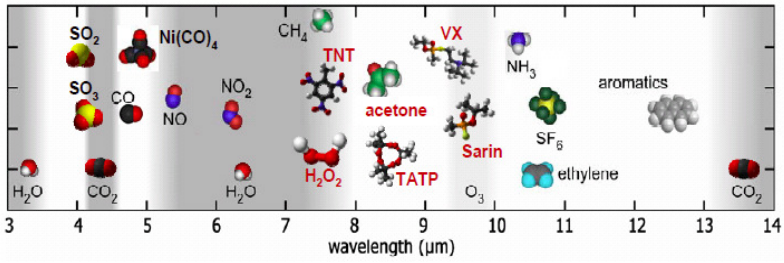

Figure 7.2: Longueur d'onde d'absorption de quelques molécules d'intérêt.

Une seconde application des sources moyen infrarouges sont les communications en espace libre [2]. En complément des fibres optiques, qui sont presque saturées, ou en remplacement des ondes radios, pour augmenter le débit en augmentant la fréquence de la porteuse, les ondes moyen-infrarouges permettent un transport efficace de l'information, tout en étant beaucoup moins sensibles aux effets de la turbulence lors de la propagation dans l'atmosphère.

Enfin, les contre-mesures optiques nécessitent également une source moyen infrarouge de forte puissance et avec des bonnes propriétés de modulation. L'objectif est en effet de brouiller un missile à tête chercheuse dans le moyen infrarouge, qui suit la signature

thermique d'un avion. Comme expliqué en Figure 7.3, l'avion peut dévier le missile en émettant un fort signal moyen infrarouge modulé, qui va brouiller le détecteur.

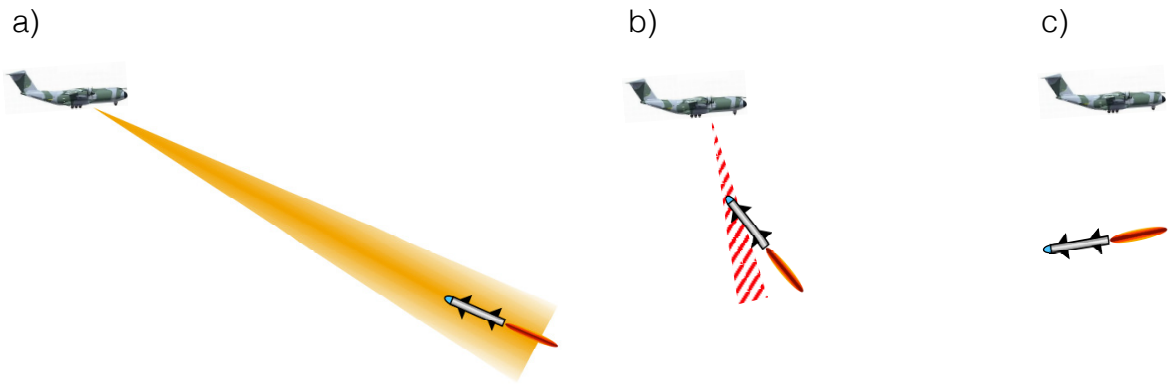

Figure 7.3: Scénario de contre-mesure optique. a) Un missile qui traque le point chaud d'un avion est détecté. b) Un fort signal moyen infrarouge est émis depuis l'avion pour brouiller le missile. c) La trajectoire du missile est déviée.

Objectifs de la thèse

L'objectif de cette thèse est d'améliorer les propriétés d'émission de LCQ émettant dans le moyen infrarouge en appliquant de l'injection ou de la réinjection optiques, c'est à dire en injectant dans la zone active la lumière émise par un seconde laser ou une partie de la lumière émise par le laser après réflexion sur un miroir. Ces contrôles externes optiques ont été étudiés en détails dans les diodes lasers proches infrarouges, et permettent d'améliorer sensiblement un certain nombre de propriétés, telles que la puissance émise, la largeur de raie, la qualité du spectre optique, le bruit ou la bande passante de modulation.

Cependant, ces phénomènes peuvent aussi déstabiliser le laser, voire le rendre chaotique. Comme la réinjection optique peut provenir de réflexions parasites sur des éléments du montage expérimental, il est important de savoir si un LCQ soumis à de la réinjection peut avoir un comportement instable ou chaotique, pour mieux contrôler les performances du laser.

Réinjection optique dans les lasers à cascade quantique

LCQ étudiés

Dans cette section, les LCQ étudiés sont des laser Fabry-Perot ou à contre-réaction distribuée (DFB) émettant autour de 5.6 μm. La zone active est inspirée de [54] et constituée de 30 périodes d'AlInAs/GaInAs crûes par épitaxie à jet moléculaire (MBE) sur un cladding en InP faiblement dopé (10^{17} cm^{-3}). Le cladding supérieur en InP est ensuite recrû par épitaxie en phase vapeur aux organométalliques (MOCVD).

Dans le cas du LCQ DFB, le cladding supérieur est conçu suivant [55] pour obtenir une émission monomode. On ajoute un réseau métallique de surface, avec une efficacité de couplage $\kappa \approx 4$ cm^{-1}, résultant en un κL proche de 1.

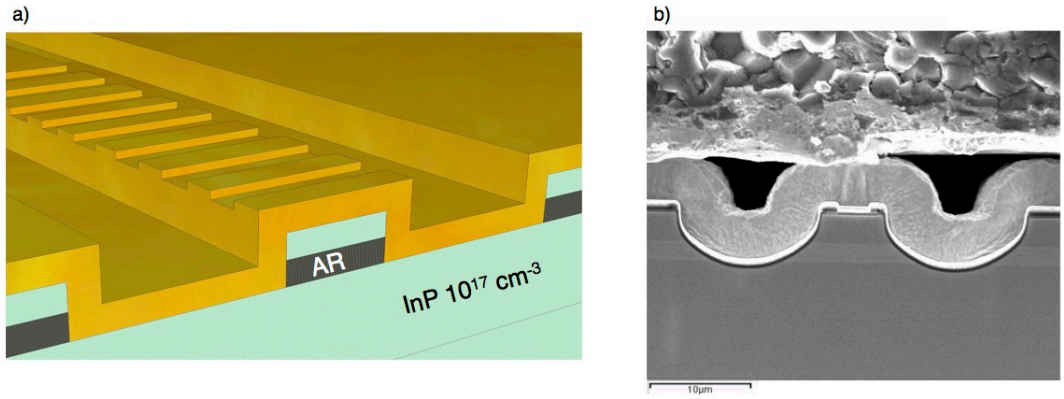

Figure 7.4: a) Schéma et b) image MEB du LCQ DFB étudié. La région active, indiquée 'AR' sur a), apparaît en gris clair sur b).

Enfin, le laser est fabriqué avec un procédé double tranché standard et un traitement haute-réflectivité (R>95%) est appliqué sur la facette arrière. Le LCQ est monté epi-side down pour une meilleure extraction de la chaleur. Figure 7.4 présente un schéma et une image par microscopie électronique (MEB) à balayage de la structure étudiée.

Montage expérimental

Le LCQ étudié est inséré dans le montage expérimental décrit en Figure 7.5. La lumière émise par le laser est collimatée par une lentille de très courte focale ($f = 1.87$ mm) et de grande ouverture numérique ($ON = 0.87$), puis divisée en deux fois par une lame séparatrice 40/60.

Une partie de la lumière est réfléchie sur un miroir pour être réinjectée dans le laser. La longueur de cavité externe L_{ext} est soigneusement contrôlée, ainsi que le taux de réinjection f_{ext}, défini comme le rapport entre puissance émise et puissance réinjectée, qui peut être variée en tournant l'angle d'un polariseur.

L'autre voie sert à la détection, et le signal est envoyé sur un puissance-mètre, un spectromètre à transformée de Fourier (FTIR) pour mesurer les spectres optiques ou une photodiode rapide en tellurure de mercure-cadmium (MCT).

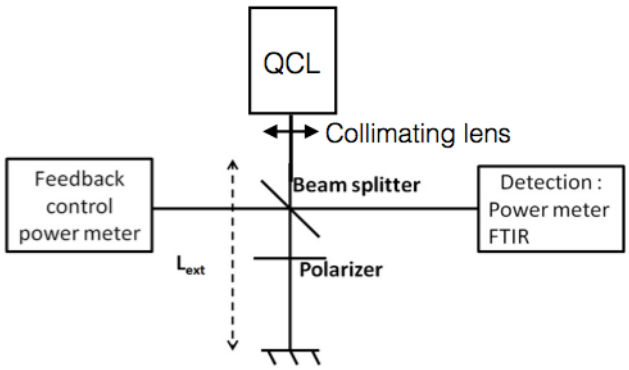

Figure 7.5: Schéma du montage expérimental de réinjection dans les LCQ.

Etude numérique de la réinjection

Rigoureusement, chaque zone active du LCQ correspond à un laser à 3 niveaux, il faudrait donc considérer $5 \times N_{pd}$ équations, où N_{pd} est le nombre de périodes. En pratique, on utilise un modèle à trois niveaux globaux. Lorsque le laser est soumis à un champ électrique

complexe $E = \sqrt{S}e^{i\phi}$, les équations de taux du LCQ sous réinjection optique peuvent s'écrire:

$$\frac{dN_3}{dt} = \eta \frac{I}{q} - \frac{N_3}{\tau_{32}} - \frac{N_3}{\tau_{31}} - G_0 \Delta N S \tag{7.1}$$

$$\frac{dN_2}{dt} = \frac{N_3}{\tau_{32}} - \frac{N_2}{\tau_{21}} + G_0 \Delta N S \tag{7.2}$$

$$\frac{dN_1}{dt} = \frac{N_3}{\tau_{31}} + \frac{N_2}{\tau_{21}} - \frac{N_1}{\tau_{out}} \tag{7.3}$$

$$\frac{dS}{dt} = \left(N_{pd} G_0 \Delta N - \frac{1}{\tau_p} \right) S + \beta N_{pd} \frac{N_3}{\tau_{sp}} + 2k\sqrt{S(t)S(t-\tau_{ext})}\cos(\Delta\phi) \tag{7.4}$$

$$\frac{d\phi}{dt} = \frac{\alpha}{2}\left(N_{pd} G_0 \Delta N - \frac{1}{\tau_p} \right) - k\sqrt{\frac{S(t-\tau_{ext})}{S(t)}}\sin(\Delta\phi) \tag{7.5}$$

où N_j est la densité de porteurs du niveau j, avec $\Delta N = N_3 - N_2$, η l'efficacité de conversion, I le courant de pompe. τ_{ij} correspond au temps de vie des porteurs entre les niveaux i et j, τ_{out} est le temps caractéristique que met l'électron pour aller dans l'injecteur par effet tunnel, τ_{sp} est le temps de vie d'émission spontanée, τ_p est le temps de vie des photons dans la cavité laser. G_0 correspond au gain modal net sur une période, α est le facteur de couplage phase-amplitude and β le facteur d'émission spontané. $\Delta\phi$ est défini comme $\Delta\phi = \omega_0\tau_{ext} + \phi(t) - \phi(t-\tau_{ext})$, avec τ_{ext} le temps aller-retour dans la cavité externe. Enfin, k est le coefficient de feedback, défini selon :

$$k = \frac{1}{\tau_{in}} 2C_l\sqrt{f_{ext}} \tag{7.6}$$

où τ_{in} est le temps aller-retour dans la cavité interne et C_l le coefficient de couplage externe. Pour une laser Fabry-Perot, il est s'exprime comme :

$$C_l = \frac{1 - R_2}{2\sqrt{R_2}} \tag{7.7}$$

avec R_2 le coefficient de réflexion de la facette orientée vers la cavité externe. Dans le cas d'un laser DFB, l'expression du coefficient C_l est bien plus compliquée, et dépend des réflectivités complexes aux deux facettes [79].

Paramètres des LCQ étudiés

Les paramètres internes de la structure étudiée sont calculés à partir d'un logiciel de simulation d'hétérostructures appelé METIS. Il permet d'obtenir les fonctions d'onde, comme représenté en Figure 7.6 a, ainsi que les temps de vie caractéristiques. De plus, la simulation thermique des modes de la cavité avec COMSOL permet d'extraire l'indice de groupe et le facteur de recouvrement de la structur (Figure 7.6 b). Tous ces paramètres sont résumés dans le Tableau 7.1.

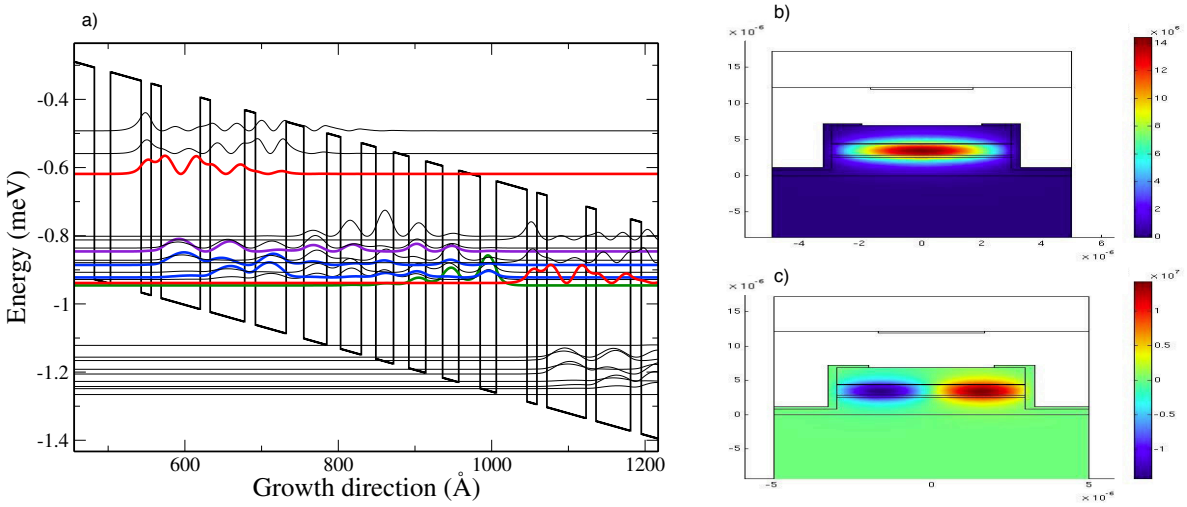

Figure 7.6: a) Fonctions d'onde de la structure LCQ étudiée, simulées avec METIS. En rouge, niveau $|3\rangle$ de deux périodes consécutives, en violet niveau $|2\rangle$, en bleu niveau $|1\rangle$, divisé en deux états phonons, en vert état de l'injecteur. b) Simulation de modes au premier ordre avec COMSOL. c) Simulation de modes au second ordre.

Parameter	Value	Parameter	Value
Temps de vie des porteurs 3-2 τ_{32}	2.27 ps	Indice de groupe n_g	3.2
Temps de vie des porteurs 3-1 τ_{31}	2.30 ps	Facteur de confinement Γ_{opt}	68%
Temps de vie des porteurs 2-1 τ_{21}	0.37 ps	Gain modal net G_0	1.2×10^4 s^{-1}
Temps de fuite des porteurs τ_{out}	0.54 ps	Temps de vie des photons τ_p	4.74 ps

Table 7.1: Laser parameters

Facteur α et compression de gain

Les simulations décrites précédemment ne permettent pas d'extraire l'efficacité de conversion η, qui sera extrait des courbes puissance-courant-tension (PIV) de chaque laser, ni le facteur α. Ce dernier quantifie le couplage entre les parties réelles et imaginaires de la susceptibilité non-linéaire [37], c'est à dire entre le gain différentiel et l'indice ou, de manière équivalente, le couplage entre la phase et l'amplitude du champ dans la cavité laser:

$$\alpha = -\frac{d\left[\Re(\chi(N))\right]/dN}{d\left[\Im(\chi(N))\right]/dN} = \frac{-4\pi}{\lambda}\frac{dn/dN}{dg/dN} \Leftrightarrow \frac{d\phi/dt}{dI/dt} = \frac{\alpha}{2I} \tag{7.8}$$

Ce paramètre est crucial à connaître pour un laser semi-conducteur car il régit la largeur de raie, la réponse du laser sous modulation, les propriétés dynamiques du laser, ainsi que la filamentation dans les lasers à large zone active.

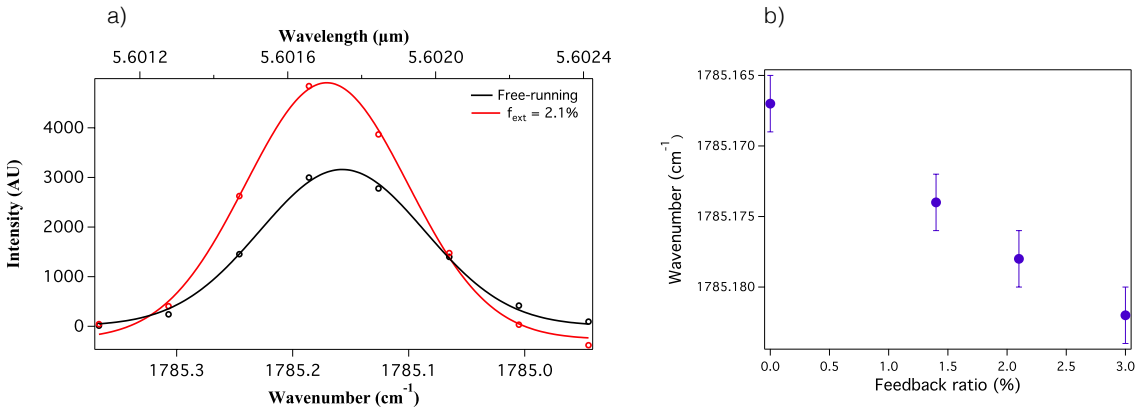

Figure 7.7: Evolution de la longueur d'onde du LCQ sous réinjection optique. a) Spectres optiques et fits gaussiens du LCQ sans réinjection et avec faible réinjection f_{ext} =2.1%. b) Décalage en longueur d'onde en fonction du taux de réinjection.

Pour la structure LCQ étudiée, le facteur α est mesuré à partir de deux méthodes différentes basées sur la réinjection optique. La première technique consiste à suivre la longueur du LCQ Fabry-Perot quand il est soumis à une faible réinjection (voir Figure 7.7). En effet,

l'équation 7.5 en état stationnaire donne:

$$\alpha = \frac{\omega_0 - \omega_s}{k\cos(\omega_s \tau_{ext})} - \tan(\omega_s \tau_{ext}) \tag{7.9}$$

où ω_0 est la fréquence angulaire du laser solitaire, et ω_s la fréquence angulaire du laser réinjecté. Pour le laser Fabry-Perot de dimensions 3 mm × 6 μm, à 10°C et proche du seuil, la valeur extraite est : $\alpha = 1.3 \pm 0.5$.

La seconde méthode consiste à mesurer l'interférogramme obtenu par auto-mélange. Il s'agit encore une fois de réinjection optique, mais le miroir est monté sur un actuateur piezo-électrique et décrit un mouvement sinusoïdal. A partir des points remarquables, indiqués sur la Figure 7.8, que sont deux zéros consécutifs Φ_{Z1} et Φ_{Z2}, un minimum Φ_{min} et un maximum Φ_{max} , et de la période T de l'interférogramme, on peut en déduire le facteur α [52] :

$$\alpha = \frac{\Phi_{max} - \Phi_{min} - 0.5T}{\Phi_{Z2} - \Phi_{Z1} - 0.5T} \tag{7.10}$$

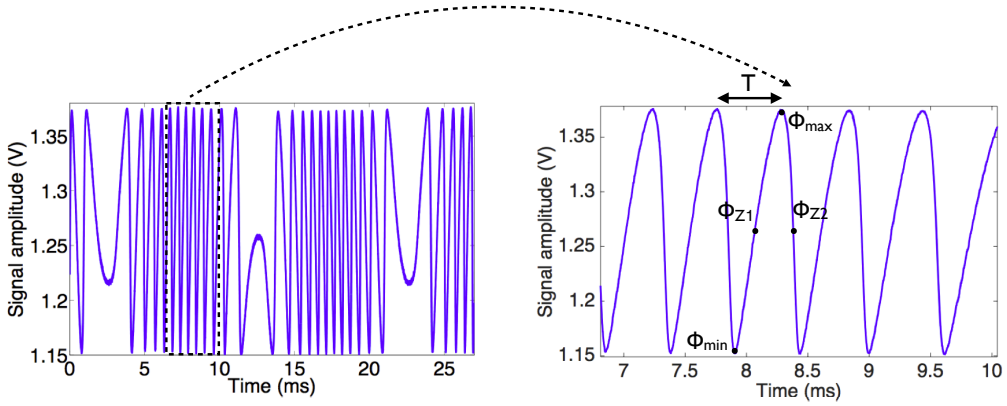

Figure 7.8: Self-mixing interferometer of the QCL under study.

Les résultats pour un LCQ DFB de dimensions 2 mm × 9 μm sont présentés en Figure 7.9 a en fonction du courant normalisé par rapport au seuil:

$$a = \left(\frac{I}{I_{th}} - 1\right) \tag{7.11}$$

On observe une forte dépendance du facteur α en fonction du courant de pompe, avec

des valeurs allant de 0.8 à 2.9. De plus, les résultats obtenus avec les deux méthodes sont parfaitement cohérents.

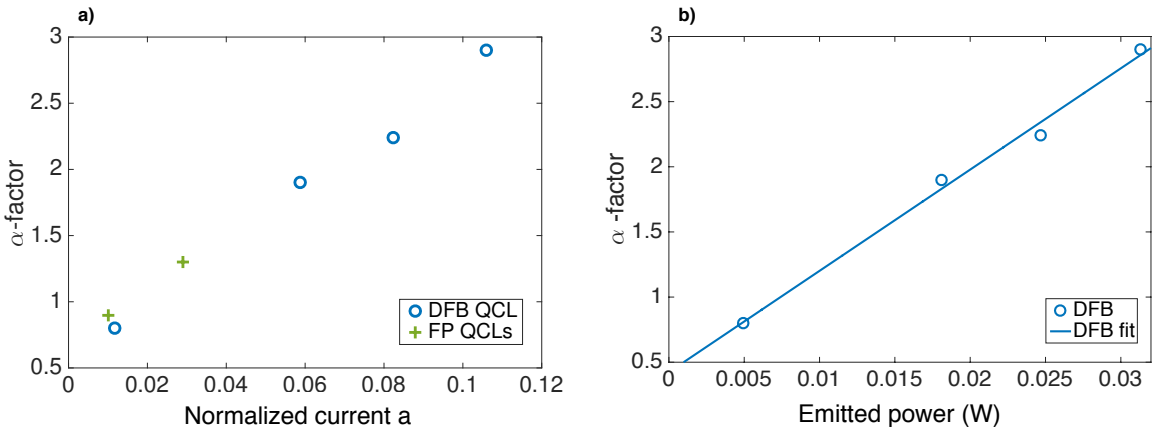

Figure 7.9: a) Evolution du facteur α en fonction du courant de pompe normalisé, et comparaison entre les deux méthodes à 10°C. b) Evolution du facteur α en fonction de la puissance optique émise par le LCQ DFB.

Suivre l'évolution du facteur α en fonction de la puissance optique P_{opt} émise par le LCQ permet d'obtenir le coefficient de compression de gain ϵ_P, puisque :

$$\alpha = \alpha_0(1 + \epsilon_P P_{opt}) \tag{7.12}$$

où α_0 est le facteur α au seuil. La compression de gain correspond à une diminution de la valeur de gain lorsque le courant de pompe augmente [137]. Cela est dû à des non-linéarités sur le gain induites par l'échauffement des porteurs ou par du hole burning spatial ou spectral [138], et le gain s'exprime comme :

$$G = \frac{G_0}{1 + \epsilon_S S} \tag{7.13}$$

avec G_0 le gain linéaire, S la densité de photons et ϵ_S le coefficient de compression de gain exprimé en densité de photons. De plus, on a : $\epsilon_S S = \epsilon_P P_{opt}$, on en déduit $\alpha_0 = 0.4$ et $\epsilon_S = 4.5 \times 10^{-15}$ cm^3 pour le LCQ étudié. Cette valeur est plus élevée que dans les lasers à

puits ou à boîtes quantiques, mais serait cohérente avec le fort hole burning spatial démontré dans les LCQ.

Impact de la réinjection sur les propriétés statiques du LCQ

Lorsqu'on soumet un LCQ Fabry-Perot à de la réinjection optique, sa caractéristique courant-puissance $P(I)$ est modifiée. On observe une réduction du seuil, ainsi qu'une augmentation de la puissance optique, comme le montre la Figure 7.10 a. De plus, à fort taux de réinjection, des ondulations apparaissent sur la $P(I)$. Elles sont dues à des interférences alternativement constructives et destructives entre les modes de la cavité externe et ceux de la cavité interne, dont l'intervalle spectral libre varie avec le courant à cause de l'échauffement de la zone active.

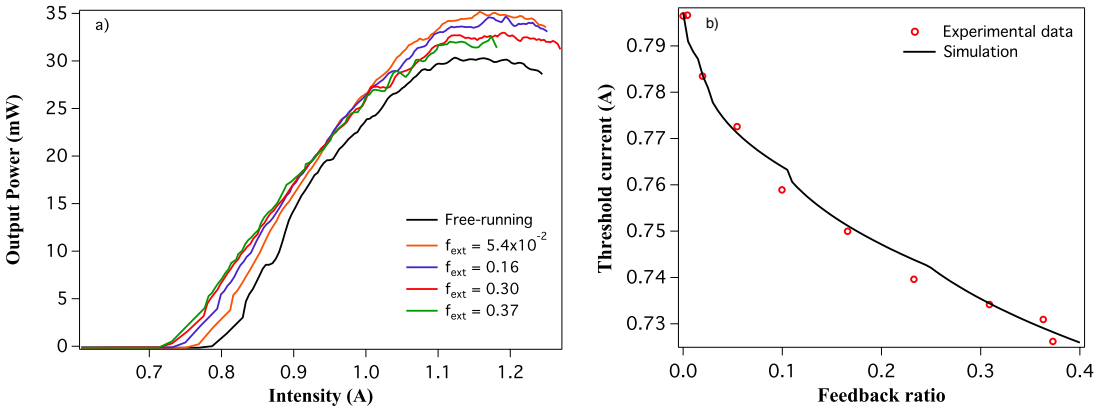

Figure 7.10: Effet de la réinjection optique sur la P(I) du LCQ Fabry-Perot de 4 mm × 6 μm. a) $P(I)$ à différents taux de réinjection, avec une cavité externe de 15 cm. b) Diminution du seuil expérimentale et numérique en fonction du taux de réinjection.

De plus, on peut suivre numériquement la réduction du seuil en fonction du taux de réinjection, puisque :

$$I_{th} = \frac{q}{\eta}\frac{\tau_{32}+\tau_{31}}{\tau_{31}(\tau_{32}-\tau_{21})}\frac{1}{N_{pd}G_0}\left[\frac{1}{\tau_p} - 2k\cos(\omega_s\tau_{ext})\right] \tag{7.14}$$

où ω_s est le mode de cavité externe pour lequel la largeur de raie est minimale. Comme le montre la Figure 7.10 b, il y a un excellent accord entre la simulation et l'expérience, ce qui

permet de valider la valeur $\alpha = 1.3$.

Cette dépendance du seuil en fonction du taux de réinjection optique permet de mesurer la quantité de réinjection parasite provenant d'une fibre optique microstructurée en chalcogénure. Comme le montre la Figure 7.11, pour deux clivages de l'extrémité de la fibre, on obtient des taux de réinjection de 11% et 15%, ce qui est très élevé, et pourrait empêcher l'utilisation de fibre moyen infrarouges pour des applications nécessitant une grande stabilité et pureté spectrale du LCQ. Pour compenser cette réinjection, il faudrait appliquer un traitement anti-réflexions sur la fibre ou la cliver en biais, comme c'est le cas pour les fibres proche infrarouges, ou utiliser systématiquement un isolateur optique en sortie du LCQ.

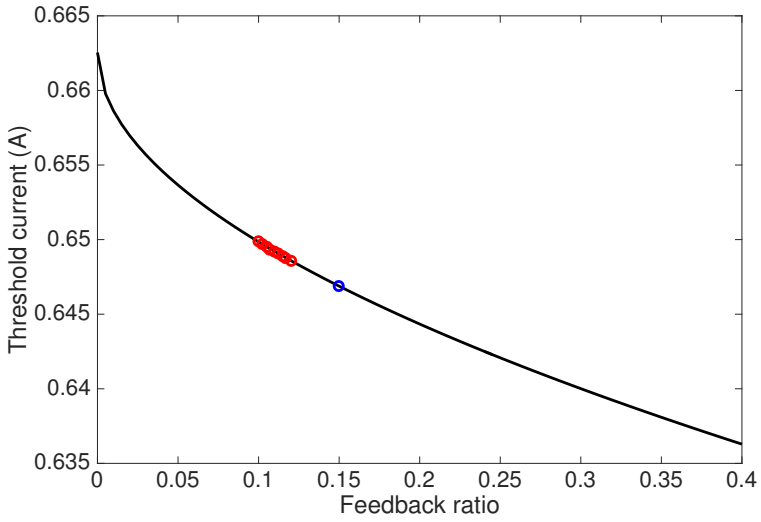

Figure 7.11: Réduction du seuil d'un LCQ due à de la réinjection optique après réflexions sur une fibre pour deux séries de mesures, en rouge et en bleu respectivement, et extraction du taux de réinjection associé.

De plus, l'étude des spectres optiques du LCQ DFB permet d'identifier cinq régimes de réinjection (voir Figure 7.12 a) similaires à ceux observés dans les lasers interbandes [74]. A très faible taux de réinjection, le laser est stable et monomode, et la puissance émise dépend de la phase de l'onde réinjectée. En augmentant progressivement le taux de réinjection, le LCQ passe par un régime qui correspond à un battement entre deux modes, puis par un régime monomode sur un mode qui n'est plus le mode d'émission du laser solitaire. Le quatrième régime correspond à une déstabilisation du laser, caractérisée par une forte

remontée des modes adjacents et une augmentation du bruit. Enfin, à très fort taux de réinjection, l'émission du LCQ est à nouveau stable, avec une très forte puissance. Il s'agit du régime de cavité étendue, où le laser devient une petite zone active dans une cavité longue, dont l'une des extrémités est le miroir de réinjection.

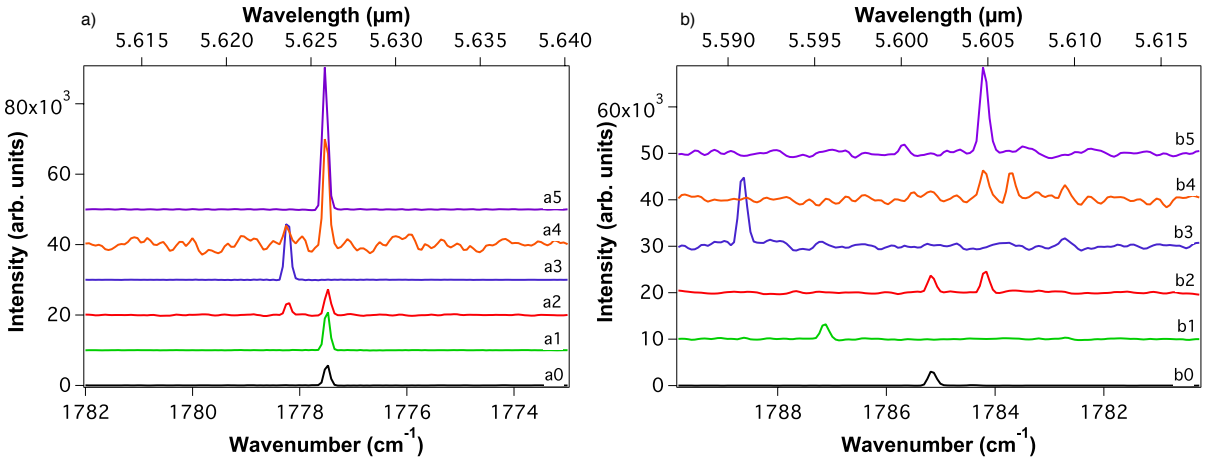

Figure 7.12: Régimes de réinjection des LCQ étudiés. a) LCQ DB, avec une longueur de cavité externe de 15 cm. a0: Laser solitaire. a1: Régime I, $f_{ext} = 9.1 \times 10^{-4}$. a2: Régime II, $f_{ext} = 5.1 \times 10^{-3}$. a3: Régime III, $f_{ext} = 3.2 \times 10^{-2}$. a4: Régime IV, $f_{ext} = 0.13$. a5: Régime V, $f_{ext} = 0.25$. b) LCQ Fabry-Perot, avec une longueur de cavité externe de 13 cm. b0: Laser solitaire. b1: Régime I, $f_{ext} = 1.4 \times 10^{-3}$. b2: Régime II, $f_{ext} = 1.7 \times 10^{-2}$. b3: Régime III, $f_{ext} = 0.14$. b4: Régime IV, $f_{ext} = 0.18$. b5: Régime V, $f_{ext} = 0.25$.

On retrouve les mêmes régimes dans le cas du LCQ Fabry-Perot (voir Figure 7.12 b), sauf que les modes adjacents sont moins éteints, et que la longueur d'onde d'émission varie beaucoup plus car elle n'est pas fixée par le réseau DFB.

En mesurant les taux de réinjection limites des différents régimes en fonction de la longueur de cavité externe, on peut tracer la cartographie de réinjection du LCQ DFB, comme le montre la Figure 7.13. En comparant avec celle tracée pour les lasers interbandes [74], on observe que les LCQ sont beaucoup plus résistants à la réinjection, car les régimes I, III et V, qui correspondent à une émission stable, sont beaucoup plus étendus, et que la frontière entre les régimes I et II, qui marque la première déstabilisation dues à la réinjection, apparaît à un taux de réinjection beaucoup plus élevé que dans les diodes lasers.

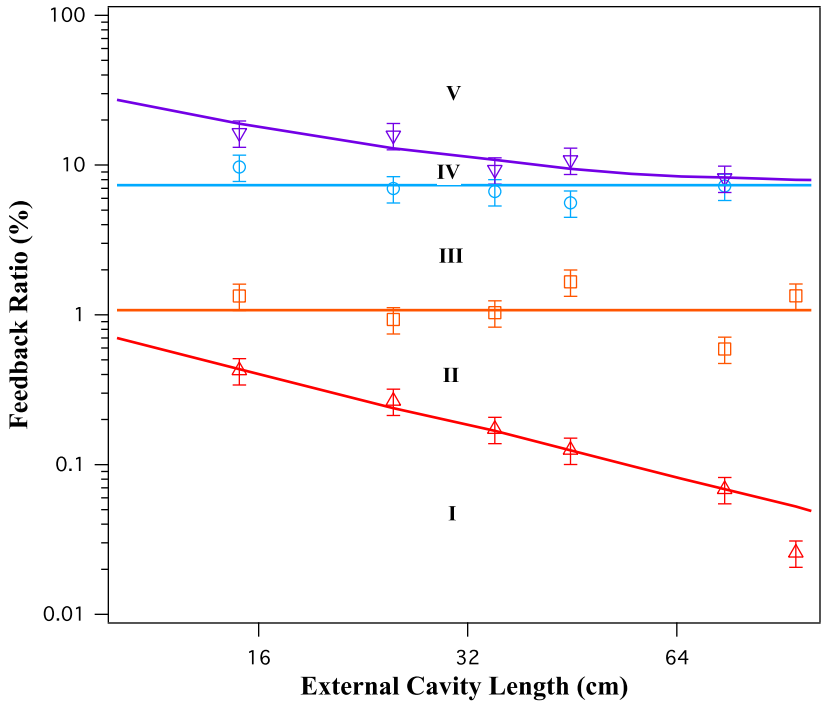

Figure 7.13: Cartographie de réinjection des différents régimes du LCQ DFB, en fonction de la longueur de cavité externe et du taux de réinjection, mesuré à 10°C pour un courant de pompe de 435 mA.

Le régime IV, qui correspond à du chaos dans les diodes lasers, est d'amplitude très réduite dans les LCQ mais est bien présent, on peut donc se demander s'il s'agit également de chaos dans ces structures.

Impact sur les propriétés dynamiques du LCQ

Pour conclure sur l'éventuelle apparition de chaos dans les LCQ moyen infrarouges soumis à de la réinjection optique, on étudie la trace temporelle. On se place à très faible courant, car c'est là que le chaos est le plus susceptible d'apparaître. On choisit $P = 0.02$, avec:

$$P = \frac{\tau_p G_N N_{th}}{2} \left(\frac{I}{I_{th}} - 1 \right) \tag{7.15}$$

et $G_N = N_{pd} G_0$.

A certains paramètres de réinjection, les traces temporelles, représentées en Figure 7.14, font apparaître la superposition de deux périodes, une rapide à la fréquence de la cavité

externe et une lente de quelques dizaines de MHz.

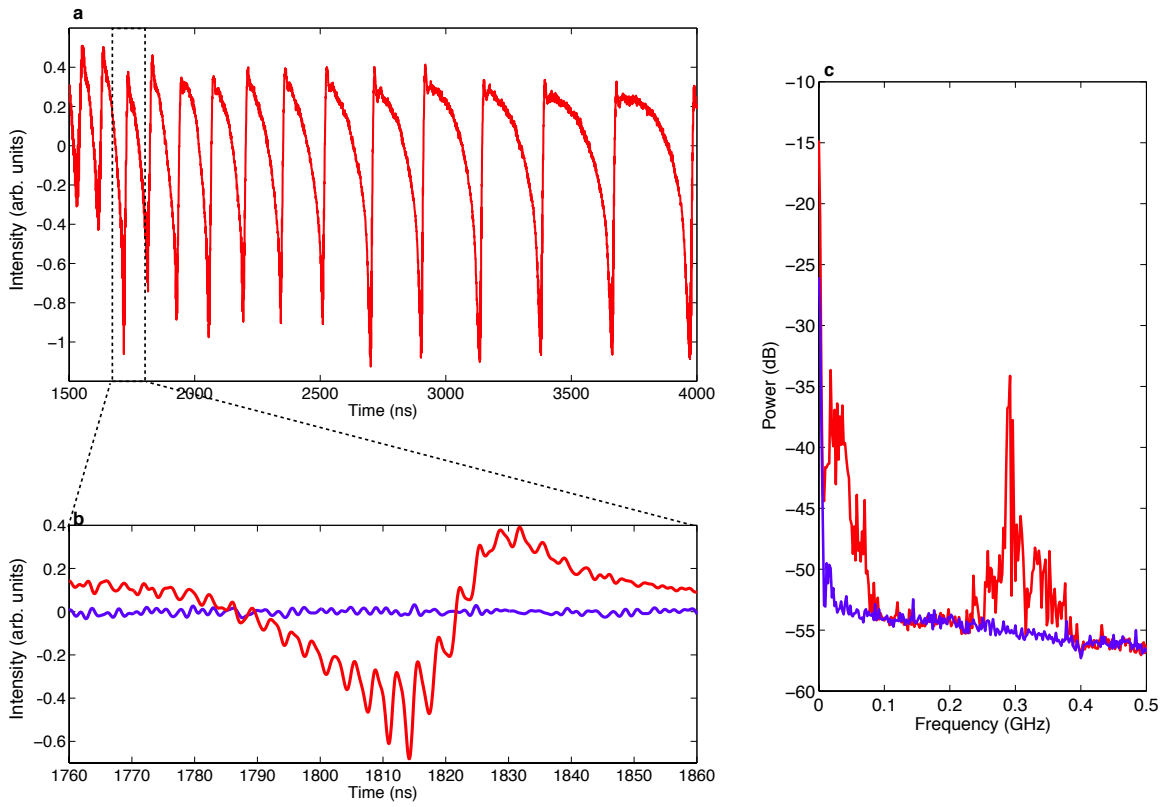

Figure 7.14: Trace temporelle typique pour $P = 0.02$, $L_{ext} = 45$ cm et $f_{ext} = 3.13\%$. a) Trace temporelle montrant des fluctuations lentes. b) Zoom sur une période des fluctuations lentes, des oscillations à la fréquence de la cavité externe apparaissent (en rouge), par rapport au laser solitaire (en bleu). c) Spectres électriques qui confirment l'apparition de deux fréquences d'oscillations, une lente et une rapide pour le laser soumis à de la réinjection (en rouge) par rapport au laser solitaire (en bleu).

L'étude de la statistique de la période entre deux oscillations lentes successives donne un histogramme en exponentielle décroissante, avec une zone interdite pour des faibles périodes [106]. On en conclut qu'il s'agit de fluctuations basses fréquences (LFF) qui sont une signature de chaos. Il y a donc bien apparition de chaos dans un LCQ soumis à de la réinjection pour certains paramètres.

En augmentant progressivement le taux de réinjection, on peut tracer le diagramme de bifurcation expérimental du LCQ DFB sous réinjection, qui représente les extrema d'intensité en fonction du taux de réinjection (voir Figure 7.15). A faible taux de réinjection, le signal

émis est stable, et l'on ne voit que du bruit sur les traces temporelles. Au-delà de la première bifurcation de Hopf, qui a lieu à $f_{ext} = 0.59\%$, le laser commence à osciller à la fréquence de la cavité externe, puis des LFF viennent se superposer à partir de $f_{ext} \geq 2.66\%$. Enfin, vers $f_{ext} = 4\%$, le laser se restabilise.

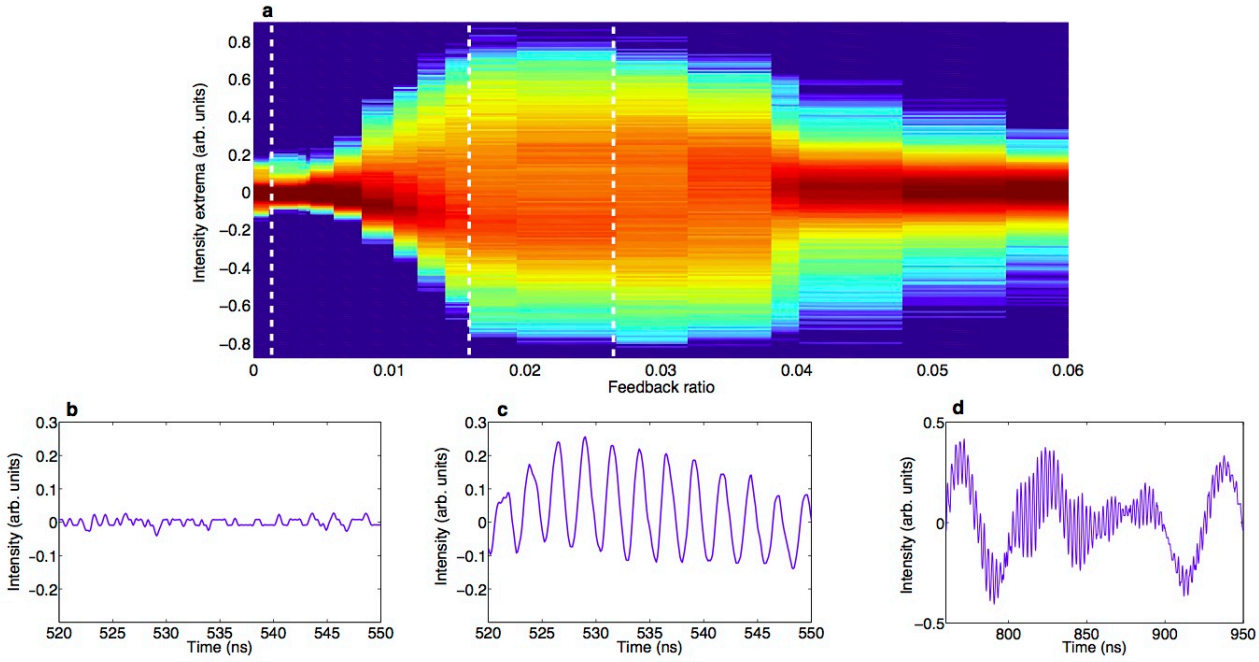

Figure 7.15: Diagramme de bifurcation expérimental pour $P = 0.02$ et $L_{ext} = 35$ cm, et traces temporelles associées. a) Diagramme de bifurcation expériemental, avec en blanc les points où sont enregistrées les traces temporelles. b) Trace temporelle pour $f_{ext} = 0.11\%$, montrant un signal stable. c) Trace temporelle pour $f_{ext} = 1.58\%$, montrant des oscillations à la fréquence de cavité externe. d) Trace temporelle pour $f_{ext} = 2.66\%$, montrant des oscillations à la fréquence de cavité externe et des LFF.

Ce diagramme de bifurcation avec une première bifurcation de Hopf à la fréquence de cavité externe est typique de ceux observés pour les lasers à gaz classe A [111], alors que dans les lasers semiconducteurs classe B, la dynamique est gouvernée par les oscillations de relaxation. Cette observation de dynamique classe A dans les LCQ soumis à de la réinjection peut s'expliquer par l'absence d'oscillation de relaxation dans les LCQ à cause du très fort facteur d'amortissement, et est confirmée par l'étude numérique du diagramme de

bifurcation, où l'on étudie les équations de Lang et Kobayashi [78]:

$$\frac{dY}{ds} = (1 + i\alpha)\, Z\, Y \; + \; \eta \; exp(-i\Omega_0\theta)\, Y(s - \theta) \tag{7.16}$$

$$T\,\frac{dZ}{ds} = P - Z - (1 + 2Z)\; |Y|^2 \tag{7.17}$$

mais avec les paramètres correspondant aux LCQ, notamment un rapport entre temps de vie des porteurs et temps de vie des photons $T = 0.265$. Le diagramme de bifurcation numérique, montré en Figure 7.16, confirme les observations expérimentale, la dynamique classe A et l'apparition de chaos.

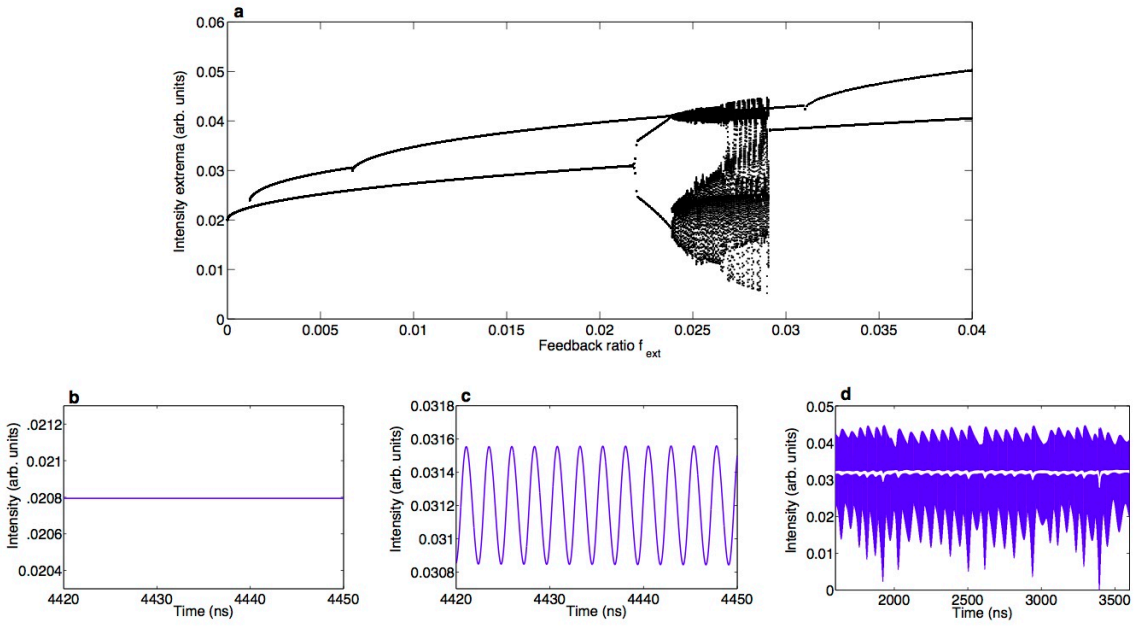

Figure 7.16: Diagramme de bifurcation numérique pour $P = 0.02$ et $L_{ext} = 35$ cm, et traces temporelles associées. a) Diagramme de bifurcation numérique. b) Trace temporelle pour $f_{ext} = 0.11\%$, montrant un signal stable. c) Trace temporelle pour $f_{ext} = 2.14\%$, montrant des oscillations à la fréquence de cavité externe. d) Trace temporelle pour $f_{ext} = 2.59\%$, montrant des oscillations à la fréquence de cavité externe et des LFF.

Les LCQ chaotiques pourraient servir de sources pour de nouvelles applications, telles que des LIDAR chaotiques moyen infrarouges, des contre-mesures imprévisibles ou des communications en espace libre sécurisée par chaos.

Effet sur les LCQ à large zone active

Les LCQ à large zone active sont des sources intéressantes pour des applications telles que les contre-mesures optiques ou la spectroscopie de haute précision car ils délivrent de fortes puissances optiques [145]. Cependant, les propriétés spatiales de ces lasers sont souvent détériorées à cause d'effets thermiques et optiques, dus à l'existence de plusieurs modes transverses dans la cavité, ce qui engendre du beam steering ou du hole burning spatial. Le LCQ ne fonctionne plus sur le mode fondamental et le champ lointain est typiquement bi-lobe, ce qui limite l'usage de ces lasers pour des applications où la pureté spatiale est très importante.

En appliquant de la contre-réaction optique sur ces structures, on peut compenser ces effets dus aux modes transverses d'ordres supérieurs. Par exemple, la Figure 7.17 présente l'évolution du champ proche d'un LCQ de 32 μm de large en fonction du taux de réinjection, par rapport au laser solitaire représenté sur la première courbe, et en fonction de l'angle du miroir de réinjection.

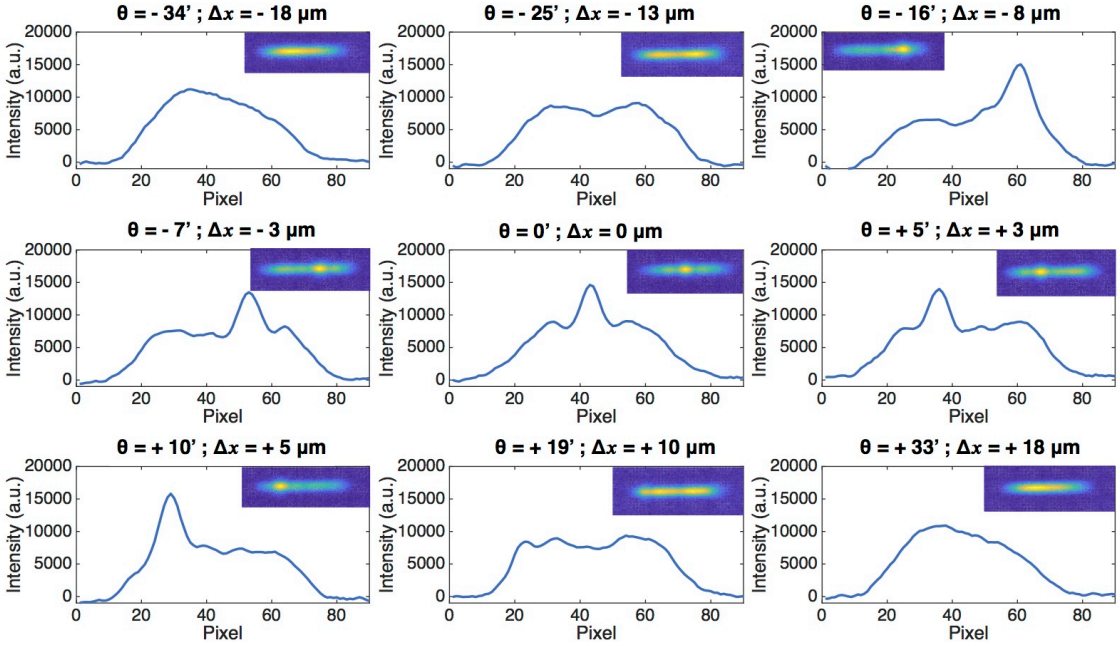

Figure 7.17: Profils de champs proches à la facette du LCQ pour différents angles de réinjection, exprimés à la fois en minutes d'arc et en déplacement sur la facette en fonction de la position centrale. Les courbes en insert correspondent aux champs proches enregistrés sur la caméra.

De plus, réaliser un filtrage spatial en plaçant un diaphragme dans la cavité externe permet de sélectionner uniquement la partie centrale du faisceau à réinjecter et de favoriser le mode fondamental, comme illustré sur la Figure 7.18.

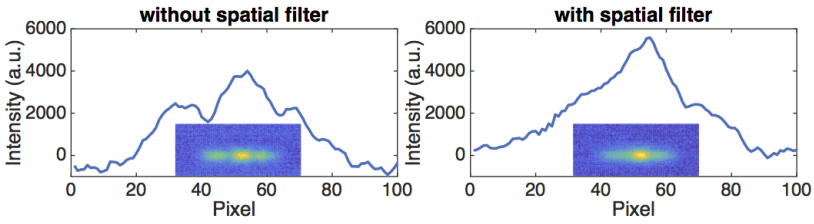

Figure 7.18: Champs proches à la facette du laser pour une réinjection centrée et deux ouvertures du diaphragme. Le diagramme est complètement ouvert (a) et partiellement fermé pour transmettre uniquement le lobe central (b).

Sur un laser moins large, de 14 μm, mais présentant un fort beam steering, correspondant à une non-uniformité du gain dû à un champ électrique qui est une combinaison linéaire des champs des différents modes transverses, on parvient avec une réinjection centrée à compenser complètement ce beam steering, et le laser émet parfaitement sur le mode fondamental, comme le montre la Figure 7.19.

Comme sur le LCQ à zone active plus étroite, la réinjection optique peut également modifier les propriétés dynamiques des lasers à large zone active, elle pourrait notamment faire apparaître de la filamentation dans les LCQ. Une étude dynamique sera donc nécessaire pour compléter ces observations sur les propriétés spatiales.

Injection optique dans les lasers à cascade quantique

Comme la réinjection optique, l'injection optique, qui consiste à envoyer la lumière d'un premier laser maître dans un second laser esclave permet de modifier significativement les propriétés d'émission du laser esclave. On dit que ce dernier est verrouillé lorsque sa longueur d'onde se calque sur celle du maître. Dans la zone de verrouillage, les propriétés de l'esclave sont améliorées, notamment en terme de finesse spectrale, de bande passante de modulation ou de bruit d'intensité.

En négligeant l'émission spontanée, quand l'esclave est soumis à un champ électrique $E = \sqrt{S}e^{i\phi}e^{i\omega_{SL}t}$ et le maître à un champ $E_{inj} = \sqrt{S_{inj}}e^{i\omega_{ML}t}$, les équations de taux du LCQ

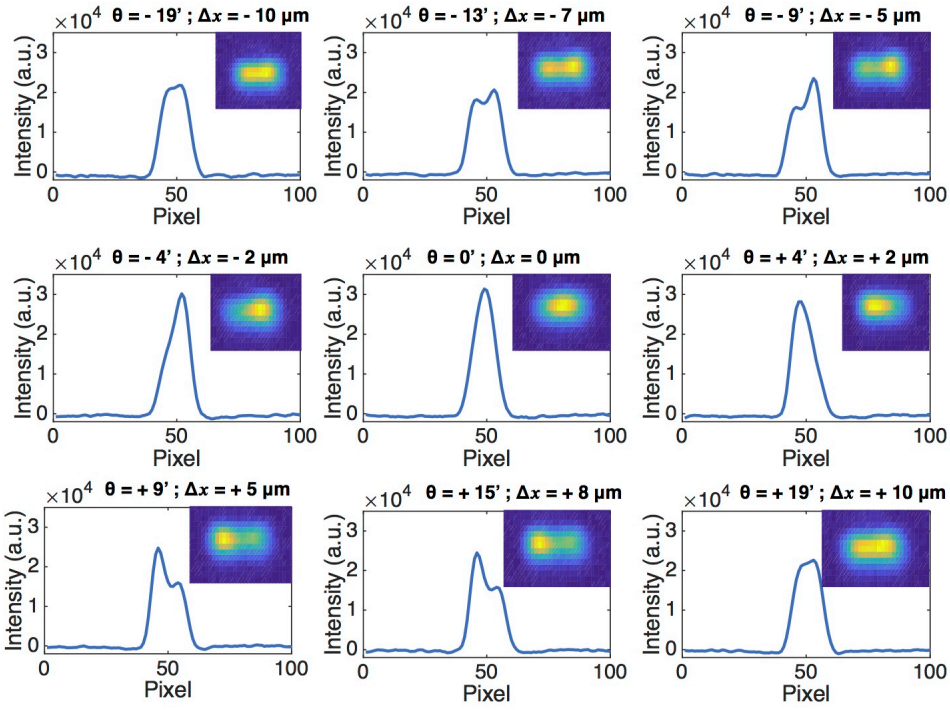

Figure 7.19: Effet de la réinjection optique sur un LCQ de 14 μm de large qui présente un fort beam steering.

soumis à de l'injection sont :

$$\frac{dN_3}{dt} = \eta \frac{I}{q} - \frac{N_3}{\tau_{32}} - \frac{N_3}{\tau_{31}} - G_0 \Delta N S \tag{7.18}$$

$$\frac{dN_2}{dt} = \frac{N_3}{\tau_{32}} - \frac{N_2}{\tau_{21}} + G_0 \Delta N S \tag{7.19}$$

$$\frac{dN_1}{dt} = \frac{N_3}{\tau_{31}} + \frac{N_2}{\tau_{21}} - \frac{N_1}{\tau_{out}} \tag{7.20}$$

$$\frac{dS}{dt} = \left(N_{pd} G_0 \Delta N - \frac{1}{\tau_p} \right) S + 2k\sqrt{S_{inj} S} \cos(\phi) \tag{7.21}$$

$$\frac{d\phi}{dt} = \frac{\alpha}{2} \left(N_{pd} G_0 \Delta N - \frac{1}{\tau_p} \right) - \Delta\omega - k\sqrt{\frac{S_{inj}}{S}} \sin(\phi) \tag{7.22}$$

où N_j est la densité de porteurs du niveau j, avec $\Delta N = N_3 - N_2$, η est l'efficacité de conversion, I est le courant de pompe. τ_{ij} correspond au temps de vie des porteurs entre les niveaux i et j, τ_{out} est le temps de fuite de l'électron à travers l'injecteur, τ_p est le temps de vie des photons dans la cavité. G_0 correspond au gain modal net sur une période, N_{pd} au nombre de périodes et α au couplage phase-amplitude. $\Delta\omega$ est le désaccord de fréquence,

défini par $\Delta\omega = \omega_{ML} - \omega_{SL}$. Enfin, k est le coefficient d'injection:

$$k = \frac{1}{\tau_{in}} 2C_l \tag{7.23}$$

avec τ_{in} le temps aller-retour dans la cavité laser et C_l le coefficient de couplage externe, défini comme dans le cas de la réinjection.

L'analyse analytique de ces équations de taux [197] donne les limites de la zone de verrouillage, comme représenté en Figure 7.20 pour différents jeux de paramètres. Ici encore, le LCQ a une réponse de type classe A à l'injection optique. En effet, le laser esclave est toujours verrouillé pour un désaccord de fréquence nul, et il n'y a pas de zone de chaos ni de verrouillage instable, uniquement des zones de bistabilités entre deux solutions stables ou entre une solution stable et une solution stable et une solution périodique. Ces zones de bistabilités sont situées entre la courbe de Saddle-Node (en bleu) et les courbes de bifurcation de Hopf (en rouge).

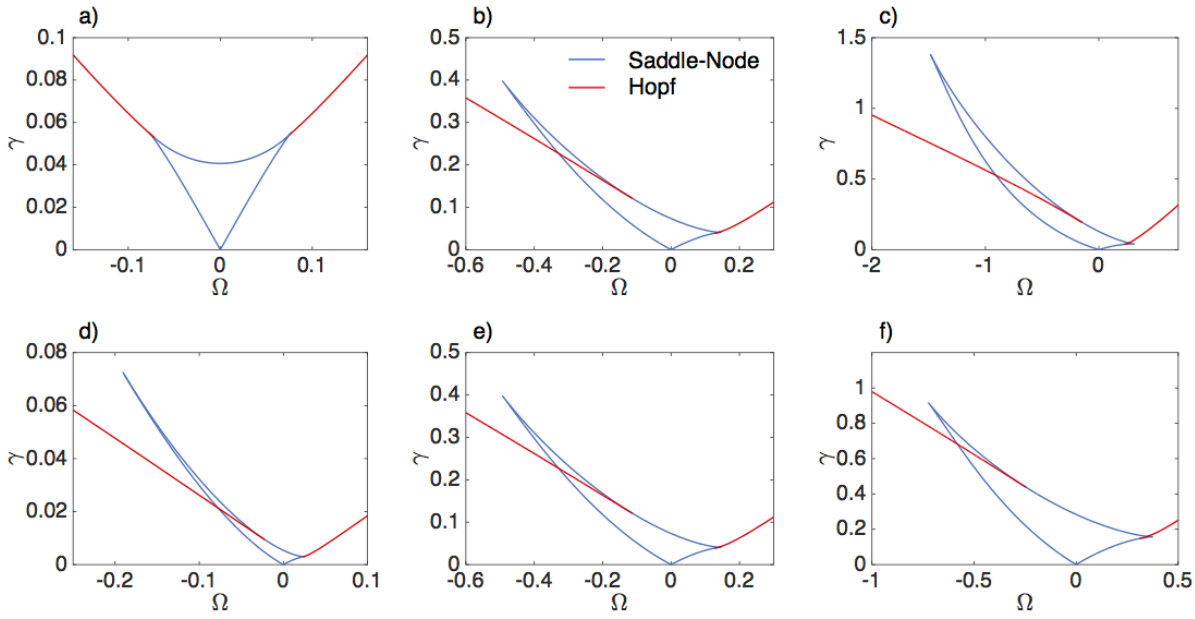

Figure 7.20: Simulations analytiques pour un LCQ Fabry-Perot soumis à de l'injection optique. Première ligne: courant de pompe constant $I = 1.5$ A et a) $\alpha = 0$, b) $\alpha = 1.5$ and c) $\alpha = 3$. Deuxième ligne: $\alpha = 1.5$ fixé et d) $I = 1.25$ A, e) $I = 1.5$ A, f) $I = 2$ A.

Une autre méthode pour obtenir la carte de verrouillage d'un LCQ sous injection optique

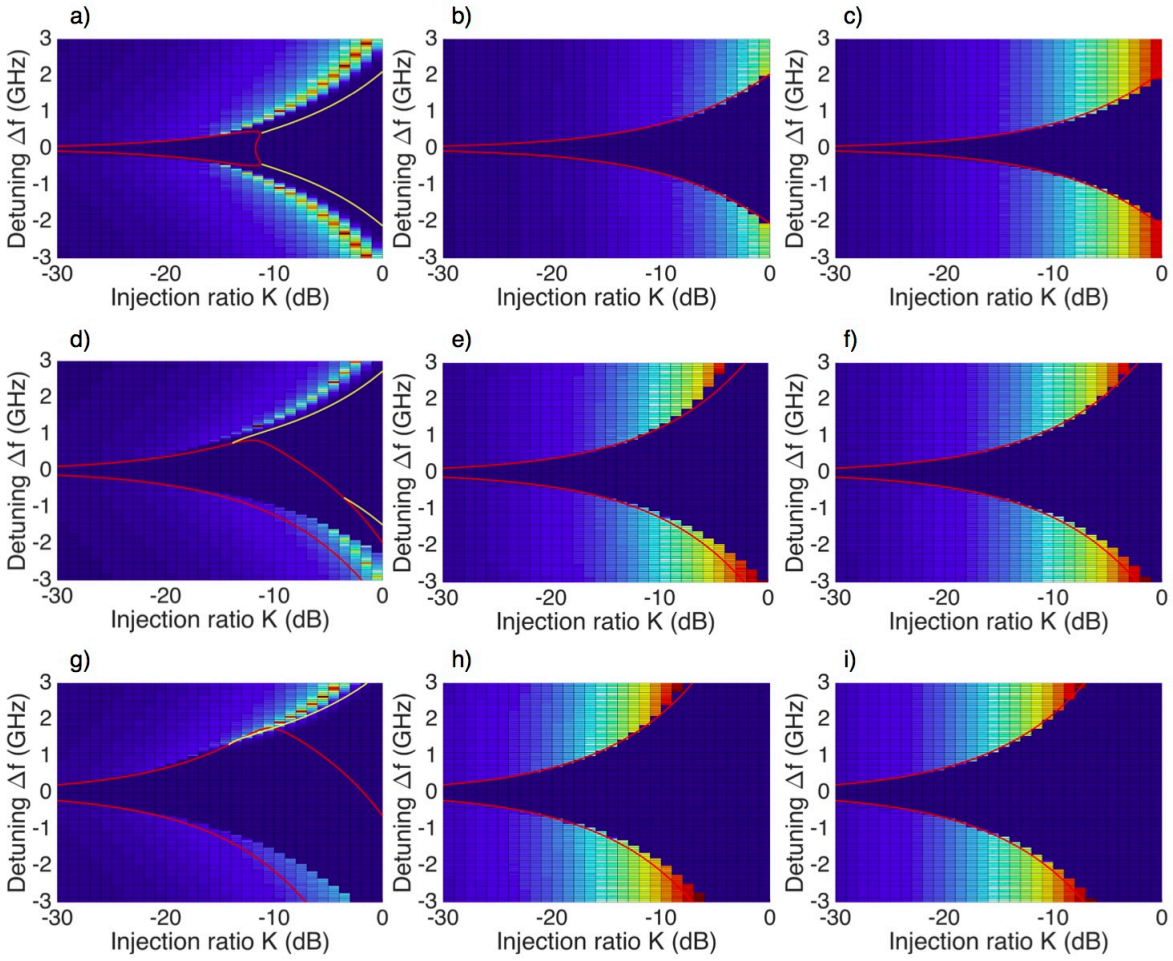

Figure 7.21: Simulations numériques superposées aux résultats analytiques (rouge pour Saddle-Node et jaune pour Hopf) pour le LCQ Fabry-Perot soumis à de l'injection optique. Première ligne : $\alpha = 0$ et a) $I = 1.25$ A, b) $I = 1.5$ A, c) $I = 2$ A. Deuxième ligne : $\alpha = 1.5$ et d) $I = 1.25$ A, e) $I = 1.5$ A, f) $I = 2$ A. Troisième ligne : $\alpha = 3$ et g) $I = 1.25$ A, h) $I = 1.5$ A, i) $I = 2$ A.

est de résoudre numériquement les équations de taux en chaque point $(K,\Delta f)$, avec $K = \sqrt{S_{inj}/S}$ le taux d'injection et Δf le désaccord de fréquence entre le maître et l'esclave.

Cette méthode de simulation numérique donne non seulement accès aux limites de la zone de verrouillage, mais également au comportement du LCQ en dehors de cette zone, comme illustré sur la Figure 7.21 où la carte d'injection est tracée pour différents jeux de paramètres. Les limites de verrouillage à fort courant coïncident bien avec les courbes de Saddle-Node obtenues par simulation analytique. Le très léger décalage entre les deux courbes peut s'expliquer par les approximations réalisées dans le cas analytique.

De plus, hors de la zone de verrouillage on obtient des oscillations périodiques, qui ne sont

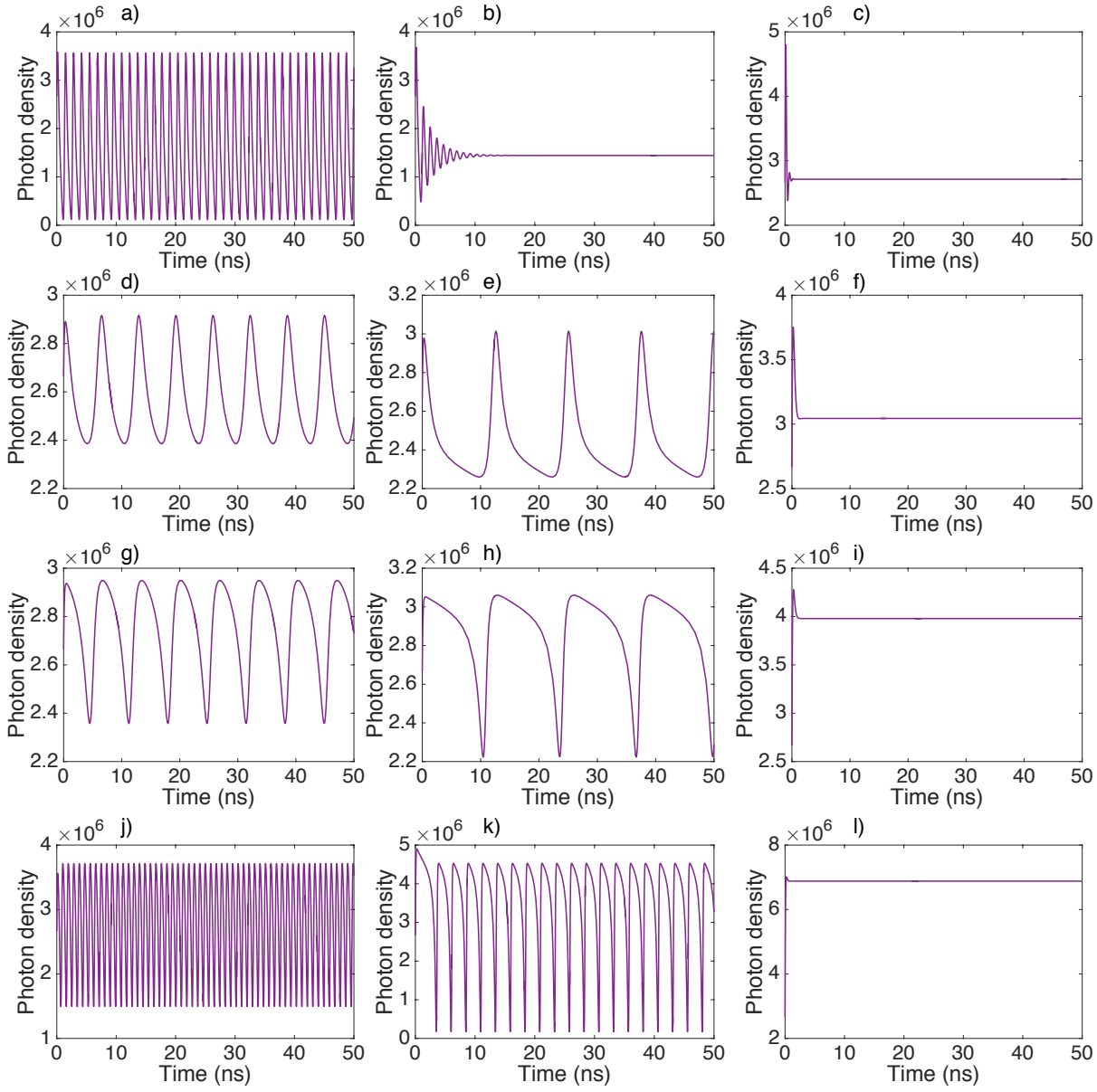

Figure 7.22: Traces temporelles numériques pour le LCQ Fabry-Perot soumis à de l'injection optique, avec $\alpha = 1.5$ and $I = 1.25$ A . Première ligne : $\Delta f = +1.05$ GHz et a) $K = -14$ dB, b) $K = -13$ dB, c) $K = -6$ dB. Deuxième ligne : $\Delta f = +0.2$ GHz et d) $K = -30$ dB, e) $K = -27$ dB, f) $K = -15$ dB. Troisième ligne : $\Delta f = -0.2$ GHz et d) $K = -29$ dB, e) $K = -26$ dB, f) $K = -12$ dB. Quatrième ligne : $\Delta f = -1.2$ GHz et d) $K = -15$ dB, e) $K = -8$ dB, f) $K = -2$ dB.

pas parfaitement sinusoïdales et dont la forme dépend du désaccord et du taux d'injection, comme illustré en Figure 7.22. Au contraire, à faible courant juste au-dessus du seuil, la bifurcation de Hopf de la simulation analytique apparaît dans une gamme raisonnable de paramètres, et cela correspond sur les traces temporelles numériques à des oscillations périodiques sinusoïdales à la fréquence du désaccord entre le maître et l'esclave. On observe également ponctuellement des oscillations de très forte amplitude. Opéré très proche du seuil, un LCQ soumis à de l'injection optique pourrait donc servir de source pour un oscillateur photonique accordable en variant le désaccord ou comme générateur d'ondes scélérates.

Cependant, des mesures expérimentales restent nécessaires pour vérifier que toutes ces dynamiques ont effectivement lieu dans un LCQ soumis à de l'injection optique.

Conclusions et perspectives

Cette thèse a donc montré que la réinjection optique peut grandement améliorer les propriétés d'émission des LCQ en terme de puissance optique, de courant de seuil ou de pureté spectrale. De plus, la réinjection permet d'améliorer la qualité spatiale de faisceau des LCQ à large zone active, qui fournissent des sources de forte puissance. En ce sens, un LCQ sous réinjection optique devient une source moyen infrarouge à hautes performances pour des applications comme les contre-mesures optiques, la spectroscopie de gaz ou les communications en espace libre.

Cependant, la réinjection optique peut aussi induire une déstabilisation du LCQ, avec une émission multimode, voire chaotique, qu'il faut éviter pour les applications citées précédemment. Notamment, une fibre optique moyen infrarouge en chalcogénure peut générer jusqu'à 15% de réinjection parasite. Il est donc crucial de généraliser l'utilisation des isolateurs optiques moyen infrarouge pour empêcher une réinjection non contrôlée. Au contraire, un LCQ chaotique peut être une source pour de nouvelles applications, telles que du LIDAR chaotique moyen infrarouge, des communications en espace libre sécurisées par chaos ou des contre-mesures imprévisibles.

D'après les simulations réalisées, l'injection optique pourrait également être exploitée dans les LCQ pour améliorer les propriétés d'émission, et notamment la bande passante de

modulation, dans la zone de verrouillage. De plus, de nouvelles dynamiques apparaissent hors de la zone de verrouillage, avec une émission périodique à faible courant dont la fréquence est celle du désaccord entre le maître et l'esclave. Un LCQ sous injection optique non-verrouillé pourrait donc servir de sources à d'autres applications, comme un générateur d'ondes scélérates ou un oscillateur photonique accordable.

Photonique non-linéaire dans les lasers à cascade quantique moyen infrarouges

Louise JUMPERTZ

RESUME : Les lasers à cascade quantique émettant dans le moyen-infrarouge sont des lasers semiconducteurs unipolaires qui sont devenus des sources couramment utilisées pour des applications telles que la spectroscopie de gaz, les communications en espace libre ou les contre-mesures optiques. Appliquer une perturbation externe, typiquement une contre-réaction optique ou de l'injection optique, entraîne une forte modification des propriétés d'émission du laser à cascade quantique. La contre-réaction optique influe sur les propriétés statiques du laser Fabry-Perot ou à contre-réaction répartie, conduisant à une augmentation de la puissance, à une diminution du seuil, à une modification du spectre optique qui peut devenir monomode ou multimode, et à une amélioration de la qualité de faisceau dans les lasers à ruban large fortement multimode transverses. Cela induit également un comportement dynamique différent, et un laser à cascade quantique soumis à de la contre-réaction peut osciller périodiquement ou même devenir chaotique : ce travail présente la toute première observation d'instabilités optiques dans le moyen-infrarouge. De plus, une étude numérique de l'injection optique montre que les lasers à cascade quantique peuvent se verrouiller optiquement sur une plage de plusieurs gigahertz, sur laquelle leur stabilité devrait être accrue et leur bande passante de modulation significativement augmentée. Une dynamique prometteuse apparaît également en dehors de la zone de verrouillage, avec l'apparition d'oscillations périodiques à une fréquence accordable ainsi que des événements isolés de forte intensité. Un laser à cascade quantique soumis à un contrôle externe peut donc être une source très performante pour les applications moyen-infrarouges usuelles, mais pourrait aussi en adresser de nouvelles, telles que des oscillateurs photoniques accordables, des générateurs d'événements rares, des LIDAR chaotiques, des communications sécurisées par chaos ou des contre-mesures imprévisibles.

MOTS-CLEFS : laser à cascade quantique, réinjection optique, dynamique non-linéaire

ABSTRACT : Mid-infrared quantum cascade lasers are unipolar semiconductor lasers, which have become widely used sources for applications such as gas spectroscopy, free-space communications or optical countermeasures. Applying external perturbations such as optical feedback or optical injection leads to a strong modification of the quantum cascade laser properties. Optical feedback impacts the static properties of mid-infrared Fabry-Perot and distributed feedback quantum cascade lasers, inducing power increase, threshold reduction, modification of the optical spectrum, which can become either single- or multimode, and enhanced beam quality of broad-area transverse multimode lasers. It also leads to a different dynamical behavior, and a quantum cascade laser subject to optical feedback can oscillate periodically or even become chaotic : this work provides the first analysis of optical instabilities in the mid-infrared range. A numerical study of optical injection furthermore proves that quantum cascade lasers can injection-lock over a few gigahertz, where they should experience enhanced stability and especially improved modulation bandwidth. Furthermore, some promising dynamics appear outside the locking range with periodic oscillations at a tunable frequency or high-intensity events. A quantum cascade laser under external control could therefore be a source with enhanced properties for the usual mid-infrared applications, but could also address new applications such as tunable photonic oscillators, extreme events generators, chaotic LIDAR, chaos-based secured communications or unpredictable countermeasures.

KEY-WORDS : quantum cascade laser, optical feedback, nonlinear dynamics

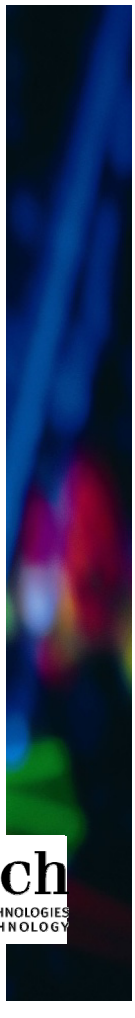

TELECOM ParisTech

EDiTE

ParisTech
INSTITUT DES SCIENCES ET TECHNOLOGIES
PARIS INSTITUTE OF TECHNOLOGY